

8-2010

HIGH TEMPERATURE RARE EARTH COMPOUNDS: SYNTHESIS, CHARACTERIZATION AND APPLICATIONS IN DEVICE FABRICATION

Joseph R. Brewer

University of Nebraska - Lincoln, jrbrewer6@gmail.com

Follow this and additional works at: <http://digitalcommons.unl.edu/chemistrydiss>



Part of the [Inorganic Chemistry Commons](#), and the [Materials Chemistry Commons](#)

Brewer, Joseph R., "HIGH TEMPERATURE RARE EARTH COMPOUNDS: SYNTHESIS, CHARACTERIZATION AND APPLICATIONS IN DEVICE FABRICATION" (2010). *Student Research Projects, Dissertations, and Theses - Chemistry Department*. 9. <http://digitalcommons.unl.edu/chemistrydiss/9>

This Article is brought to you for free and open access by the Chemistry, Department of at DigitalCommons@University of Nebraska - Lincoln. It has been accepted for inclusion in Student Research Projects, Dissertations, and Theses - Chemistry Department by an authorized administrator of DigitalCommons@University of Nebraska - Lincoln.

HIGH TEMPERATURE RARE EARTH COMPOUNDS: SYNTHESIS,
CHARACTERIZATION AND APPLICATIONS IN DEVICE
FABRICATION

by

Joseph Reese Brewer

A DISSERTATION

Presented to the Faculty of

The Graduate College at the University of Nebraska

In Partial Fulfillment of Requirements

For the Degree of Doctor of Philosophy

Major: Chemistry

Under the Supervision of Professor Chin Li “Barry” Cheung

Lincoln, Nebraska

August, 2010

HIGH TEMPERATURE RARE EARTH COMPOUNDS: SYNTHESIS, CHARACTERIZATION AND APPLICATIONS IN DEVICE FABRICATION

Joseph Reese Brewer, Ph. D.

University of Nebraska, 2010

Adviser: Chin Li “Barry” Cheung

As the area of nanotechnology continues to grow, the development of new nanomaterials with interesting physical and electronic properties and improved characterization techniques are several areas of research that will remain vital for continued improvement of devices and the understanding in nanoscale phenomenon. In this dissertation, the chemical vapor deposition synthesis of rare earth (RE) compounds is described in detail. In general, the procedure involves the vaporization of a $RECl_x$ ($RE = Y, La, Ce, Pr, Nd, Sm, Gd, Tb, Dy, Ho$) in the presence of hydride phase precursors such as decaborane and ammonia at high temperatures and low pressures. Unlike traditional single source precursor techniques such as metal-organic chemical vapor deposition, the materials produced are of extremely high chemical purity. The crystallographic orientation of as-synthesized rare earth hexaboride nanostructures and gadolinium nitride thin films was controlled by judicious choice of specific growth substrates and modeled by analyzing x-ray diffraction powder patterns and crystallographic models.

The vapor-liquid-solid mechanism was used in combination with the chemical vapor deposition process to synthesize single crystalline rare earth hexaboride nanostructures. Unlike previously reported synthetic techniques to generate rare earth hexaborides, my synthesis provided control over the tip diameter of the nanomaterials,

was applicable to all available rare earth metals and utilized a chemical scheme that was much less toxic. Furthermore, the synthesis provided the first ever doped rare earth hexaboride nanowires. The as produced materials showed excellent electronic properties and could be applicable to many different types of electronic applications.

The rare earth hexaboride nanostructures were then implemented into two existing technologies to enhance their characterization capabilities. First, the rare earth hexaboride nanowires were used as a test material for the development of a TEM based local electrode atom probe tomography (LEAP) technique. The TEM based LEAP technique is the first to combine atomic resolution crystallographic imaging with angstrom scale 3D compositional mapping. This technique also provided some of the first quantitative compositional information of the rare earth hexaboride systems and is applicable to a wide range of nanowire materials. Second, due to the rigidity and excellent conductivity of the rare earth hexaborides, nanostructures were grown onto tungsten wires for the development of robust, oxidation resistant nanomanipulator electronic probes for semiconductor device failure analysis.

Acknowledgements

I would like to acknowledge everyone who has helped me in completing my doctoral studies at the University of Nebraska. First and foremost, I would like to extend my unconditional gratitude to my wife Kayla and my three children Brianna, Nicholette and Landon; for without their support through this long and often trying process, none of this would have been possible.

I would especially like to thank my advisor, Dr. Chin Li “Barry” Cheung for his true mentorship throughout this process. He has helped increase my understanding of materials synthesis and characterization to a level I did not think possible when I first joined his research group and has provided me all the tools necessary to succeed after graduation. I am also very grateful to my exceptional doctoral committee and wish to thank the late Dr. Rebecca Lai, Dr. Wonyoung Choe, Dr. Yongfeng Lu and Dr. T. Adrian George for their support, encouragement, discussions and collaborations on my research. I am extremely grateful to my collaborator, Dr. David Diercks at the University of North Texas, for his world class characterization of our nanostructured materials.

I would like to thank the Physics/Chemistry and Astronomy instrument shop and the Department of Chemistry’s electronic shop for all their help. Their assistance in equipment design and manufacturing and their advice on circuit designs has been invaluable to my success as a graduate student. I would also like to thank the Morrison Microscopy Core Research Facility and especially You “Joe” Zhou, Han Chen and Terri Fangman for all their assistance with in SEM and TEM imaging.

I would like to thank my laboratory group members, Gonghua Wang, Neil Lawrence, Hsin Yu Li, Zane Gernhart, Robert Jacobberger and Mike Thompson for all

their help and for their insightful discussions. I would like to especially thank Zane, Robert and Hsin for all the work they have done assisting in the assembly and maintenance of equipment and the synthesis materials.

I would also like to thank the educators that have inspired me to pursue a career in chemistry. I am grateful to Mr. Hoff, my high school physics and chemistry instructor, for introducing me to the physical sciences and encouraged me to participate in after school science activities. I am extremely grateful to Dr. Ryan Winburn and Dr. Robert Crackel at Minot State University for all their support and guidance when I was an undergraduate and convincing me to become a chemist instead of a physicist.

Finally, I would like to dedicate this dissertation to my beloved family (Kayla, Brianna, Nicholette and Landon) who I can never thank enough for their unconditional love and support and to the memory of Dr. T. Adrian George who inspired me to continue my doctoral studies.

Contents

Chapter 1	1
1.1 Introduction.....	1
1.2 Theory and Background.....	3
1.2.1 Electrical Resistance	3
1.2.2 Electrical Resistivity	4
1.2.3 Van der Pauw and Hall effect	7
1.2.3.1 Van der Pauw	9
1.2.3.2 Hall effect.....	12
1.2.4 X-ray diffraction	16
1.3 Focus of this dissertation	22
1.4 References.....	23
Chapter 2: Synthesis of rare earth hexaboride by low pressure chemical vapor deposition: From nanostructures to thin films.....	26
2.1 Introduction.....	26
2.2 Nanostructured materials synthesis mechanisms.....	29
2.3 Synthesis of REB ₆ micro- and nanostructures	31
2.3.1 Introduction.....	31
2.3.2 Synthesis development: Pt catalyzed growth.....	36
2.3.3 Experimental methods	43
2.3.4 Results.....	45
2.3.4.1 Structure identification and characterization	45
2.3.4.2 Growth mechanism	51
2.3.5 General synthesis of REB ₆ nanostructures: Pd-catalyzed growth	56

2.3.6 Experimental methods	64
2.3.7 Results.....	64
2.3.7.1 Pd-catalyzed growth.....	64
2.3.7.2 Electronic properties	70
2.3.7.3 Temperature dependent growth morphology	74
2.3.7.4 Substrate directed crystallographic orientation.....	93
2.4 Conclusions.....	107
2.5 References.....	108
2.6 Appendix.....	113
Chapter 3: Local electrode atom probe tomography	134
3.1 Introduction.....	134
3.2 Experimental methods	140
3.2.1 LEAP technique development	140
3.2.2 LEAP data analysis	144
3.3 Results.....	144
3.4 Y doped NdB_6	155
3.5 Conclusions.....	161
3.6 References.....	162
Chapter 4: REB_6 nanostructure device application	164
4.1 REB_6 nanowire electron emitters.....	164
4.1.1 Introduction.....	164
4.1.2 Experimental methods	170
4.1.3 Results.....	172
4.1.4 Conclusions.....	179
4.2 REB_6 nanoobelisks as nanomanipulator probes	179

4.2.1 Introduction.....	179
4.2.2 Experimental methods	182
4.2.2.1 Tungsten probe preparation	182
4.2.2.2 REB ₆ nanoobelisk growth.....	185
4.2.3 Results.....	185
4.3 Conclusions.....	190
4.4 References.....	191
Chapter 5: Growth of gadolinium nitride thin films by chemical vapor deposition	194
.....	
5.1 Introduction.....	194
5.2 Experimental methods	196
5.3 Characterization	199
5.3.1 X-ray diffraction	199
5.3.2 Growth rate	200
5.3.3 Surface structure	202
5.3.4 Growth model	202
5.4 Conclusion	206
5.5 References.....	208
Chapter 6: Conclusions	211
6.1 Summary and future directions.....	211

Chapter 1

1.1 Introduction

One of the most important processes in the development of modern technology is the synthesis of new high-temperature materials with unique physical and electronic properties.¹ Materials with semiconducting and metallic transport properties, high melting points ($>1400^{\circ}\text{C}$) and low reactivities are of particular interest for application as robust electrical interconnects in electronic devices. Promising materials of this type are rare-earth compounds of scandium, yttrium and the lanthanides with non-metal compounds such as borides, nitrides and sulfides.

Though referred to traditionally as rare, this group of metals are as abundant as some of the first row transition metals such as copper and nickel.² Even the “rarest” of the metals, lutetium, is more abundant than silver in the earth’s crust.³ (Table 1) Scandium, yttrium and the lanthanides are close in location on the periodic table, lending to their similar physical and chemical properties. They are all transition metals with unfilled internal electron shells: Yttrium has an unfilled 4-*d* shell, lanthanum has an unfilled 5-*d* shell, and the lanthanides have unfilled 4-*f* levels, no 5-*f* shell at all and several with only one 5-*d* electron.¹ These similarities extend beyond the metals and are manifested in the compounds they form.

Compounds formed by the reactions of these rare-earth metals with non-metals can be characterized by the superposition of various types of bonds which in turn determine the resultant physical and chemical properties. Of the greatest interest is that fact that the lanthanides possess deep lying unfilled 4-*f* electron shells that cannot directly take part in

Table 1.1 Abundance of rare earth elements in the Earth's upper crust

<u>Element</u>	<u>Atomic Symbol</u>	<u>Atomic Number</u>	<u>Upper Crust Abundance, ppm^{2,3}</u>
Yttrium	Y	39	22
Lanthanum	La	57	30
Cerium	Ce	58	64
Praseodymium	Pr	59	7.1
Neodymium	Nd	60	26
Promethium	Pm	61	not yet found in nature
Samarium	Sm	62	4.5
Europium	Eu	63	0.88
Gadolinium	Gd	64	3.8
Terbium	Tb	65	0.64
Dysprosium	Dy	66	3.5
Holmium	Ho	67	0.80
Erbium	Er	68	2.3
Thulium	Tm	69	0.33
Ytterbium	Yb	70	2.2
Lutetium	Lu	71	0.32

chemical bonding.¹ However, these 4-*f* electrons can influence the character of the chemical bonds formed and thus the electronic properties of the resulting compounds through *f* → *d* transitions due to the closeness of the 4-*f* and 5-*d* energy levels.

The wide variations in bonding character due to these *f* → *d* transitions and low lying unfilled d-states in rare-earth compounds are what provide for the possibility of varying the chemical and physical properties of these compounds and producing materials with specific properties. To this end, rare-earth compounds have found many applications ranging from electron emitting materials, reflective and refractory coatings, electron filters and oxidation resistant electrodes for electronic devices. Recently, researchers have found renewed interest in rare earth hexaborides and mononictides as materials synthesis has decreased to the nanoscale and new electronic device architectures are developed.⁴⁻¹⁴

1.2 Theory and background

1.2.1 Electrical resistance

Electrical resistance is the measure of the opposition to the flow of electrons through a circuit. The flow of electrons, defined as current (*I*), is directly proportional to the potential difference (*V*) applied across a circuit and inversely proportional to the resistance (*R*) between them. The mathematical relationship is known as Ohm's Law and is described by the equation:

$$I = V/R \tag{1.1}$$

where the units of *I*, *V* and *R* are amps, volts and ohms respectively.

Ideally, comparison of different materials electronic properties can be made as the resistance does not depend on the amount of current passing through or the potential

difference applied across the object.¹⁵ The electrical resistance would therefore be a fundamental property of a material and can be used for characterization purposes. However, this is only true if the materials under comparison have identical dimensions.

Besides dimensions, the electrical resistance can also be altered by several other factors such as thermal motion (vibration) of atoms in the crystal lattice and defects and impurity atoms to name a few. In metals, the Fermi level (the level of highest electron density) at 0 Kelvin is the same for all the atoms and allows for relatively easy passage of electrons from one atom to the next. Thermal motion of atoms, which slightly displaces the atom from its preferred crystalline position, and dopant/impurity atoms, which perturb the well aligned Fermi levels, leads to increased scattering centers in the material and increased resistance.

In semiconductors however, the Fermi level is in between the valence band and conduction band. This means that for an intrinsic semiconductor at 0 Kelvin, its resistance will be infinite as there is no electron population in the conduction band. However, once the semiconductor is doped (extrinsic) or the temperature is increased, electrons density within the conduction band is increased and the resistance of the semiconductor will then decrease. The phenomenon of increased or decrease resistance with an increase in temperature is one of the traditional ways of identifying charge transport properties and determining if a material is a metal or semiconductor.

1.2.2 Electrical resistivity

Utilizing measurements of resistance to compare material quality or current carrying capabilities of different materials is problematic however, as identical dimensions are necessary to make accurate comparisons. To further improve the characterization of

materials, a more intrinsic measurement (which does not depend on sample shape) was developed known as resistivity. Quantitatively, resistivity (ρ) is defined as the proportionality constant between the electric field (voltage(V) / length (l)) impressed across a homogenous material and the total particle current per unit area (current(I) / cross-sectional area(A)) flowing in the material.¹⁶

$$\rho = (V/l) / (I/A) \quad (1.2)$$

By applying Ohm's law, resistivity can be related to measured resistance by the equation:

$$\rho = R * (l/A) \quad (1.3)$$

Unfortunately, measurement of resistivity by this straight forward approach is quite difficult as the semiconductor or metal needs to be formed into a bar with precise dimensions, the resistance to current flow due to the contacts needs to also be determined, and is not adaptable or practical for current state-of-the-art device dimensions and architectures.¹⁶ (Figure 1.1)

Due to these limitations, a new method, more adaptable to industry requirements, was developed called the four-point probe technique. In this method, the measurement involved applying a known current between two contacts and measuring the potential difference between another set of contacts. By conducting the measurement in this manner, the contact resistance could be neglected and the technique was adaptable to a wide range of materials dimensions and shapes.

The four-point collinear probe technique, a specific type of four-point probe technique, is the most widely employed of the resistivity measurement techniques. In

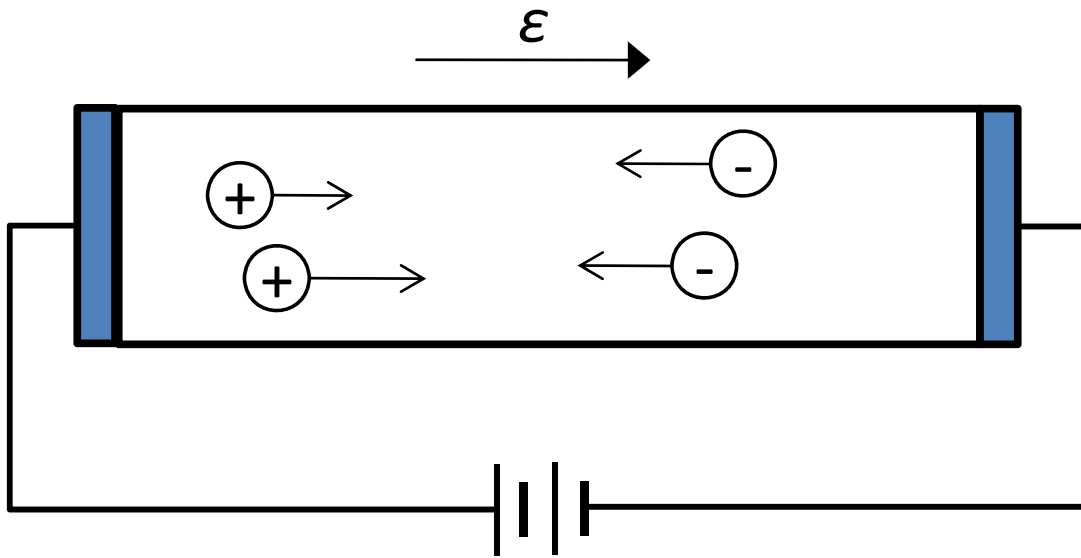


Figure 1.1 Schematic representation of a bar type resistivity measurement showing directionality of the charge flow upon application of an electric field.

general, 4 evenly spaced collinear probes are brought in contact with the surface of the material to be tested. (Figure 1.2) A known current, I , is passed through the two outer probes while the potential difference V developed is measured between the two interior probes.^{16, 17} The measurement is conducted in the forward and reverse direction to ensure contact quality to the sample. An average resistivity is then calculated from:

$$\rho = 2\pi s(V/I)f \quad (1.4)$$

where s is the probe-to-probe spacing and f is a correction factor. The correction factor depends on the sample thickness and whether the bottom of the measured material is in contact with a metal or an insulator. A graphical form of the correction factor can be found in the ASTM standard F84.¹⁸ This nondestructive technique is designed for use in the processing of semiconductor wafers.

1.2.3 Van der Pauw and Hall effect

Though the 4-point collinear probe technique proved invaluable for materials testing, the technique suffered from several drawbacks: The method gave erroneous results for samples that were irregularly shaped and it was not easily adaptable to different sample sizes. Furthermore, after decades of testing, it was found the resistivity was not a fundamental property of a material, as different materials can have the same resistivities.¹⁵ It was also found that even given a specific material, resistivity may differ depending on how it was synthesized. Resistivity alone could not explain all electronic observations, especially among semiconductors. To this end, the Van der Pauw and Hall effect techniques were developed.

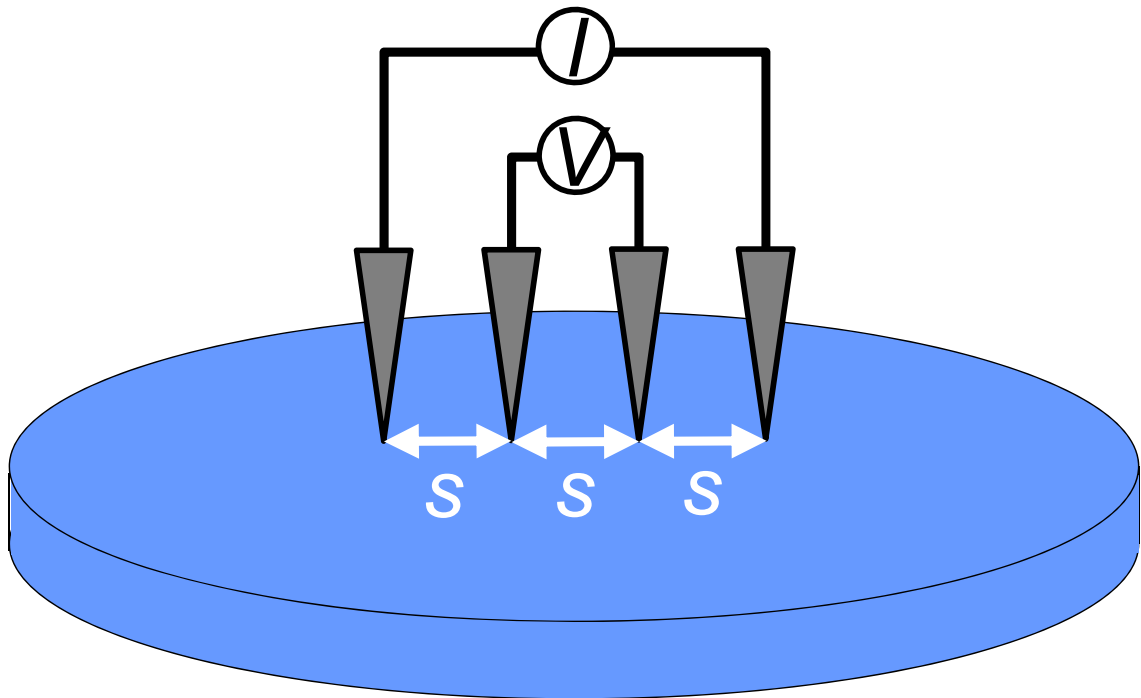


Figure 1.2 Schematic representation of the probe arrangement, placement and biasing in a 4-point collinear probe measurement.

1.2.3.1 Van der Pauw technique

Figure 1.3 depicts a model for the Van der Pauw technique contact placement. The method can be employed to samples with regular (rectangular or square) shapes and irregular shapes. In general, 4 contacts are placed on the periphery of the sample. For resistivity measurements, the current is sourced in the forward and reverse directions between adjacent contacts. The potential generated is then measured across the remaining two contacts. The eight resistance measurements, calculated from Ohm's law, should all be positive.¹⁵

$$R_{21,34} = V_{34}/I_{21}, R_{12,43} = V_{43}/I_{12}, \quad (1.5)$$

$$R_{32,41} = V_{41}/I_{32}, R_{23,14} = V_{14}/I_{23},$$

$$R_{43,12} = V_{12}/I_{43}, R_{34,21} = V_{21}/I_{34},$$

$$R_{14,23} = V_{23}/I_{14}, R_{41,32} = V_{32}/I_{41}$$

In order to determine the validity of the measurements, two requirements must be met:

- 1) Measurement consistency requires that for current reversal:

$$R_{21,34} = R_{12,43} \quad (1.6)$$

$$R_{32,41} = R_{23,14}$$

$$R_{43,12} = R_{34,21}$$

$$R_{14,23} = R_{41,32}$$

- 2) The reciprocity theorem also requires:

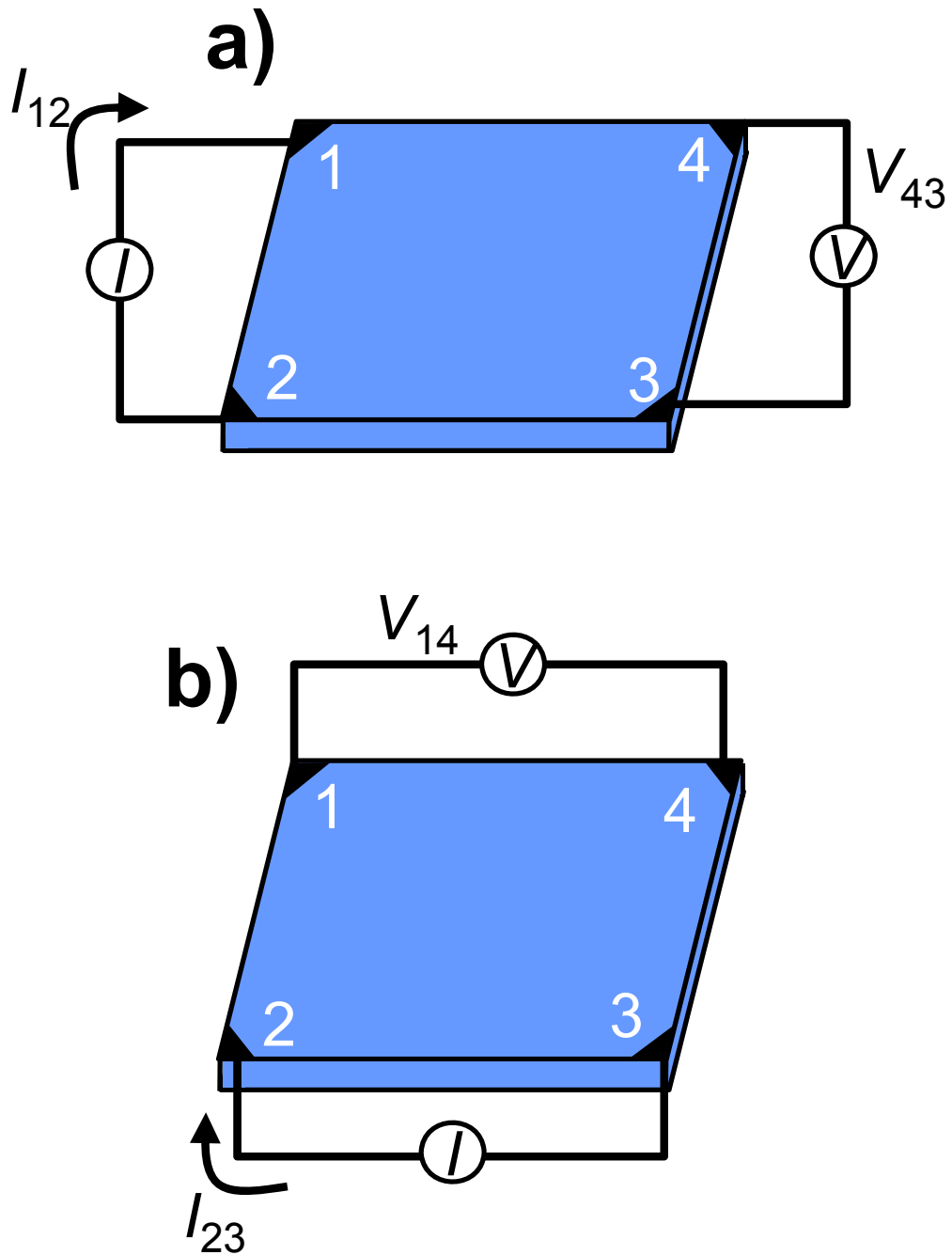


Figure 1.3 Schematic of the contact placement for the Van der Pauw measurement. (a) and (b) illustrate the current sourcing direction and the voltage measurement for I_{12} and I_{23} respectively.

$$R_{21,34} + R_{12,43} = R_{43,12} + R_{34,21}, \text{ and} \quad (1.7)$$

$$R_{32,41} + R_{23,14} = R_{14,23} + R_{41,32}$$

If any of the above fails to be within 5%, the source of error should be investigated. Sources of error may include: 1) Poor contact between one or more probes and the sample, 2) visible damage to the sample such as cracks (especially around the contacts), 3) exposure to sunlight during the measurement (semiconductors will generate photoinduced currents) and 4) variable sample temperature during measurement.

The objective of this resistivity measurement is to determine the sheet resistance (R_s) from two characteristic resistances (R_a and R_b). R_a and R_b are calculated from four specific measured resistances and averaged:¹⁵

$$R_a = (R_{21,34} + R_{12,43} + R_{43,12} + R_{34,21})/4 \quad (1.8)$$

$$R_b = (R_{32,41} + R_{23,14} + R_{14,23} + R_{41,32})/4$$

R_a and R_b are related to R_s through the Van der Pauw equation:

$$\exp(-\rho R_a/R_s) + \exp(-\rho R_b/R_s) = 1 \quad (1.9)$$

This equation can be solved numerically for R_s using the following iteration routine:¹⁵

- 1) Set the error limit $\delta = 0.0005$, corresponding to 0.5%
- 2) Calculate the initial value of z_i , or $z_0 = 2 \ln(2)/[\pi(R_a + R_b)]$
- 3) Calculate the i^{th} iteration of $y_i = 1/\exp(\pi z_{i-1} R_a) + 1/\exp(\pi z_{i-1} R_b)$
- 4) Calculate the i^{th} iteration of z_i where

$$z_i = z_{i-1} - [(1 - y_i)/\pi]/[R_a/\exp(\pi z_{i-1} R_a) + R_b/\exp(\pi z_{i-1} R_b)]$$

- 5) When $(z_i - z_{i-1})/z_i$ is less than δ , stop and calculate the sheet resistance $R_s = 1/z_i$

The bulk electrical resistivity can then be calculated using:

$$\rho = R_s d \quad (1.10)$$

where d is the thickness of the conducting layer.

1.2.3.2 Hall effect

The Hall measurement is used to determine the sample sheet carrier density, n_s , bulk carrier type, n or p (n -type and p -type respectively), bulk carrier density and mobility of charge carriers. When used in combination with the Van der Pauw measurement, can provide not only the intrinsic electronic properties of the material but the fundamental charge transport properties also.

The underlying principle behind the Hall effect is the Lorentz force. This force is a combination of electric force (potential applied to the sample) and magnetic force (magnetic field applied to the sample). When an electron moves along a path perpendicular to the direction of an applied magnetic field, it “feels” a magnetic force acting normal to both directions. (Figure 1.4)¹⁵ Electrons subject to the Lorentz force initially drift away from the current direction resulting in a potential drop across the sample known as the Hall voltage (V_H). The Hall voltage magnitude is given by:

$$V_H = IB/qnd \quad (1.11)$$

Where I is the current, B is the strength of the magnetic field, d is the sample thickness, q is the electrons elementary charge (1.602×10^{-19} C) and n is the bulk charge density. By measuring V_H and knowing the values of sample thickness, current and magnetic field, one can now determine the density of charge carries, n , in the sample. Also, the sign of the Hall voltage can be us to describe the type of charge carriers in the system; negative for n -type conductors and positive for p -type conductors.

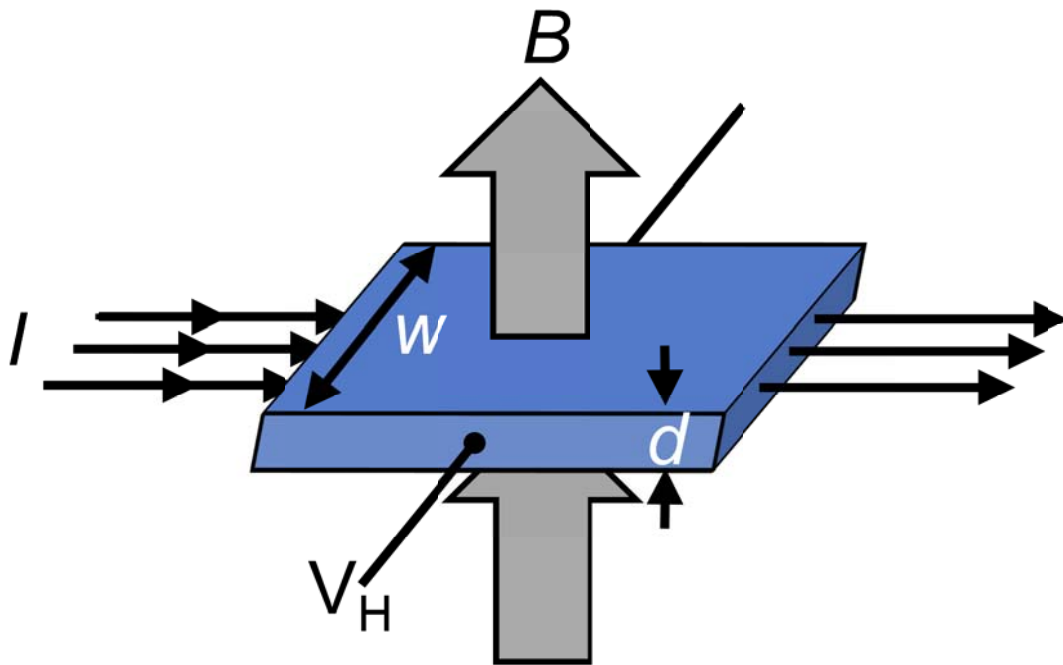


Figure 1.4 Schematic of the Hall effect principle.

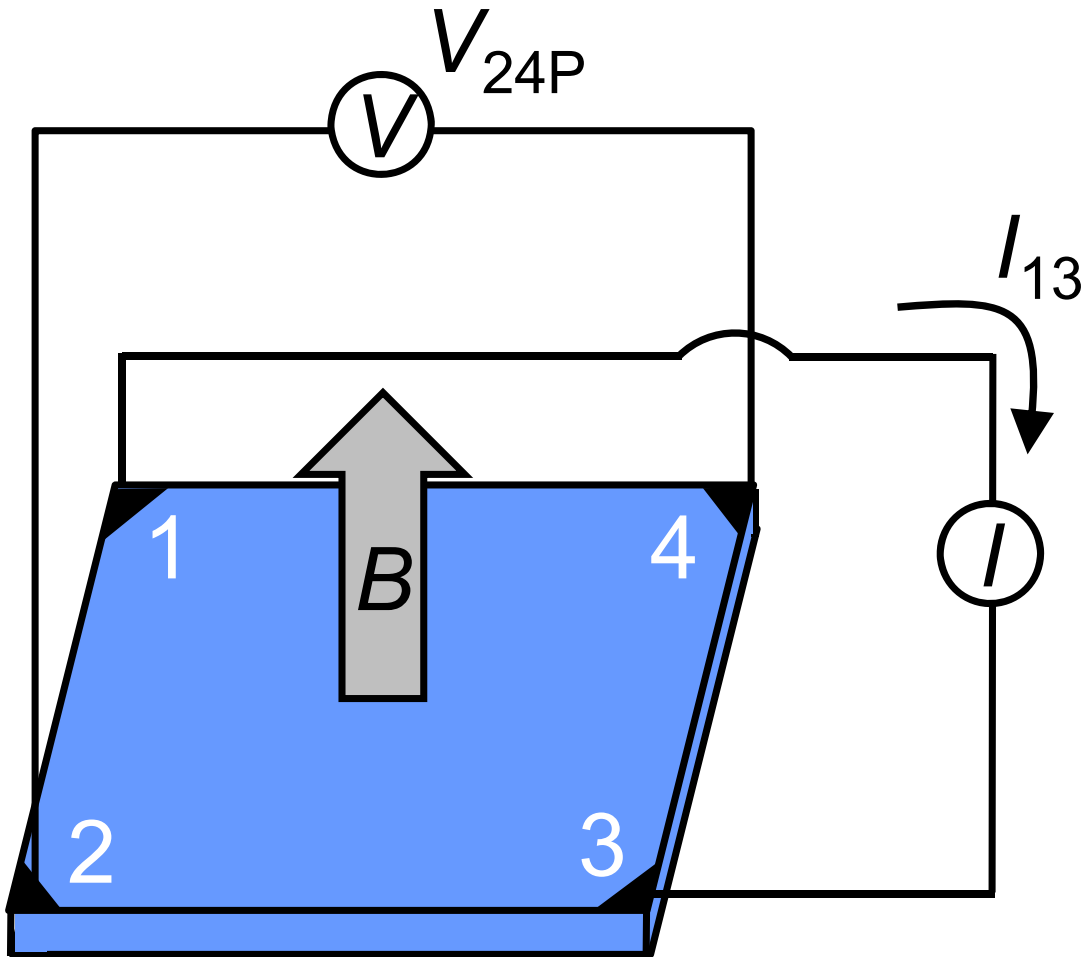


Figure 1.5 Schematic of the contact placement in a Hall effect measurement. Illustrates the current sourcing direction and the voltage measurement for I_{13} and V_{24p} .

The Hall measurement is carried out using a 4-point probe measurement system, similar to the Van der Pauw measurement. (Figure 1.5) However, unlike the Van der Pauw measurement which utilizes adjacent contacts for sourcing and measuring, the Hall measurement utilizes adjacent contacts and is under the presence of a magnetic field. The procedure for Hall measurement is as follows:¹⁵

- 1) Apply a positive magnetic field B (positive z -direction).
- 2) Apply current into contact 1 through contact 3 (I_{13}) and measure the voltage from contact 2 to contact 4 (V_{24}).
- 3) In a manner similar to the Van der Pauw measurement, now apply current I_{31} and measure voltage V_{42} to validate contact integrity.
- 4) Likewise, apply current I_{24} and I_{42} and measure voltage V_{13} and V_{31} respectively.
- 5) Apply a negative magnetic field B (negative z -direction).
- 6) Repeat steps 2-4 to obtain the final 4 voltage measurements.

There are now eight measured Hall voltages; 4 voltages under positive magnetic field influence (V_{13P} , V_{31P} , V_{24P} , and V_{42P}) and 4 voltages under negative magnetic field influence (V_{13N} , V_{31N} , V_{24N} , and V_{42N}). These values are then used to calculate the following (be careful to maintain the sign of the voltages as the offset is used to determine the carrier type):

$$V_C = V_{24P} - V_{24N}; V_D = V_{42P} - V_{42N}; V_E = V_{13P} - V_{13N} \text{ and } V_F = V_{31P} - V_{31N} \quad (1.12)$$

The sample type is then calculated from the polarity of the voltage sum:

$$V_{\text{sum}} = V_C + V_D + V_E + V_F \quad (1.13)$$

A positive sign indicates a p -type conductor while a negative sign indicates an n -type conductor. By modify the relationship determined in (11), the carrier concentration n can now be calculated from

$$p = 8 \times 10^{-8} IB / (qd V_{\text{sum}}), \text{ if } V_{\text{sum}} \text{ is positive} \quad (1.14)$$

$$n = |8 \times 10^{-8} IB / (qd V_{\text{sum}})|, \text{ if } V_{\text{sum}} \text{ is negative}$$

where B is the magnetic field in gauss (G), I is in amps (A) and d is in centimeters.

The velocity that the carriers have when an electric field is applied across a sample is known as the mobility, μ . Mobility can be calculated from the R_s determined from the van der Pauw measurement (9) and the carrier concentration (14):

$$\mu = 1 / qndR_s \quad (1.15)$$

The units of mobility are $\text{cm}^2\text{V}^{-1}\text{s}^{-1}$ and either n or p from (14) can be used for the carrier concentration, depending on the carrier type.

With the Van der Pauw and Hall effect measurement techniques, one should be able to completely characterize the electronic properties almost any sample. Great care should be taken to completely understand the limitation of the current source and voltage source used for measurements. For the cases of very low resistivity materials ($<10^{-4}$ ohm cm) and high resistivity materials ($>10^8$ ohm cm), specialty source and measure units may need to be utilized and alternative contact arrangements may have to be applied.

1.2.4 X-ray diffraction

A crystal can be defined as solid formed by a repeating, three-dimensional pattern of atoms, ions, or molecules and having fixed distances between constituent parts.¹⁹ It is also relevant to mention that about 95% of all solids can be defined under this category.¹⁹ Furthermore, nearly all materials of interest for electronic applications also fall under this

category. It is therefore of great importance that the crystalline properties of the materials under analysis can also be determined, not just the electronic properties.

As every atom has slightly different ionic radii, electronegativity, and shapes and orientations of surrounding electron densities, when they bond together in crystalline structures, the distances between the constituent parts will be specific to the atoms taking part in that bonding. Techniques available to determine the spacing between these constituent parts, and therefore the quality of the crystal, are numerous and include high resolution transmission electron microscopy (HRTEM), selected area electron diffraction (SAED), electron energy loss spectroscopy (EELS), electron backscatter diffraction (EBSD), and x-ray diffractometry (XRD). Of these techniques, x-ray diffraction is one of the simplest, most common techniques for determining crystalline properties.

X-ray diffraction is based on Sir W.H. Bragg and Sir W.L. Bragg's observation that cleaved surfaces of a crystal reflect x-ray beams at certain angle of incidence. Figure 1.6 is a schematic representing x-ray diffraction from a crystalline surface. It should be noted that beam one and beam two are in phase and parallel as they approach the crystal lattice in a and b. In Figure 1.6a, beam one and two are in-phase and parallel when exiting the crystal leading to constructive interference. However, as the 2θ angle is changed ($2\theta'$), there is a phase shift in x-ray beam one and two and they are no longer in phase which leads to destructive interference and no signal.²⁰

An equation describing the constructive interference within crystalline materials can be easily derived by considering the requirements necessary to have diffraction occur. As an x-ray beam leaves an x-ray source, all of the beams that make up that source are parallel and in phase. This is true until the beam strikes the surface of a crystalline

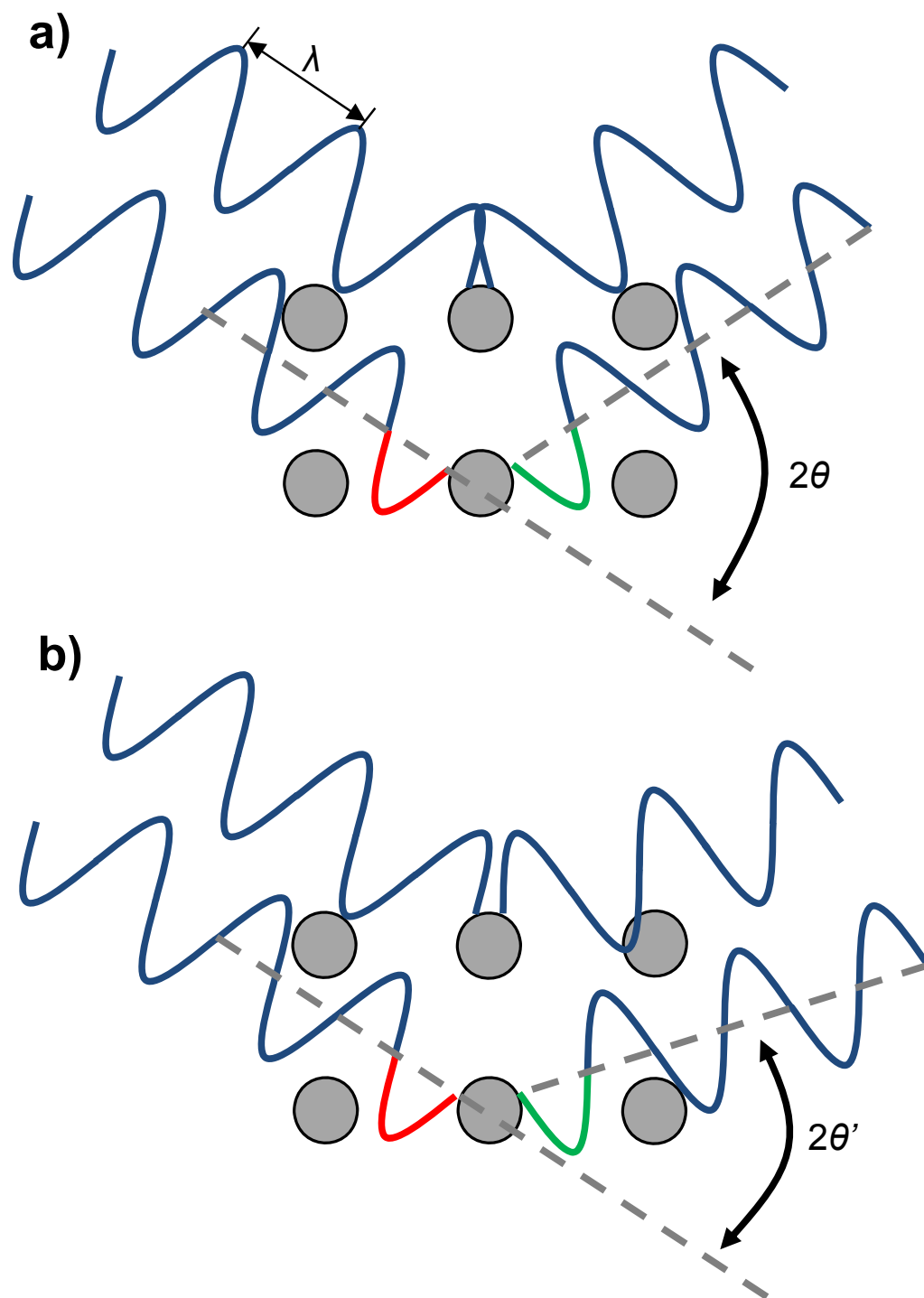


Figure 1.6 Schematic representation of constructive (a) and destructive (b) interference in x-ray powder diffraction.

material. As beam 1 collides with the crystal, it is diffracted by a surface atom. (Figure 1.7) However, beam 2 does not collide with a surface atom and penetrates the surface. Beam 2 then collides with an atom in the second layer and is diffracted out of the crystal. In order to be in-phase, beam 2 must travel the distance $AB + BC$ in order to continue traveling adjacent and parallel with Beam 1. This distance is an integral n of the x-ray wavelength λ :

$$n\lambda = AB + BC \quad (1.16)$$

Recognizing d , the spacing between atomic planes, as the hypotenuse of a right triangle, trigonometry can be used to relate d to the values of AB and BC :

$$AB = d \sin\theta \quad (1.17)$$

Due to the requirements of in phase and parallel, $AB = BC$ for constructive interference and equation (16) now becomes

$$n\lambda = 2AB \quad (1.18)$$

Substituting equation (17) into equation (18), we obtain the equation known as Bragg's Law:

$$n\lambda = 2d \sin\theta \quad (1.19)$$

where λ is the wavelength of the incident x-ray beam, θ is the angle of incidence, d is the spacing between the atomic layer and n is an integer.²⁰

By using a fixed wavelength radiation source, determining the d spacing from a diffraction experiment becomes very straight forward. The relationships developed by Bragg's Law also provide an excellent means to fingerprint crystal structures, as the same material will always give the same diffraction pattern. Changes in the diffraction pattern will indicate changes in the crystal structure such as rearrangement of the atom into

different crystal structures (leading to different diffraction patterns) or impurities which can cause strain in the lattice (leading to increases or decreases in the lattice spacing values).

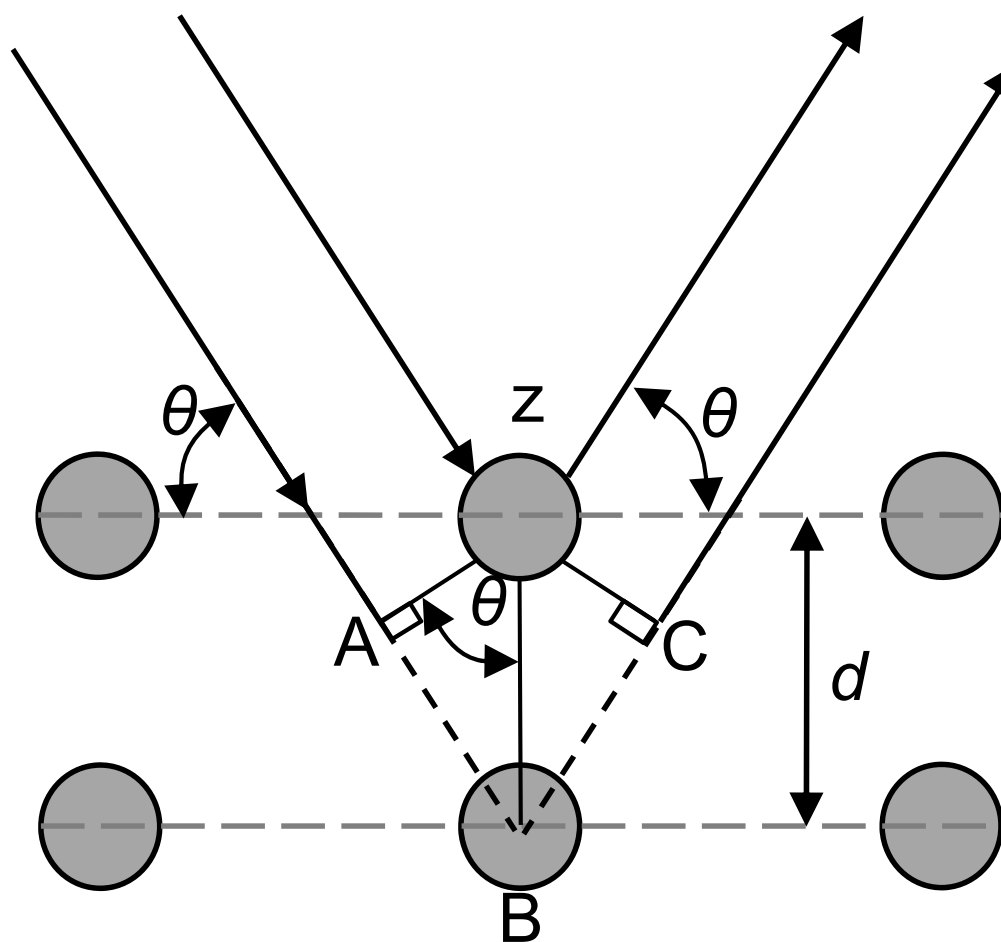


Figure 1.7 Schematic depicting the derivation of Bragg's Law.

1.3 Focus of this dissertation

This dissertation is meant to serve as a complete guide for the synthesis and characterization of rare earth compounds containing boron and nitrogen. Chapter 2 is the development of a chemical vapor deposition (CVD) technique for the synthesis of crystalline rare earth boride (REB_6) nanostructures. Chapter 2 also includes the characterization of their physical properties by XRD, transmission and scanning electron microscopy and their electronic properties by Van der Pauw and Hall effect measurements. Chapter 3 discusses the development of a compositional analysis technique known as local electrode atom probe tomography for the determination of the 3D composition of individual REB_6 nanowires at the atomic level. Chapter 4 discusses the implementation of REB_6 nanostructures in field emission arrays and nanomanipulator probe assemblies. Chapter 5 is the further development of the CVD hydride phase synthesis developed in Chapter 2 and its application toward the synthesis of gadolinium nitride thin films. Finally, Chapter 6 reviews the entirety of the dissertation and elaborates on future directions of several sections.

1.4 References

1. Samsonov, G.V. High-temperature compounds of rare earth metals with nonmetals (Consultants Bureau, New York, 1965).
2. Taylor, S.R. & McLennan, S.M. The continental crust :its composition and evolution : an examination of the geochemical record preserved in sedimentary rocks (Blackwell Scientific, Oxford; Boston, 1985).
3. Kilborn, B. A lanthanide lanthology, part 1 A-L (Molycorp, Inc., 67750 Bailey Road, Mountain Pass, CA, 1993).
4. Wei, W., Jiang, K.L., Wei, Y., Liu, P., Liu, K., Zhang, L.N., Li, Q.Q. & Fan, S.S. LaB₆ tip-modified multiwalled carbon nanotube as high quality field emission electron source. *Appl. Phys. Lett.* **89**, 3 (2006).
5. Xu, J.Q., Chen, X.L., Zhao, Y.M., Zou, C.Y. & Ding, Q.W. Single-crystalline PrB₆ nanowires and their field-emission properties. *Nanotechnology* **18**, 5 (2007).
6. Xu, J.Q., Zhao, Y.M., Ji, X.H., Zhang, Q. & Lau, S.P. Growth of single-crystalline SmB₆ nanowires and their temperature-dependent electron field emission. *J. Phys. D-Appl. Phys.* **42**, 6 (2009).
7. Xu, J.Q., Zhao, Y.M., Shi, Z.D., Zou, C.Y. & Ding, Q.W. Single-crystalline SmB₆ nanowires. *J. Cryst. Growth* **310**, 3443-3447 (2008).

8. Xu, J.Q., Zhao, Y.M. & Zhang, Q.Y. Enhanced electron field emission from single-crystalline LaB₆ nanowires with ambient temperature. *J. Appl. Phys.* **104**, 4 (2008).
9. Xu, J.Q., Zhao, Y.M. & Zou, C.Y. Self-catalyst growth of LaB₆ nanowires and nanotubes. *Chem. Phys. Lett.* **423**, 138-142 (2006).
10. Xu, T.T., Zheng, J.G., Nicholls, A.W., Stankovich, S., Piner, R.D. & Ruoff, R.S. Single-crystal calcium hexaboride nanowires: Synthesis and characterization. *Nano Lett.* **4**, 2051-2055 (2004).
11. Zhang, H., Tang, J., Zhang, Q., Zhao, G.P., Yang, G., Zhang, J., Zhou, O. & Qin, L.C. Field emission of electrons from single LaB₆ nanowires. *Adv. Mater.* **18**, 87-91 (2006).
12. Zhang, H., Zhang, Q., Tang, I. & Qin, L.C. Single-crystal line CeB₆ nanowires. *J. Am. Chem. Soc.* **127**, 8002-8003 (2005).
13. Zhang, H., Zhang, Q., Tang, J. & Qin, L.-C. Single-Crystalline LaB₆ Nanowires. *J. Am. Chem. Soc.* **127**, 2862-2863 (2005).
14. Zhang, H., Zhang, Q., Zhao, G.P., Tang, J., Zhou, O. & Qin, L.C. Single-crystal line GdB₆ nanowire field emitters. *J. Am. Chem. Soc.* **127**, 13120-13121 (2005).
15. Thurber, W.R. (ed. Technology, T.N.I.o.S.a.) (December 3, 2008).
16. Pierret, R.F. Semiconductor fundamentals (Addison-Wesley Pub. Co., Reading, MA, 1988).
17. Yeager, J. & Hrusch-Tupta, M.A. (eds.) Low level measurements (Keithley Instruments Inc., 28775 Aurora Rd, Cleveland, OH., 1998).
18. American Society for, T. & Materials. Annual book of ASTM standards. (1970).

19. Connolly, J. (Department of Earth and Planetary Sciences, University of New Mexico 2009).
20. Langford, J.I. & Louer, D. Powder diffraction. *Rep. Prog. Phys.* **59**, 131-234 (1996).

Chapter 2

Synthesis of rare earth hexaborides by low pressure chemical vapor deposition: From nanostructures to thin films

2.1 Introduction

REB₆ have received renewed research interest in recent years because of their interesting physical and electronic properties, extremely high melting points and low work function.¹⁻⁸ Depending on the particular RE element, they may possess other unique properties such as type II superconductivity, semiconductivity (either *n*- or *p*-type conductivities), and fluctuating valence.^{6, 9-12} The electrical resistivities of the REB₆ systems generally range from $15 \times 10^{-6} \Omega\text{-cm}$ to $2 \times 10^{-4} \Omega\text{-cm}$, making them ideal cathodes and metallic interconnects in electronic applications.¹⁰ (Table 2.1) Structurewise, the unit cells of REB₆ are quite simple: An octahedron boron cluster located in the center of a cubic cage with corners occupied by RE atoms. (Figure 2.1) This cubic lattice structure is very rigid due to the interconnected bonding between boron cages of adjacent unit cells, leading to possible lattice matching that is nearly perfect across the entire range of cubic RE materials.¹⁰ (Table 2.1) Nanoscaled dimension design would provide access to materials with enhanced electron collection and injection properties and unique heterojunction and doped materials properties. Due to the nearly perfect lattice matching, heterojunction or doped materials would not suffer from traditional problems such as scattering at boundaries or dopant sites as the lattice perturbs very little at the interfaces.

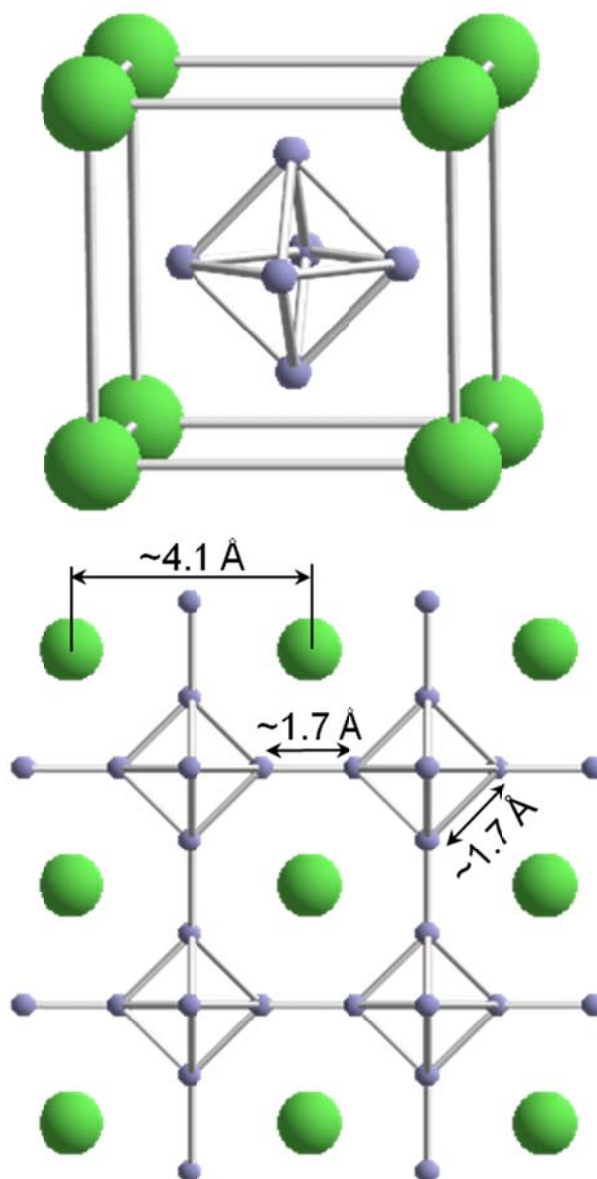


Figure 2.1 REB_6 unit cell and approximate lattice parameters. The large atoms at the corners (green) are the RE atoms and the smaller atoms (blue) located at the corners of the octahedron in the center of the cubes are B.

Table 2.1 REB₆ lattice constant *a*

<u>REB₆</u>	<u>Lattice Constant (Å)¹⁰</u>
YB ₆	4.10
LaB ₆	4.15
CeB ₆	4.14
PrB ₆	4.13
NdB ₆	4.13
SmB ₆	4.13
EuB ₆	4.19
GdB ₆	4.11
TbB ₆	4.10
DyB ₆	4.10
HoB ₆	4.10
ErB ₆	4.11
TmB ₆	4.11
YbB ₆	4.15
LuB ₆	4.11

2.2 Nanostructured materials synthesis mechanisms

There are many different techniques for synthesizing nanomaterials or structures with nanosized tips: Chemical vapor deposition (CVD), which has subgroups of catalyst-assisted, laser-assisted, plasma-assisted, and self-catalyzed, molecular beam epitaxy, laser ablation, sol-gel, and hydrothermal synthesis are the most common. Though each synthetic method has its positives and negatives, catalyst-assisted CVD has been shown to be a very effective method for synthesizing high aspect ratio single crystal nanostructures with consistent tip diameters.

Synthesis of single crystal nanowires via CVD commonly involves a vapor phase reaction coupled with a metal catalyst particle deposited on a substrate. In many instances, this process is conducted at high temperatures, $>500\text{ }^{\circ}\text{C}$ and low pressures, 10^{-3} - 10^{-1} torr (though it is not a requirement). The catalyst particle, which is thought to enhance the growth rate as compared to the bulk, possibly leads to preferential decomposition of the precursor gases at or near the particles surface. The decomposition of the precursor can lead to several types of interaction with the catalyst particle: The vapor reacts with the catalyst particle (self-catalyzed process) leading to consumption of the particle over time, the decomposed vapor can alloy with the catalyst particle and redeposit (vapor-liquid-solid, VLS, process), or the vapor can deposit preferentially on the catalyst particles (vapor-solid, VS, process). For any of the above mentioned catalyst-assisted CVD growth models, the diameter of the nanowire is typically determined by the catalyst particle size. However, of these techniques, the VLS deposition is considered by many to provide the best control over diameter and crystallinity.¹³

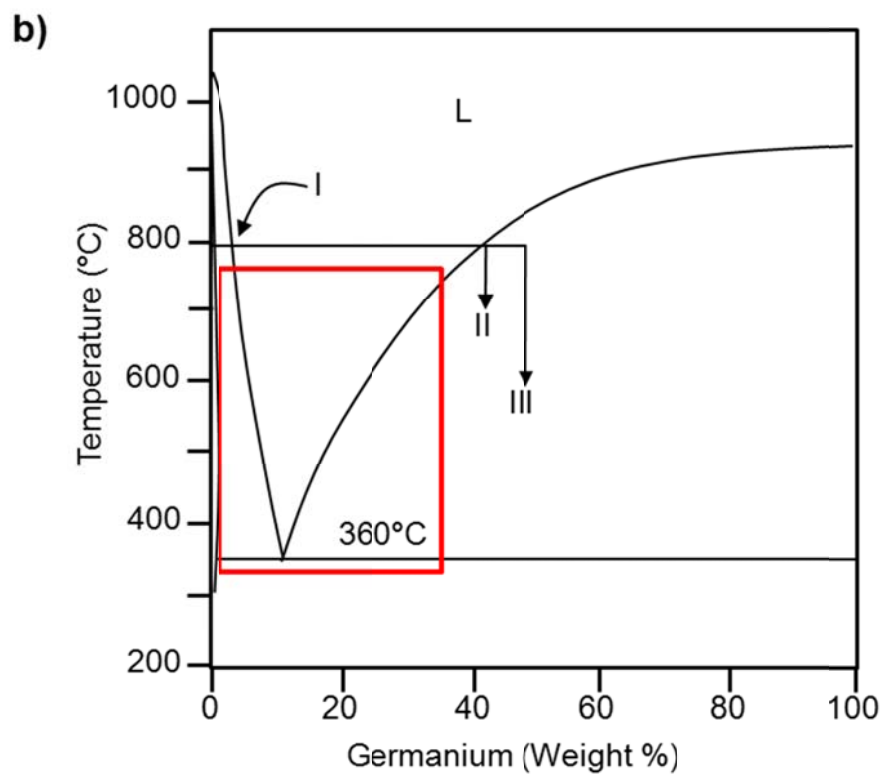
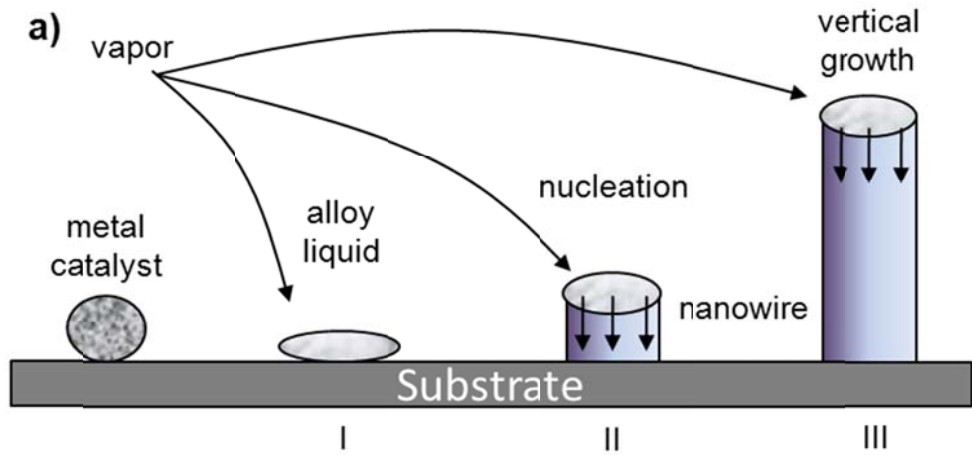


Figure 2.2 a) Schematic illustration of VLS nanowire growth mechanism including three stages I) alloying, II) nucleation, and III) axial growth. The three stages are projected onto a conventional Au-Ge binary phase diagram; b) to show the compositional and phase evolution during the nanowire growth process.

The VLS process, more specifically, typically begins with a solid metal particle which then alloys with the incoming precursor vapors and forms a liquid droplet (vapor-liquid).^{14, 15} (Figure 2.2a) When the liquid droplet becomes supersaturated, materials begin to preferentially deposit at the alloy-substrate interface due to the lower potential energy of the solid substrate surface (liquid-solid). Materials will continue to deposit at the liquid-solid interface until either the gas precursor flow is stopped, or the catalyst particle is poisoned or consumed.

This process can also be visualized by analyzing the binary phase diagram of proposed VLS systems.¹⁴ (Figure 2.2b) In most instances, VLS involves the use of a metal particles and the deposition of a non-metal such as a semiconductor. When analyzing the binary phase diagram for its VLS characteristics, one of the most important attributes is the formation of a low temperature liquid-eutectic phase (red square). At a temperature above the lowest temperature of the liquid-eutectic, an isothermal line is drawn from the metal side of the phase diagram to the non-metal side of the phase diagram. It is critical that the isothermal line is drawn such that it crosses two bi-phasic (liquidous) lines. The crossing of the liquidous line into the eutectic region indicates the solid-liquid transformation of the metal drop upon alloying with the precursor gases. The liquid alloy continues to dissolve precursor gases and becomes supersaturated. The crossing the second liquidous lines indicates the precipitation of the crystalline material from the supersaturated liquid alloy and the formation of the wire.

2.3 Synthesis of REB₆ micro- and nanostructures

2.3.1 Introduction

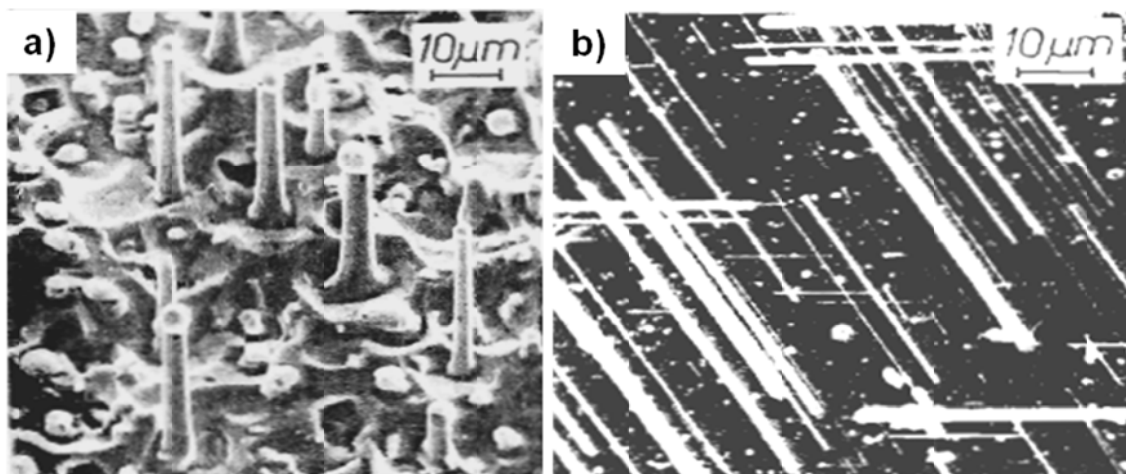


Figure 2.3 LaB₆ whiskers grown by VLS. a) Wire growth using gold catalyst and b) wire growth using platinum catalyst.¹⁶

One of the earliest reported syntheses of LaB_6 in whisker/nanowire form was in 1978 by.¹⁷ However, they were only able to show limited control over the dimensions of the materials. In 1981 and 1986, researchers found that much better control over the growth can be obtained through the use of a catalyst-assisted CVD process involving BBr_3 , LaB_2 , H_2 and catalyst particles of platinum and gold.^{16, 18} Materials grown were typically several hundred nanometers in diameter or larger with catalyst particles at the tips of most materials. (Figure 2.3) However, quality of the synthesized wires was not determined as characterization techniques to evaluate the materials had not been developed to a sufficient extent.

After several decades of little activity, growth of the REB_6 nanostructures was revisited as device application of nanomaterials increased drastically. In 2005, researchers at the University of North Carolina-Chapel Hill published a group of paper on the synthesis of LaB_6 , GdB_6 and CeB_6 nanowires with diameters from 20 nm to several hundred nm, while employing a similar synthetic process utilized in the synthesis of hexaboride whiskers.¹⁹⁻²¹ The as-synthesized wires were both single and poly-crystalline, with no evidence of the gold catalyst particle on the tip of the wires. (Figure 2.4)

The self-catalyzed method was utilized a year later by researchers in China for the synthesis LaB_6 nanowires and nanotubes.²²⁻²⁷ This process is quite similar to a traditional VLS model, except the catalyst particle is generally the RE metal and is sacrificial (self-catalyzed method). The technique has been applied to several RE systems with varying results. However, these materials were grown with low density, were poly-crystalline and randomly oriented with respect to the substrate surface. (Figure 2.5) Furthermore, this

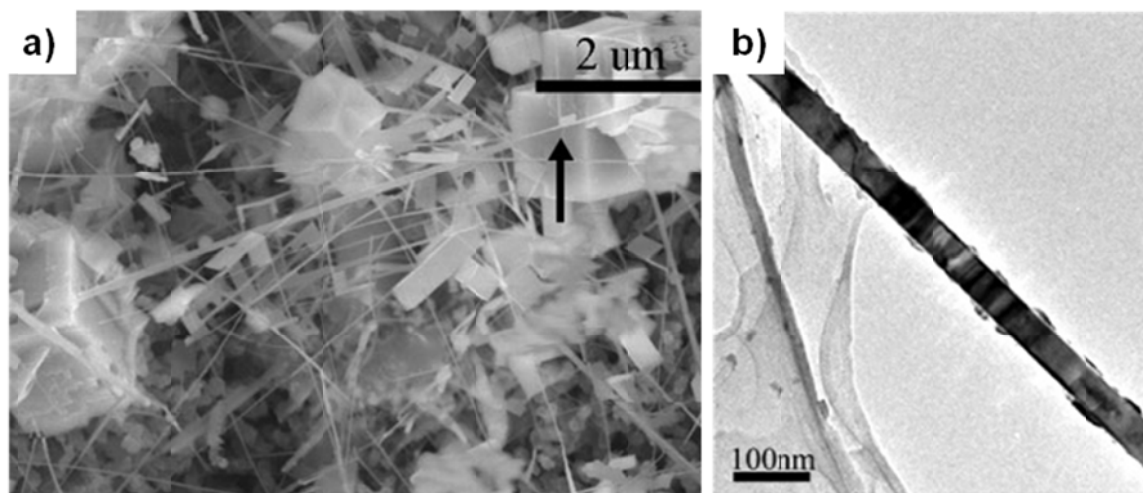


Figure 2.4 SEM and TEM images of nanowires synthesized by VLS technique. a) LaB_6 and b) CeB_6 single crystal materials.^{19, 20}

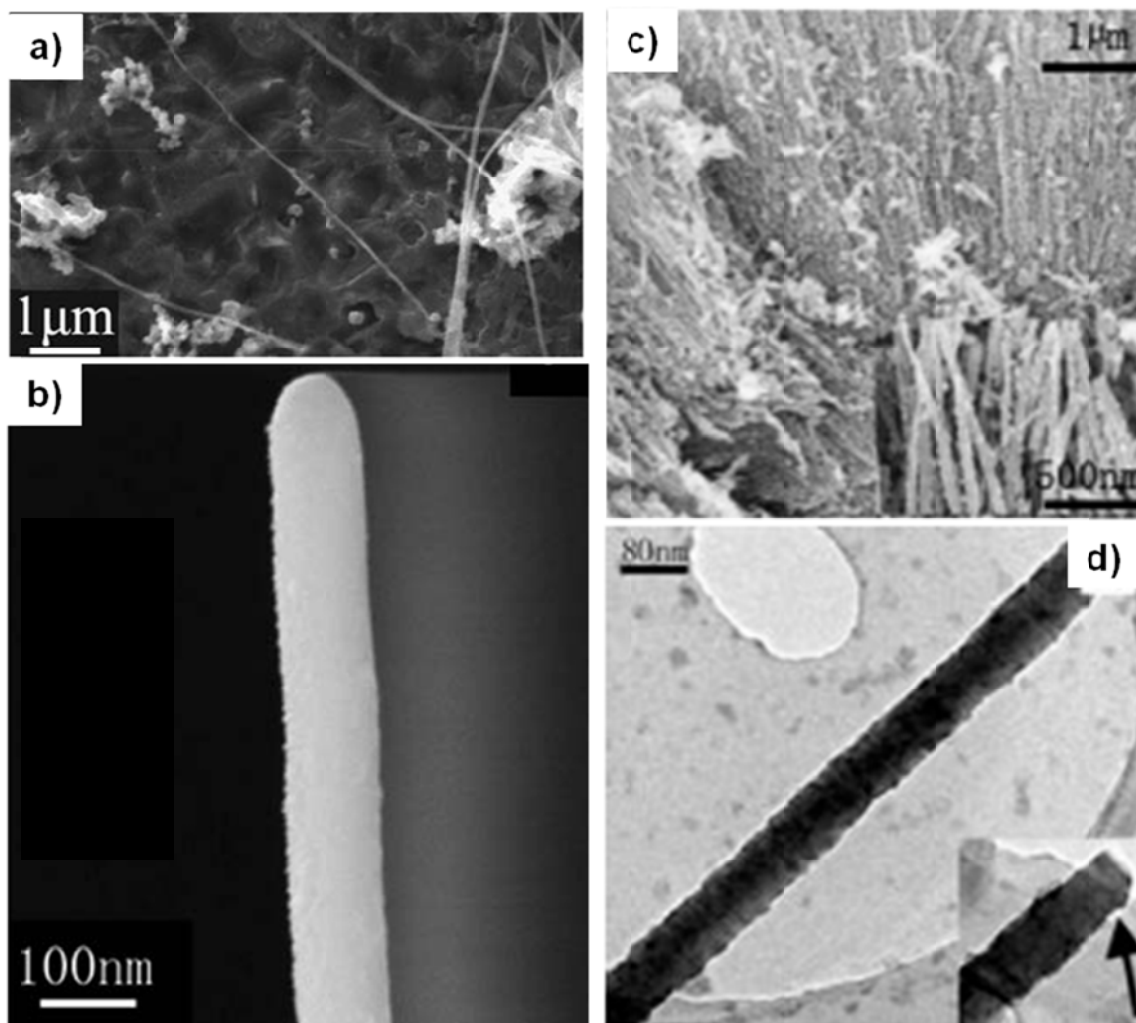


Figure 2.5 SEM and TEM images of nanowires synthesized by self-catalysis. a) and b) are LaB_6 and c) and d) are NdB_6 materials.^{25, 27}

technique is not applicable toward doping or heterostructured nanomaterial growth and limits the RE metals to be used as some have melting points in excess of 1600 °C.

Though the synthetic results are promising, materials synthesis of REB_6 is still considerably behind competing materials with respect to tip diameter size, tip diameter control and orientation with respect to the substrate. Furthermore, the current synthetic routes do not provide a feasible route for dopant incorporation or heterostructure formation; features necessary for effective materials synthesis for device applications. Until these hurdles are overcome, REB_6 materials will continue to have limited device applications.

2.3.2 Synthesis development: Pt catalyzed growth

Initial studies of VLS synthesized nanostructures were focused on gold and platinum catalysts as both worked well for the growth of micro- and nanostructured LaB_6 .^{16, 18-21} The first focus of the initial studies was to determine which of the two metal catalysts was best suited for general synthesis of REB_6 nanomaterials as this would provide the most flexibility in modify materials properties. Second was to determine a possible alternative boron precursor that is less toxic and has a lower decomposition temperature than BCl_3 .

In the discussion of VLS growth in Section 2.2, the example presented was for a single component nanowire system. However, REB_6 system is a binary system, making interpretation of the phase diagram data much more difficult. Typically, a pseudo binary phase diagram (typically constructed from ternary phase diagrams) would need to be constructed, describing the alloying behavior of the binary compound with the metal

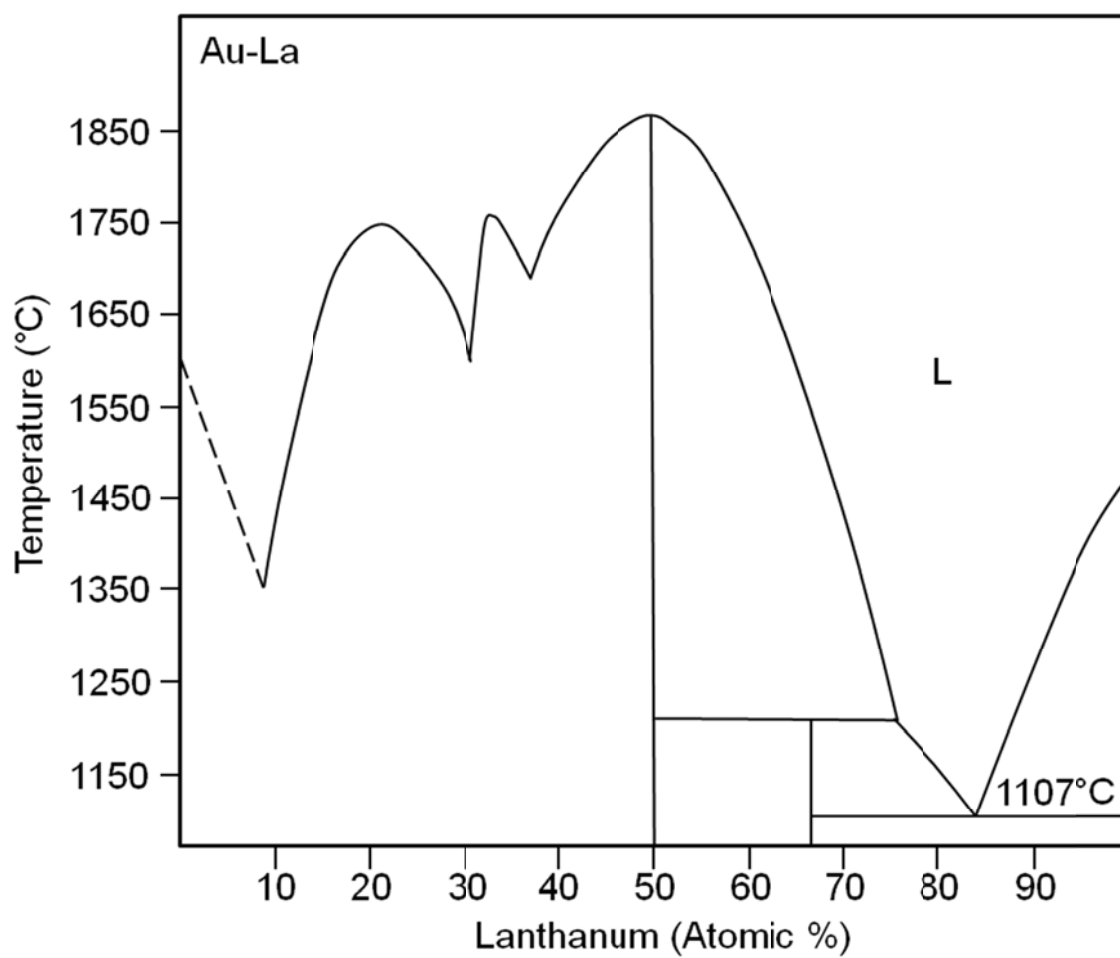


Figure 2.6 Au-La binary phase diagram. Dashed line indicates theoretical estimate.²⁸

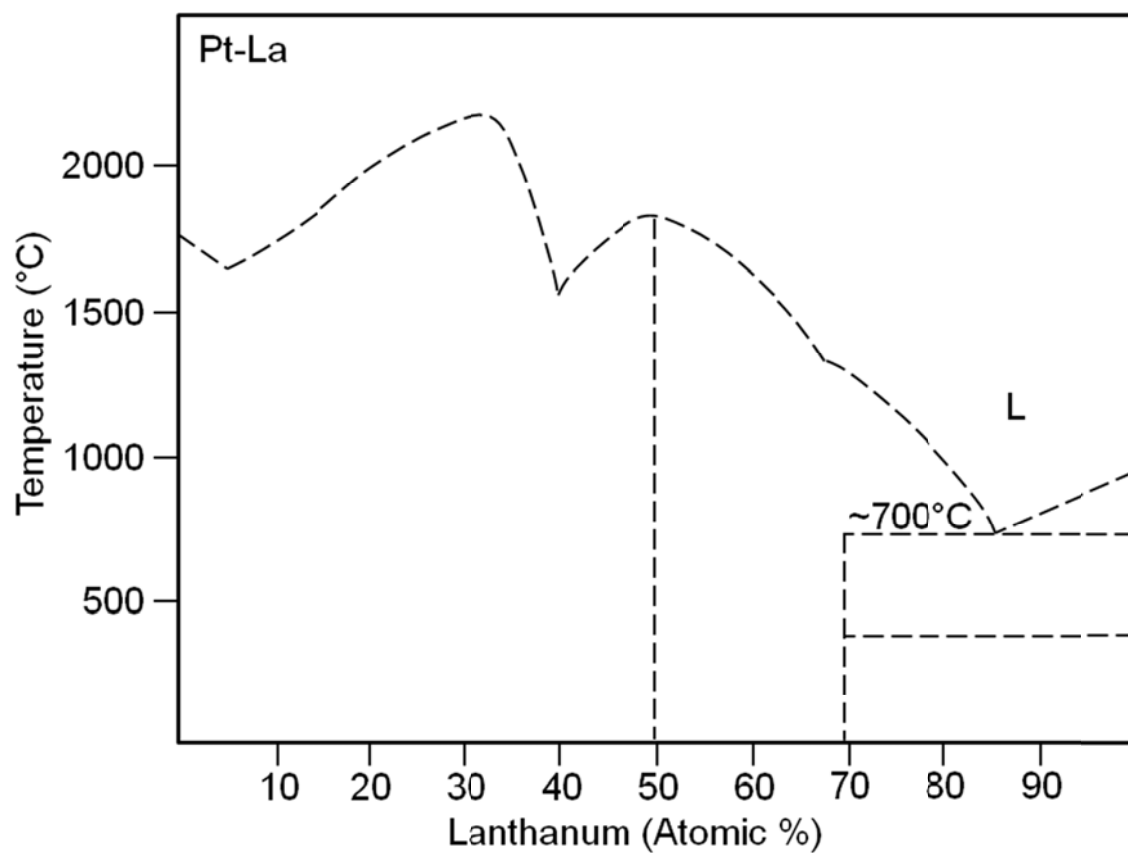


Figure 2.7 Theoretical binary phase diagram of Pt and La. Dashed lines indicate theoretical estimates.²⁸

particle. However, a pseudo binary phase diagram cannot be created for the REB₆ systems as not ternary phase diagrams exist.

To circumvent this issue of limited ternary and pseudo-binary phase diagram information, intuition was gained from analyzing the separate binary phase diagrams; metal with catalyst and boron with catalyst. Figure 2.6 and Figure 2.7 are the binary phase diagrams of La with Pt and Au.²⁸ The binary phase diagrams have all the necessary components: 1) the low temperature single phase liquid eutectic region and 2) corresponding liquidous lines. Both binary phase diagrams are very similar, with La showing similar solubility in Pt as Au but at much lower temperatures. Figure 2.8 and Figure 2.9 are the binary phase diagrams for B with Pt and Au.²⁸ Unlike with the RE with Pt and Au (which showed very similar atomic percent solubility), B is soluble in Pt to a much greater extent than in Au. Given the lower eutectic temperature of La and B with Pt than Au and the limitation of the tube furnaces, which have a maximum temperature of 1100 °C (effectively eliminating gold as a possible catalyst choice), Pt was chosen as the catalyst for the initial VLS growth trials.

After the catalyst selection was complete, choice of precursors for the CVD process was necessary. To minimize the occurrence of side reactions and possible contaminants, LaCl₃ was chosen as the metal precursor for the reaction. The choice of boron precursor was much more difficult; the precursor needed to have low toxicity to maximize safety in the laboratory and minimize implementation cost and it needed to be volatile. Of the boron gas phase precursors available, most are either boron hydrides or boron halides. Peshev provides a thermodynamic estimation of the Gibbs free energy of reaction between these two common types of boron precursors and LaCl₃.²⁹ (Figure 2.10) The

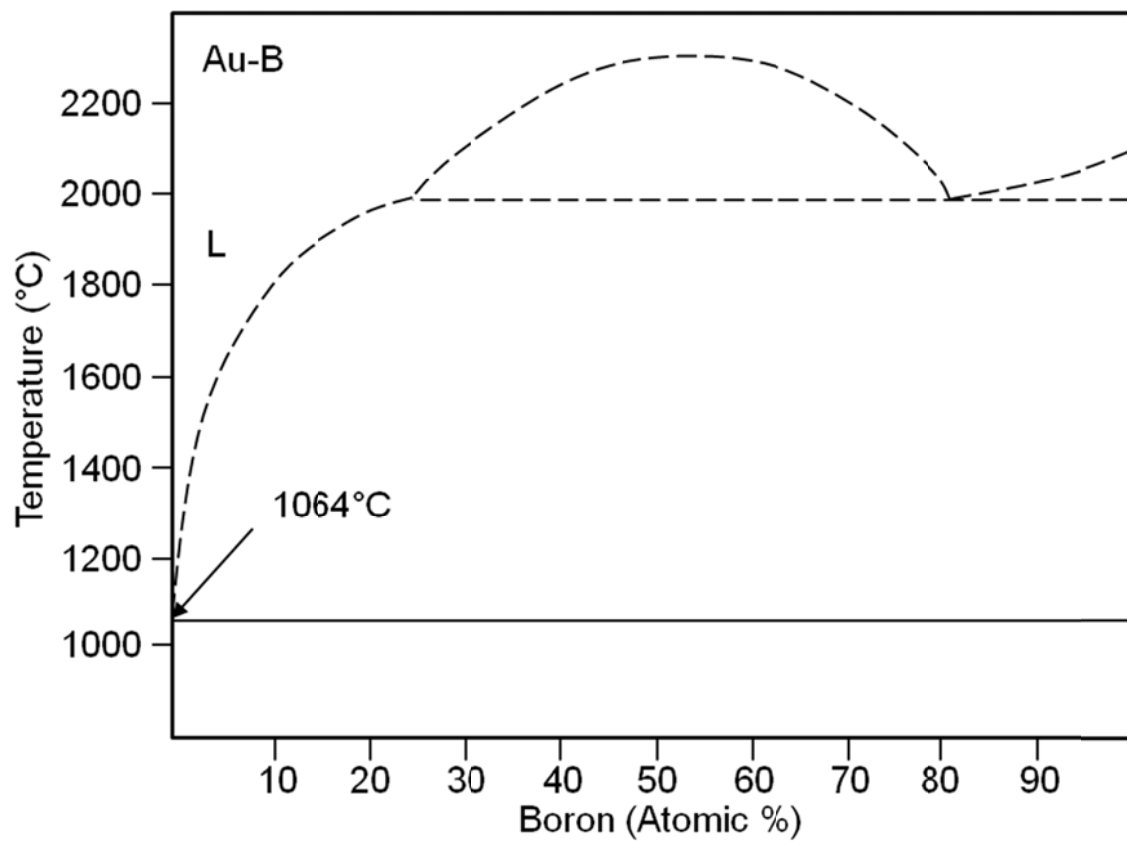


Figure 2.8 Theoretical Au-B binary phase diagram. Dashed lines indicate theoretical estimates.²⁸

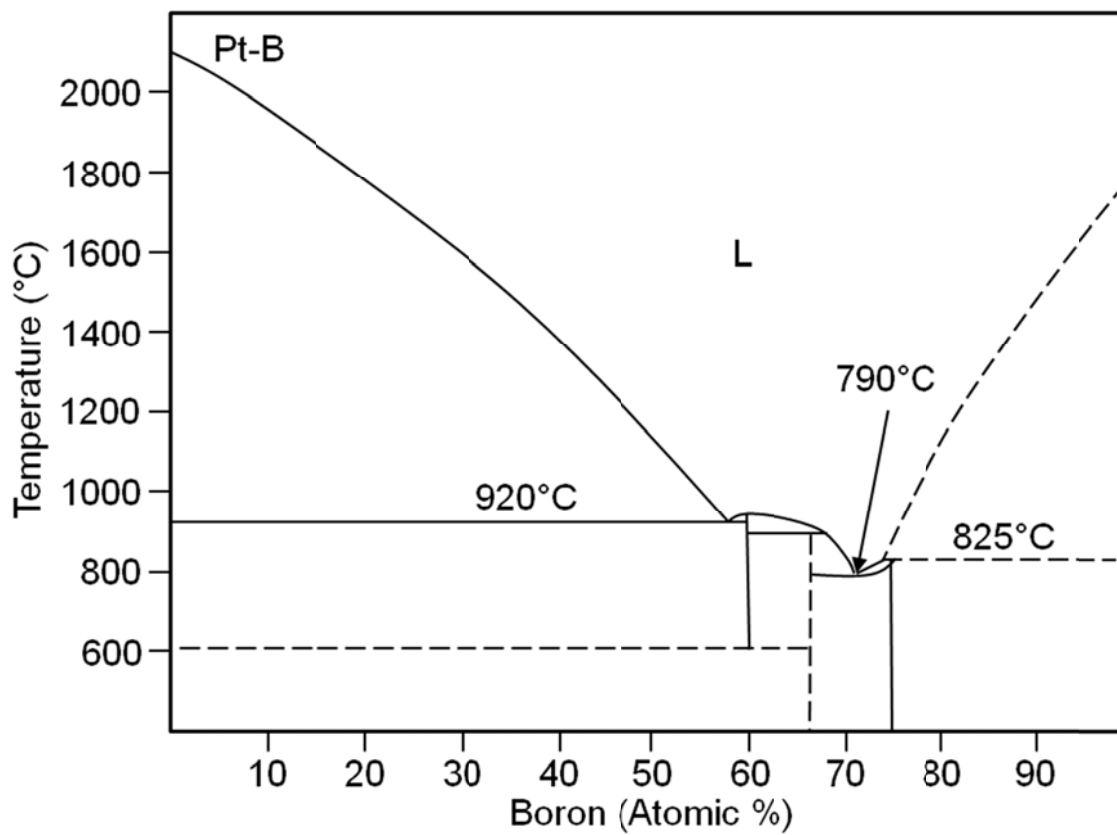


Figure 2.9 Pt-B binary phase diagram. Dashed lines indicate theoretical estimates.²⁸

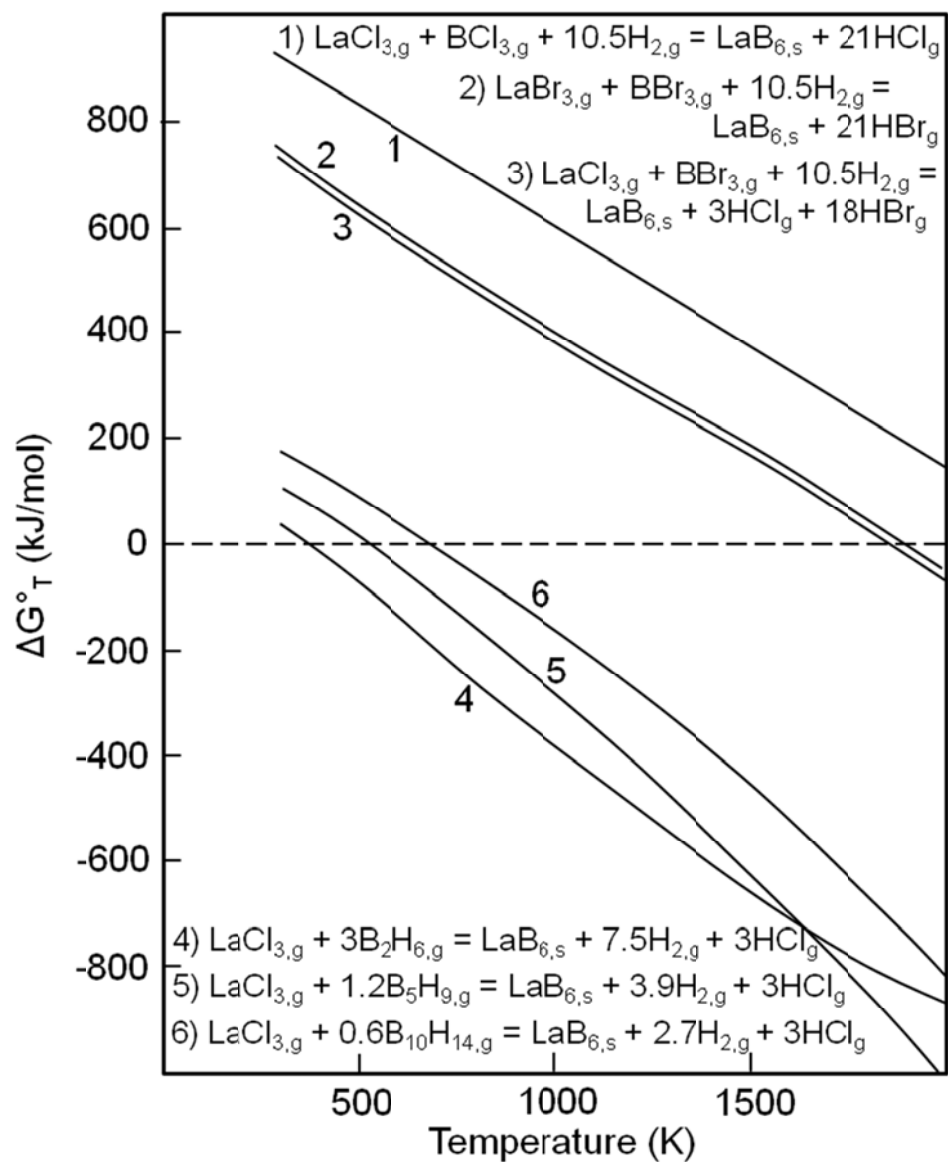


Figure 2.10 Gibbs free energy of reaction versus temperature comparison for reactions between LaCl_3 , LaBr_3 and six different B precursors.²⁹

previously mentioned papers about REB₆ wire growth used BCl₃ as a reaction source, even though the halides are thermodynamically unfavorable and are extremely toxic. Of the three hydrides mentioned in the paper, diborane is the most thermodynamically favored boron precursor but is highly toxic, pyrophoric and extremely expensive. The other two boron source materials mentioned, pentaborane and decaborane are a liquid and solid at room temperature respectively but can be easily vaporized upon slight heating (~100 °C). Though they are essentially the same thermodynamically, decaborane was chosen because it would be easier to handle, costs less, and is slightly less toxic.

2.3.3 Experimental methods

Materials synthesis was conducted in a home-built CVD reactor. (Figure 2.11) The decaborane is located upstream from the heated mass flow controller (MFC) (outlined in red) used to control the flow the decaborane. The decaborane is stored in a stainless steel bubbler submerged in a silicon oil bath and is maintained at a constant temperature of 90°C. The delivery line to the MFC was maintained at 110 °C, while the MFC and delivery line into the reactor were kept at 120-130 °C. The increase in temperature of the lines is meant to prevent the condensation of decaborane as it travel through the system. The synthesis was based on the chemical reaction below, developed in section 2.3.2:



The synthesis was performed in a tube furnace at 1000 °C and a pressure of 160 mTorr for 13 minutes. The sublimed decaborane was introduced into a 1” quartz tube at a flow rate of 0.75 sccm and mixed with argon at a flow rate of 10 sccm. Precursor LaCl₃ (0.2 g, Sigma-Aldrich, Milwaukee, WI) was placed on a quartz boat in the upstream end of the furnace. Silicon substrates (0.7 x 0.7 cm²) coated with platinum (Pt) nanoparticles

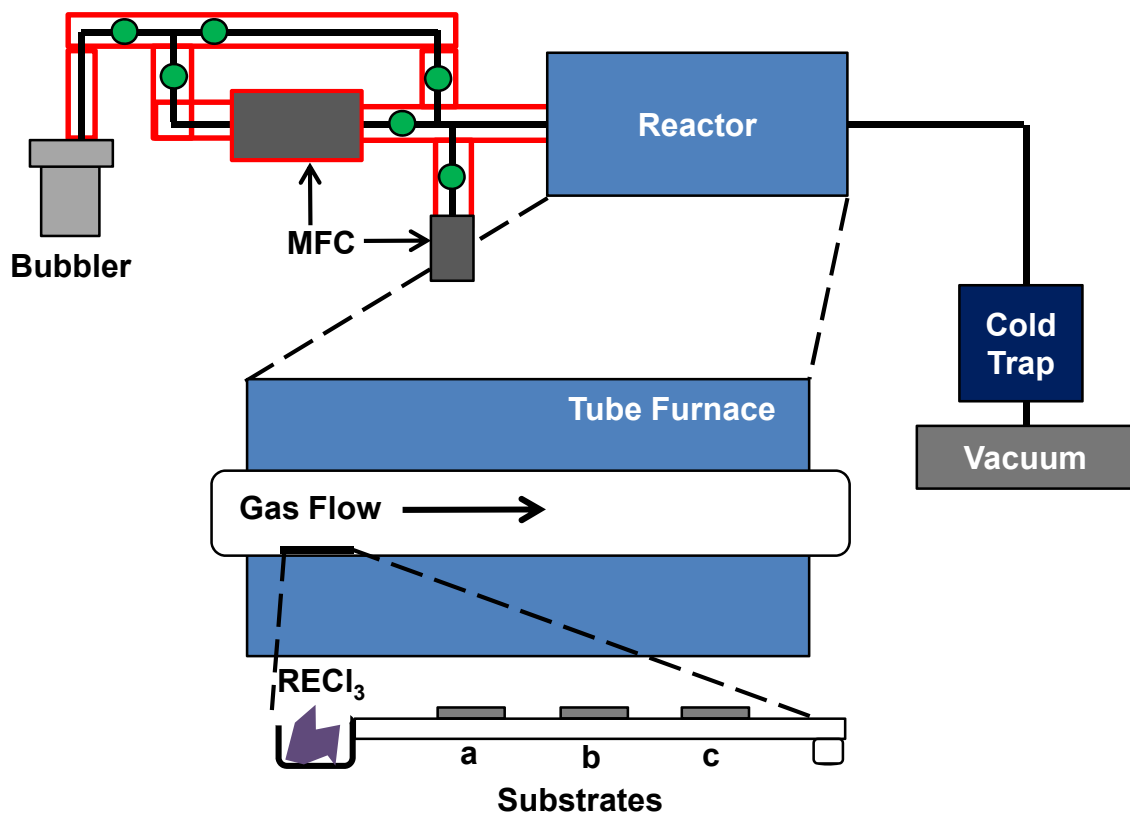


Figure 2.11 Schematic showing the set-up of the CVD system. Zoom-out sections are views of the reactor setup and quartz boat assembly. Objects outlined in red are heated and green circles represent valves.

of diameters (15 - 20 nm) were placed on the same quartz boat at locations 3-, 4-, and 5-cm from the LaCl_3 in the downstream direction. The measured local temperatures of these three positions are about 920 °C, 945 °C, and 960 °C respectively. The dark purple products were characterized with a JEOL JEM-2010 TEM with an Oxford EDX detector, a Phillips CM300 TEM with a GATAN image filter and a Hitachi S4700 Field-Emission SEM. Elemental analysis at different regions of the nanoobelisks (tips, bulk shafts, and side edges) by energy dispersive x-ray (EDX) was obtained in scanning transmission electron microscopy (STEM) mode.

2.3.4 Results

2.3.4.1 Structure identification and characterization

LaB_6 nanostructures of varying shapes from nanoobelisks to nanowires were grown at specific locations within the 920-960°C growth window. Obelisk like nanostructures of different defined pyramidal top heights, cone angles and shaft widths can be preferentially obtained by judicious placement of the substrates in a 2-cm long 920-945°C growth zone down-stream from the lanthanum precursor while wire like nanostructures, with minimal tapering along the length of the shaft, were grown in the 960°C growth zone.³⁰ (Figure 2.12)

At the lower temperature growth zone ($\sim 920^\circ\text{C}$), 3-cm down-stream from the LaCl_3 , preferential growth of nanoobelisks was obtained at a frequency of greater than 95%, with rectangular cross-sectioned nanorods accounting for the remaining structures (Figure 2.12 a and d). The pyramidal top of these obelisks typically have tip diameters of 11 ± 5 nm, very sharp cone angles of $8.7 \pm 1.3^\circ$, and heights of 753 ± 138 nm (Figure 2.13). These obelisk shafts adopt a more tapered structure with length of ~ 4 μm , width of

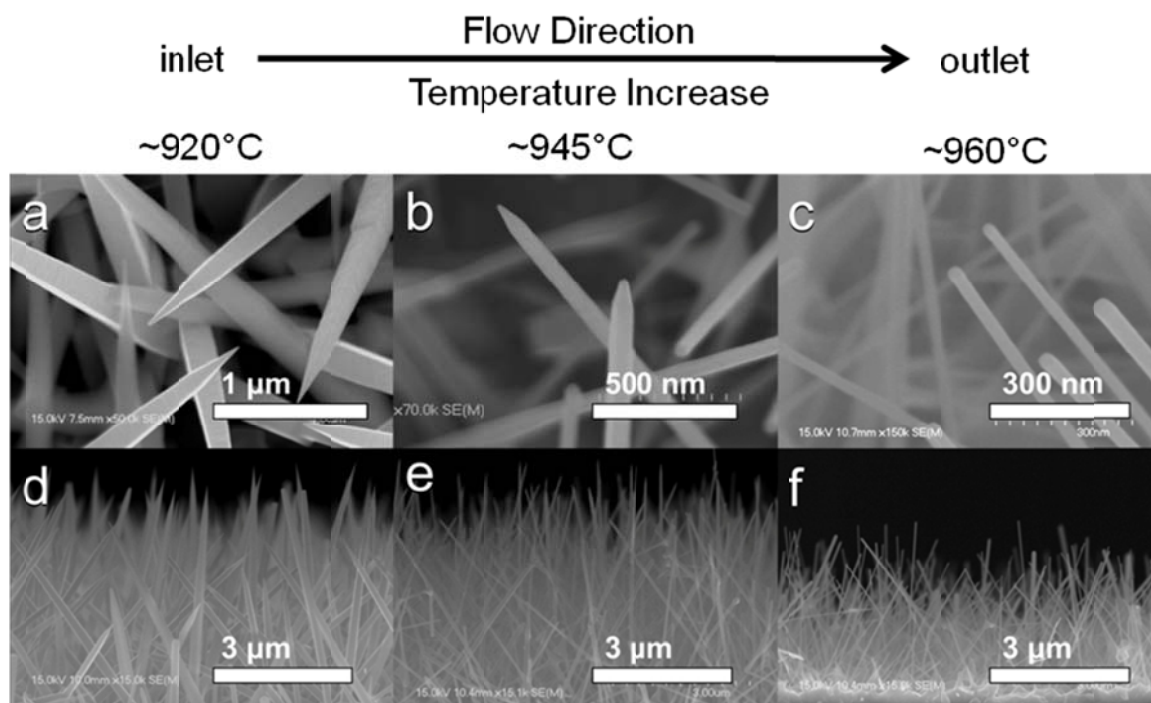


Figure 2.12 Typical SEM images of LaB_6 nanoobelisks and nanowires synthesized with substrates placed at (a) 3-cm, (b) 4-cm and (c) 5-cm down-stream from the LaCl_3 precursor. Figure 1 d, e and f are cross-section SEM images of a, b and c respectively.³⁰

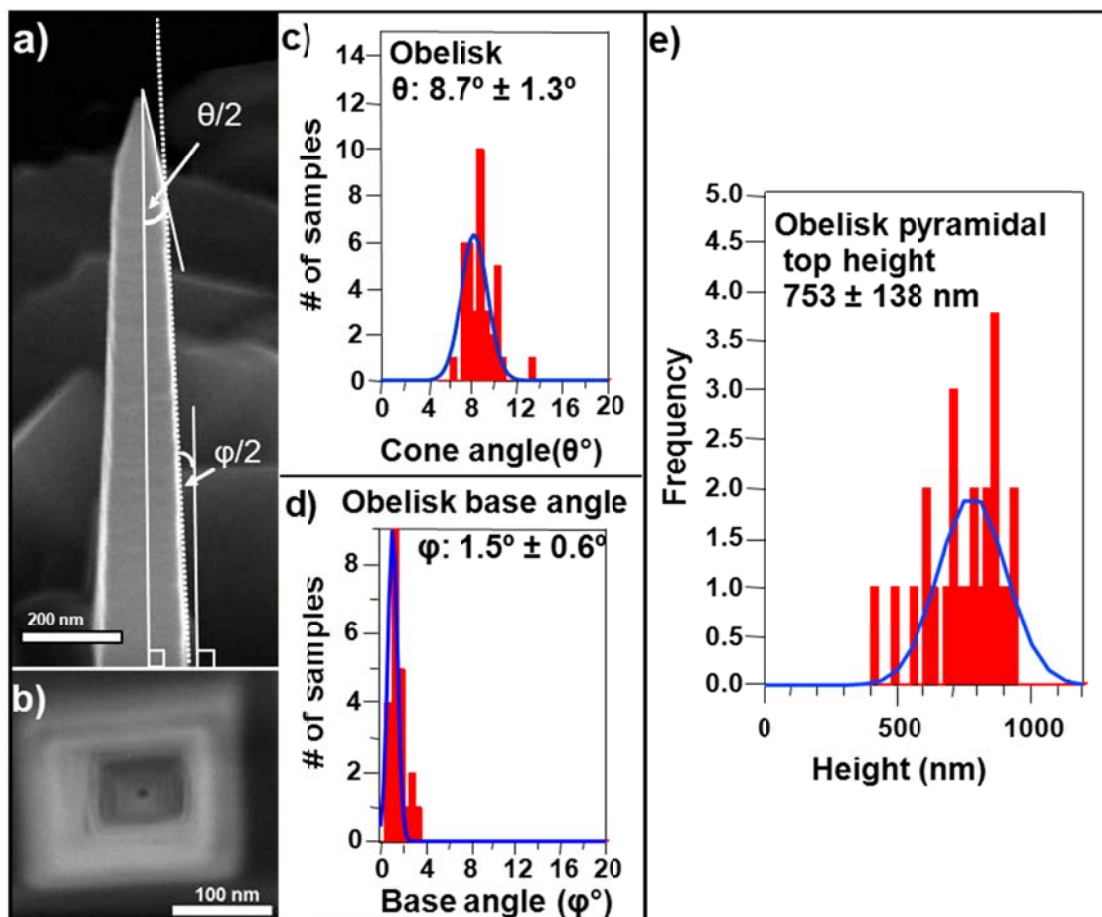


Figure 2.13 Typical SEM images of LaB₆ nanoobelisks grown at 920 °C and the statistics of corresponding cone angle and obelisk tip measurements. Histograms of c) the cone angle at the pyramidal tips, θ , d) angle of vertical declination at the base, $\phi/2$ (base angle ϕ) and e) obelisk pyramidal top height measurements.

150-250 nm at the base of the shaft and angle of vertical declination of $0.8^\circ \pm 0.3^\circ$, characterized by a $\sim 15\%$ decrease in width over a $2 \mu\text{m}$ length (Figure 2.13d). High density growth of these nanoobelisks can be routinely obtained (Figure S2).

At higher temperature growth zone ($\sim 945^\circ\text{C}$), 4-cm away from the La precursor, LaB_6 nanoobelisks with much shorter pyramidal tops and uniform width along the length of the shaft were obtained instead (Figure 2.12b and e). Compared to materials grown in lower temperature growth zone, the pyramidal tops of these structures typically have wider tip diameters of $13 \pm 9 \text{ nm}$, shorter heights of $219 \pm 52 \text{ nm}$ (Figure 2.14). However, the cone angles of these tips remain sharp ($10.8 \pm 2.2^\circ$). While the length of these shorter tip obelisks is in general $\sim 5 \mu\text{m}$, their shaft is mostly of uniform width ($85 \pm 10 \text{ nm}$) with less than 20 % variation over the entire length of the structure, which correlates to an angle of vertical declination at the base of $0.35 \pm 0.15^\circ$.

At the highest temperature growth region ($\sim 960^\circ\text{C}$) 5-cm away from the La precursor, LaB_6 nanowires were preferentially grown (Figure 2.12c and f). Compared to the nanoobelisk structures, the nanowires exhibit very little tapering along the length of the wire, with most of the material having no measurable vertical declination. Though they are also generally capped by a nanoparticle like structure, the nanowires are characterized by larger tip diameters and a larger diameter distribution, $30 \pm 20 \text{ nm}$.

The chemical identity and crystallinity of these LaB_6 nanostructures were examined by X-ray diffraction, TEM and EDX elemental analysis. Figure 2.15 illustrates the typical x-ray diffraction pattern of LaB_6 nanostructures. The XRD pattern was matched with ICDD pattern *00-034-0427* which confirmed that the materials were indeed LaB_6 .³¹ Comparison of the ICD pattern also suggested that the materials were grown with a

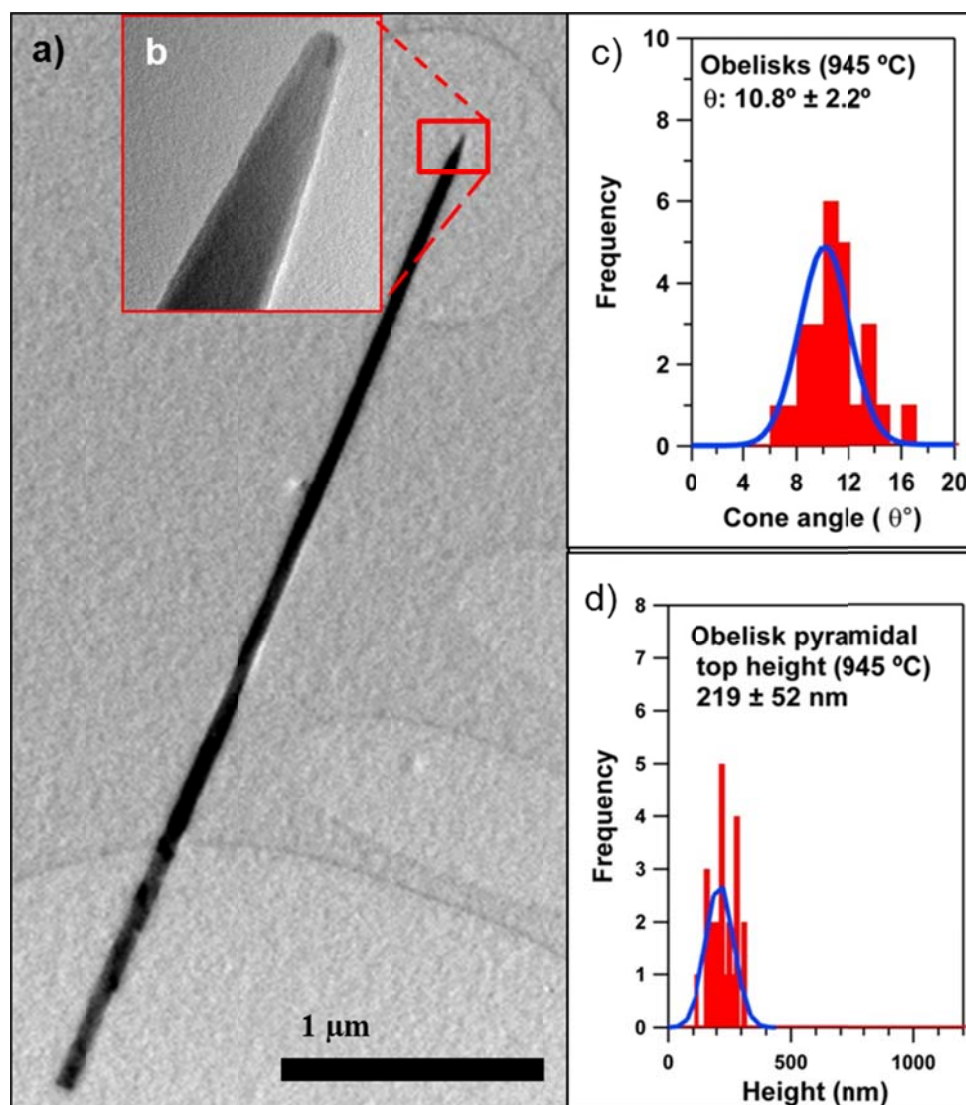


Figure 2.14 TEM images of a LaB6 nanoobelisk synthesized at 945 °C with its cone angle histogram. a) Low magnification TEM image of a nanoobelisk and b) zoom-in image of the obelisk tip. c) and d) are histograms of the obelisk cone angle, θ , and heights of the pyramidal top, respectively.

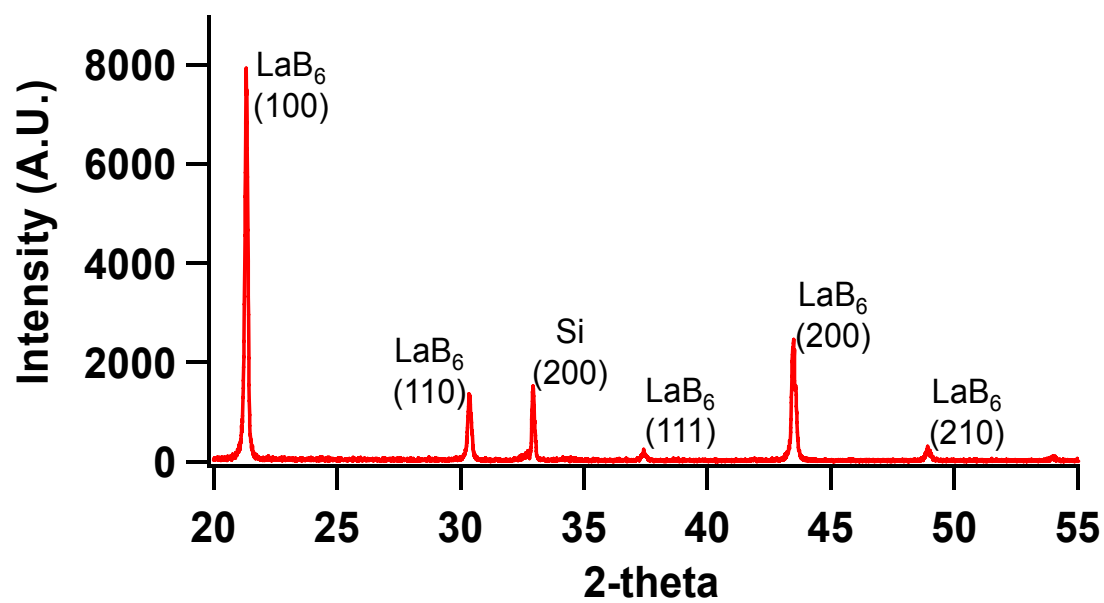


Figure 2.15 Typical XRD powder pattern of CVD LaB₆ nanowire arrays grown on a (100) Si wafer.

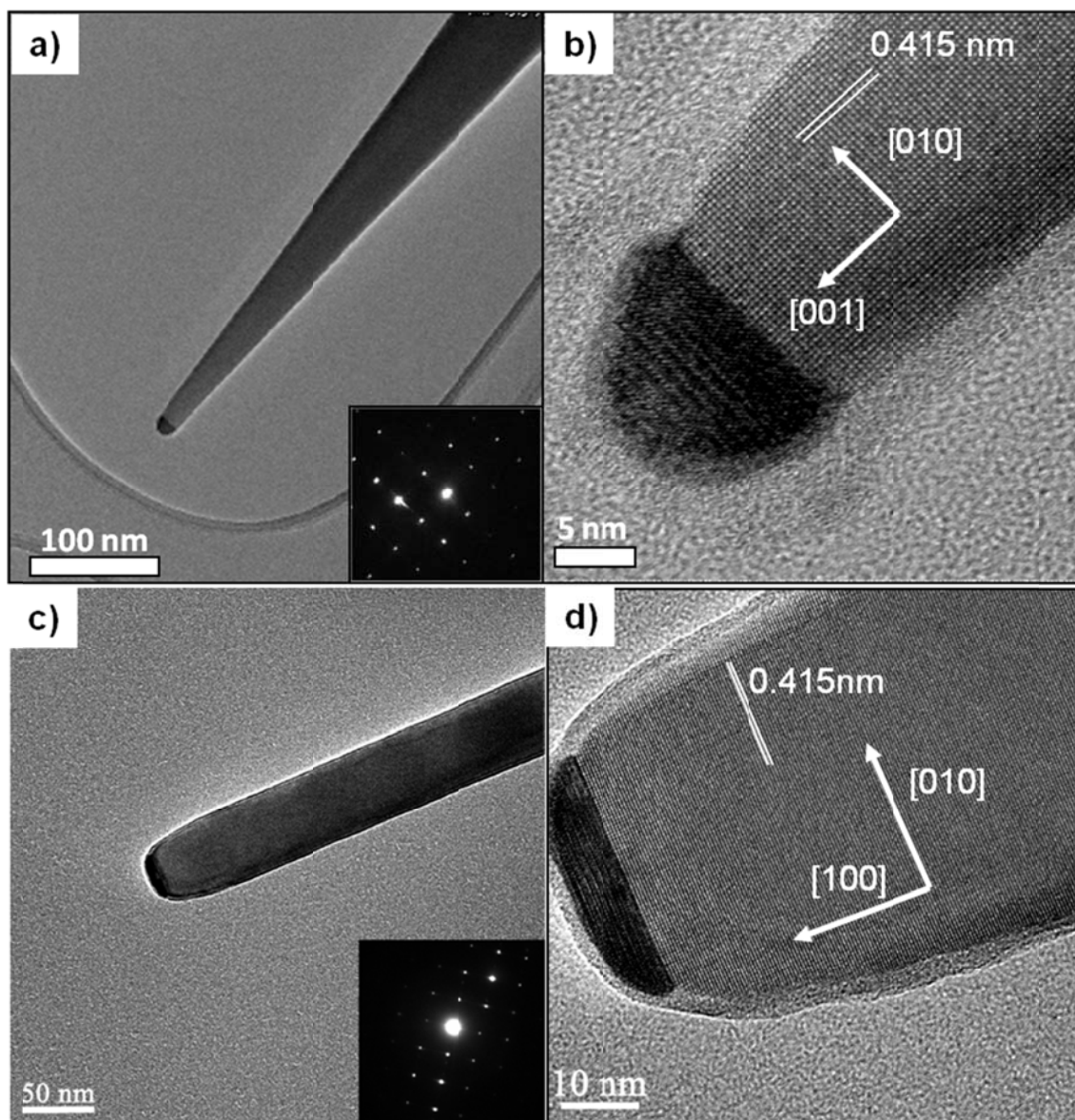


Figure 2.16 TEM images of a 920 °C LaB₆ nanoobelisk (a and b) and 960 °C nanowire (c and d).

preferred [001] growth direction. To elucidate growth direction of the individual nanowires, samples were examined in the TEM. Figure 2.16 depicts the high resolution imaging and SAED patterns of an obelisk and nanowire tip. High resolution TEM images along with the selected area electron diffraction patterns reveal the single-crystalline nature of the LaB₆ nanostructures, which exhibited lattice spacing of *ca.* 4.15 Å (Figure 2.16b and d). Growth directions of these nanostructures were determined to be mostly along the direction as determined by SAED. Dark regions, indicative of a high z material, were found at the ends of most obelisks and wires. Elemental mapping of the obelisk by EDX confirms the presence of boron and lanthanum in the appropriate regions of these obelisk structures (Figure 2.17). The silicon signal in the EDX spectrum is attributed to background contaminations from silicon substrates as suggested by findings in other metallic boride synthesis, however, it cannot ruled out the Pt particle and Si substrates may have alloyed prior to the growth during the temperature ramping. The copper signal is from the copper TEM grid. The EDX spectrum at the edge of the nanoobelisk also reveals the identity of the thin amorphous coating, typically several nanometers thick, to most likely be a small over-coating of boron. The EDX spectrum at the obelisk tip indicates that the dark region is a Pt-rich material containing boron and lanthanum, suggesting that a vapor-liquid-solid growth mechanism may be involve in the materials growth as suggested in Section 2.3.2. (Figure 2.14)

2.3.4.2 Growth mechanism

A time trial growth study was conducted for further insights into the growth of the obelisk structures at 920°C. Structures of samples with reaction duration periods of 3, 5, 9 and 13 minutes were analyzed using SEM (Figure 2.18). Figure 2.18e depicts a

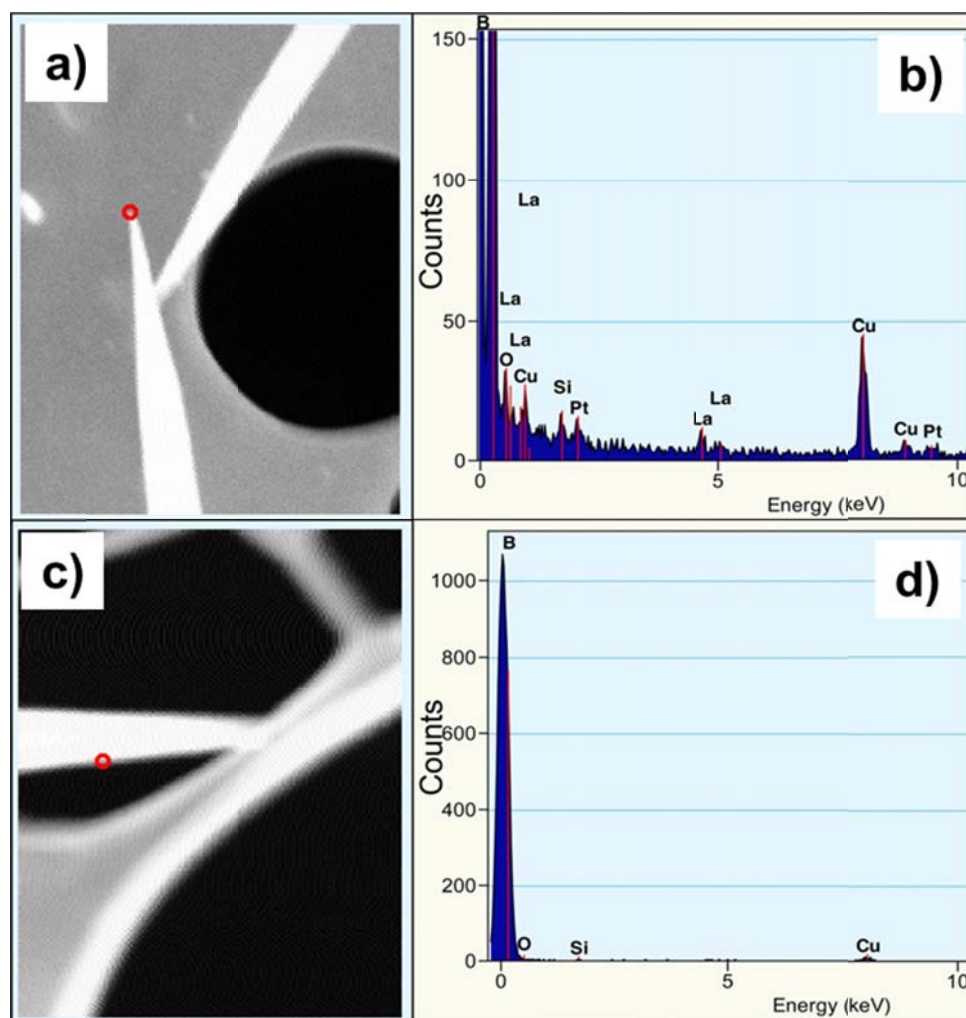


Figure 2.17 STEM images and EDX spectra at (a and b) the tip and edge (c and d) of a 920 °C LaB_6 nanoobelisk, respectively. The red circles indicate the locations on the obelisk where the EDX spectra were obtained. A rectangular window was used for the EDX measurement along the edge of the obelisk.

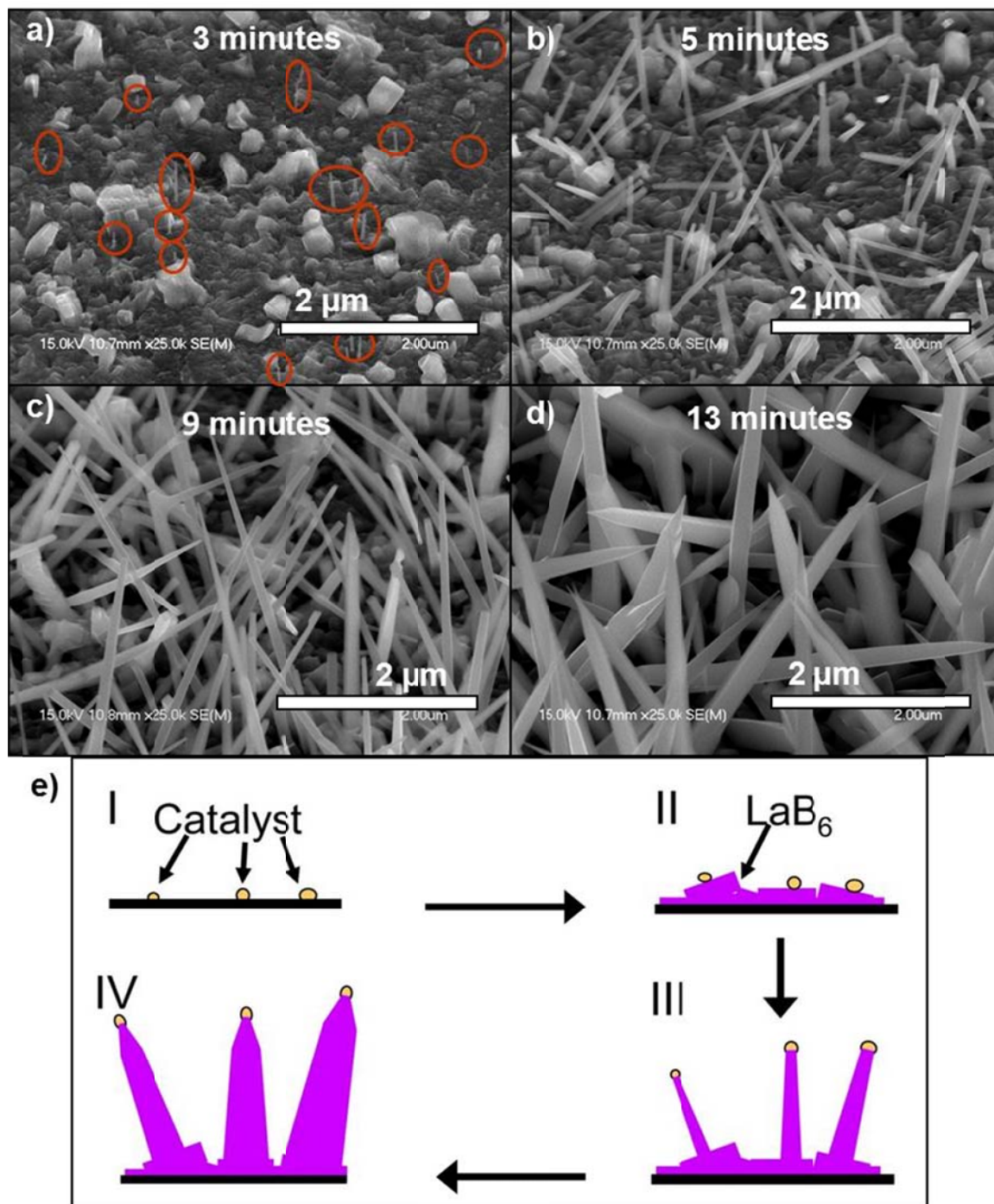


Figure 2.18 Time trial growth study of LaB_6 nanoobelisk. SEM images of the samples prepared with growth periods of a) 3 minutes, b) 5 minutes, c) 9 minutes and d) 13 minutes. The red circles in a) are locations of initial nanomaterial growth. e) A schematic of a possible growth model for the obelisks in four stages.³⁰

schematic of a possible growth mechanism for the nanoobelisks. Initially, a thin layer of cubic-shaped polycrystalline film of LaB_6 was deposited on the silicon substrate coated with Pt particles. Some Pt particles migrated to the faceted surfaces of these cubic crystals and catalyzed the growth of LaB_6 nanowires. These vapor-saturated particles were elevated off the substrate as the wires were formed via the typical VLS process. During the 5-9 minute growth periods, the observed increase in the heights and widths of the materials suggests the growth process followed a continuous VLS type vertical growth with lateral growth due to secondary deposition. The competition between this slow secondary deposition and vertical growth likely initiated the development of tapered wires (Figure 2.18b and c). The evolution of these wires into obelisk structures occurred between the 9- and 13-minute reaction periods (Figure 2.18d). As this sample was in close proximity of LaCl_3 precursor, it received high precursor flux which attributes to the large base widths of obelisks and faster lateral growths. Once the LaCl_3 precursor was significantly depleted, the local concentration at the growth zone decreased until the remaining precursor flow was completely exhausted. This decrease in concentration was expected to cause a decrease in the ratio of lateral vs. vertical growth, leading to the growth of pyramidal tops of the obelisks. While this proposed multi-stage growth model is qualitative due to the finite time needed for the complete depletion of precursor materials at the end, it is consistent with observations in growth experiments such as the multi-stage growth of zinc oxide nanotips on flat top nanowires.

Another indication of this pyramidal top growth due to the change in precursor flux could be inferred from the structures of materials grown in reaction zones with a faster halt in precursor concentration. Since the on-start decomposition temperature of

decaborane is low (170 °C), most of the decaborane decomposes at the inlet of the furnace. Thus, the flux of decaborane reaching the sample is much smaller at positions located further downstream and less secondary deposition is expected. This implication is verified by the uniform shaft dimension of obelisks with shorter pyramidal top obtained at 945 °C (Figure 2.12b and e). These results are in line with the expectation of shorter pyramidal growth time with a faster depletion of source materials after the precursor shutoff in the downstream regions. Growth of only flat top uniform-diameter LaB₆ nanowires at farther downstream further illustrates the importance of precursor flux change in the geometries of material tip growth. The present type of materials growth mode, as compared to kinetically favored growth of specific facets, which allows for only fixed cone angles,³² lend us the possibility to modulate the cone angles of nanostructures by varying the local change in precursor flux. Nevertheless, we cannot eliminate crystal dislocations as possible explanations for this pyramidal top growth. Yet further HRTEM studies at the ~50-nm long pyramid-shaft interface were ineffective due to the large sample thickness.

Section 2.3.5 General synthesis of REB₆ nanostructures: Pd-catalyzed growth

Though the Pt catalyzed VLS growth proved a very effective method for growth of high density nanowire arrays of LaB₆, the catalyst was not able to synthesize several of the rare-earth systems such as HoB₆ and YB₆. These finding effectively limit the catalysts ability for dopant incorporation and heterojunction formation and lead to the search for a new catalyst particle which could be effective for the growth of all REB₆ materials.

As mentioned in Section 2.3.2, the catalyst particle of interest should be able to form a liquid eutectic with B and the RE metal at temperatures below 1100 °C (the operating maximum of our tube furnace). Since the RE metals of interest number about 14 elements, investigation into new catalyst materials began by searching for metals with high B solubility. Beyond providing much smaller search parameters, the limitation of high B solubility also served another purpose; phase control of the hexaboride. In the binary phase diagrams of REB_6 materials, there are essentially two regions that exist outside of the hexaboride: (1) A metal-rich/boron-deficient region in which several different stable crystalline phases co-exist and (2) a boron-rich/metal-deficient region in which usually only hexaboride and boron co-exist with occasionally dodecaboride.²⁸ (Figure 2.19) It was conjectured that by utilizing a catalyst particle with high boron solubility, synthesis of REB_6 , the higher B content crystalline phase, would be preferential. For example, Figure 2.20 represents the binary phase diagram for the Pd-B binary system.²⁸ As compared to Au, Figure 2.8, Pd can dissolve a much higher percentage of B. Figure 2.20 and 2.21 also present the binary phase diagrams of Ni and Pt with B.²⁸ Comparison shows that Ni, Pd and Pt can dissolve more B than Au, with Pt and B having a much lower liquid eutectic temperature than B with Pd and Ni.

From the B solubility limits in the catalyst particle, Pt would appear to still be the best choice. However, as previously mentioned, synthesis of YB_6 nanowires was not attainable. The reason is that Y has only sufficient solubility in Pd and Ni, not Pt, below 1100 °C.²⁸ (Figure 2.22-2.24) This implies that both Pd and Ni can serve as a catalyst material for VLS growth of YB_6 whereas Pt would require higher reaction temperatures. Furthermore, since the Pd-B liquid alloy has a lower eutectic temperature than the Ni-B

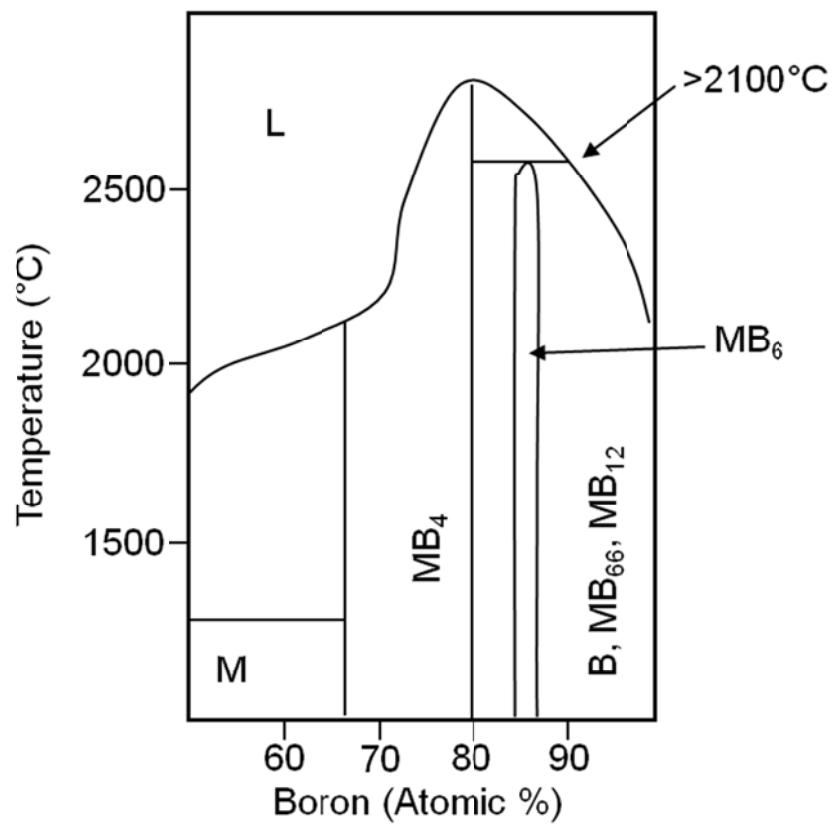


Figure 2.19 General representation of a RE-B binary phase diagram.²⁸

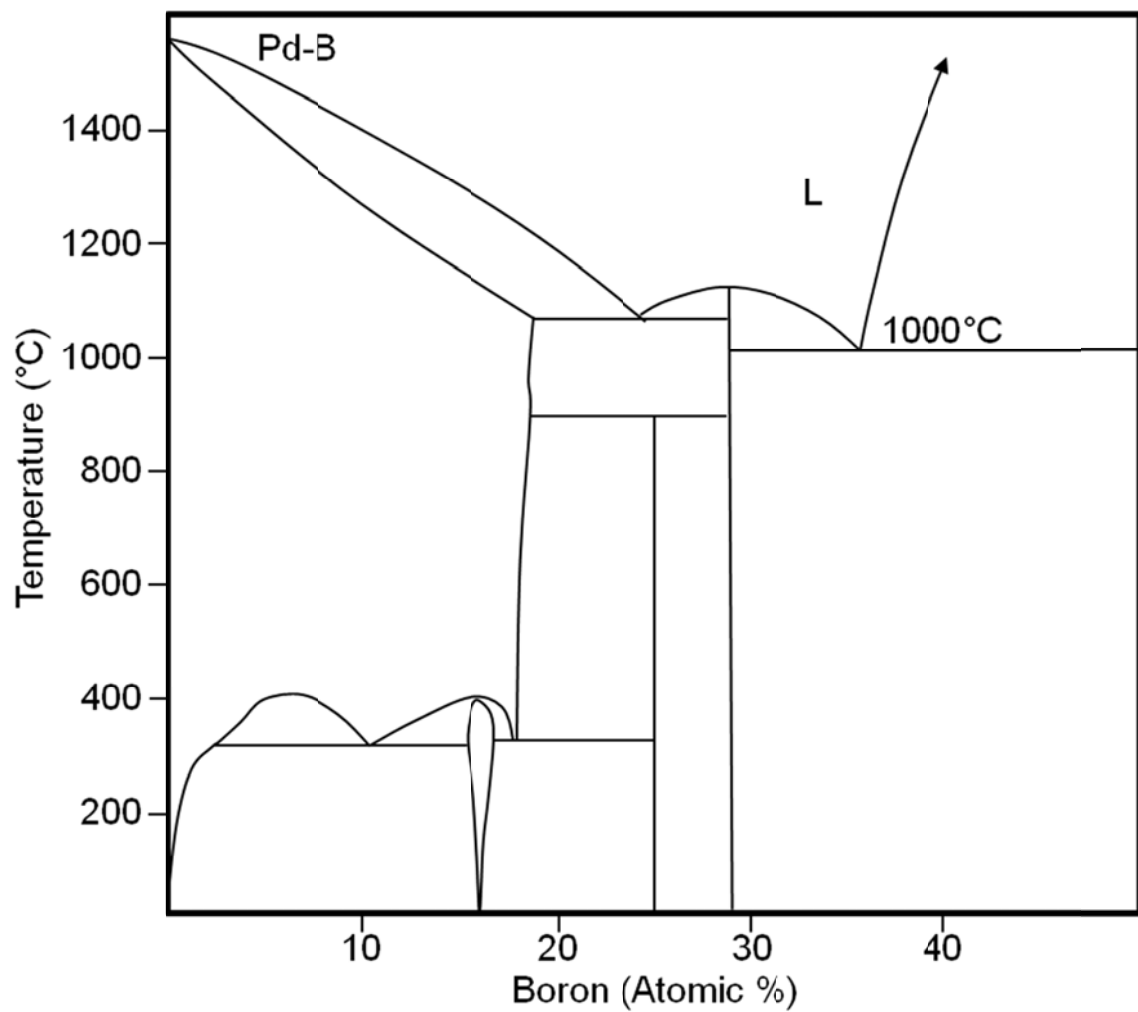


Figure 2.20 Pd-B binary phase diagram.²⁸

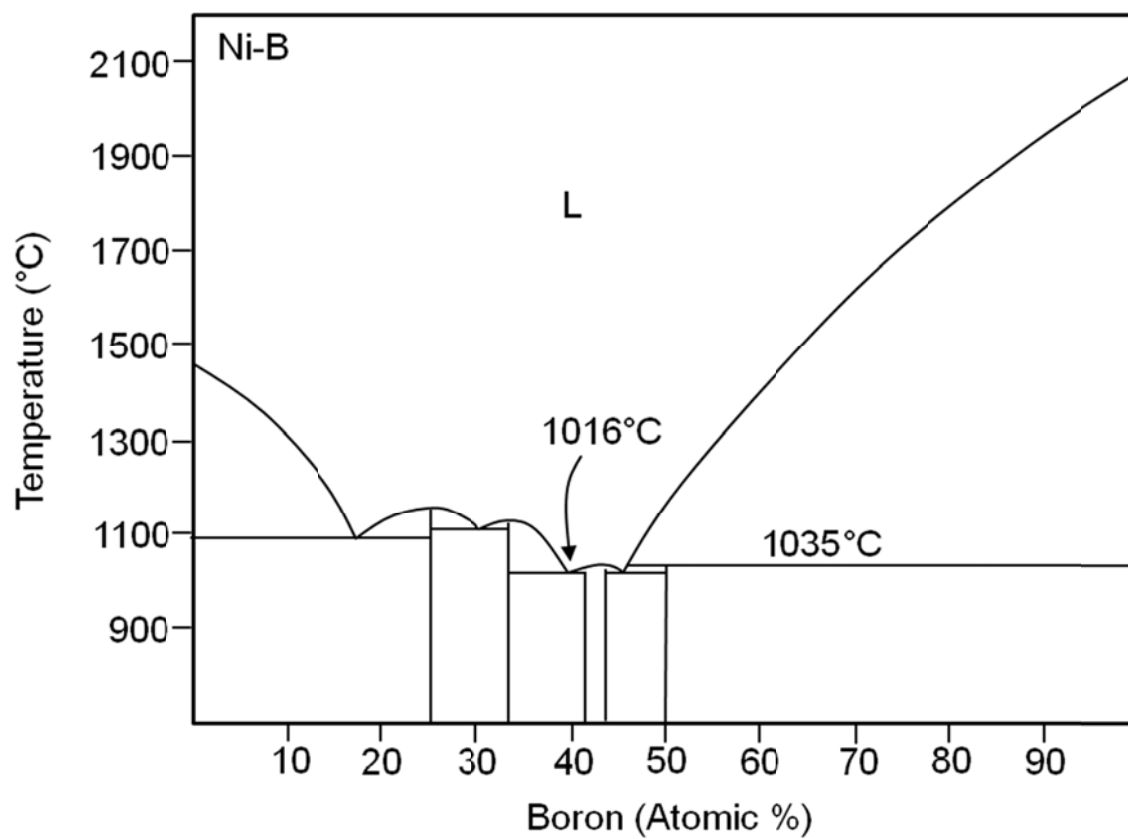


Figure 2.21 Ni-B binary phase diagram.²⁸

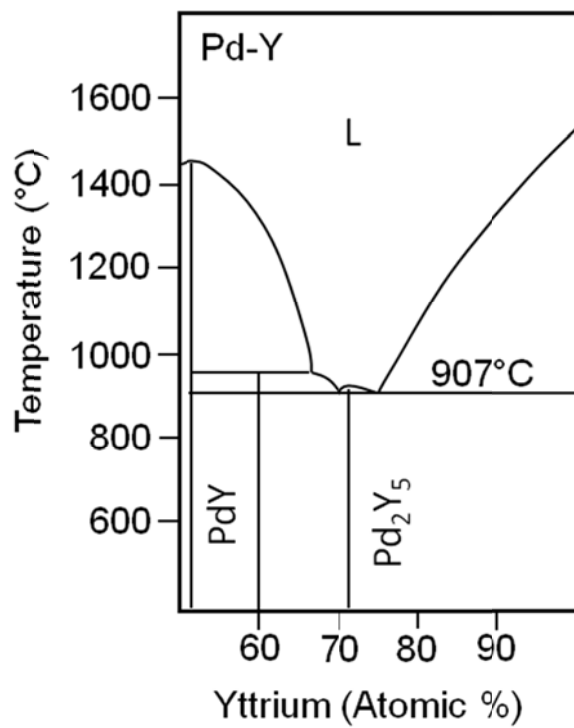


Figure 2.22 Liquid eutectic region of the Pd-Y binary phase diagram.²⁸

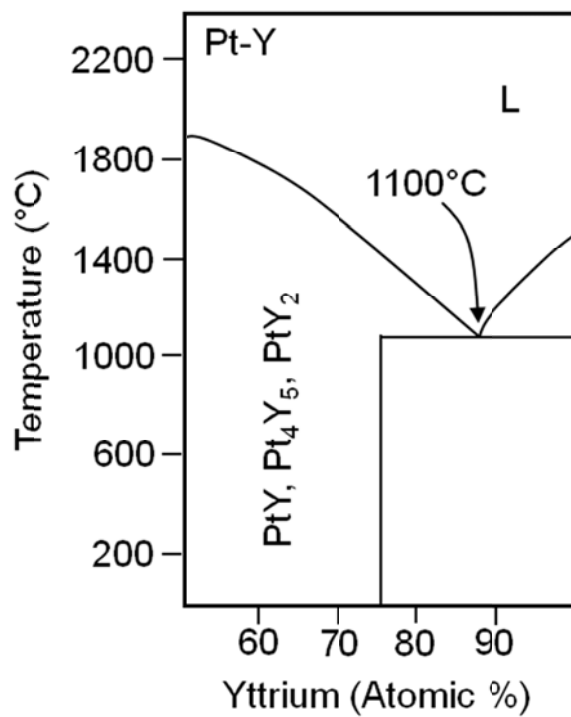


Figure 2.23 Liquid eutectic region of the Pt-Y binary phase diagram.²⁸

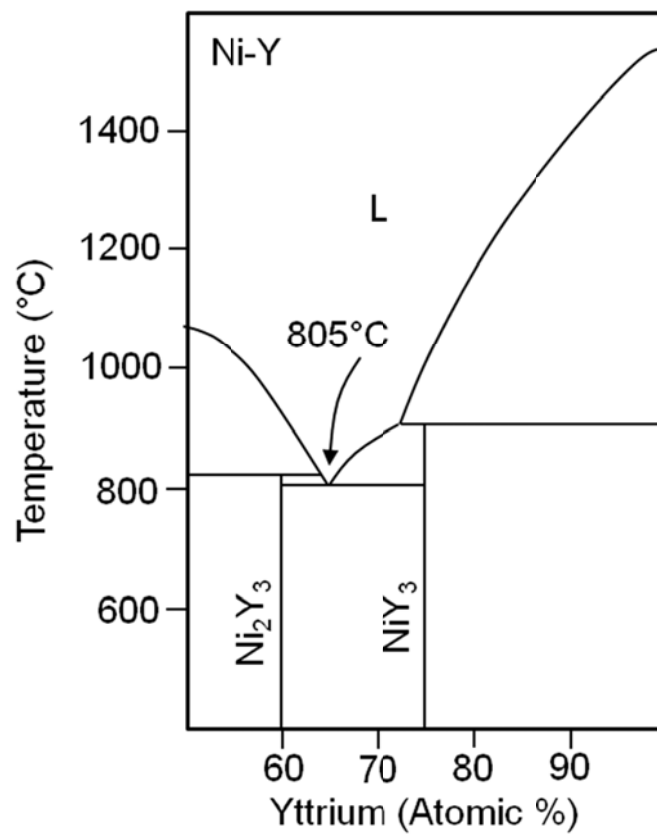


Figure 2.24 Liquid eutectic region of the Ni-Y binary phase diagram.²⁸

liquid alloy, Pd would be a preferred catalyst material for the universal growth of RB_6 nanowires systems. Upon comparison of all the RE-Pd phase diagrams, a reaction temperature of 1000°C was chosen for the reported growth conditions due to the solubility limits of boron (Figure 2.20).

2.3.6 Experimental methods

REB_6 nanostructures were prepared by a chemical vapor deposition (CVD) scheme via the VLS mechanism using metal chloride and decaborane source materials, similar to the Pt catalyzed method.³⁰ Pd nanoparticles were drop-coated onto (100) Si wafer substrates, placed on a quartz reactor boat along with the $RECl_3$ and then loaded into the horizontal tube furnace. The catalysts were synthesized by reduction of $[\text{PdCl}_4]^{2-}$ to yield Pd nanoparticles of 37 ± 6 nm in diameter.³³ The reaction was carried out at 1000°C and 160 mTorr under an argon and decaborane flow mixture. The $RECl_3$ was located in the colder, up-stream section of the reactor at a temperature between 700 and 850°C . Table 2.2 provides a list of melting points of $RECl_3$ which was used to determine the position (and therefore temperature) the source material would be located.

The resulting materials were characterized by a field emission scanning electron microscope (FE-SEM) operated at 15 kV, an X-ray diffractometer (XRD) using Cu $K\alpha$ x-ray source of about 1.544 \AA and a transmission electron microscope (TEM) operated at 200 kV with selected area electron diffraction (SAED) and EDX.

2.3.7 Results

2.3.7.1 Pd-catalyzed growth

Table 2.2 RECl₃ melting points

<u>RECl₃</u>	<u>Melting Point (°C)*</u>
YCl ₃	721
LaCl ₃	860
CeCl ₃	848
PrCl ₃	786
NdCl ₃	784
SmCl ₃	686
EuCl ₃	632
	(decomposition temperature)
GdCl ₃	609
TbCl ₃	588
DyCl ₃	680
HoCl ₃	718
ErCl ₃	774
TmCl ₃	Not available
YbCl ₃	875
LuCl ₃	905

* All values are for anhydrous chlorides

To confirm the finding of the binary phase diagrams, synthesis of YB_6 was conducted with both the Pd and Pt nanoparticles using the synthetic method outline above. Figure 2.25 shows the results of the growth using Pt (a) and Pd (b) nanoparticles respectively. SEM imaging shows there is significant growth of YB_6 nanowires on the Pd catalyzed substrates while the Pt catalyzed substrate yields only a thin film. This is likely due to the lack of yttrium solubility with Pt at the temperatures used for synthesis. Though the evidence is only circumstantial, it provides insight into the growth and also indicates that Pd may be a suitable catalyst for the general synthesis.

Synthesis of the remaining REB_6 systems was conducted using available $RECl_3$ and judicious placement indicated by the chlorides melting point. Figure 2.26 shows the SEM cross-section images of 6 of the 10 systems synthesized by the Pd catalyzed method. The remaining REB_6 cross-sections can be found in the appendix. Substrate position was judiciously chosen to correspond to nanowire growth (section 2.3.2). Figure 2.27 are the TEM images and SAED images of several nanowire systems. The remaining images along with the EDX spectrum can be found the appendix. Analysis indicates the materials are capped by a metal particle, are single crystalline and have [100] growth direction, similar to materials synthesized by the Pt catalyzed method. Compositional analysis by EDS was also very similar to that of the Pt catalyzed nanowires. The EDS indicated Pd was indeed at the tip of the nanowires and that the RE, B, Si and O were present. However, do to the secondary x-ray emission by the RE metal, nothing more than qualitative data can be obtained from the EDS spectrum.

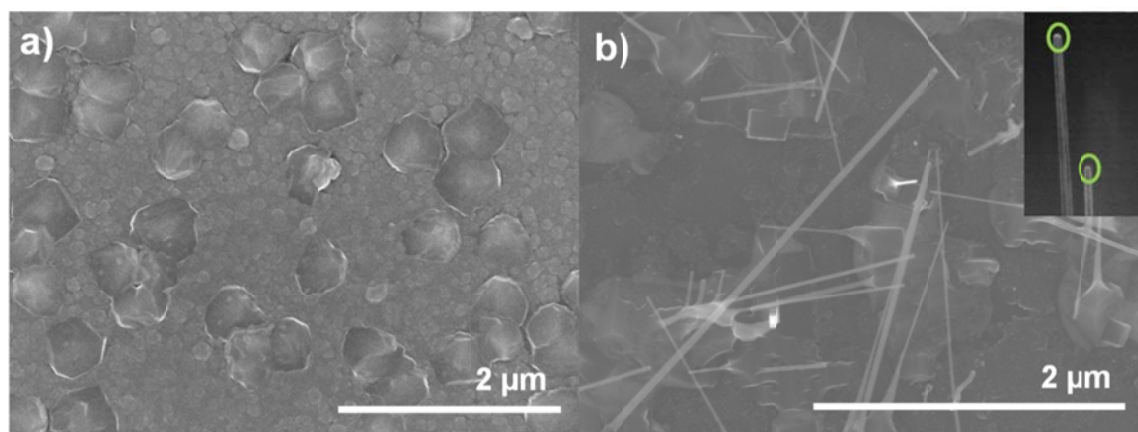


Figure 2.25 SEM images YB₆ nanowire synthesis catalyzed by: a) Pt nanoparticles and b) Pd nanoparticles. Inset in b) is a zoom-in image of nanowire tips with circles indicating the presence of high-z material.

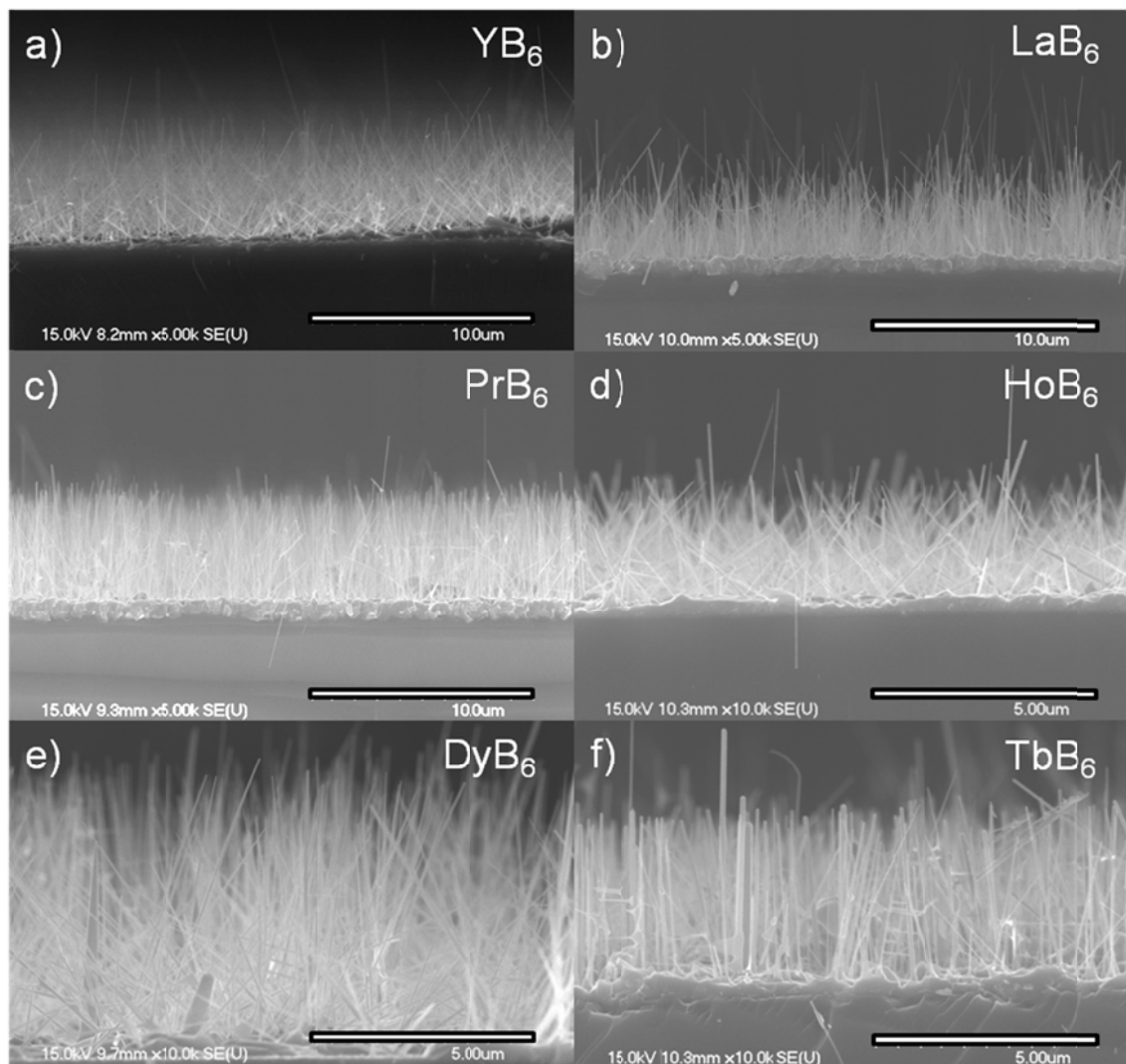


Figure 2.26 Cross-sectional SEM images of different REB_6 nanowire systems. (RE = Y, La, Pr, Ho, Dy, Tb) Scale bars are 10 μm .

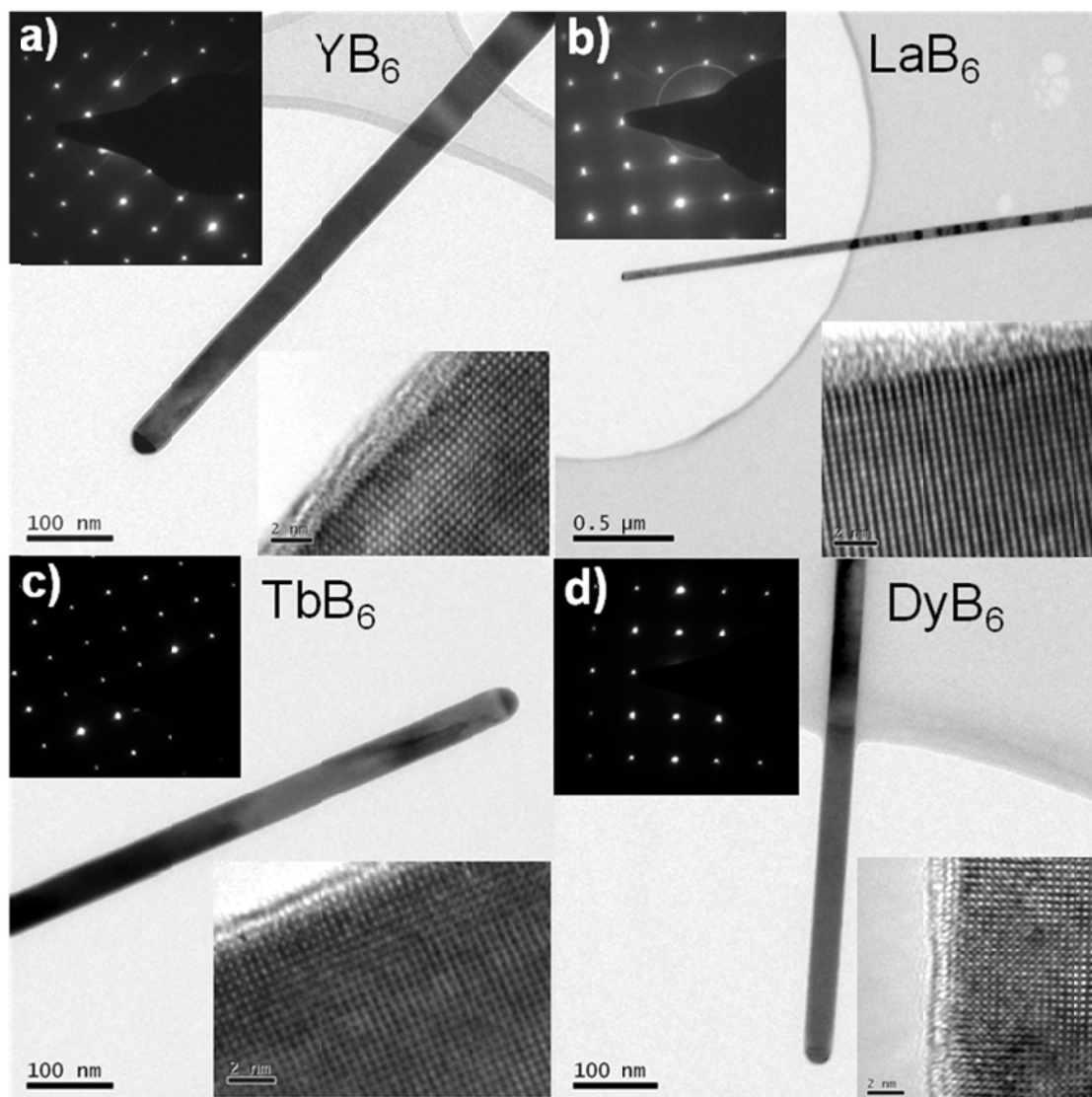


Figure 2.27 TEM images of REB₆ nanowires (RE = Y, La, Tb and Dy). Insets in a)-d) are SAED pattern (top left corners) and HRTEM images (bottom right corners) for the respective nanowires.

2.3.7.2 Electronic properties

Electronic measurements of the REB₆ materials were conducted to further determine the quality of the materials synthesized. CVD deposited films were analyzed as equipment for determining the properties of single nanowires was not available. Samples were loaded onto a 4-point probe sample board (Ecopia, South Korea). Four point resistivity and Hall effect measurements were conducted as outlined in Chapter 1.2.³⁴⁻³⁶ A Keithley 2410 sourcemeter was used to source current, a Keithley 2182A nanovoltmeter was used to measure the voltage, and a Keithley 7001 switch system with a 7012-S 4x10 matrix card (Keithley Instruments, Inc., Cleveland, OH) was used to control switching of the probes for the Van der Pauw and Hall effect measurements. Diagrams of the switch system and lead connections are presented in Figure 2.28 and Figure 2.29 respectively.

Resistivity and Hall effect results are presented in Table 2.3 and compared to previously reported literature values.¹⁰ It was found that the materials have metallic type resistivity and are very close to the reported literature values. Furthermore, samples of SmB₆ were found to show the characteristic p-type conduction expected from the material at room temperature, but had higher carrier concentrations and lower resistivity.

Samples at two different growth positions were tested and compared to determine if the location of the growth, which we have previously shown changes the shape but not the crystallinity, changed the electronic properties significantly. (Table 2.3) There was a small increase in the resistivity and carriers, but a decrease in the mobility. This may be due to a small increase in the metal's concentration due to decreased boron flux further into the furnace. The excess metal atoms would act as scattering sites in the lattice and increase both the resistivity (increase the resistance) and the carrier concentration but

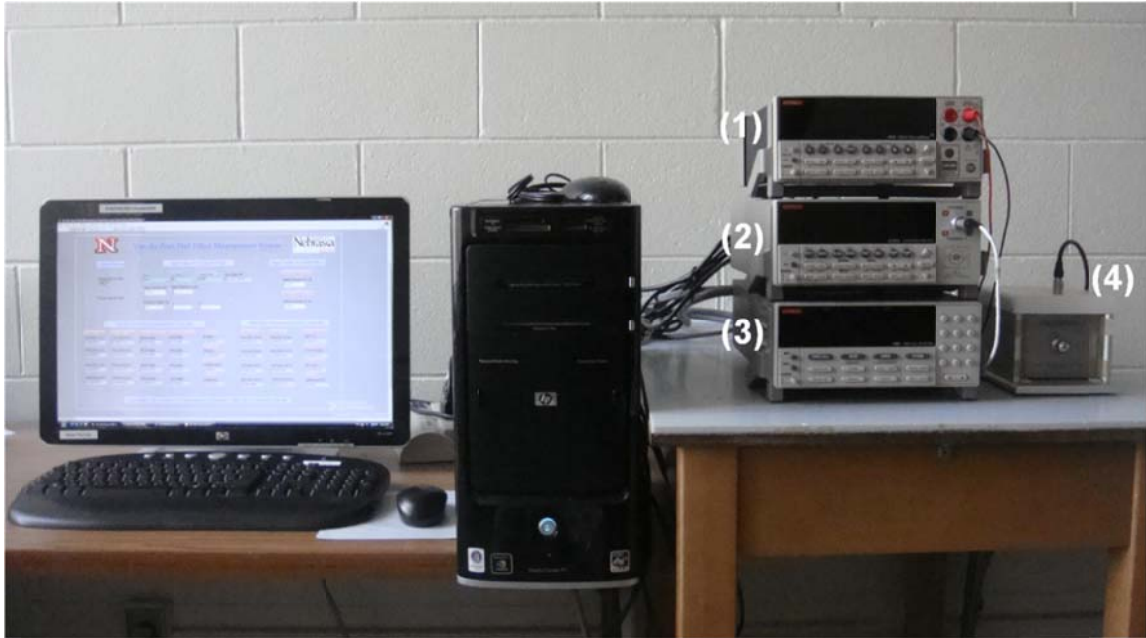


Figure 2.28 Van der Pauw and Hall effect system for measurement of RES electronic properties. (1) Keithley 2410 source meter, (2) Keithley 2182A nanovoltmeter, (3) Keithley 7001 switch system, and (4) Sample holder with a 0.5 Tesla fixed field magnet

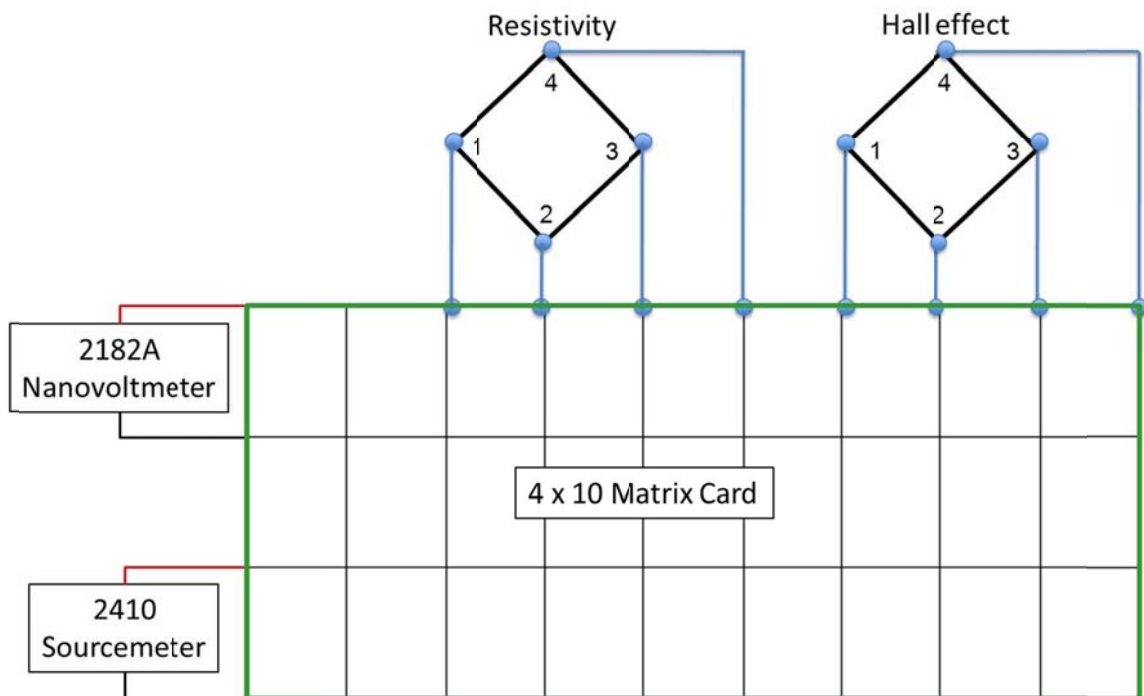


Figure 2.29 Schematic for the connection of the 2410, 2182A and sample connections to the 4 x 10 matrix card (outlined in green). Cables connecting the matrix card to the sample are exchanged when switching from the resistivity measurement to Hall effect measurement.

Table 2.3 Resistivity and Hall effect measurement results

<u>REB₆</u>	<u>Resistivity</u> ($\mu\Omega\text{-cm}$)	<u>Mobility</u> (cm^2/Vs)	<u>Resistivity (lit.)¹⁰</u> ($\mu\Omega\text{-cm}$)
LaB ₆ (920°C)	-20.3	308	-15.0
LaB ₆ (960°C)	-48.4	107.2	-15.0
CeB ₆	-60	191.8	-29.4
NdB ₆	-29.9	21.6	-20.0
SmB ₆	11.7	11.3	207.0
DyB ₆	-38.0	0.5	-

Note

1. Negative signs denote *n*-type conductivity.
2. No sign denotes *p*-type conductivity.

decrease the mobility (same reason as the resistivity). This suggests that though similar in crystal structures, the more “ideal” materials electronically may be the ones synthesized in the upstream (obelisk) position.

2.3.7.3 Temperature dependent growth morphology

Though section 2.3.4.2 discusses the position dependent growth of the REB₆ nanomaterials at fixed furnace temperature synthesis, there is still need for further understanding of how temperature of our precursors and CVD system direct the apparent VLS growth of the nanostructures. To determine their effect, neodymium boride nanostructures were prepared by the Pd-catalyzed chemical vapor deposition (CVD) scheme, section 2.3.6.³⁷ The synthesis was processed in a 1-inch quartz tube heated in a 2-ft long horizontal furnace between 795 and 950 °C and at a pressure of *ca* 150 mTorr for 10 min. In a typical CVD run, 0.3 g NdCl₃·6H₂O (99.9% Sigma-Aldrich, Milwaukee, WI) was loaded on a quartz boat at the upstream end of the quartz tube (15.5 cm from the centre of the furnace). The substrate supports for the growth of the nanostructures were silicon wafer substrates (size: 1 x 1 cm²) topped with a 20 nm thick silicon nitride film (University Wafer, Boston, MA). The support substrates were evenly coated with Pd nanoparticles by a drop-casting method and then placed in the quartz tube furnace at a location 3 cm in the down-stream direction from the neodymium chloride source. The system was pumped to a base pressure of 2 mTorr. During the heating step, the system was annealed at 300 °C and 500 °C for 5 min. each to remove the water in the NdCl₃ precursors. When the furnace reached the desired temperature, 0.75 sccm decaborane (B₁₀H₁₄, Alfa Aesar, Ward Hill, MA) and 10 sccm argon (99.999 %, Linweld, Lincoln,

NE) were introduced into the reactor for 10 min. The decaborane started to pyrolyze upon entering the heated zone near the entrance of the furnace. After the reaction, the samples were cooled to room temperature in a flow of 120 sccm argon. To examine the effect of the reaction temperature on the growth of neodymium boride nanostructures, experiments were performed at furnace set temperatures of 900, 950, 1000 and 1050 °C. The corresponding local temperatures measured at the sample location were 795, 850, 915 and 940 °C, respectively.

The surface morphology of the samples was studied by field emission scanning electron microscopy (FE-SEM, Hitachi S4700 operated at 15keV (Hitachi High Technologies America, Inc. Pleasanton, CA)). Detailed crystal structures of individual nanostructures were studied by transmission electron microscopy (TEM, Tecnai G2 F20 S-Twin operated at 200keV (FEI, Hillsboro OR)) and selected area electron diffraction (SAED). The elemental compositions of the samples were analyzed by an energy dispersive x-ray spectrometer (EDS, EDAX Inc, Mahwah, NJ) equipped with the TEM. Each TEM sample was prepared by drop-casting a solution of sample sonicated in ethanol onto a holey carbon film mounted on a copper TEM grid support. X-ray diffraction (Bruker AXS D8 Discover with GADDS area (Bruker AXS Inc., Madison, WI)) was also performed on the samples to examine the crystallinity and crystal structure of the bulk samples. The weighted average wavelength of the Cu K α x-ray source for the x-ray diffractometer is 1.5417 Å.

The morphological structures and chemical compositions of NdB₆ nanomaterials were found to be strongly influenced by the reaction temperatures to yield different 1-D nanostructures – curly nanowires and tapered straight nanowires. Typically, at a low

reaction temperature (795 °C), curly amorphous wires with length ranging from about 400 nm to 4 μm were obtained. (**Sample 1**, Figure 2.30a and e) The base and tip diameter of these wires are 278 ± 26 nm and 60 ± 17 nm respectively. No crystalline facets or atomic lattices are observed in the high resolution transmission electron microscopy (HRTEM) images of these wires. (Figure 2.31a and e) The diffusive diffraction rings in the corresponding SAED pattern suggest no long range crystalline order in this sample. (Figure 2.31i) The nearly amorphous nature of the sample was further confirmed by the weak NdB_6 diffraction peaks detected in the XRD spectra of the sample film. (Figure 2.32) EDX spectra of these wires reveal that they are mainly composed of boron with low neodymium content. The weak silicon peak shown in the spectrum is probably due to the silicon species migrated from the substrate or the quartz tube. The oxygen signal could come from the surface oxide formed on the materials. (Figure 2.33)

At a reaction temperature of 850 °C, the as-produced neodymium boride nanostructures (**Sample 2**) underwent a structural transition from close-to-amorphous to partially crystalline materials. SEM images of **Sample 2** show that this sample consists of a thin film with curly wires. Cube-like “knot” structures which indicate localized secondary growth were often found on these wires (Figure 2.30b and f). The average diameters of these wires are 290 ± 48 nm, whereas those of the cube-like structures are 312 ± 45 nm. A HRTEM image (Figure 2.31f) of the crystalline cube-like “knot” areas (arrowed area in Figure 2.31b) shows lattice planes with lattice spacings matching the interplanar distance of neodymium hexaboride (110) planes. The corresponding SAED pattern of this sample region (Figure 2.31j) also verifies the single-crystalline nature of this region.

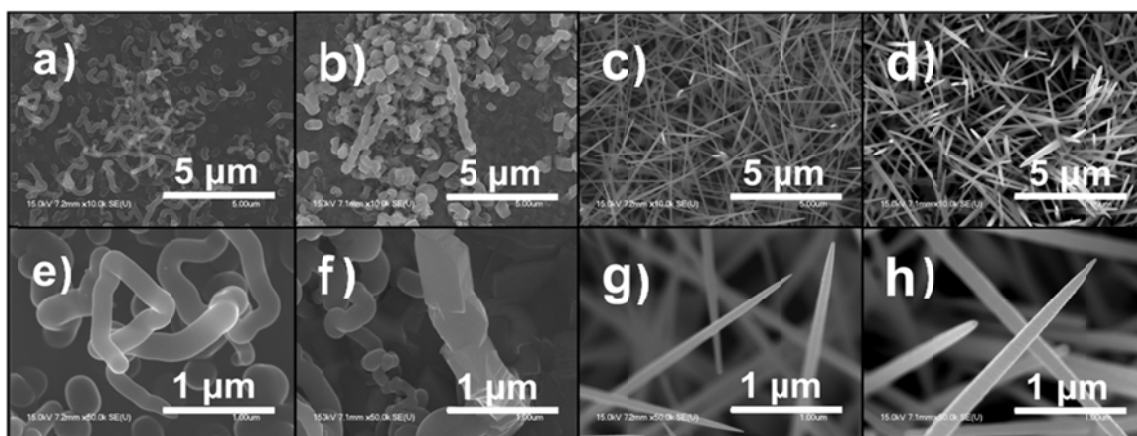


Figure 2.30 SEM images of neodymium boride samples synthesized by chemical vapor deposition with NdCl_3 and $\text{B}_{10}\text{H}_{14}$ at a) 795 °C, b) 850 °C, c) 915 °C and d) 940 °C. Figures e), f), g) and h) are the corresponding zoom-in images.

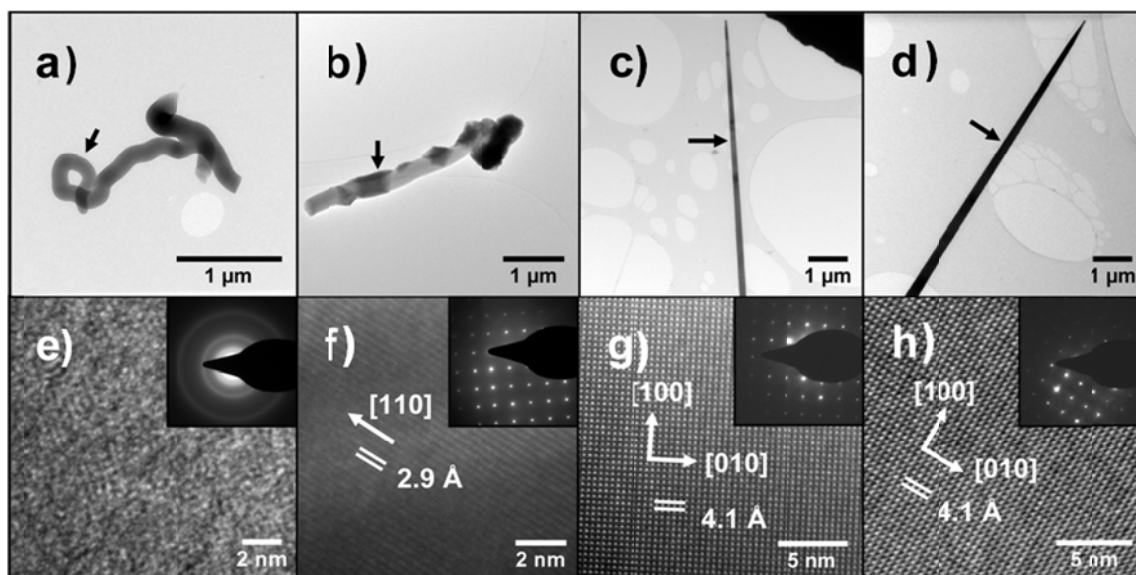


Figure 2.31 TEM images of neodymium boride samples synthesized by chemical vapor deposition with NdCl_3 and $\text{B}_{10}\text{H}_{14}$ at a) 795 °C, b) 850 °C, c) 915 °C and d) 940 °C. Figures e), f), g) and h) are HRTEM images of nanowire bulk areas indicated by the arrows in figures a), b), c) and d), respectively. The insets are the corresponding selected area electron diffraction patterns.

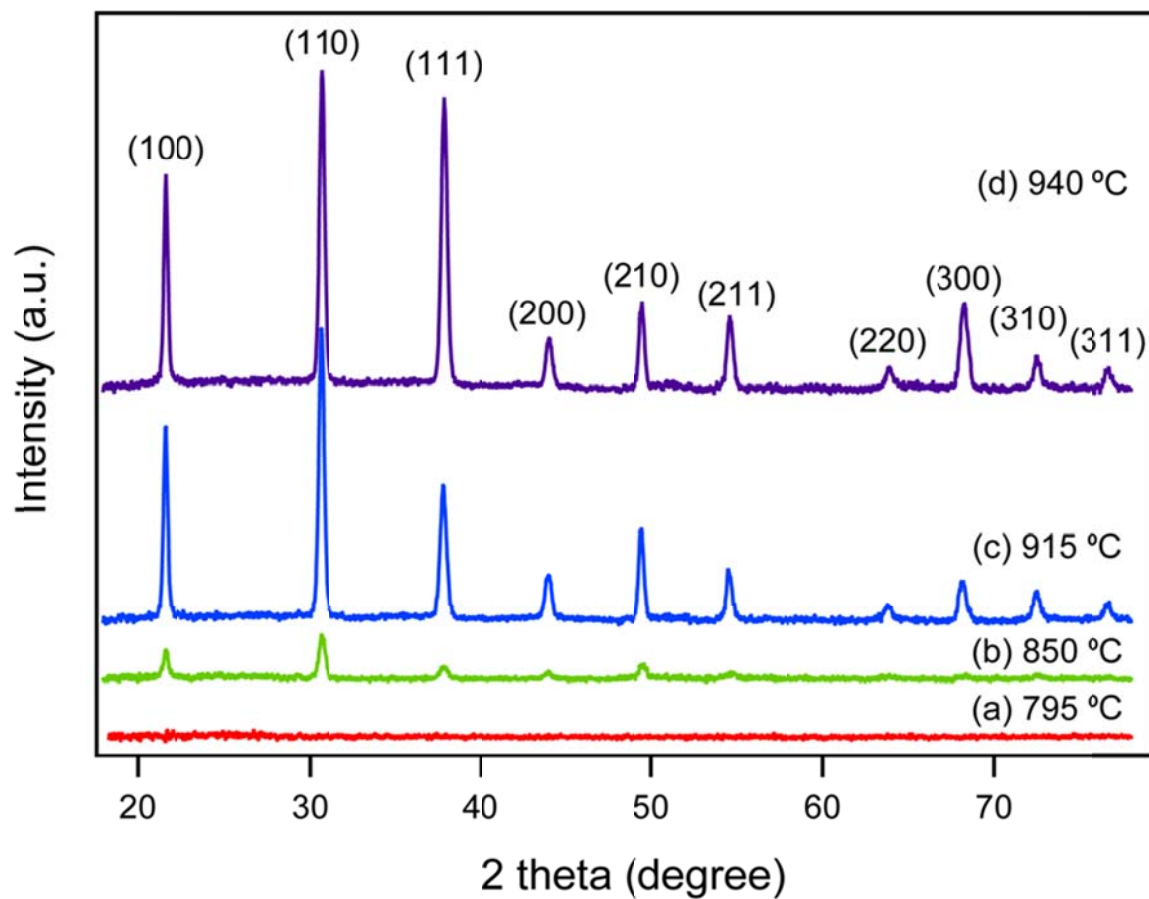


Figure 2.32 XRD spectra of *Sample 1, 2, 3* and *4* synthesized by chemical vapor deposition at (a) 795 °C, (b) 850 °C, (c) 915 °C and (d) 940 °C. The peaks attributing to NdB_6 phase are indexed in the figure.

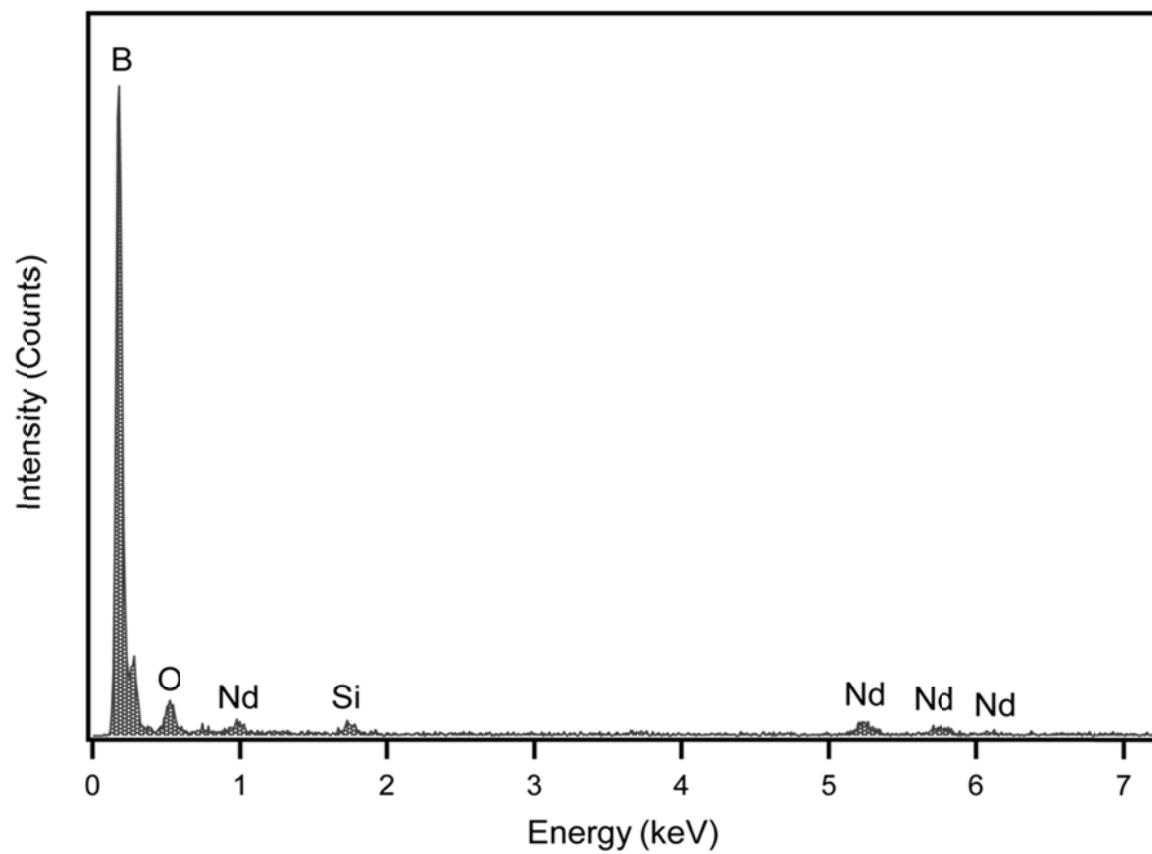


Figure 2.33 EDX spectrum of the nanowire synthesized at 795 °C (*Sample 1*) shown in Figure 2.31a.

Although the curly nanowires in *Sample 2* have low crystallinity like the ones in *Sample 1*, the localized “knot” areas are highly crystalline and have well-defined crystalline planes. A closer look into another “knot” area of the same nanowire (circled in Figure 2.34a) reveals two planes ((110) and (111)) in the cubic structure. The zoom-in HRTEM images of the square boxed regions (noted as **i** and **ii**) in the Figure 2.34b show hexagonal and parallel lattice fringes respectively. (Figure 2.34c and d) The lattice spacings in both regions are about 2.9 Å, which matches the interplanar distance of NdB₆ (110) crystal planes. So in region **i**, it is clear that the incident beam is along a <111> direction; whereas in region **ii**, the incident beam is along a lower symmetry direction that is still parallel to one family of {110} planes. This is also confirmed by the fast Fourier transform (FFT) patterns of these regions. The presence of both neodymium and boron in the material is also verified in the EDX spectra of this sample. (Figure 2.35) The EDX spectra also show that the “knot” area is richer in Nd than the bulk of the curly nanowire found in *Sample 1*, which agrees well with the structural transition from boron-rich amorphous nanowire to partially crystalline neodymium boride. The peaks in the corresponding XRD spectrum of *Sample 2* suggest the presence of NdB₆ in the sample.³⁸ (Figure 2.32b)

After a 10 min. CVD reaction run at 915 °C, films (*Sample 3*) obtained have a dark blue to violet color which indirectly indicates the formation of NdB₆ phase material.³⁹ High density tapered nanowires of length $10.3 \pm 0.6 \mu\text{m}$ are typical features found in the SEM images of this sample. (Figure 2.34c) The tip size of these tapered nanowires varies from *ca.* 8 to 60 nm. (Figure 2.30c and g) HRTEM images and SAED patterns (Figure 2.31g and k) of this sample suggest that these nanowires are single-crystalline with a lattice spacing of *ca.* 4.1 Å which matches the unit cell parameter of cubic NdB₆ and a preferred [100]

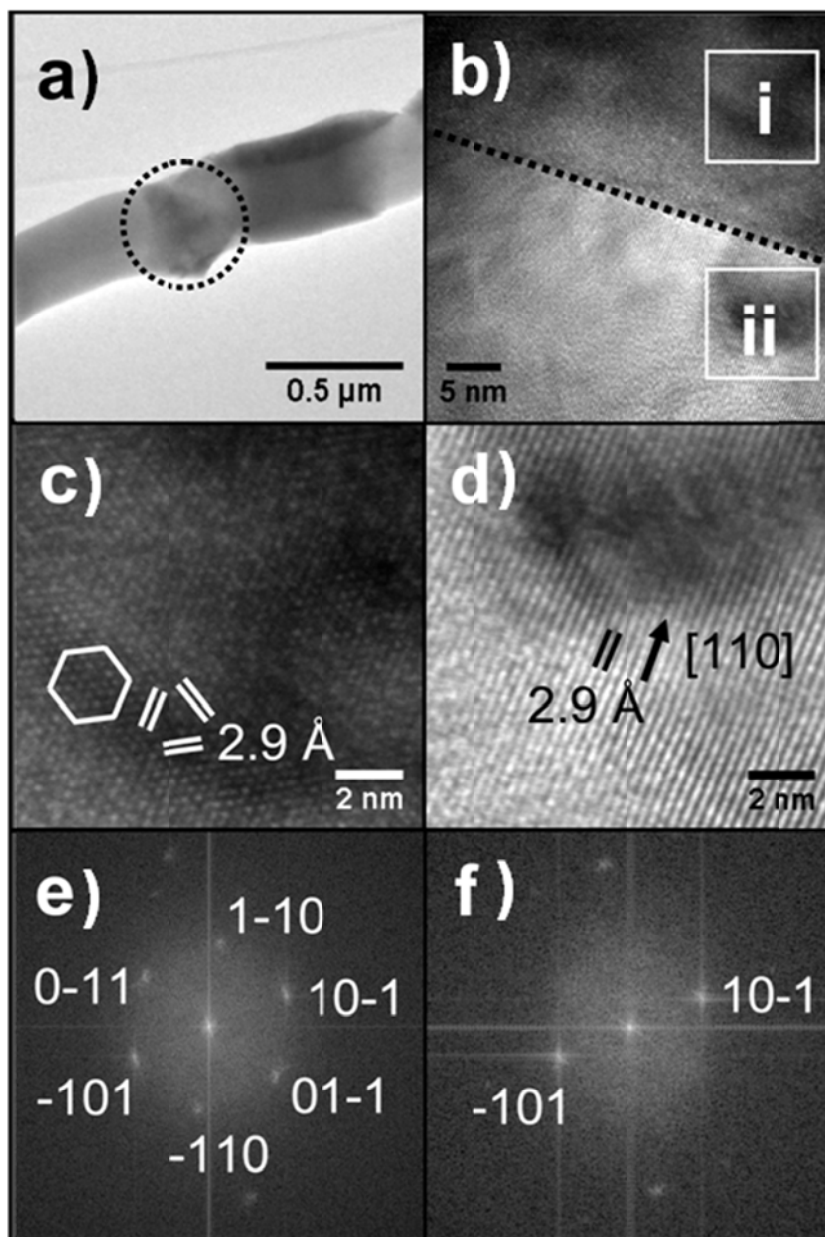


Figure 2.34 TEM images of a curly neodymium boride nanowire synthesized at 850 °C.

a) HRTEM image of the nanowire; b) Zoom-in image of the circled area in a); c) and d): Further zoom-in images of marked areas i and ii in b); e) and f): FFT patterns of c) and d).

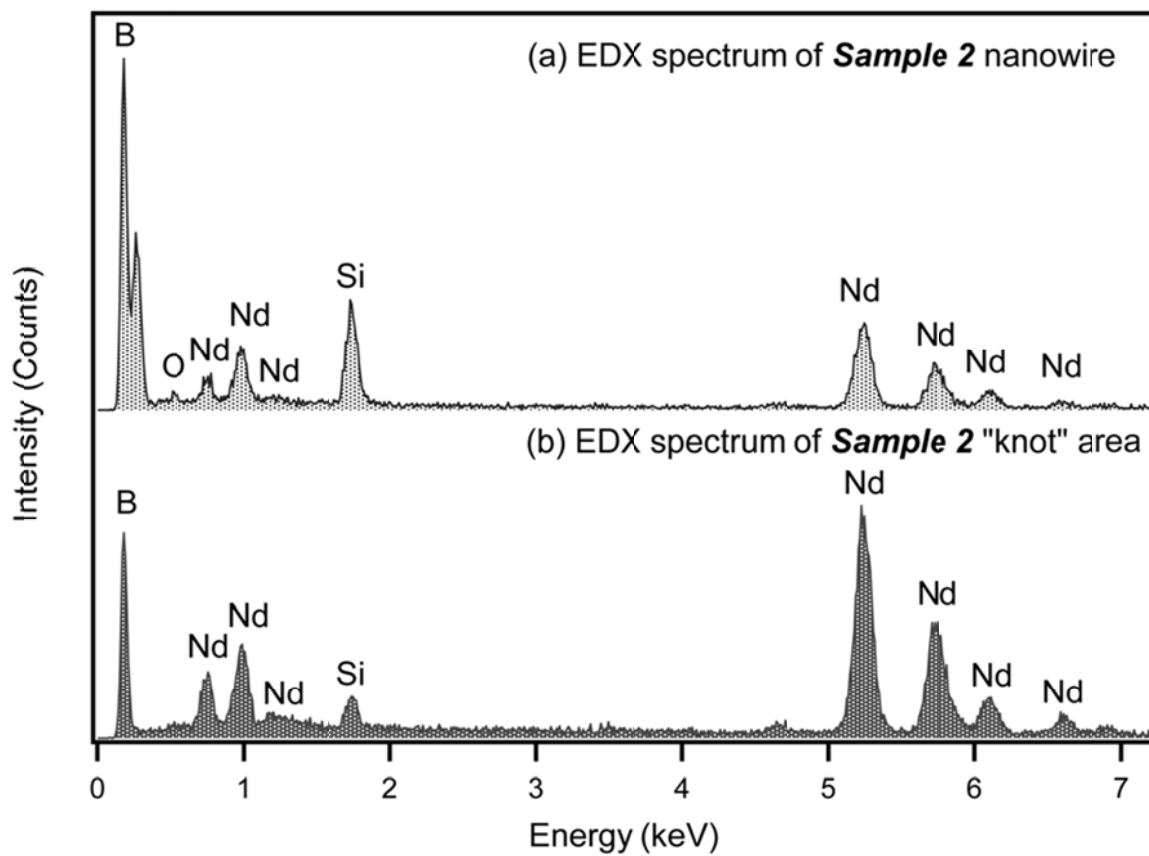


Figure 2.35 EDX spectra of (a) the bulk and (b) the “knot” area of the neodymium boride nanowire synthesized at 850 °C (**Sample 2**) shown in Figure 2.31b.

growth direction. EDX spectrum of the nanowire bulk confirms the presence of Nd and B in the materials. (Figure 2.36) Sometimes, a crystalline particle can be found at the end of a nanowire tip. For example, Figure 2.37a shows a hemisphere shaped particle at the end of nanowire tip depicted in Figure 2.31c. The diameter of the tip particle is about 45 nm. The lattice fringes of the particle (Figure 2.37b and c) show the corresponding lattice spacings of 5.4 Å and 2.3 Å, which match the inter-planar distance of (020) and (002) crystal planes of base-centered orthorhombic NdPd (ICDD Card No. 47-1394).⁴⁰ The FFT pattern of the tip area (Figure 2.37d) clearly indicates the diffraction pattern of this particular NdPd structure and confirms its crystalline property. Strong electron induced x-ray emission signals for both Pd and Nd are present in the EDX spectrum of the dark tip particle while no observable Pd signal is detected in the spectrum of the nanowire bulk. (Figure 2.36) The copper signals in the EDX spectra came from the copper TEM grid. The presence of Pd-rich hemispherical particles found at the tips of most 1-D nanostructures provides an indirect evidence of the vapor-liquid-solid (VLS) growth mechanism for the present nanostructure growth. The XRD spectrum of *Sample 3* provides an additional evidence that all diffraction peaks can be indexed as cubic NdB₆ phase (Space Group: Pm-3m) and the peaks are in good agreement with reference to the cubic unit cell structure of NdB₆ (ICDD Card No 11-0087).³⁸ (Figure 2.32c)

At the highest reaction temperature 940 °C, the CVD reaction also yielded high density crystalline neodymium boride 1-D nanostructure films with dark blue to violet color (*Sample 4*). The average length $14.3 \pm 1.2 \mu\text{m}$ of the 1-D nanostructures of *Sample 4* is larger than the nanowires grown at 915 °C. (Figure 2.30d, h and 2.31d) In addition to nanowires, this sample also contains nanoobelisks, 1-D nanostructures with different

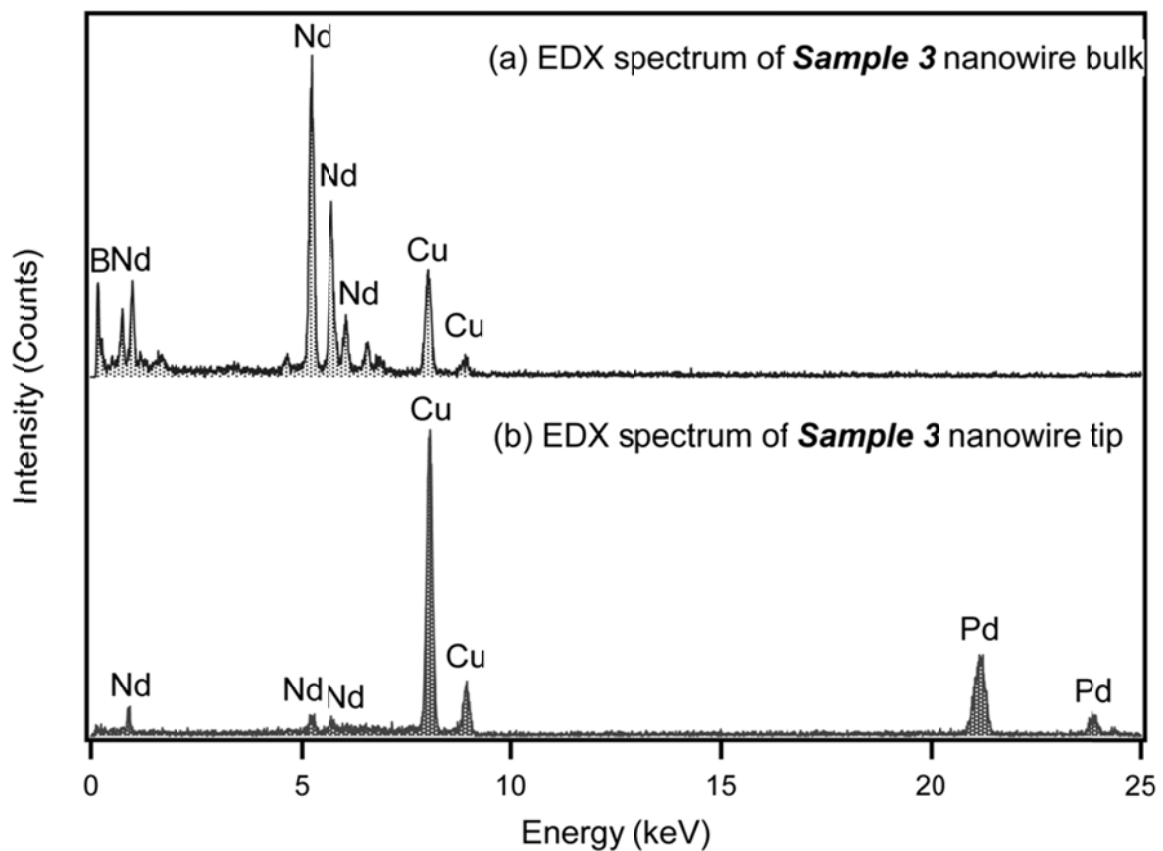


Figure 2.36 EDX spectra of (a) the bulk and (b) the tip particle of the neodymium boride nanowire synthesized at 915 °C (**Sample 3**) shown in Figure 2.31c.

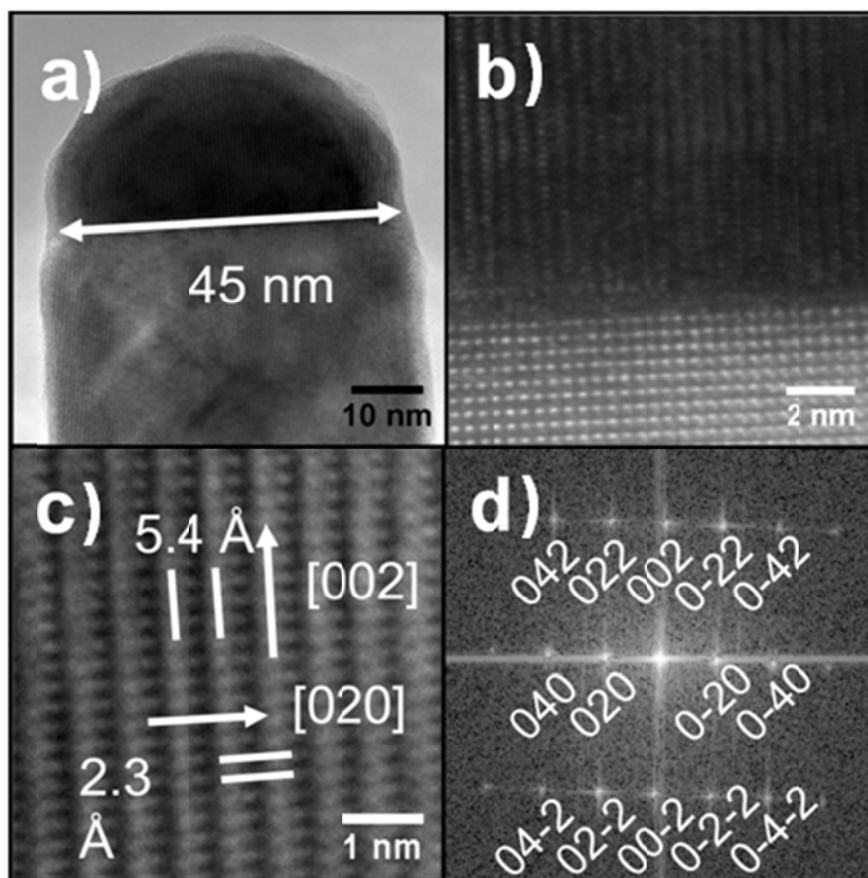


Figure 2.37 TEM images of the tip area of a neodymium boride nanowire synthesized at 940 °C. a) TEM image of the nanowire tip; b) HRTEM image of the joint area; c) HRTEM image of the tip particle; d) FFT pattern of area in c).

tapering angles at their tips and their shafts.³⁰ (Figure 2.30d) The lattice fringe of the bulk 1-D nanostructure is *ca.* 4.1 Å, which is very close to the *d* spacing value of NdB₆ (100) planes. The SAED pattern (Figure 2.311) indicates that these 1-D nanostructures have a preferred growth along the [100] direction. Note that the faint ring appeared in the center of the SAED pattern is an artifact due to the projection of the diffraction aperture. Similar to **Sample 3**, the corresponding EDX spectrum shows the presence of Nd and B in the nanowire found in **Sample 4**, and strong Pd signals in the tip particle of the same nanowire. (Figure 2.38) The XRD spectrum of **Sample 4** contains a set of strong diffraction peaks matching those of NdB₆.³⁸ (Figure 2.32d)

The growth mechanisms of neodymium borides nanostructures at the four selected reaction temperatures can be deduced from the structural and chemical composition data described in the results section. Figure 2.39 shows the proposed schematic diagram for the growth of neodymium boride nanostructures at these 4 reaction temperatures. In general, as revealed by the cross-sectional views of **Samples 1, 2, 3 and 4**, the wire-like structures are often found to grow on the top of thin films. (Figure 2.40) This implies that the films were likely deposited first on these substrates in the initial stage of the reaction. At a reaction temperature of 795 °C, an amorphous thin film of thickness about 250 nm was usually formed with curly nanowires on the substrates (**Sample 1**). Even though the local temperature of the substrates is above the eutectic temperature for Nd-Pd binary systems²⁸, due to the temperature gradient along the tube furnace, the NdCl₃ precursor was at a measured local temperature 720 °C, which is below its melting point (785 °C).⁴¹ This leads to a lower vapor pressure of the NdCl₃ and thus insufficient supply of NdCl₃ to the catalysts. Consequently, only curly boron rich wires were formed.

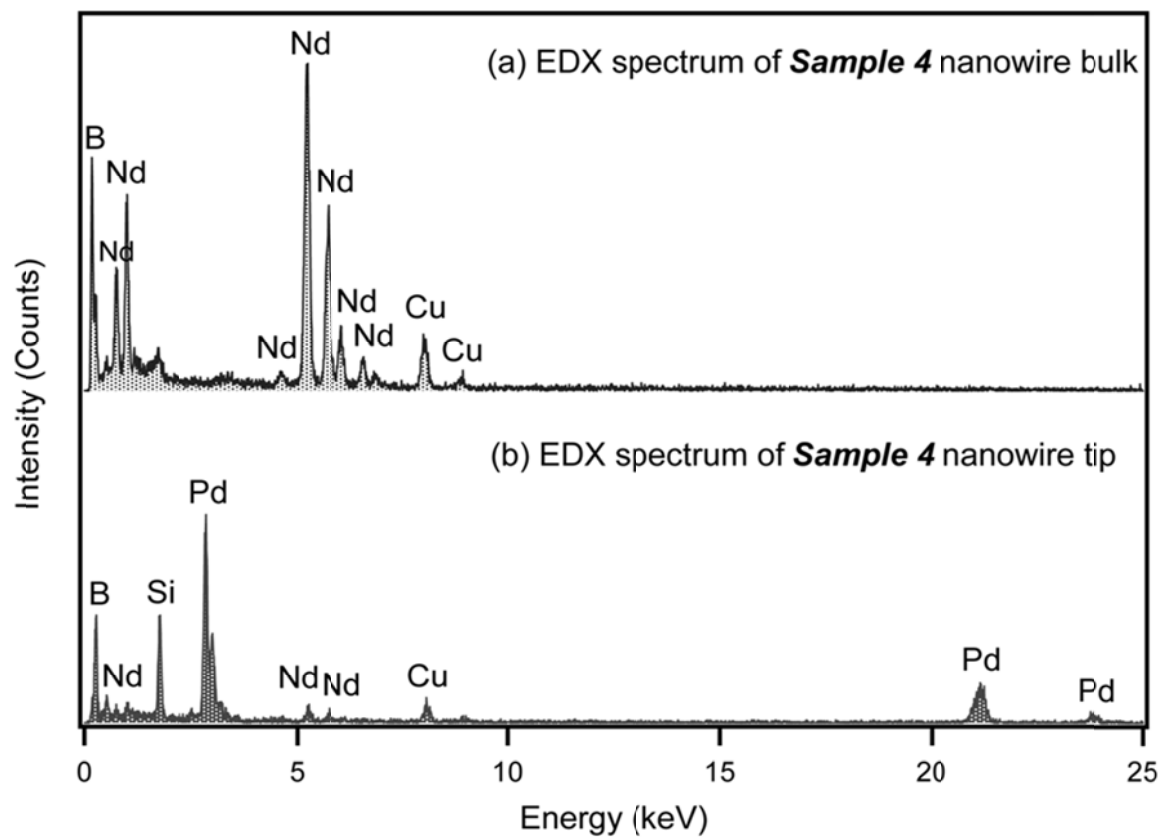


Figure 2.38 EDX spectra of (a) the bulk and (b) the tip particle of the neodymium boride nanowire synthesized at 940 °C (**Sample 4**) shown in Figure 2.31d.

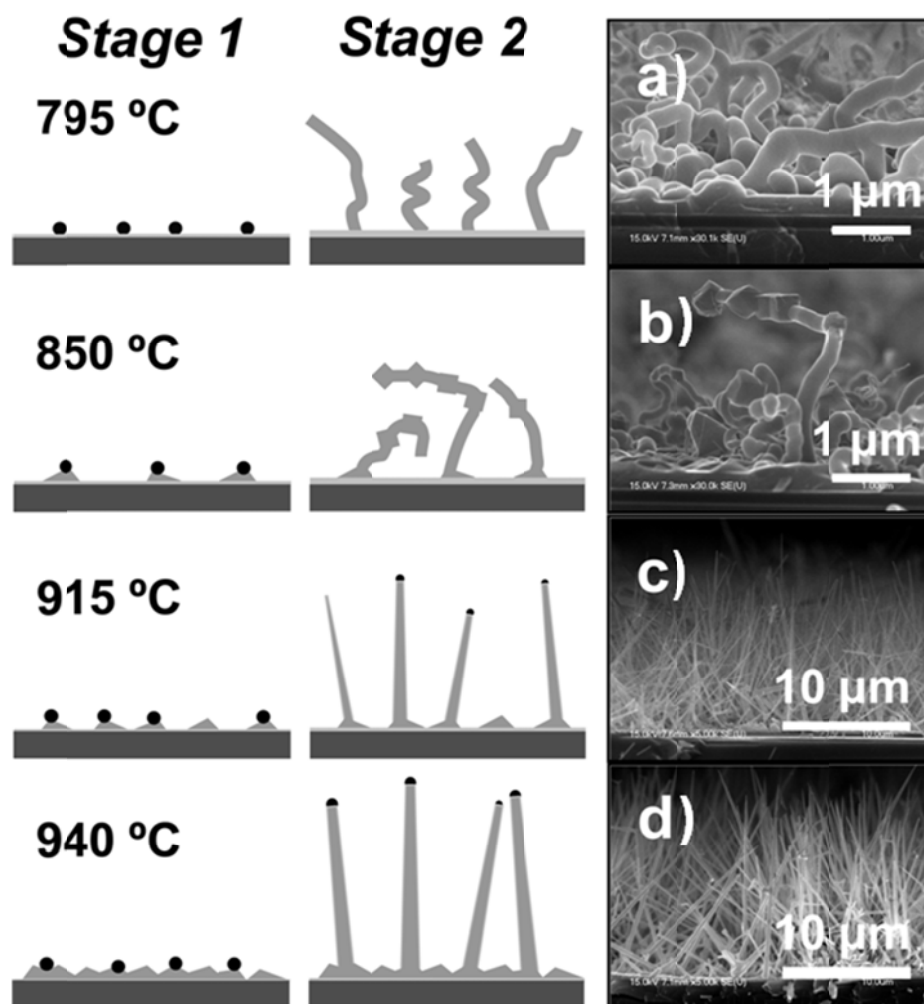


Figure 2.39 Schematic diagram model for the growth of neodymium boride nanostructures by chemical vapor deposition with NdCl_3 and $\text{B}_{10}\text{H}_{14}$ at 795 °C, 850 °C, 915 °C and 940 °C (not drawn to scale). The model diagram consists of Pd catalyst nanoparticles (black), silicon nitride coated silicon substrates (dark gray), and deposited neodymium boride thin films and nanowires (light gray). Figures 5 a), b), c) and d) are the corresponding cross-sectional view SEM images of *Sample 1*, *2*, *3* and *4* synthesized at the indicated temperatures, respectively.

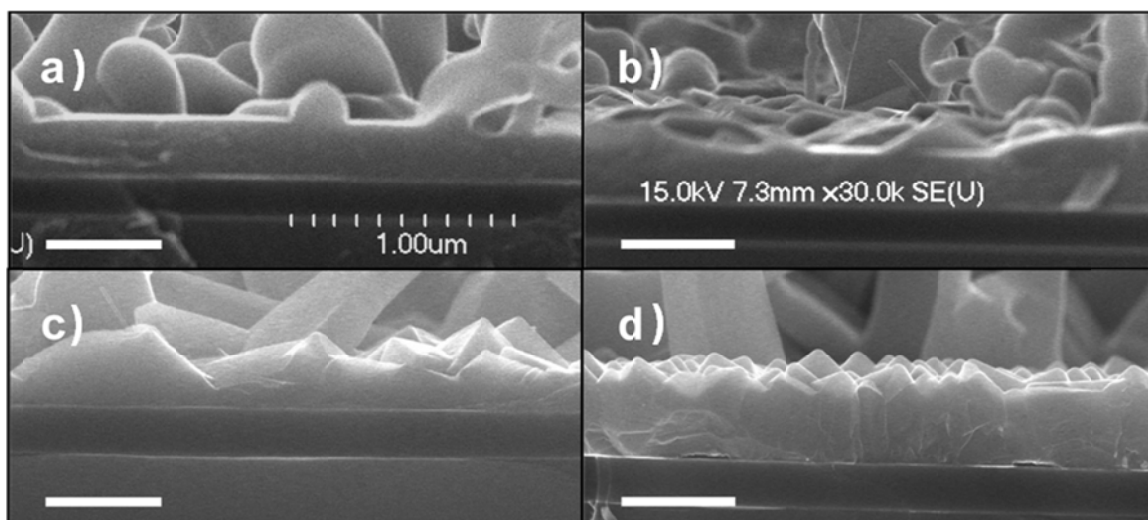


Figure 2.40 Cross-sectional view SEM images of films at the bottom of neodymium boride samples synthesized by chemical vapor deposition at a) 795 °C, b) 850 °C, c) 915 °C and d) 940 °C. The scale bars are 500 nm.

At the next higher reaction temperature 850 °C (*Sample 2*), while the general morphology of the samples produced and possible growth mechanisms appear to be similar to those produced at 795 °C, there is a big difference between these two cases. With a 55°C increase in the temperature profile, the vapor pressure of the NdCl_3 drastically increased, and consequently some NdB_6 crystalline phase was formed in the film, which was confirmed by the XRD data. (Figure 2.32 and 2.23b) However, the flux of Nd precursor or its concentration in the catalyst particles is still probably not high enough at this reaction temperature to produce stoichiometric NdB_6 nanowires. Instead, growth of localized NdB_6 cube-like “knot” structures are often found along the curly nanowires which are possibly due to secondary deposition of precursor materials and nucleation of NdB_6 crystallites in these wires.

At higher reaction temperatures (915 and 940 °C), the as-produced *Sample 3* and *4* are comprised of straight tapered nanowires and nanoobelisks grown on the top of cube-like crystalline thin films. (Figure 2.39) In contrast to the amorphous or low crystallinity films obtained at lower reaction temperatures, the faceted features and XRD spectra of these sample films indicated that these films are made of highly polycrystalline NdB_6 . (Figure 2.32) The thickness and crystallite packing density of these film readily increases as the reaction temperature increases from 915 to 940 °C. (Figure 2.33c and d) From the electron microscopy data, we postulate that the crystalline films initially grown on the substrates act as templates for the subsequent growth of tapered nanowires and nanoobelisks. At such high temperatures, some Pd catalyst particles may have migrated to the vicinity of faceted surfaces of the cubic crystals. The NdCl_3 vapor supplied Nd to these Pd nanoparticles to form the Pd-Nd eutectic droplets which further absorbed boron

from decomposed decaborane to catalyze the NdB_6 nanowire and nanoobelisk growth via the typical VLS process.^{16, 18} The Pd-rich composition found in the post-annealed catalyst particles at the tips of most nanowires and nanoobelisks provide more indirect evidence for this VLS-growth process.

The 1-D nanostructures obtained at reaction temperatures 915 and 940 °C are usually tapered wires and obelisks instead of wires of constant diameters. These results are largely attributed to secondary deposition of precursor materials nucleated on the wires during the growth process. This secondary deposition leads to side wall coating and tapering at the tips.⁴² Due to an increase in precursor decomposition at higher temperatures, the tapered nanowires produced at 940 °C have larger diameters than those produced at 915 °C. The increase in secondary deposition at higher reaction temperatures can also be inferred from the tapering parameter⁴² which is defined as $\sigma = \frac{d_1 - d_2}{2L}$, where d_1 and d_2 are the diameters of the nanowire at the base and tip and L is the length of the nanowire. Assuming that the lateral and axial growth rates are constant during the growth, the tapering parameter basically estimates the ratio of the velocity of axial growth to that of the radial growth. From examining the electron microscopy images of over 30 nanowires for each sample the σ s of **Sample 3** and **4** are found to be 0.0063 ± 0.0017 and 0.0082 ± 0.0033 , respectively. These tapering parameters indicate that both samples have mild tapering and statistically the secondary deposition rate is larger at higher reaction temperatures.

While the growth process appears to be both kinetically and thermodynamically driven and thus possibly not be directly relevant to the binary phase diagrams, it was found that the use of Pd nanoparticles and modification of the experimental conditions to

vary concentrations of the precursors strongly influenced the composition and shape of neodymium boride materials. Due to a major deficiency of Nd species and a high concentration of B species at low reaction temperatures, the growth process yielded non-stoichiometric, curly and amorphous boride nanowires. The wire growth was likely governed by a Vapor-Solid mechanism as the solubility of B in Pd is likely to be insignificant due to insufficient temperature and the lack of sufficient soluble species such as Nd. As the reaction temperature increased to 795 °C, the stoichiometry of Nd:B and crystallinity of the nanowires increased to yield NdB_6 materials, probably due to an increase in NdCl_3 vapor pressure and thus sufficient metal precursor flux to generate more NdB_6 crystallites in the B-rich phase. When the temperature range was increased further, the B species became soluble in the Nd-saturated Pd particles, and single-crystalline hexaboride wires were precipitated at the interface of the liquid droplet and solid hexaboride film. After the growth, the existence of Pd-rich particles at the tips of 1D NdB_6 nanostructures grown at higher temperatures provides an indirect proof for the VLS growth mechanism at high reaction temperatures (> 900 °C). Both high flux of Nd precursor and appropriately high temperatures are necessary for such apparent VLS growth to occur.

2.3.7.4 Substrate directed crystallographic orientation

In many situations, implementation of materials toward device application generally occurs once vertical orientation of the nanowires during the growth process is achieved. In semiconductor nanowires, many have used substrate directed growth to provide the orientation both vertically and laterally. For many of the semiconductor nanowires, this

substrate directed process is rather trivial as there are many different kinds of semiconductor substrates with various crystallographic orientations available.

Modes for the oriented growth vary, but can be basically broken down into two groups; 1) direct lattice matching and 2) short range ordering.⁴²⁻⁴⁸ In the direct lattice matching, as the name implies, the unit cell structure and dimensions of the material of interest directly match (or very closely match) that of the substrate. Low stress films of very high order can be achieved when the mismatch is less than 2%. In long range ordering, the lattice of the material of interest does not need to have the same dimensions but be similar in structure and match over range of unit cell lengths. There are also many cases in which this process has been attributed and the deposited films show decreased stress as compared to similar films that have been deposited trying to use the direct lattice matching approach.

However, for the REB₆ system, many of the readily available semiconductor substrates are not applicable. This is because the cubic structure of the REB₆ system is rather incommensurate with the hexagonal or wurzite crystal structure of most semiconductors. This makes it nearly impossible for even long range ordering to occur. There are other options such as insulating oxides and possible buffer layer growth using cubic materials that may be applicable.

To determine ideal substrates for the growth of oriented REB₆ materials, both direct lattice matching and short range order substrates were investigated. Of particular interest were substrates that had cubic lattices and could either be single crystalline or deposited films. Studies began with MgO single crystal substrates as it is one of the most common substrates used for the controlled growth of cubic materials.⁴⁶ It has a rock-salt lattice

structure and a lattice constant of 0.4216 nm, making it a possible candidate for direct lattice matching. (Figure 2.41) LaAlO_3 single crystal substrates were also of interest as they are a common substrate used in the growth of cubic superconducting materials. LaAlO_3 has a pseudo cubic lattice with a lattice constant of about 0.3821 nm, making it a possible candidate for short ranged ordered growth of REB_6 thin films. (Figure 2.42) Finally, ZrN , which was deposited by ion-beam assisted deposition and has a lattice constant of about 0.457 nm, was used as both a buffer layer type directed growth method and for short range ordering. (Figure 2.43)

Figure 2.44-2.46 show the results of the substrate directed growth versus growth on various silicon substrates. It can be seen that in all cases, the growth on the cubic substrates has a much more pronounced (100) growth direction, suggesting a plane to plane matching in the growth model. However, LaAlO_3 and ZrN substrates appear to grow materials that are more single phase than the MgO . A possible explanation for this can be found by looking at the lattice mismatch between the substrate and LaB_6 . The percent mismatch was calculated by taking the absolute value of the difference of the substrate unit cell lengths and the LaB_6 unit cell lengths and then dividing by the unit cell of LaB_6 . It can be seen that the ZrN and LaAlO_3 provide for excellent lattice matching (0.11 % and 0.28 % mismatch respectively) when lattice combinations of 10:11 ($\text{ZrN}:\text{LaB}_6$) and 13:12 ($\text{LaAlO}_3:\text{LaB}_6$) are used. (Figure 2.47-2.49) MgO , which is the direct lattice matched substrate, has a mismatch of 1.6 %. This is about an order of magnitude larger mismatch than what can be obtained with ZrN and LaAlO_3 , indicating this may be the cause of the poor XRD pattern of MgO grown materials.

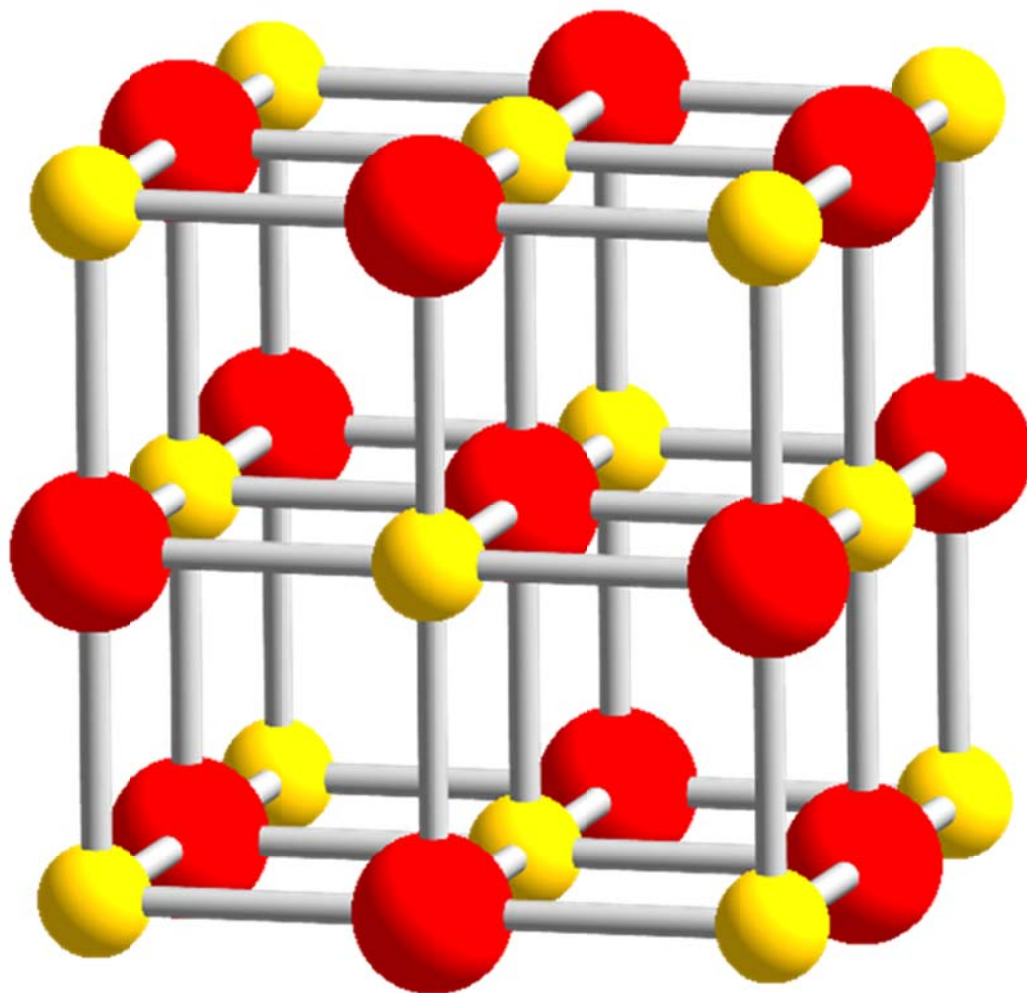


Figure 2.41 Unit cell representation of MgO (Mg:yellow; O:red).

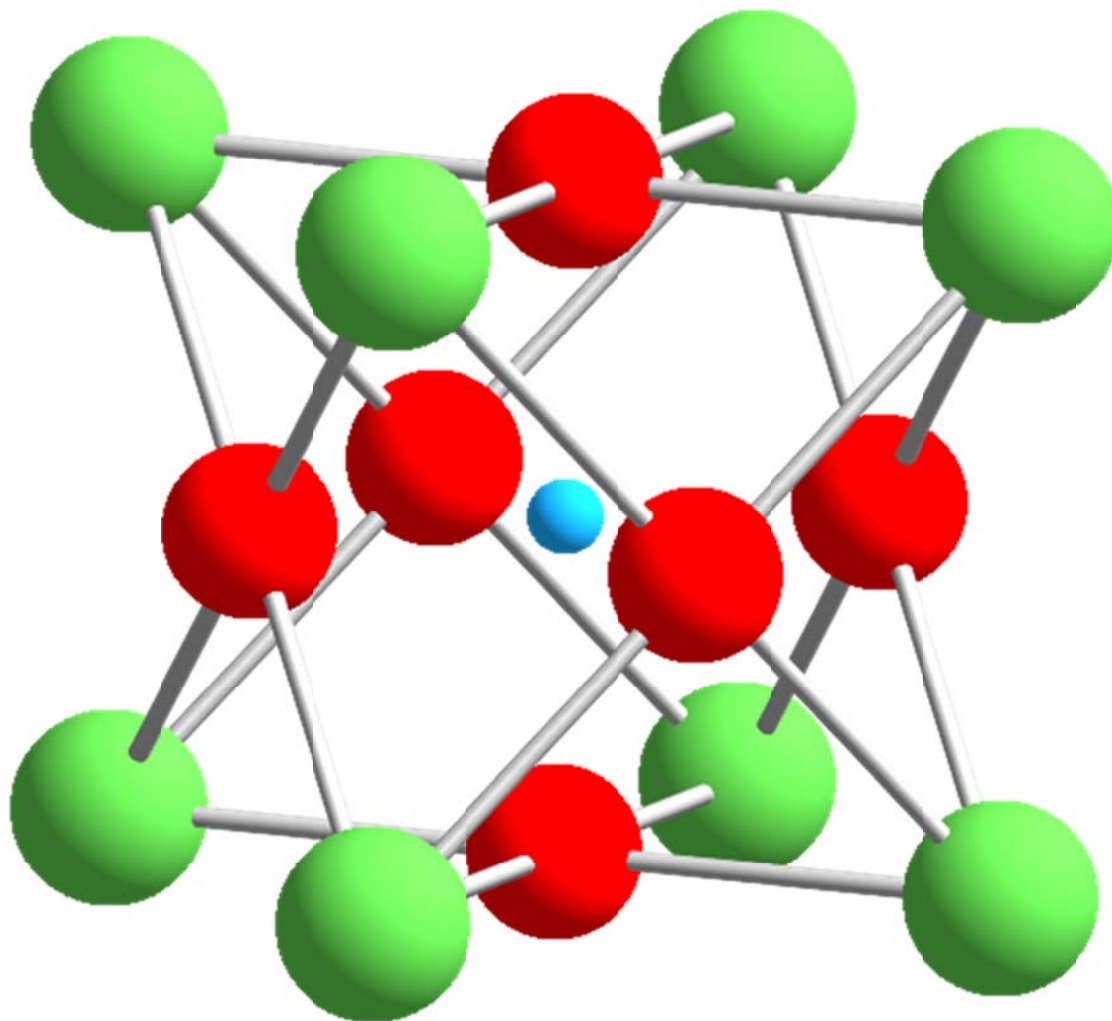


Figure 2.42 Unit cell representation of LaAlO₃ (La:olive green; O:red; Al:blue).

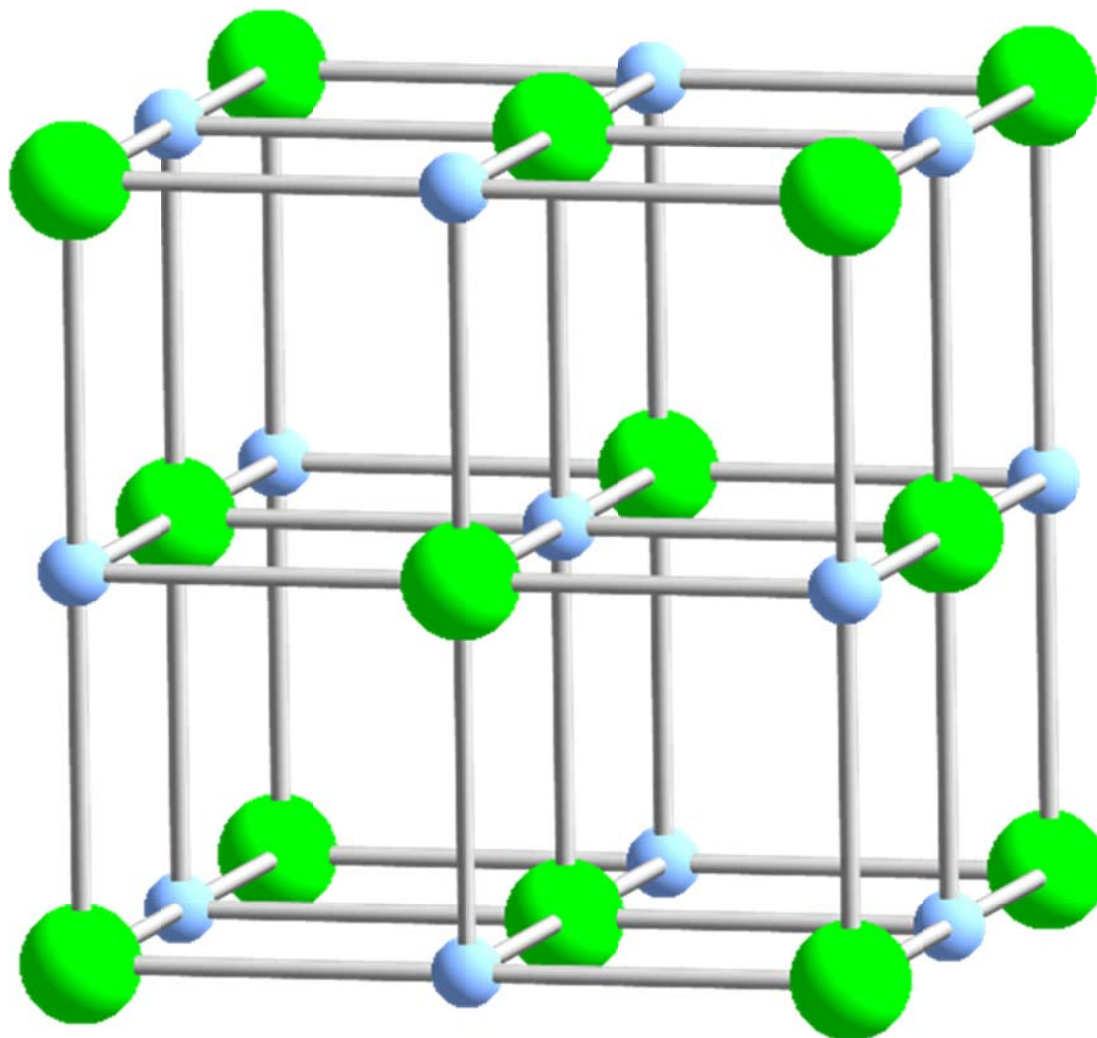


Figure 2.43 Unit cell representation of ZrN (Zr:lime green; N:baby blue).

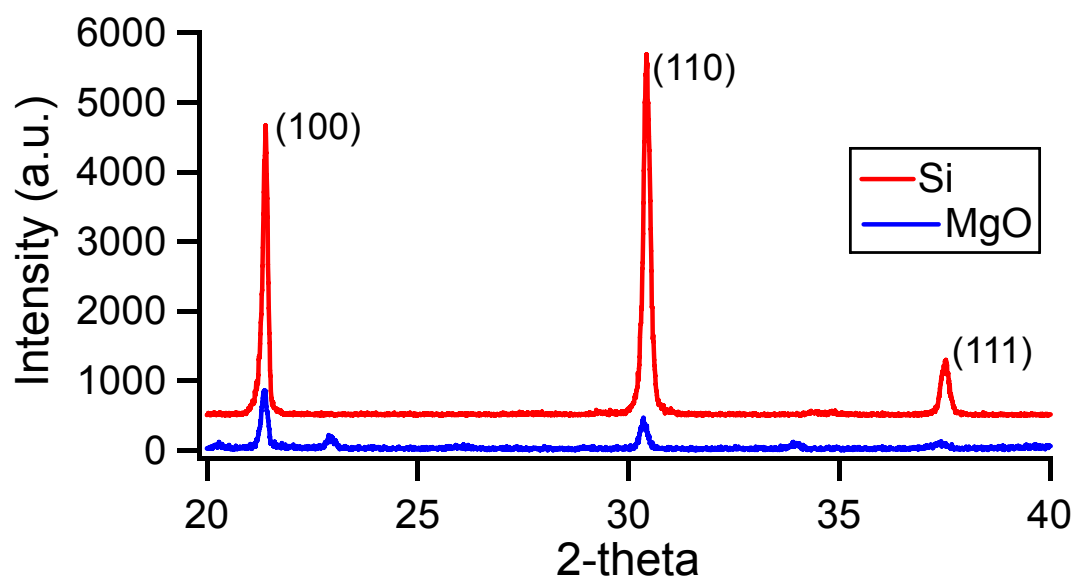


Figure 2.44 XRD powder pattern of LaB₆ films grown on (100) MgO (blue) and (100) Si wafer (red).

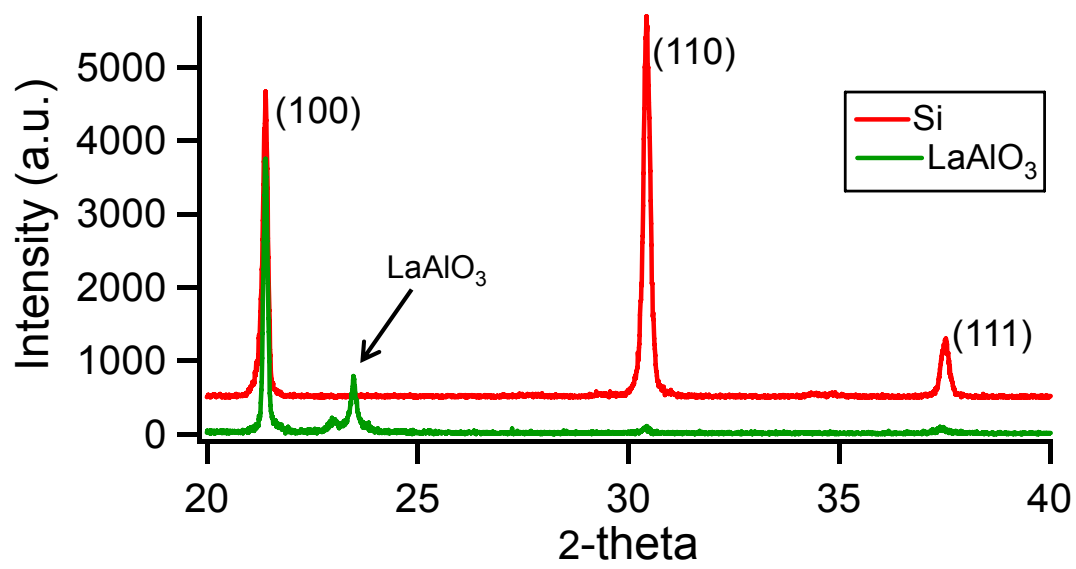


Figure 2.45 XRD powder pattern of LaB₆ films grown on (100) LaAlO₃ (green) and (100) Si wafer (red).

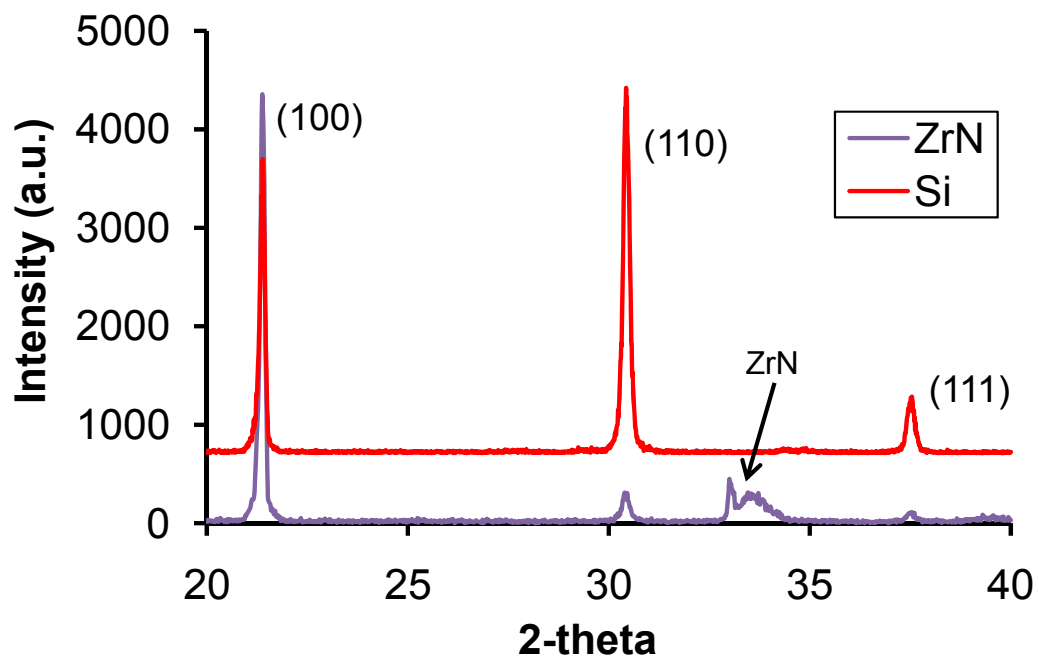


Figure 2.46 XRD powder pattern of LaB_6 films grown on IBAD-deposited ZrN (blue) and (100) Si wafer (red).

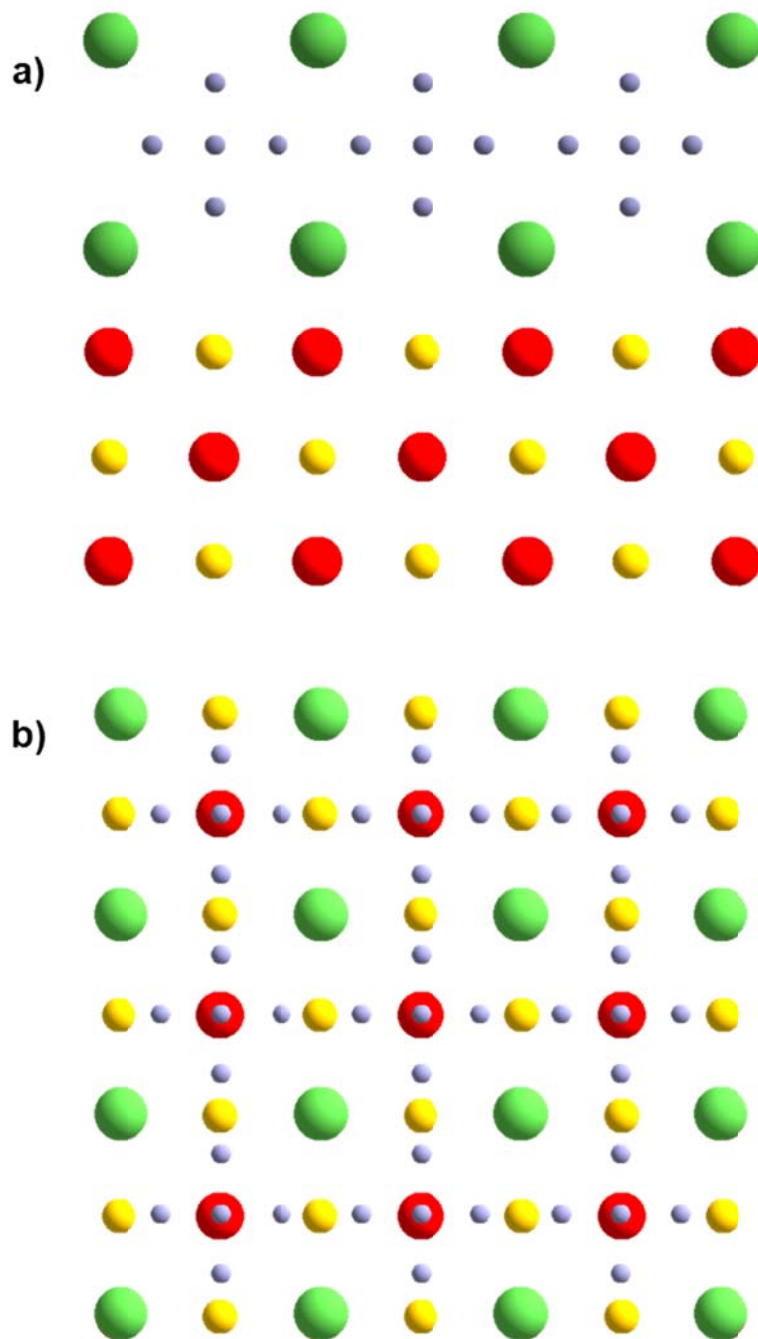


Figure 2.47 Model of the possible lattice matching scheme between LaB₆ (La:green; B:purple) and MgO (Mg:yellow; O:red). a) interface view and b) top-down view.

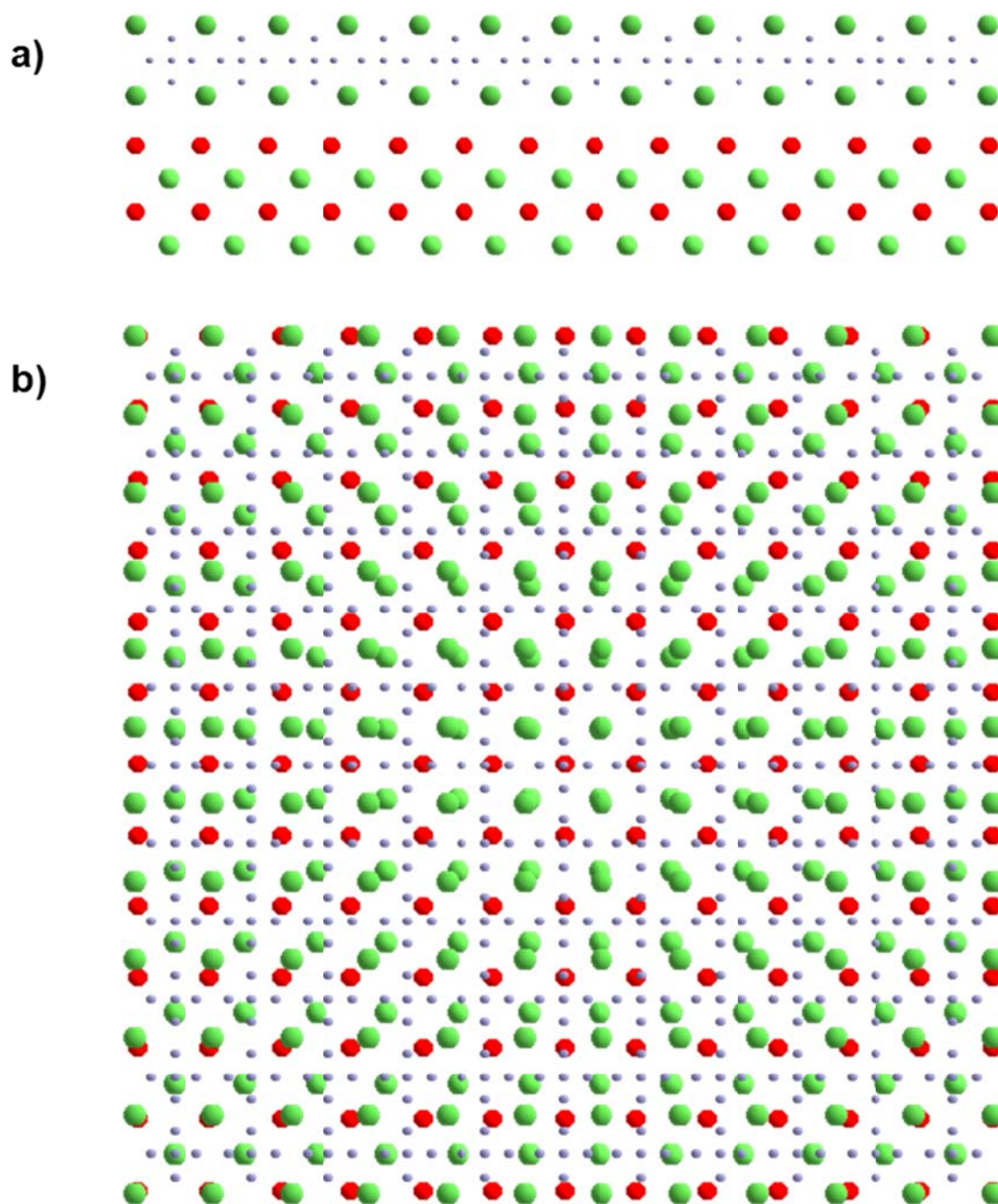


Figure 2.48 Model of the possible lattice matching scheme between LaB_6 (La:green; B:purple) and LaAlO_3 (La:green; O:red; Al: not shown). a) interface view and b) top down view.

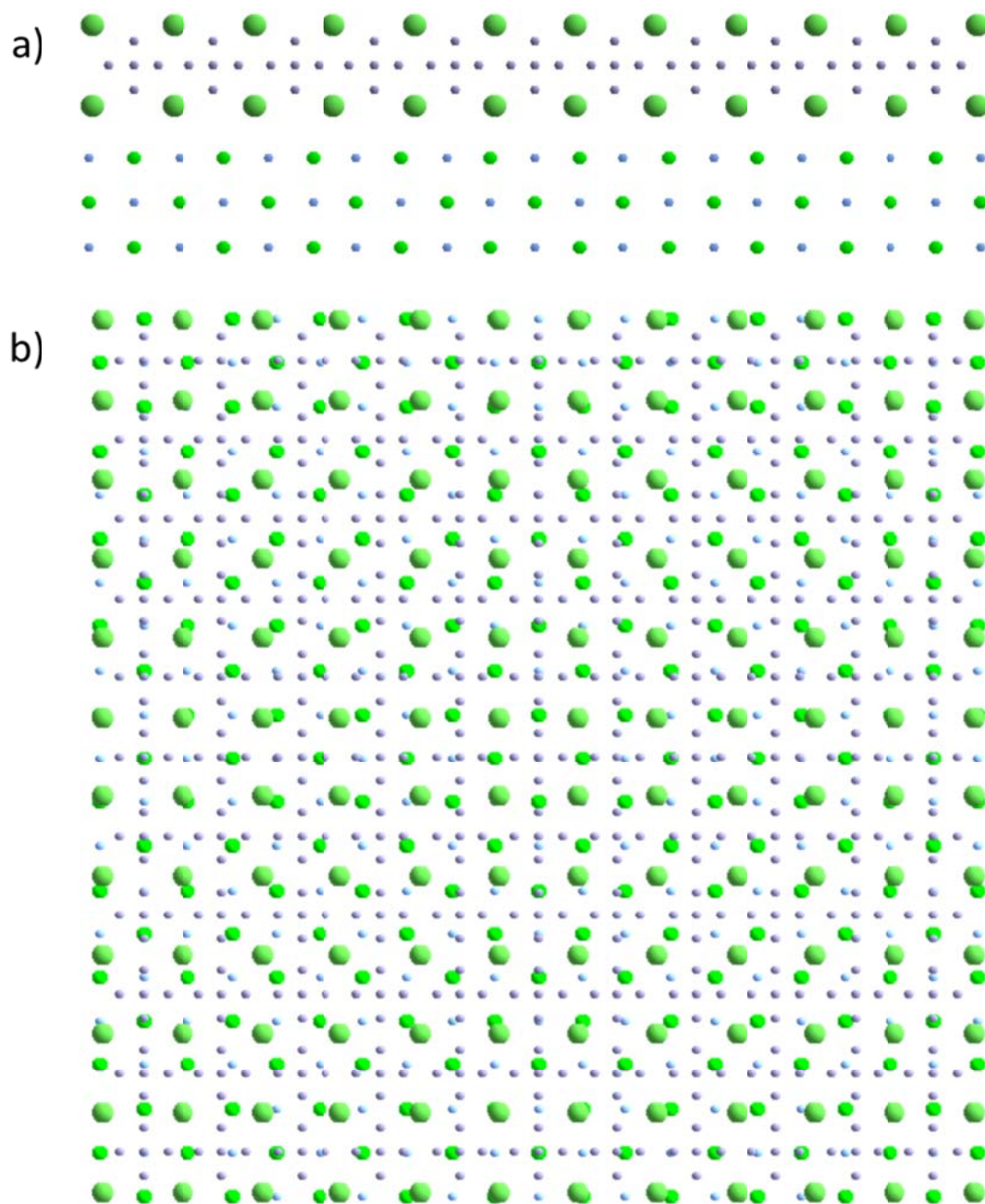


Figure 2.49 Model of the possible lattice matching scheme between (100) LaB₆ (La: green; B: purple) and (100) ZrN (Zr: lime green; N: blue). a) interface view and b) top-down view.

Figure 2.50a and b show SEM images of nanowire growth on the ZrN and LaAlO₃ substrates respectively. Even though the ZrN substrates in theory provide a better lattice match on the short-range ordering, the nanowire growth is much more oriented on the LaAlO₃. This is most likely due to the fact that the ZrN thin films are not single crystalline and the grains on the film are randomly oriented. For application toward devices, the LaAlO₃ provides much better alignment, but would have limited application because it is an insulator and is quite expensive. If better deposition techniques for the ZrN could be developed and the crystalline quality could be improved, this could be an ideal substrate for the growth of REB₆ materials for device applications.

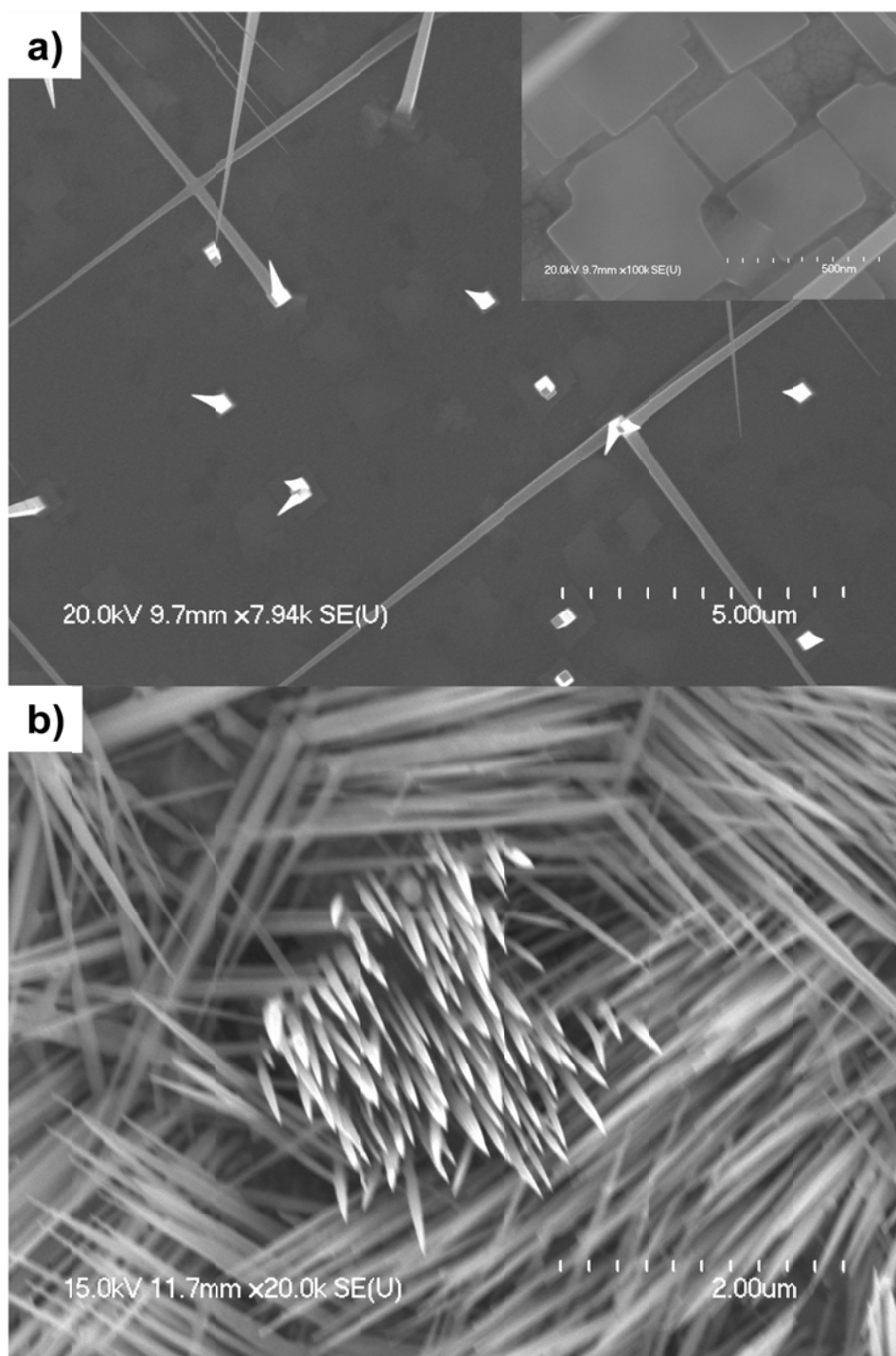


Figure 2.50 SEM images of LaB₆ nanowires grown on (a) LaAlO₃ and (b) ZrN. Inset in (a) is a zoom-in image of the LaB₆ thin film surface.

2.4 Conclusions

Single crystalline REB_6 nanowires of different growth morphologies were synthesized by chemical vapor deposition and vapor liquid solid growth. Binary phase diagrams were utilized to develop intuition about the growth process and a general synthesis methodology was developed by using Pd nanoparticles as the metal catalyst. The growth of various single-crystal nanostructures from obelisks to nanowires can be obtained by adjusting the location of the substrate within the deposition region in the tube furnace. The electronic properties of the deposited thin films at different regions in the furnace suggests that even though the materials appear very similar in crystallinity, there may be compositional differences that are altering the electronic properties of the materials. Furthermore, by adjusting the process temperature of the horizontal tube furnace, the transition from VS deposition to VLS deposition was identified, which further confirmed the proposed growth mechanism. To increase the feasibility of REB_6 nanomaterials for device application, substrate directed growth was investigated using various cubic substrates. LaAlO_3 single crystal substrates proved to be the most effective at orienting the nanowires vertically, but ZrN coated Si may be a more practical substrate if the ZrN deposition process can be improved.

2.5 References

1. Gesley, M. & Swanson, L.W. A determination of the low work function planes of LaB₆. *Surf. Sci.* **146**, 583-599 (1984).
2. Yutani, A., Kobayashi, A. & Kinbara, A. Work-functions of thin LaB₆ films. *Appl. Surf. Sci.* **70-1**, 737-741 (1993).
3. Tanaka, T., Nishitani, R., Oshima, C., Bannai, E. & Kawai, S. The preparation and properties of CeB₆, SmB₆, and GdB₆. *J. Appl. Phys.* **51**, 3877-3883 (1980).
4. Davis, P.R., Gesley, M.A., Schwind, G.A., Swanson, L.W. & Hutta, J.J. Comparison of thermionic cathode parameters of low index single crystal faces of LaB₆, CeB₆ and PrB₆. *Appl. Surf. Sci.* **37**, 381-394 (1989).
5. Schmidt, P.H., Longinotti, L.D., Joy, D.C., Ferris, S.D., Leamy, H.J. & Fisk, Z. Design and optimization of directly heated LaB₆ cathode assemblies for electron-beam instruments. *J. Vac. Sci. Technol.* **15**, 1554-1560 (1978).
6. Matkovich, V.I. Boron and refractory borides (Springer-Verlag, Berlin; New York, 1977).
7. Swanson, L.W., Gesley, M.A. & Davis, P.R. Crystallographic dependence of the work function and volatility of LaB₆. *Surf. Sci.* **107**, 263-289 (1981).
8. Swanson, L.W. & McNeely, D.R. Work functions of the (001) face of the hexaborides of Ba, La, Ce and Sm. *Surf. Sci.* **83**, 11-28 (1979).
9. Geballe, T.H., Matthias, B.T., Andres, K., Maita, J.P., Cooper, A.S. & Corenzwit, E. Magnetic ordering in the rare-earth hexaborides. *Science* **160**, 1443-1444 (1968).

10. Samsonov, G.V. High-temperature compounds of rare earth metals with nonmetals (Consultants Bureau, New York, 1965).
11. Uimin, G. & Brenig, W. Crystal field, magnetic anisotropy, and excitations in rare-earth hexaborides. *Phys. Rev. B* **61**, 60 (2000).
12. Langford, H.D. & et al. Enhancements and Fermi surfaces of rare-earth hexaborides. *J. Phys.-Condes. Matter* **2**, 559 (1990).
13. Wu, Y., Yan, H., Huang, M., Messer, B., Song, J.H. & Yang, P. Inorganic semiconductor nanowires: rational growth, assembly, and novel properties. *Chem.-Eur. J.* **8**, 1260-1268 (2002).
14. Wu, Y.Y. & Yang, P.D. Direct observation of vapor-liquid-solid nanowire growth. *J. Am. Chem. Soc.* **123**, 3165-3166 (2001).
15. Wagner, R.S. & Ellis, W.C. Vapor-liquid-solid mechanism of single crystal growth. *Appl. Phys. Lett.* **4**, 89-90 (1964).
16. Givargizov, E.I. & Obolenskaya, L.N. Regular arrays of LaB₆ whiskers grown on singlecrystal substrates by the vapour-liquid-solid method. *J. Less Common Met.* **117**, 97-103 (1986).
17. Motojima, S., Takahashi, Y. & Sugiyama, K. Chemical vapor growth of LaB₆ whiskers and crystals having a sharp tip. *J. Cryst. Growth* **44**, 106-109 (1978).
18. Givargizov, E.I. & Obolenskaya, L.N. Controlled growth of LaB₆ whiskers by the vapor-liquid-solid mechanism. *J. Cryst. Growth* **51**, 190-194 (1981).
19. Zhang, H., Zhang, Q., Tang, I. & Qin, L.C. Single-crystal line CeB₆ nanowires. *J. Am. Chem. Soc.* **127**, 8002-8003 (2005).

20. Zhang, H., Zhang, Q., Tang, J. & Qin, L.-C. Single-Crystalline LaB₆ Nanowires. *J. Am. Chem. Soc.* **127**, 2862-2863 (2005).
21. Zhang, H., Zhang, Q., Zhao, G.P., Tang, J., Zhou, O. & Qin, L.C. Single-crystal line GdB₆ nanowire field emitters. *J. Am. Chem. Soc.* **127**, 13120-13121 (2005).
22. Xu, J.Q., Chen, X.L., Zhao, Y.M., Zou, C.Y. & Ding, Q.W. Single-crystalline PrB₆ nanowires and their field-emission properties. *Nanotechnology* **18**, 5 (2007).
23. Xu, J.Q., Zhao, Y.M., Ji, X.H., Zhang, Q. & Lau, S.P. Growth of single-crystalline SmB₆ nanowires and their temperature-dependent electron field emission. *J. Phys. D-Appl. Phys.* **42**, 6 (2009).
24. Xu, J.Q., Zhao, Y.M., Shi, Z.D., Zou, C.Y. & Ding, Q.W. Single-crystalline SmB₆ nanowires. *J. Cryst. Growth* **310**, 3443-3447 (2008).
25. Xu, J.Q., Zhao, Y.M. & Zou, C.Y. Self-catalyst growth of LaB₆ nanowires and nanotubes. *Chem. Phys. Lett.* **423**, 138-142 (2006).
26. Xu, T.T., Zheng, J.G., Nicholls, A.W., Stankovich, S., Piner, R.D. & Ruoff, R.S. Single-crystal calcium hexaboride nanowires: Synthesis and characterization. *Nano Lett.* **4**, 2051-2055 (2004).
27. Ding, Q.W., Zhao, Y.M., Xu, J.Q. & Zou, C.Y. Large-scale synthesis of neodymium hexaboride nanowires by self-catalyst. *Solid State Commun.* **141**, 53-56 (2007).
28. Massalski, T.B. & International, A.S.M. Binary alloy phase diagrams (ASM International, Materials Park, Ohio, 1990).
29. Peshev, P. A thermodynamic estimation of the chemical vapor deposition of some borides. *J. Solid State Chem.* **154**, 157-161 (2000).

30. Brewer, J.R., Deo, N., Wang, Y.M. & Cheung, C.L. Lanthanum hexaboride nanoobelisks. *Chem. Mat.* **19**, 6379-6381 (2007).
31. Curtis, B.J. & Graffenberger, H. The floating zone crystal growth of lanthanum hexaboride. *Mater. Res. Bull.* **1**, 27-31 (1966).
32. Xu, C.X., Sun, X.W. & Chen, B.J. Field emission from gallium-doped zinc oxide nanofiber array. *Appl. Phys. Lett.* **84**, 1540-1542 (2004).
33. Henglein, A., Ershov, B.G. & Malow, M. Absorption-spectrum and some chemical-reactions of colloidal platinum in aqueous-solution. *J. Phys. Chem.* **99**, 14129-14136 (1995).
34. American Society for, T. & Materials. Annual book of ASTM standards. (1970).
35. Thurber, W.R. (ed. Technology, T.N.I.o.S.a.) (December 3, 2008).
36. Yeager, J. & Hrusch-Tupta, M.A. (eds.) Low level measurements (Keithley Instruments Inc., 28775 Aurora Rd, Cleveland, OH., 1998).
37. Wang, G., Brewer, J.R., Chan, J.Y., Diercks, D.R. & Cheung, C.L. Morphological evolution of neodymium boride nanostructure growth by chemical vapor deposition. *J. Phys. Chem. C* **113**, 10446-10451 (2009).
38. Perri, J.A., Binder, I. & Post, B. *J. Phys. Chem.* **63**, 616-619 (1959).
39. Singh, N., Saini, S.M., Nautiyal, T. & Auluck, S. Electronic structure and optical properties of rare earth hexaborides RB_6 (R = La, Ce, Pr, Nd, Sm, Eu, Gd). *J. Phys.-Condes. Matter* **19**, 10 (2007).
40. Chen, L. & Zhang, K. Phase diagram of neodymium-palladium ($Nd \leq 50$ at.%) system *Jinshu Xuebao* **27**, B17-B20 (1991).

41. Matignon, C. Characteristics of Some Anhydrous Chlorides of the Rare Metals. *Comptes Rendus Hebdomadaires des Seances de l'Academie des Sciences* **140**, 1339-41 (1905).
42. Wang, Y.W., Schmidt, V., Senz, S. & Gosele, U. Epitaxial growth of silicon nanowires using an aluminium catalyst. *Nature Nanotechnol.* **1**, 186-189 (2006).
43. Liu, W.R., Li, Y.H., Hsieh, W.F., Hsu, C.H., Lee, W.C., Lee, Y.J., Hong, M. & Kwo, J. Domain matching epitaxial growth of high-quality ZnO film using a Y₂O₃ buffer layer on Si (111). *Cryst. Growth Des.* **9**, 239-242 (2008).
44. Wang, Z., Liu, X., Gong, J., Huang, H., Gu, S. & Yang, S. Epitaxial growth of ZnO nanowires on ZnS nanobelts by metal organic chemical vapor deposition. *Cryst. Growth Des.* **8**, 3911-3913 (2008).
45. Hung, L.S., Zheng, L.R. & Blanton, T.N. Epitaxial growth of MgO on (100)GaAs using ultrahigh vacuum electron-beam evaporation. *Appl. Phys. Lett.* **60**, 3129-3131 (1992).
46. Gerlach, J.W., Mennig, J. & Rauschenbach, B. Epitaxial gadolinium nitride thin films. *Appl. Phys. Lett.* **90**, 061919 (2007).
47. Wang, X., Song, J., Li, P., Ryou, J.H., Dupuis, R.D., Summers, C.J. & Wang, Z.L. Growth of uniformly aligned ZnO nanowire heterojunction arrays on GaN, AlN, and Al_{0.5}Ga_{0.5}N substrates. *J. Am. Chem. Soc.* **127**, 7920-7923 (2005).
48. Fons, P., Iwata, K., Yamada, A., Matsubara, K., Niki, S., Nakahara, K., Tanabe, T. & Takasu, H. Uniaxial locked epitaxy of ZnO on the a face of sapphire. *Appl. Phys. Lett.* **77**, 1801-1803 (2000).

2.6 Appendix

Twenty figures are presented in this section. Ten of the figures represent high resolution TEM images of the different REB₆ nanowire's tip, bulk and side. The other ten figures represent to corresponding EDS spectrum of the REB₆ nanowire's tip, bulk and side.

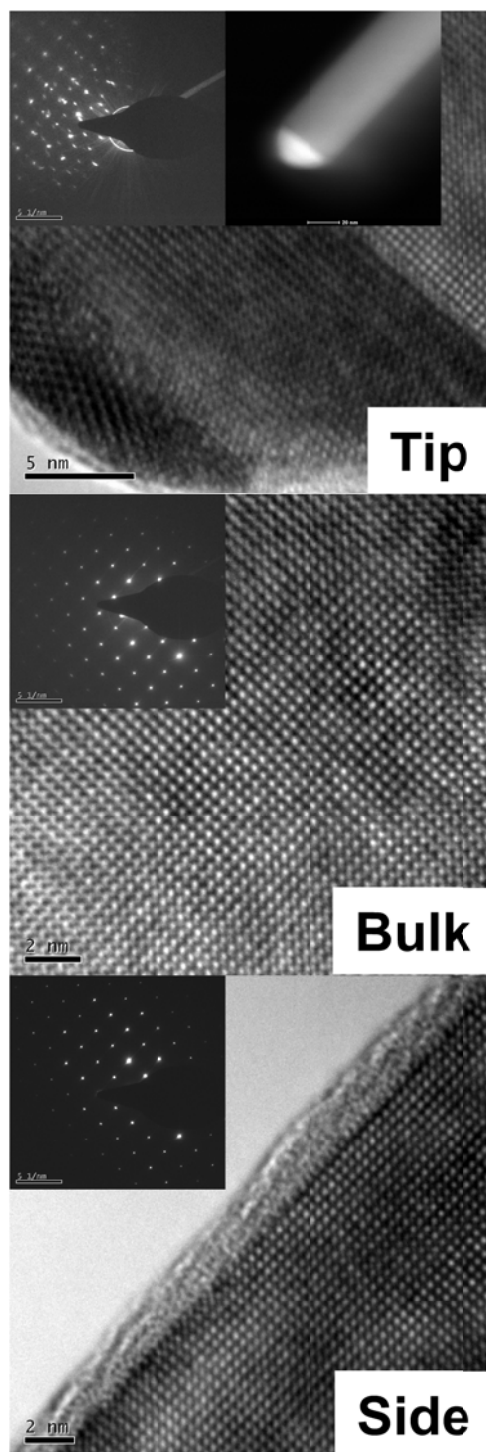


Figure A2.1 HRTEM images of a YB₆ nanowire tip, bulk and side. Insets are SAED patterns and high angle dark field image.

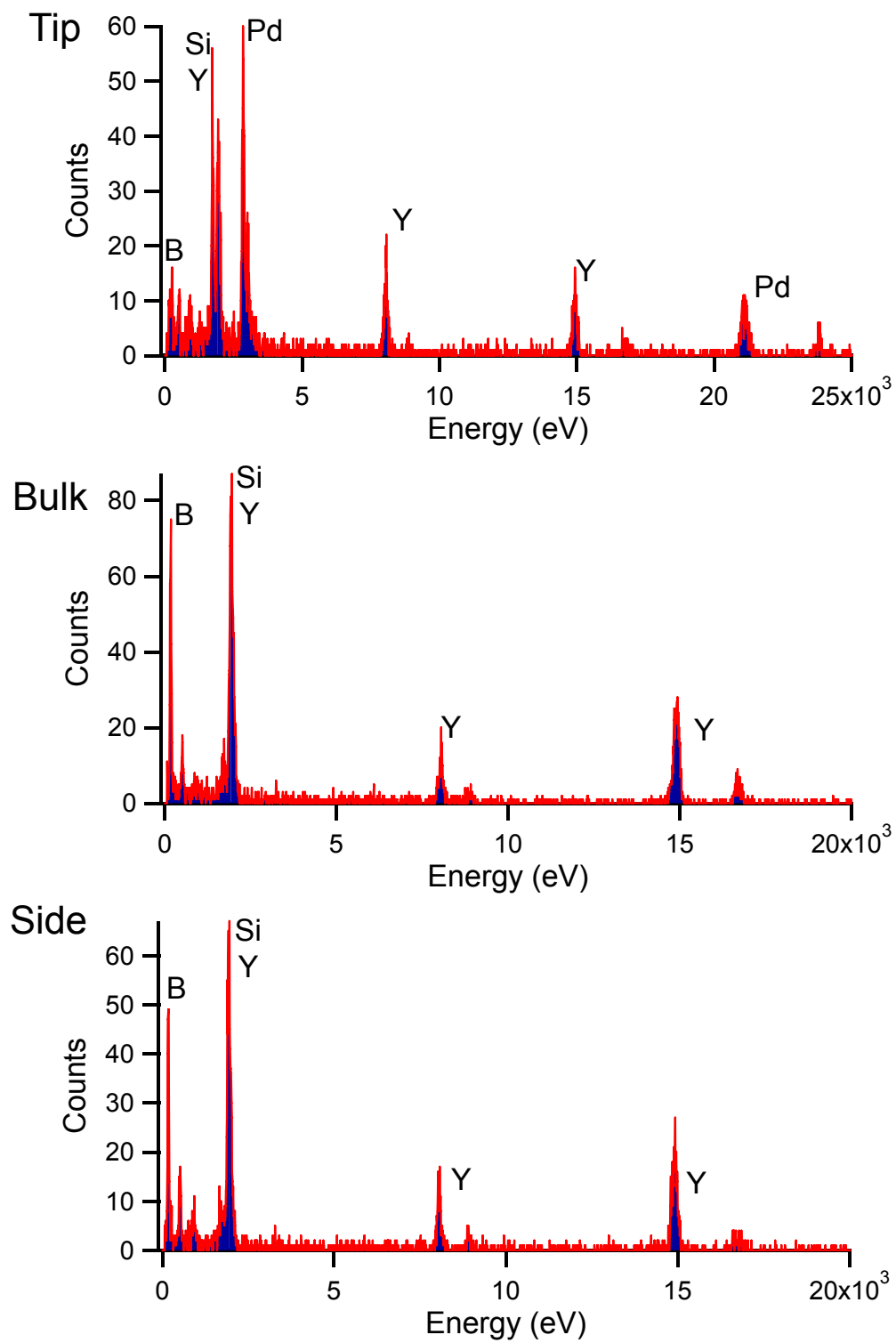


Figure A2.2 EDS patterns of the tip, bulk and side of the YB₆ nanowire in A2.1.

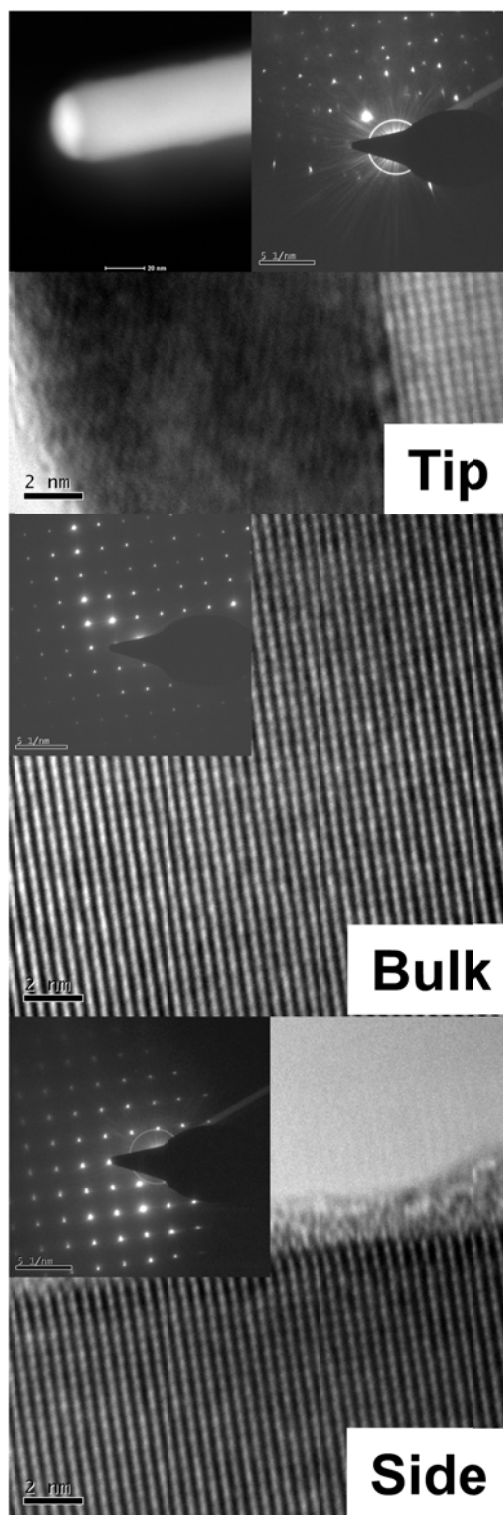


Figure A2.3 HRTEM images of a LaB₆ nanowire tip, bulk and side. Insets are SAED patterns and high angle dark field image.

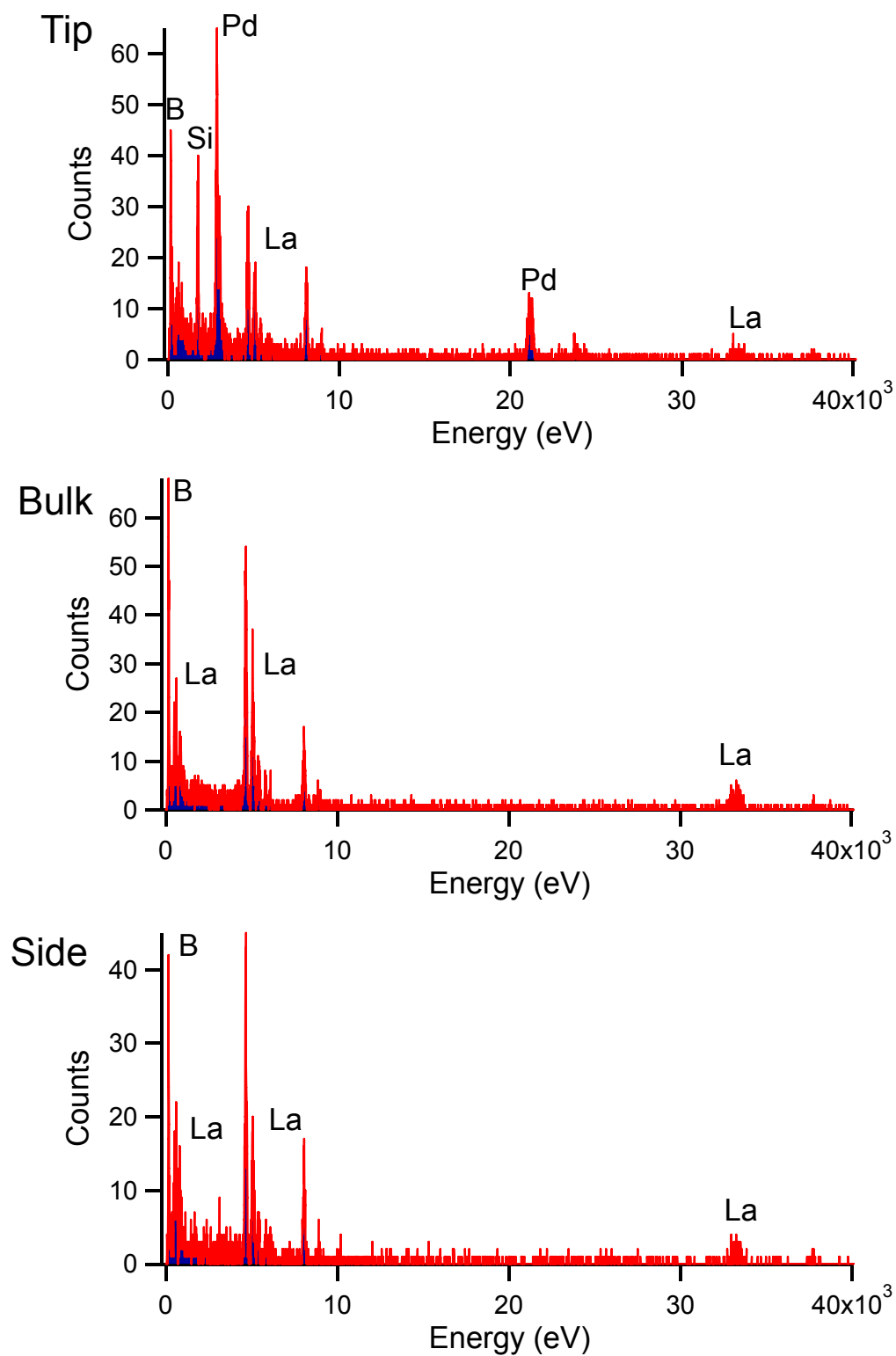


Figure A2.4 EDS patterns of the tip, bulk and side of the LaB₆ nanowire in A2.3.

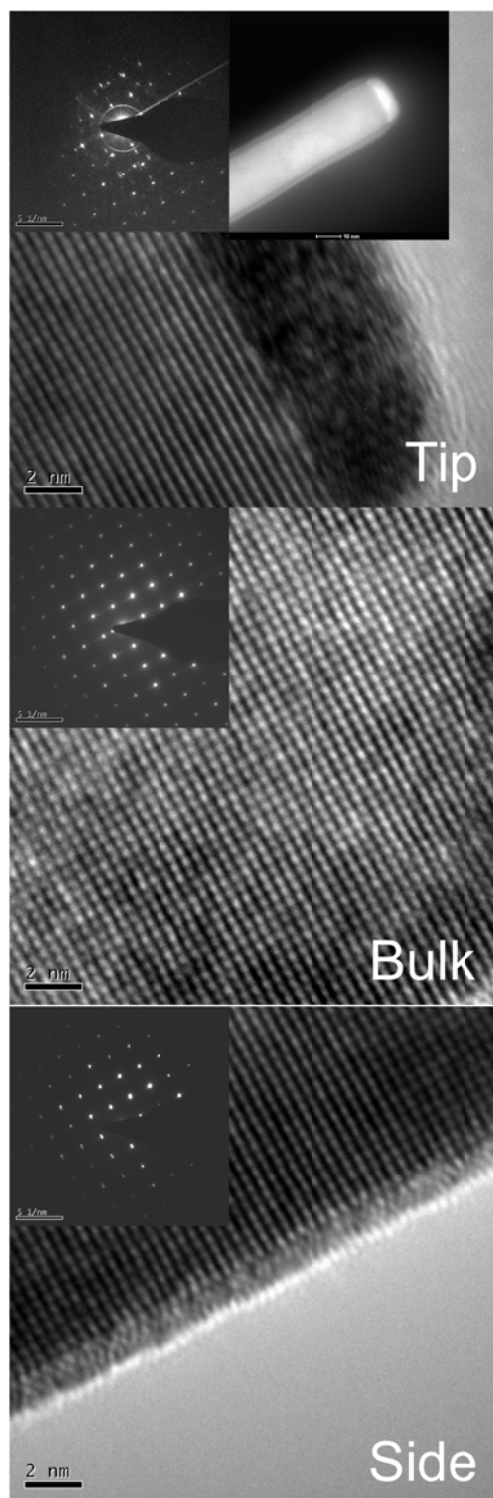


Figure A2.5 HRTEM images of a CeB₆ nanowire tip, bulk and side. Insets are SAED patterns and high angle dark field image.

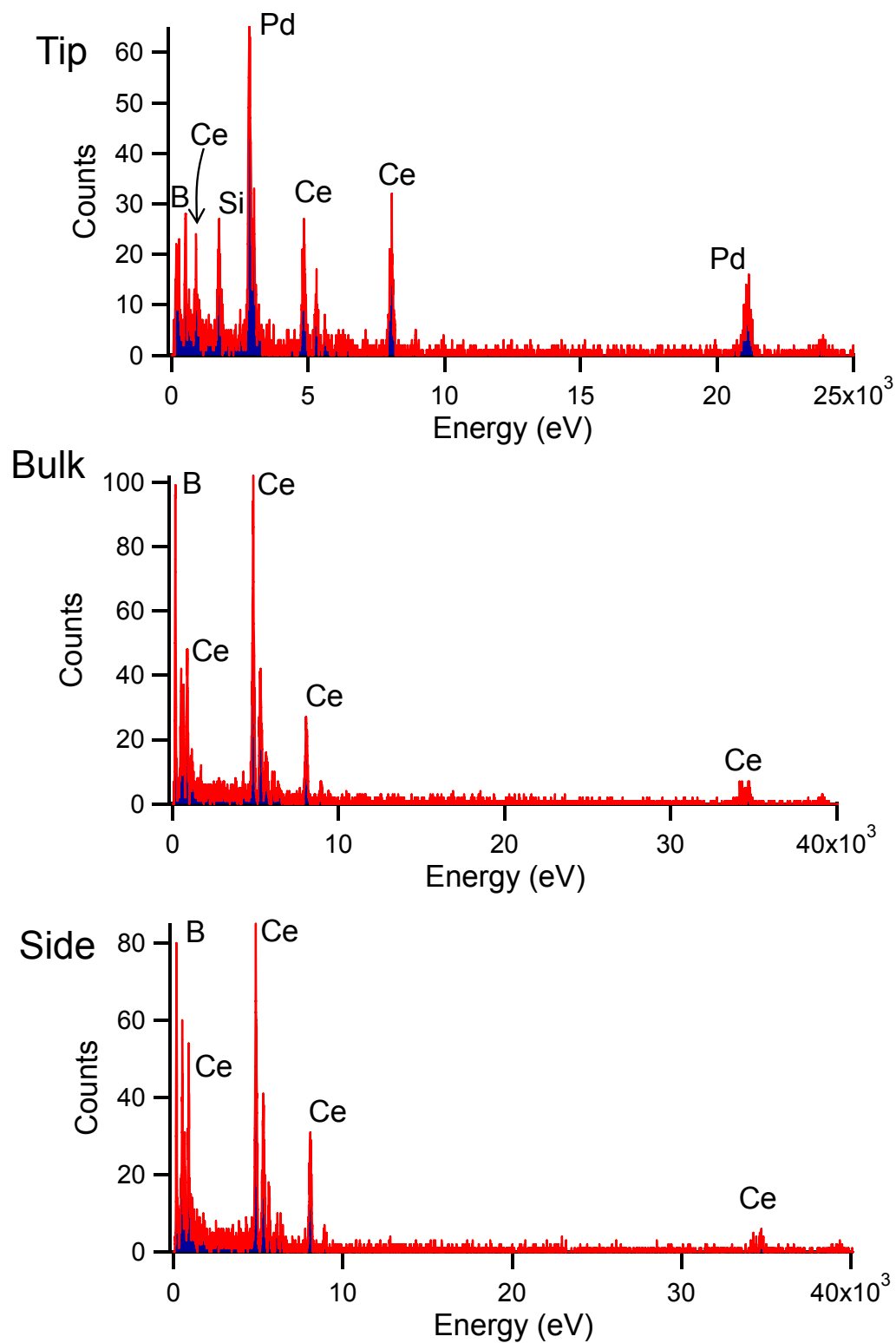


Figure A2.6 EDS patterns of the tip, bulk and side of the CeB_6 nanowire in A2.5.

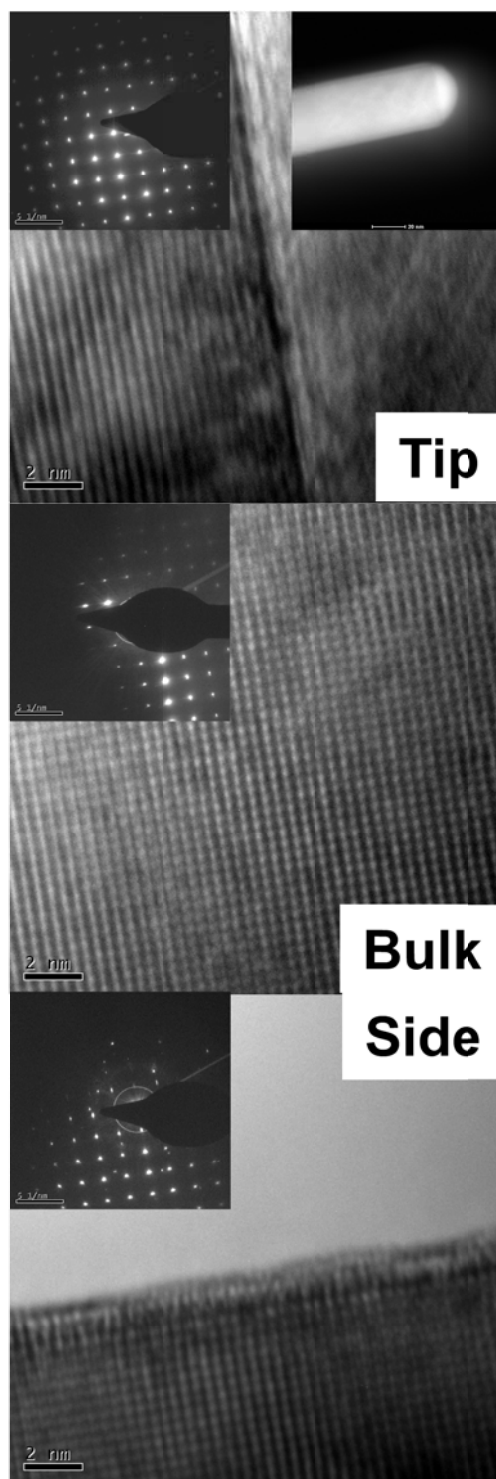


Figure A2.7 HRTEM images of a PrB_6 nanowire tip, bulk and side. Insets are SAED patterns and high angle dark field image.

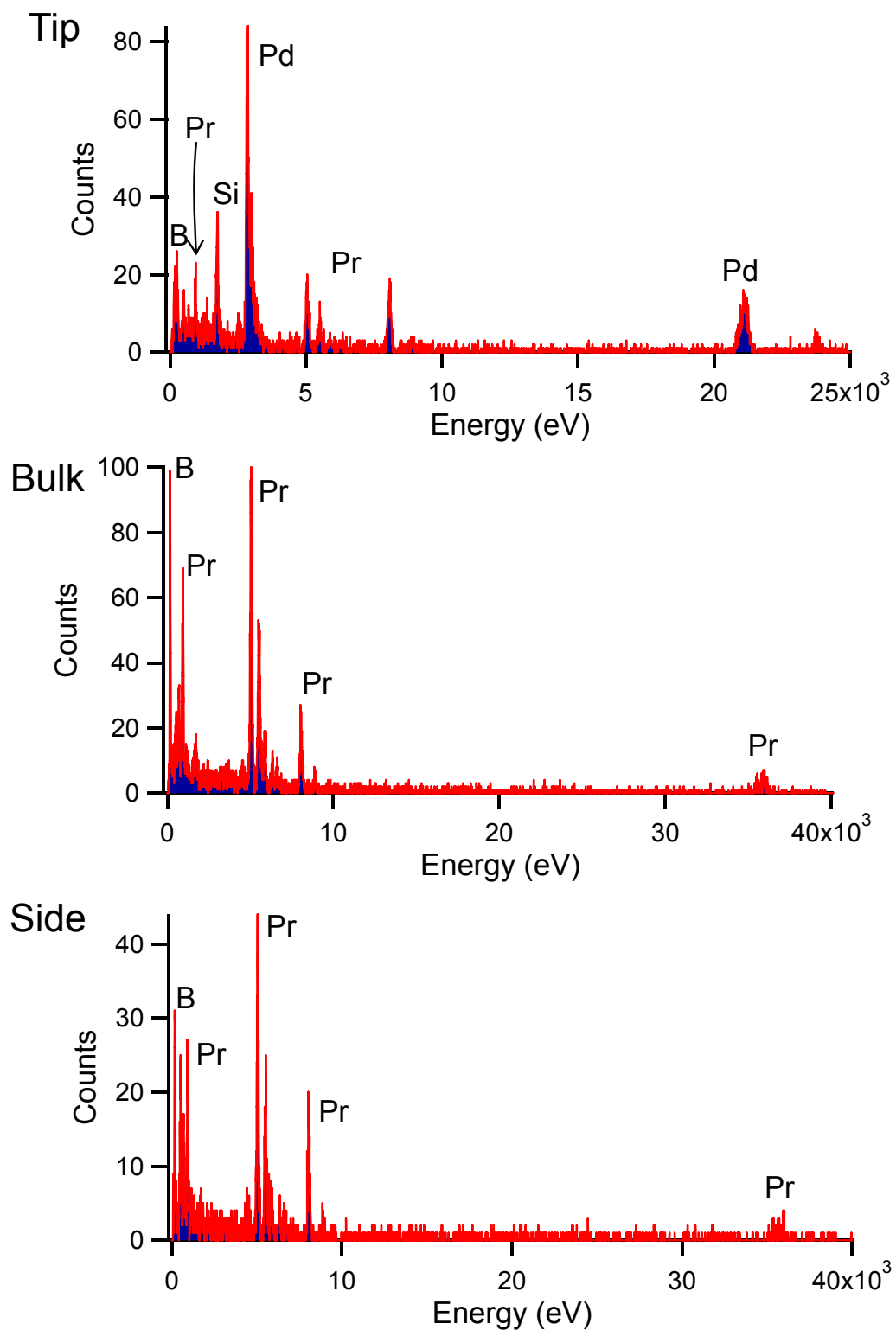


Figure A2.8 EDS patterns of the tip, bulk and side of the PrB₆ nanowire in A2.7.

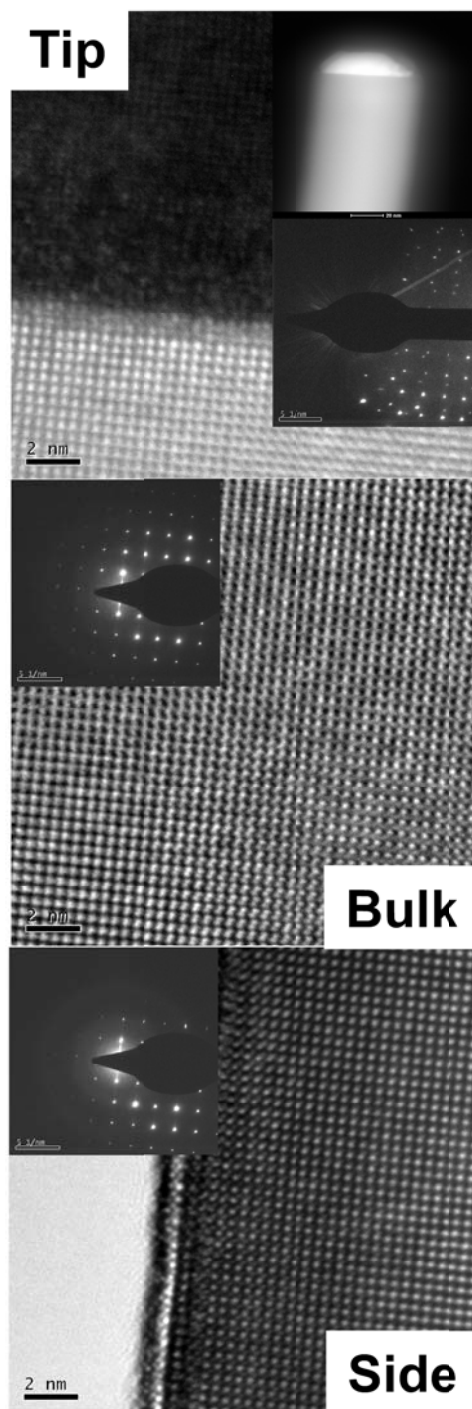


Figure A2.9 HRTEM images of a NdB_6 nanowire tip, bulk and side. Insets are SAED patterns and high angle dark field image.

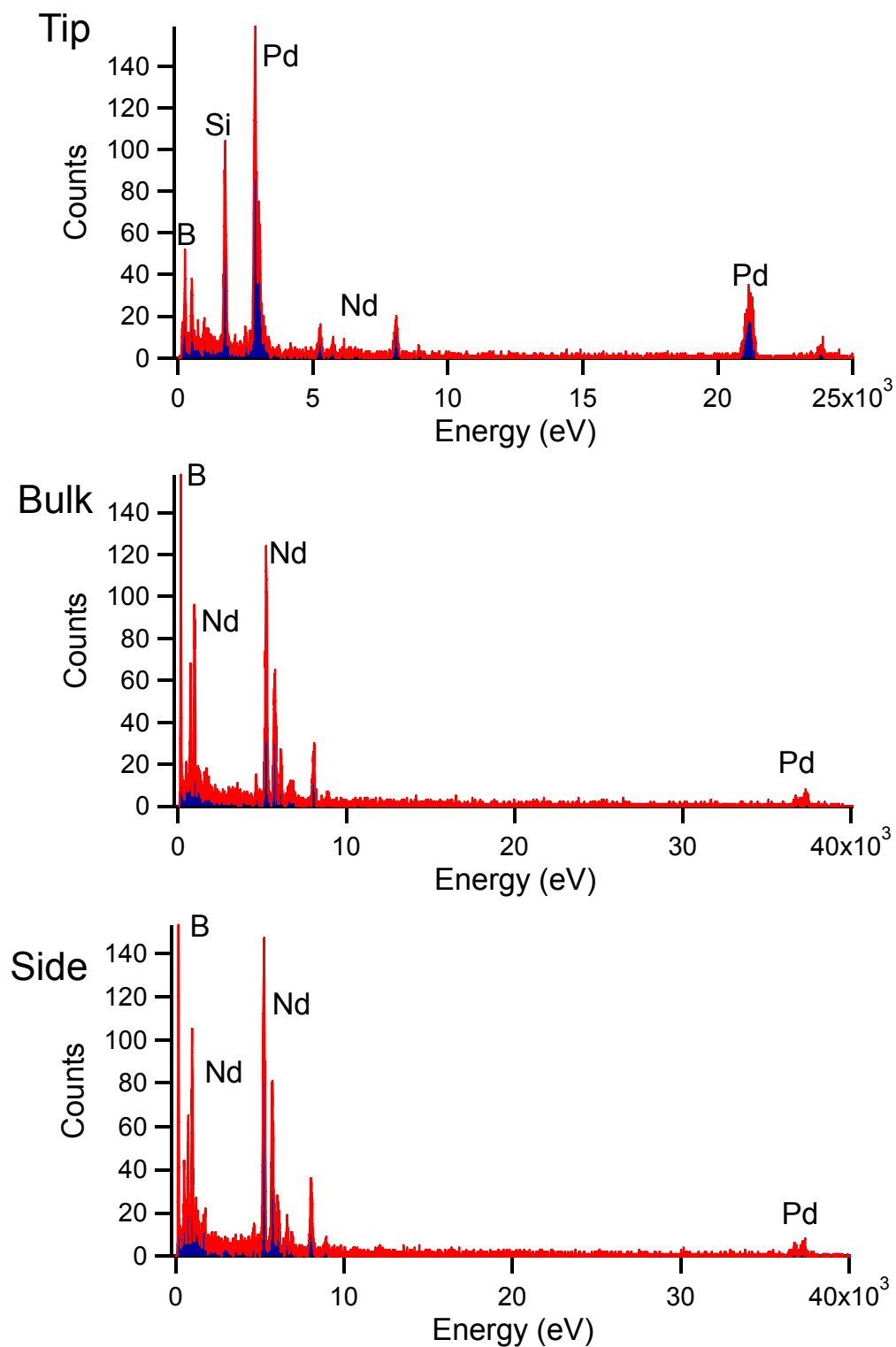


Figure A2.10 EDS patterns of the tip, bulk and side of the NdB_6 nanowire in A2.9.

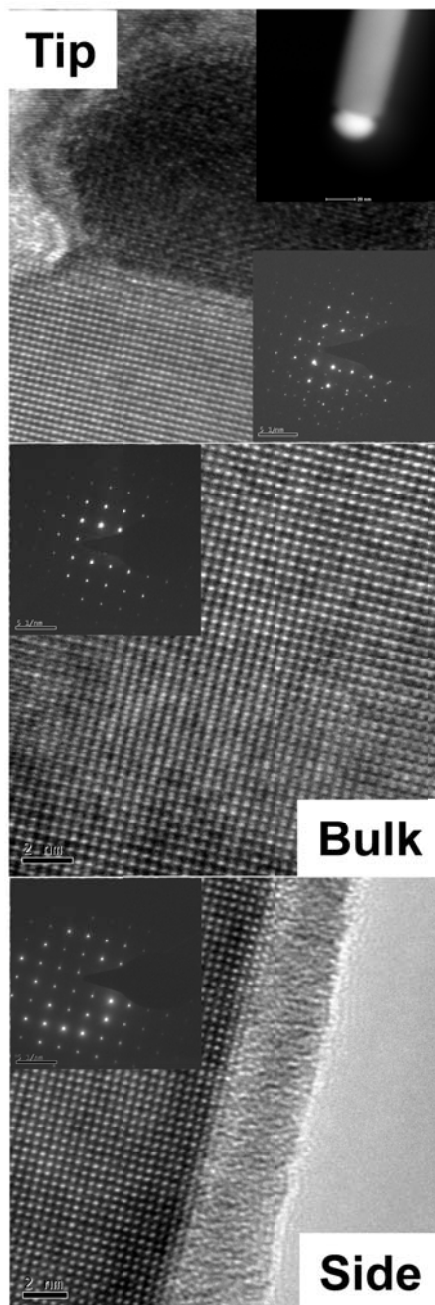


Figure A2.11 HRTEM images of a SmB_6 nanowire tip, bulk and side. Insets are SAED patterns and high angle dark field image.

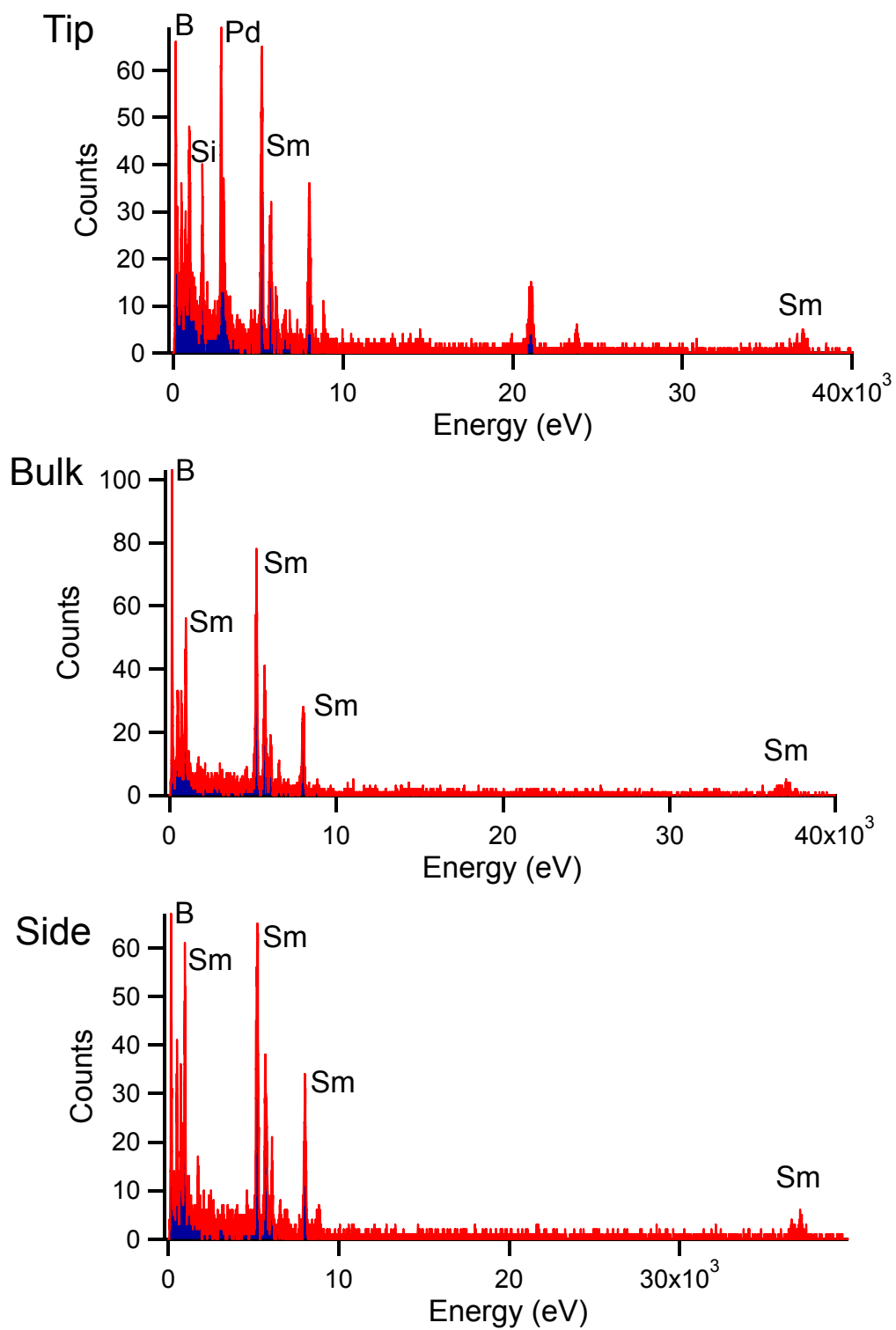


Figure A2.12 EDS patterns of the tip, bulk and side of the SmB₆ nanowire in A2.11.

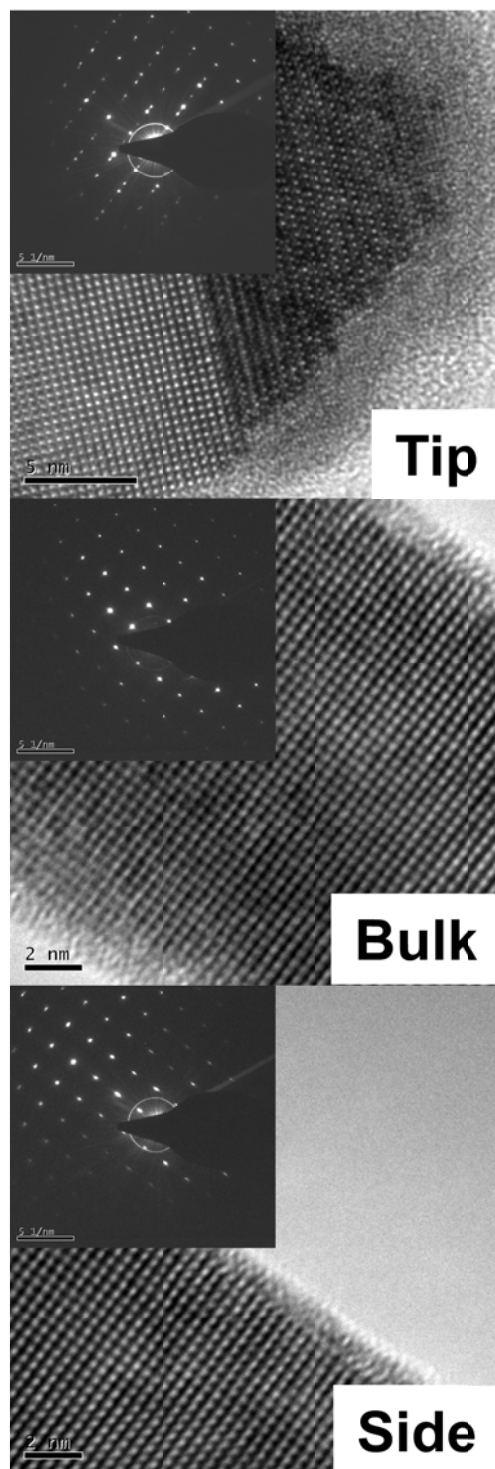


Figure A2.13 HRTEM images of a GdB₆ nanowire tip, bulk and side. Insets are SAED patterns.

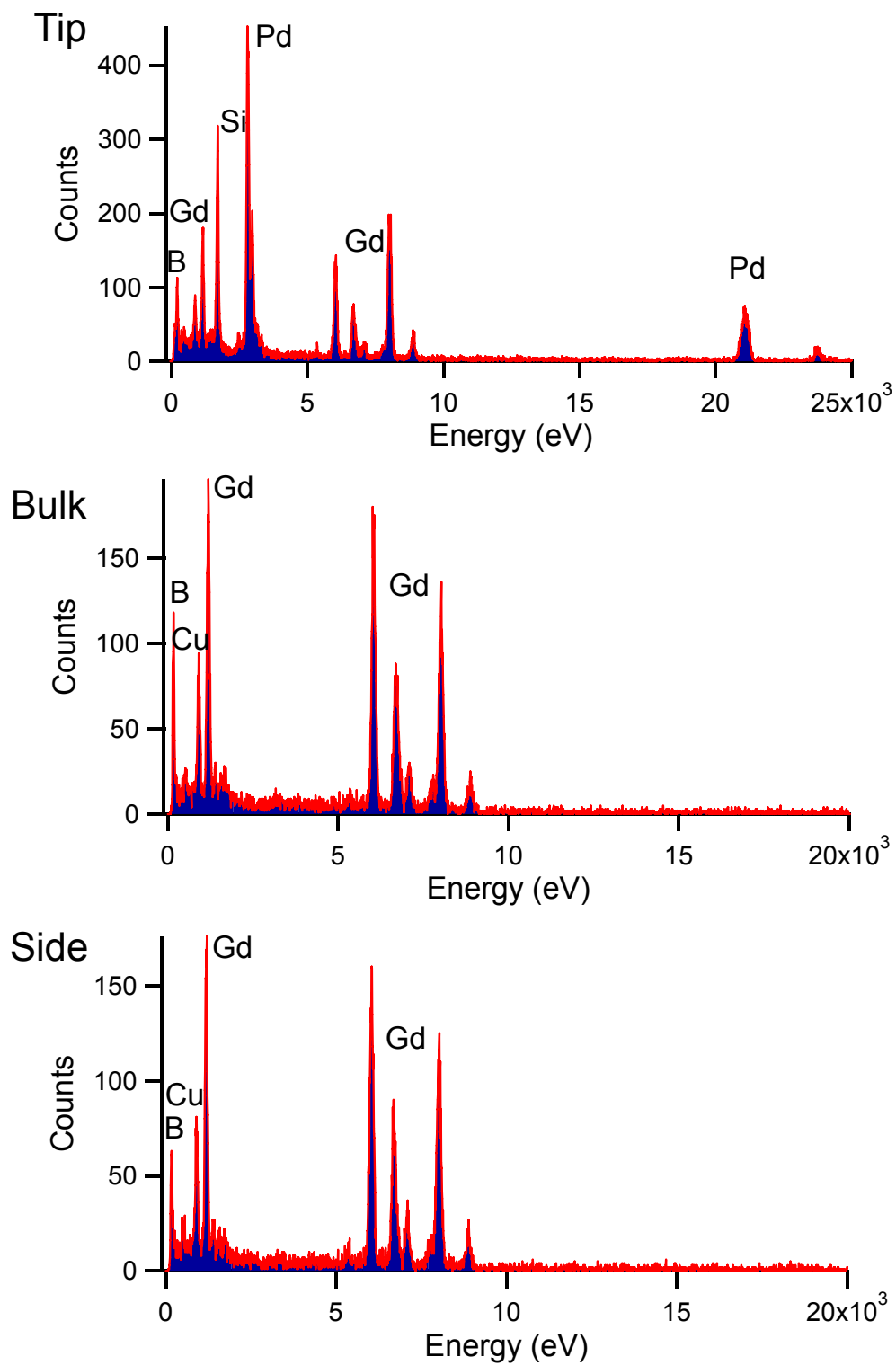


Figure A2.14 EDS patterns of the tip, bulk and side of the GdB₆ nanowire in A2.13.

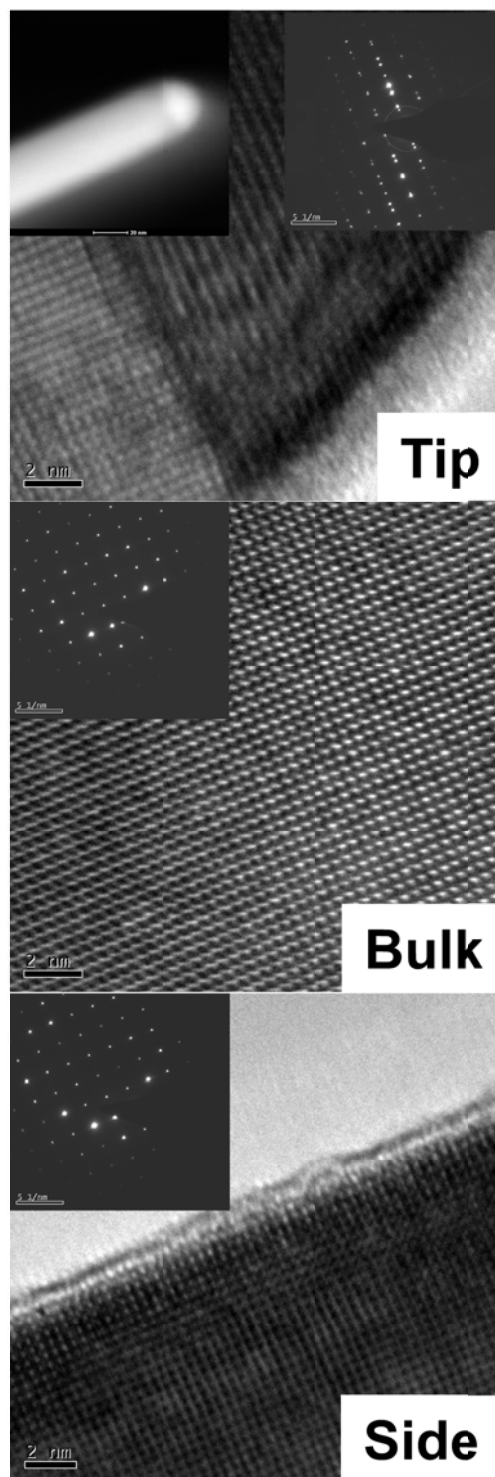


Figure A2.15 HRTEM images of a TbB₆ nanowire tip, bulk and side. Insets are SAED patterns and high angle dark field image.

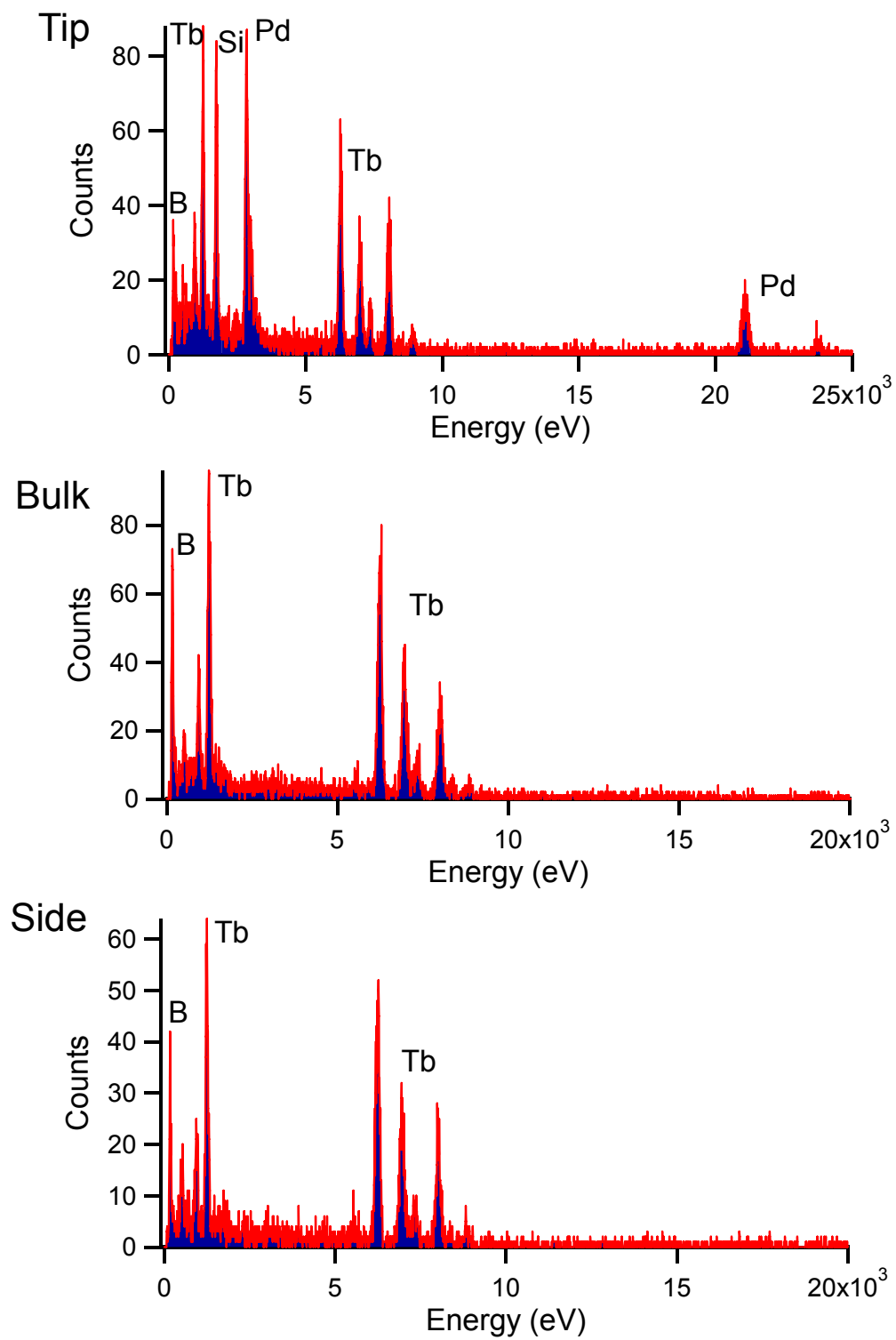


Figure A2.16 EDS patterns of the tip, bulk and side of the TbB₆ nanowire in A2.15.

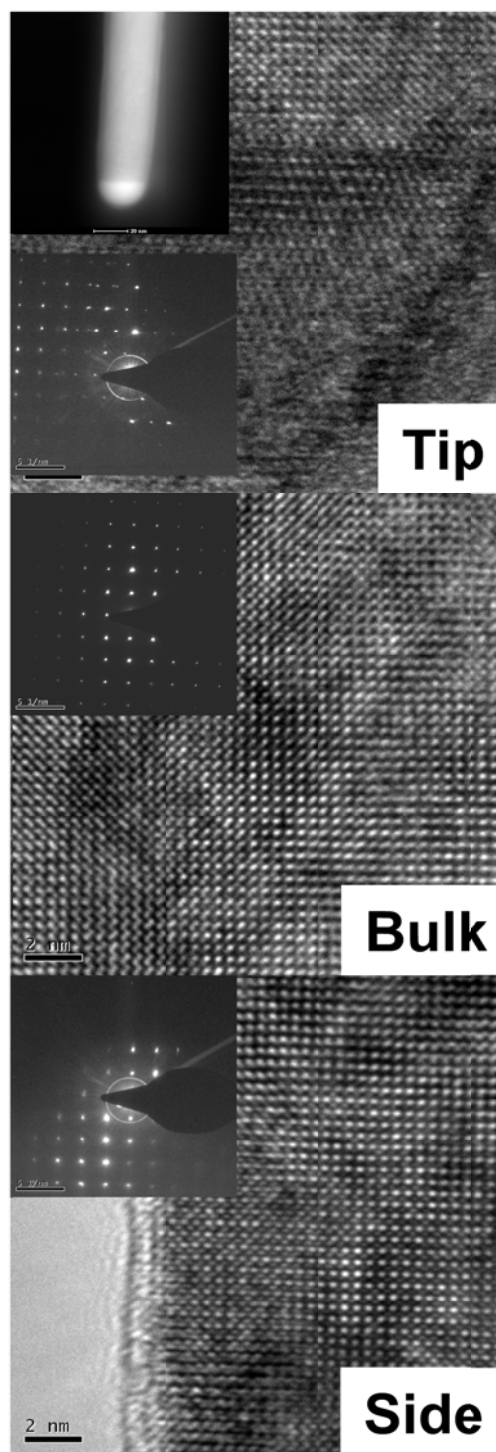


Figure A2.17 HRTEM images of a DyB₆ nanowire tip, bulk and side. Insets are SAED patterns and high angle dark field image.

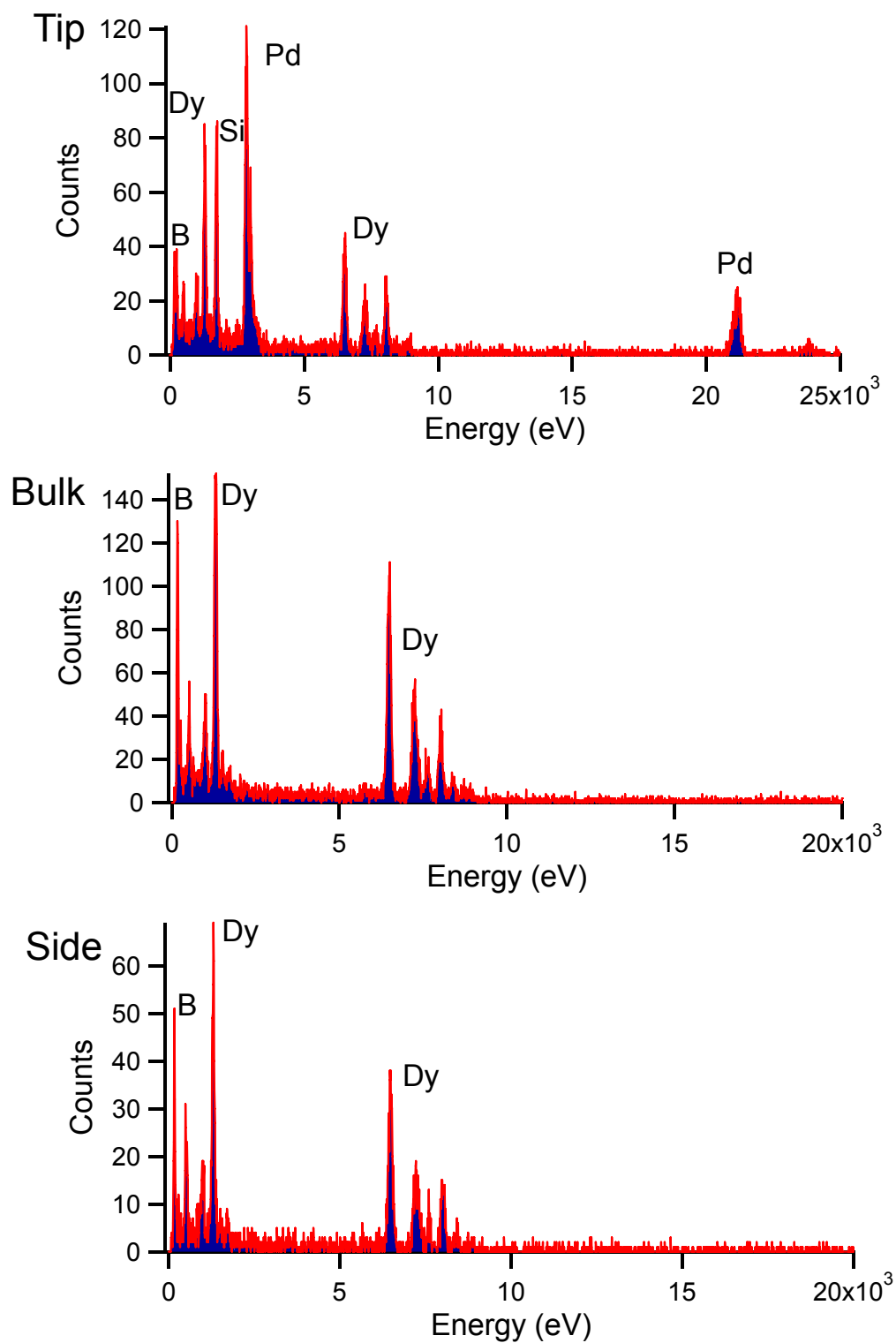


Figure A2.18 EDS patterns of the tip, bulk and side of the DyB₆ nanowire in A2.17.

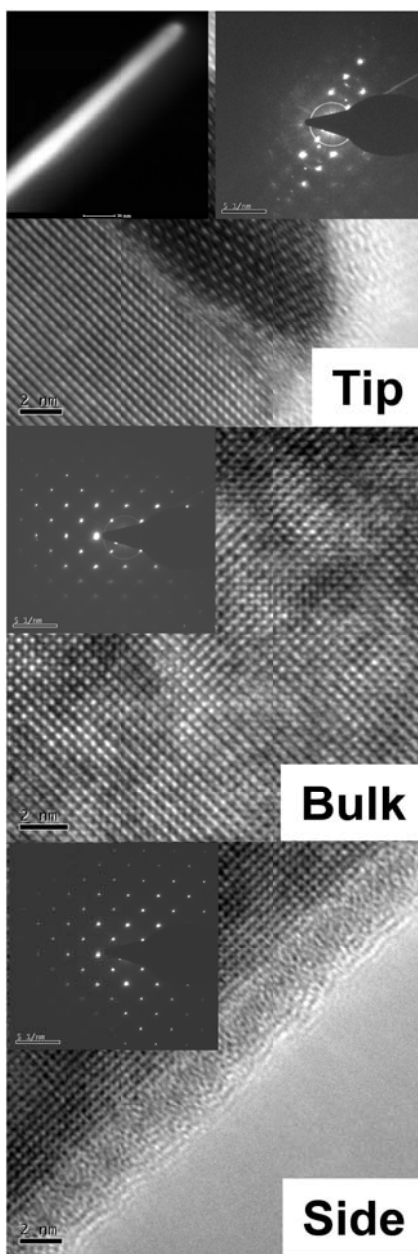


Figure A2.19 HRTEM images of a HoB₆ nanowire tip, bulk and side. Insets are SAED patterns and high angle dark field image.

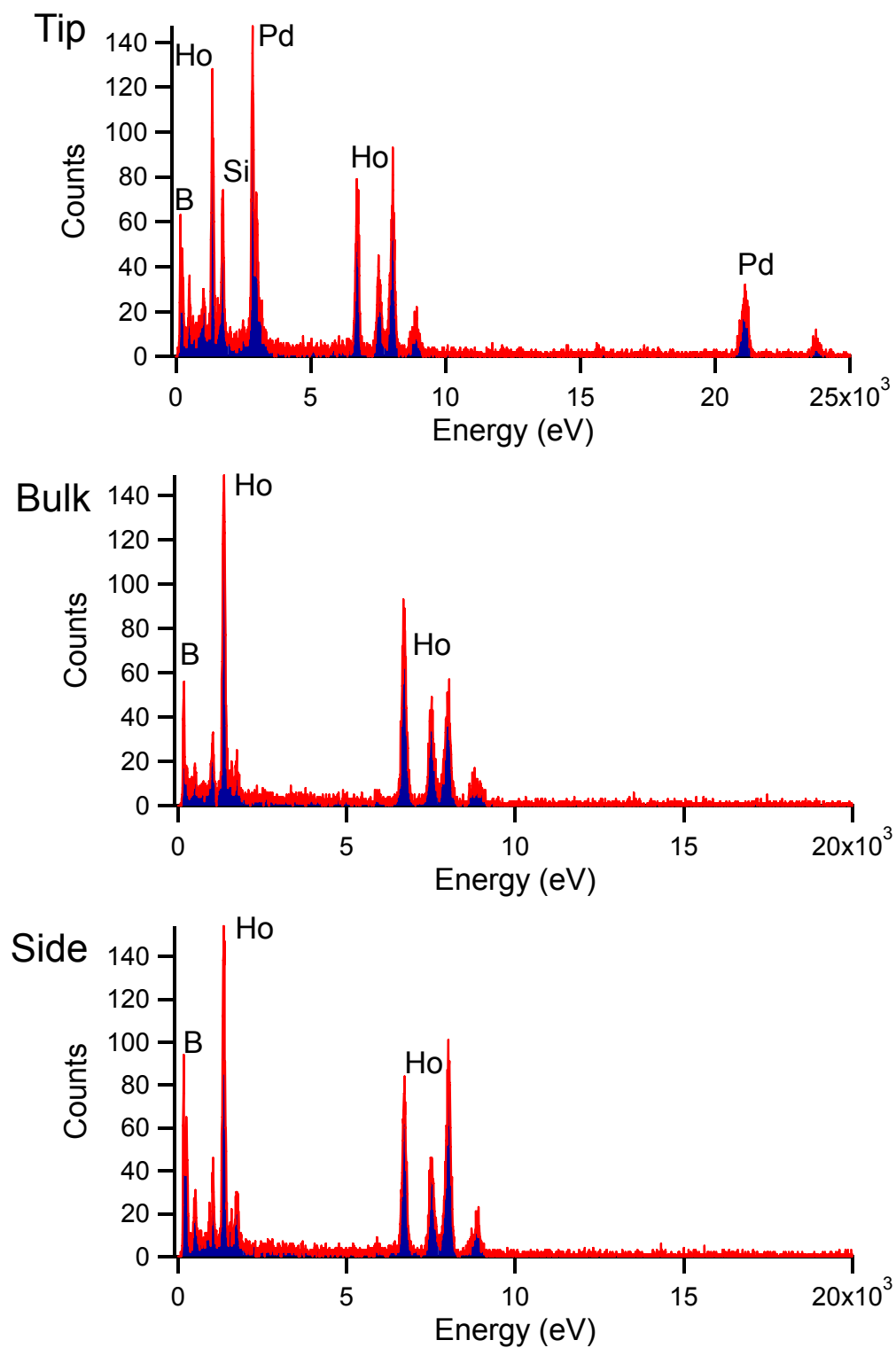


Figure A2.20 EDS patterns of the tip, bulk and side of the HoB₆ nanowire in A2.19.

Chapter 3

Local electrode atom probe tomography

3.1 Introduction

Much of the current activity in materials science is focused on the understanding properties of materials at the atomic scale. Accordingly, it is necessary for materials scientists to characterize those materials at the atomic level, both crystallographically and compositionally. Understanding the crystallographic properties of materials at the atomic level has been available for decades and has become trivial due to the wide availability of scanning tunneling microscopy, atomic force microscopy, and the z-contrast scanning and high resolution transmission electron microscopy. However, understanding the composition at that level is still rather difficult. Traditional composition analysis techniques such as energy dispersive x-ray (EDX) and x-ray photoemission spectroscopy (XPS) can really only provide information at the nanometer to micrometer levels, respectively, and only in two dimensions. EDX, which is the most common method for understanding chemical composition at the nanoscale, cannot resolve light elements (such as B) quantitatively (or even qualitative in some cases) and can only determine composition to several percent. This limitation in compositional analysis has not only affected the development of nanomaterials in our lab, but the nanomaterials community as a whole.

Atom probe field ion microscopy (APFIM) is an instrument that can determine not only the elemental identity of atoms but also provide their 3D location at the atomic level

and their concentration down to parts per million levels.¹⁻⁸ The APFIM, invented by Muller, Panitz and McLane, is a combination of a field ion microscope (FIM) and a time of flight mass spectrometer (TOFMS). The field ion microscope is a lensless point-projection microscope that can resolve the location of atoms of a pointed tip with 3D atomic resolution and was originally invented by Muller between 1951 and 1956. The FIM is based on field evaporation, which is the sublimation of atoms as ions from a microtip specimen at high electric (E) fields, and utilizes ultrahigh vacuum and cryogenic temperatures. The field evaporation in the FIM is controlled by superimposing a high-voltage pulse (V_{pulse}) on top of the positive potential (V_{ex}) that the tip is maintained at. By combining V_{pulse} with the cryogenic temperatures, materials can be evaporated from the tip in a crystal plane by crystal plane manner. Though the FIM proved effective at reconstructing atomic position of field emitted ions in 3D, it was not sufficient for compositional analysis of the ions. It wasn't until the addition of the TOFMS in 1968 was the compositional portion of the APFIM realized. (Figure 3.1) Addition of a TOFMS was universally adopted for the atom probe because it is equally sensitive to all elements and no prior knowledge of the elemental composition is necessary for the analysis. With the addition of the TOFMS, both identity and location of field evaporated ions could be determined in a 3-D manner.

The field evaporation process can be best understood by analyzing a potential energy diagram of the surface atoms.^{6, 9} (Figure 3.2) The y-axis of the diagram is potential energy of the atom while the x-axis is the distance along the escape path for the atom. In ground state, Figure 3.2a, the atom must overcome a potential energy barrier, through input of energy into the system, in order to escape out into vacuum. In APFIM, and more

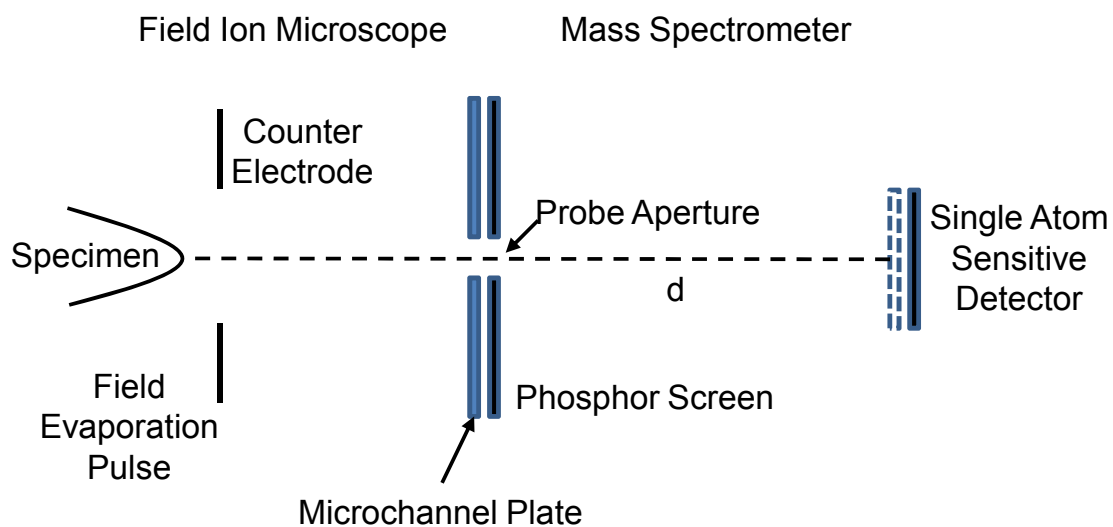


Figure 3.1 Schematic of the classic or “original” field ion microscope.⁴

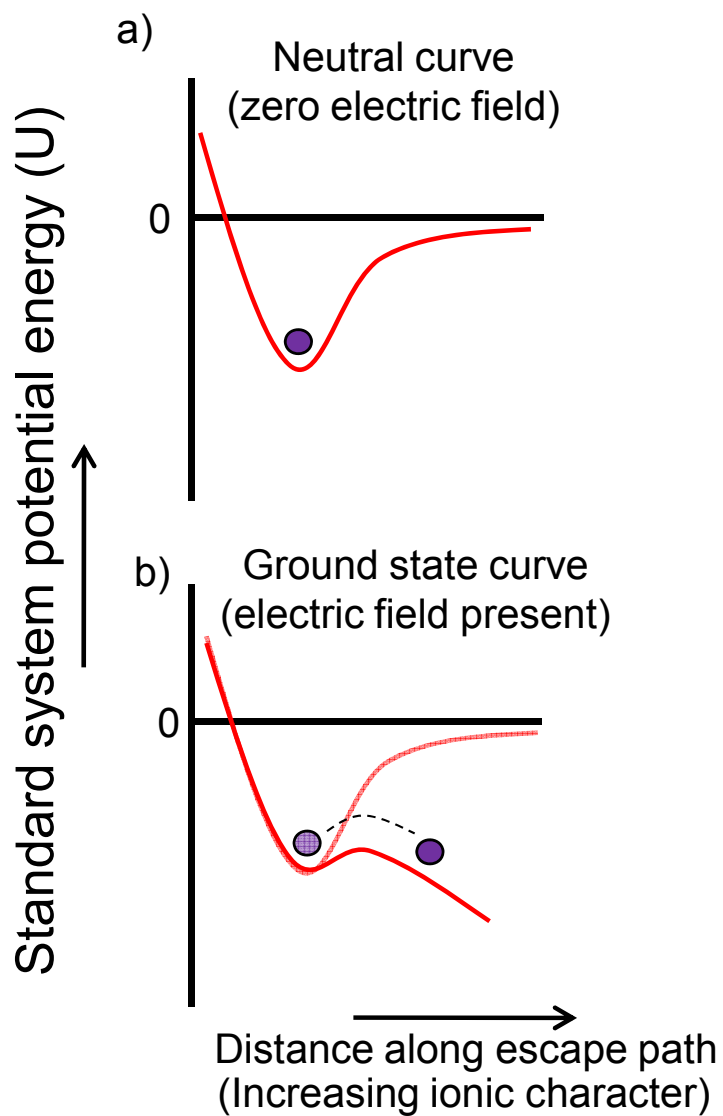


Figure 3.2 Potential energy diagram of a surface atom (purple) with no applied voltage (light red) and high applied voltage (dark red).^{6,9}

specifically voltage pulse APFIM, an electric field is applied which distorts the potential energy barrier. (Figure 3.2b) This distortion is crucial as it allows the atom to escape into vacuum while the system remains at the cryogenic temperatures (cold emission versus thermal emission).

Though the technique was impressive in its capabilities, there were several limitations to the APFIM technique as it stood: 1) the probes could not analyze large volumes of atoms ($<10^6$), 2) specific tip geometries were necessary (tip diameters $< 50\text{nm}$) and 3) only conductive materials could be analyzed (essentially limiting it to metals).⁴ This left the APFIM with only a very small window for application. As huge increases in computational power occurred over the next several decades, resurgence in interest in APFIM occurred as much larger volumes of atoms could be analyzed.

The adaption of the local electrode to the APFIM in 1995 led to an increase in probe dimension (up to 500 nm tip diameters) and analyzable sample geometries. The local electrode atom probe, or LEAP, has several advantages over the fixed electrode geometry: 1) electric (E) fields necessary for evaporation were much lower as the electrode could be positioned within several micrometers of the tip, 2) a much larger range in tip geometries and sizes could be analyzed because of the close proximity of the electrode, and 3) the positional electrode greatly increased the analysis output of the technique. The introduction of a pulse laser mode, in 2002, led to a dramatic increase in the kinds of materials that could be analyzed by LEAP. The pulse laser mode functions very similar to the field evaporated mode; the tip is maintained at a constant potential, but instead of pulsing an electric field, the energy for evaporation is provided by laser pulses. (Figure 3.3) This addition allowed for non-conductive materials, such as intrinsic

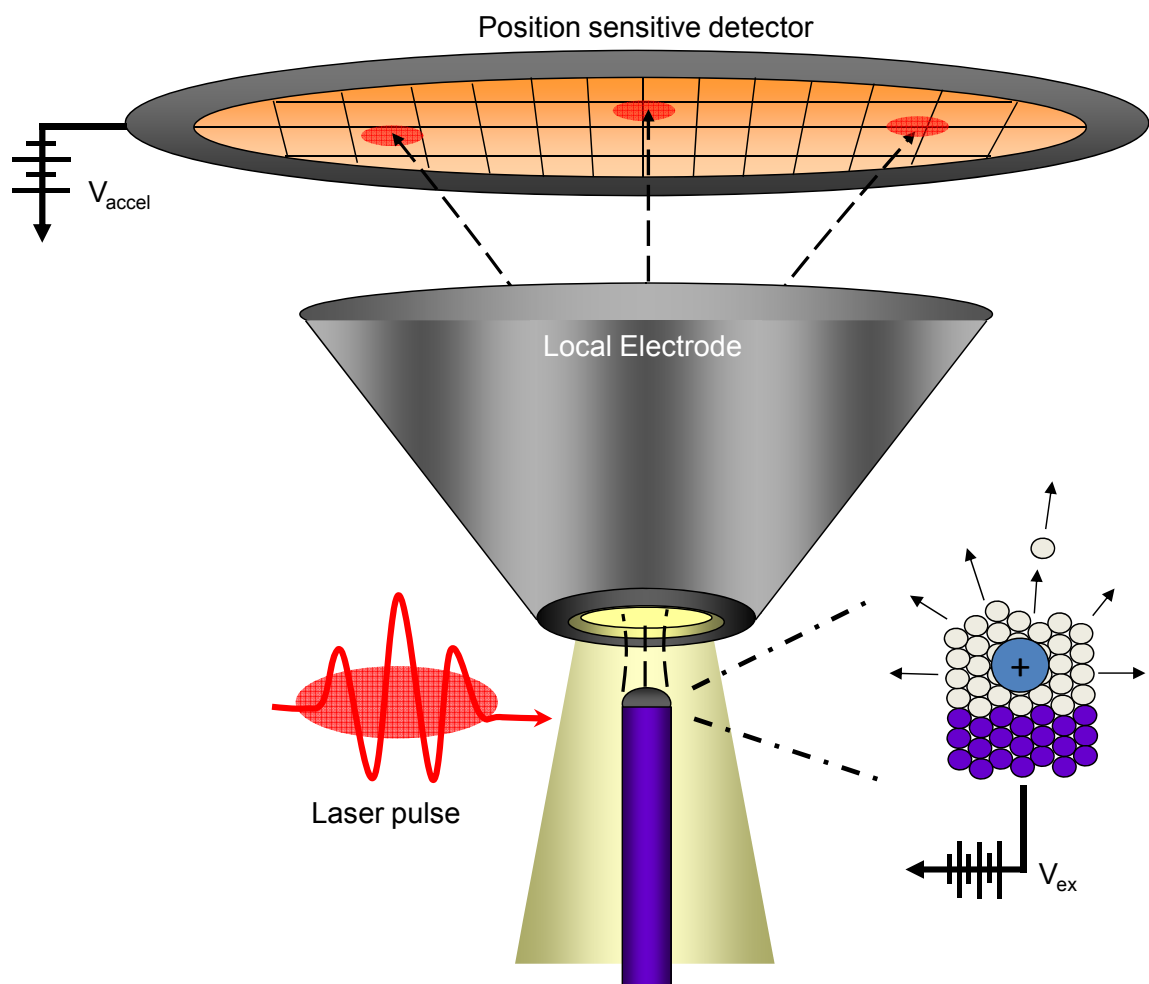


Figure 3.3 Schematic of a LEAP microscope using pulse laser mode for analysis of a nanowire.

semiconductors and even insulating oxides, to be analyzed.

Recently, the first analysis of semiconducting nanowires was accomplished at Northwestern University.⁹⁻¹² Results of the LEAP analysis of undoped InAs and Si nanowires and doped Ge nanowires found material from the catalyst particle used in VLS growth diffused throughout the nanowire and that doping the nanowires produced non-uniform lateral concentration gradients of the dopant atoms. (Figure 3.4) Though the process provided never-before-seen qualitative and quantitative data about dopant distribution and catalyst particle diffusion in nanowires, application of the technique toward their materials relied on the nanowires being well spaced and perpendicular to the substrate surface. (Figure 3.5) Oriented and templated growth, though not new, is very difficult to obtain in many nanowires systems and generally takes very sophisticated growth methods. Furthermore, since this technique utilizes an SEM for imaging purposes, there is no method for verification of crystallographic properties. In order to be able to apply this technique toward the REB_6 system and to further expand the application range and capabilities of LEAP tomography, it was necessary to develop a method to analyze the REB_6 materials that could be expanded to other materials systems.

3.2 Experimental Methods

3.2.1 LEAP technique development

As grown nanowire samples were sonicated in ethanol and dispersed onto metal mesh TEM grids. (Figure 3.6a) A grid spacing of 8 μm was used to maximize the probability of finding single nanowires of sufficient length. TEM grid and sample holder was then loaded into an FEI Nova 200 NanoLab dual beam SEM/FIB. An Omniprobe

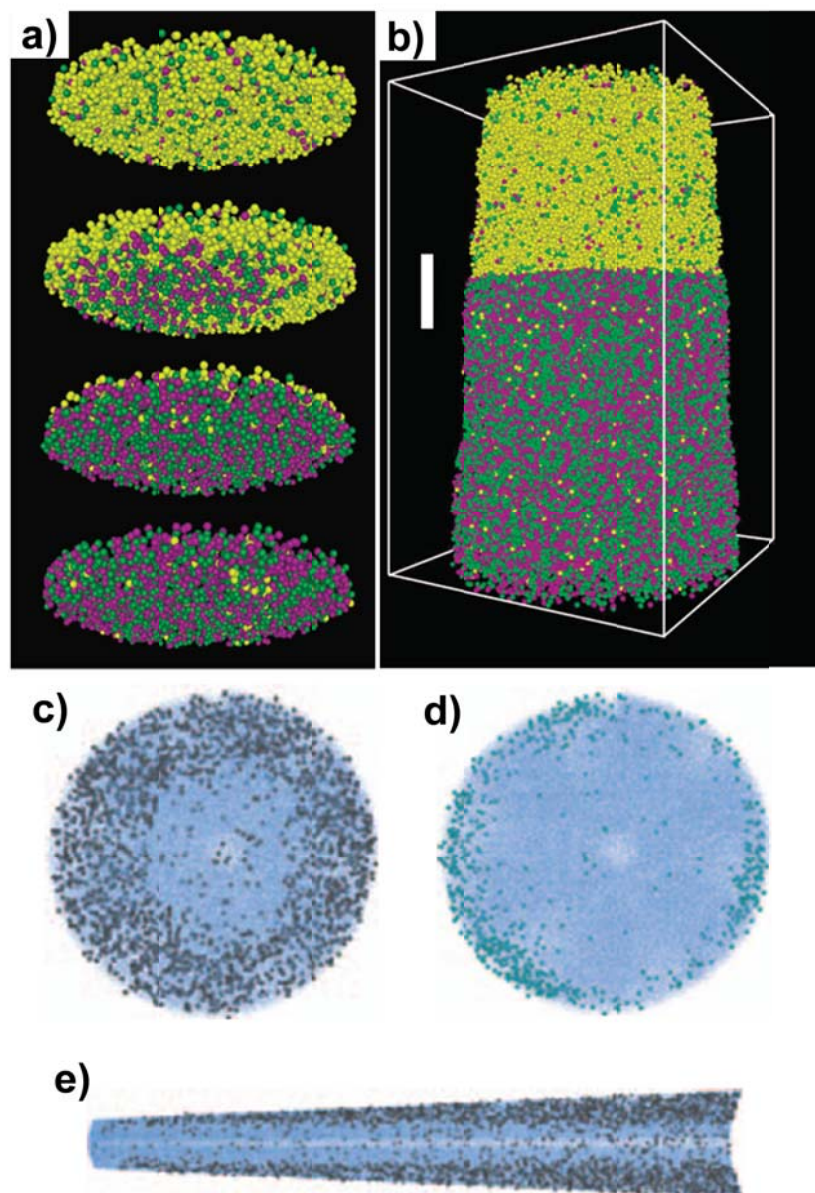


Figure 3.4 Images of LEAP reconstructions of InAs (a and b) and P-doped Ge (c-e) nanowires.^{9, 12} (a) Cross-section images of the nanoparticle:nanowire interface through white bar in b. (b) LEAP reconstruction of the Au catalyzed InAs nanowire. (c) end-on view highlighting phosphorous distribution (dark blue spheres) and (d) oxygen (light blue) in germanium (blue dots). (e) Average phosphorous concentration along the growth axis.

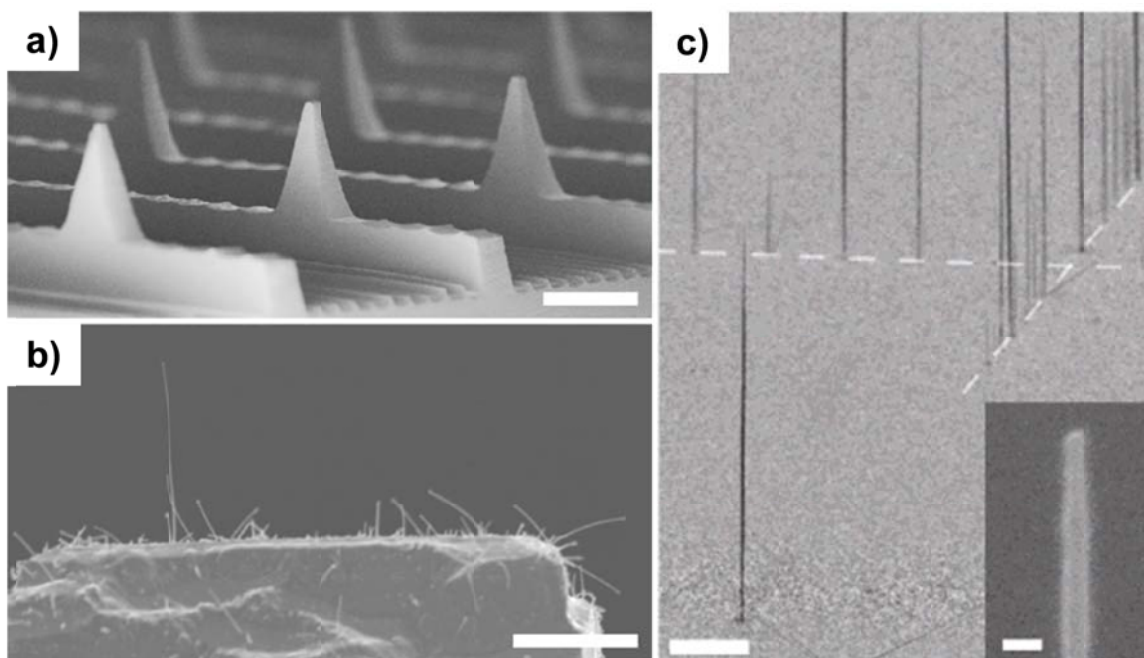


Figure 3.5 SEM images of preferred sample geometries and preparation methods for traditional LEAP analysis. Inset in (c) shows a high magnification SEM image of foreground nanowire.^{9, 11}

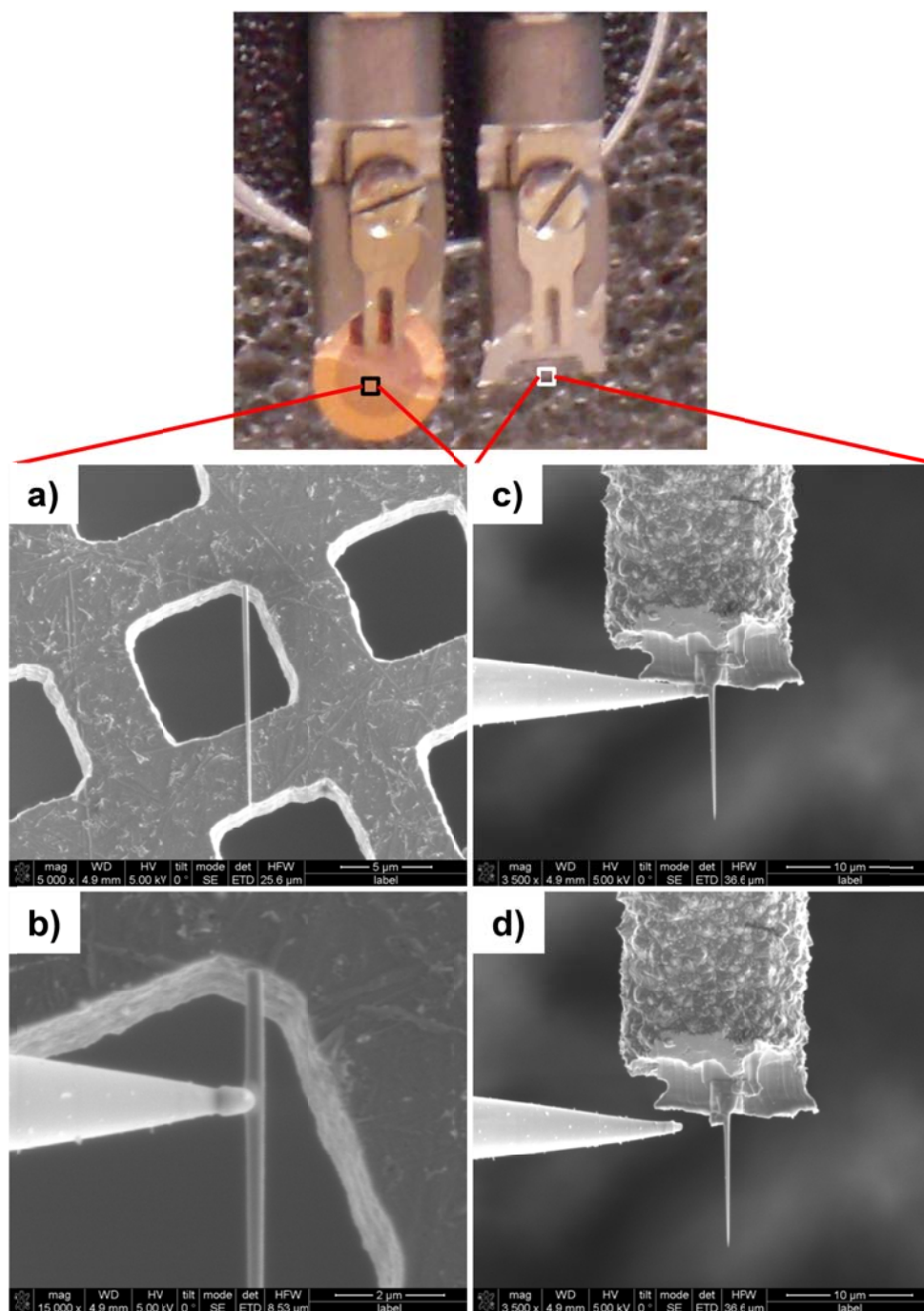


Figure 3.6 SEM images of the LEAP sample preparation process. (a) and (b) are the nanowire isolation process and (c) and (d) are the nanowire mounting process for the LEAP analysis.

nanomanipulator was then used in combination with the FIB to make a weak Pt attachment to the nanowire. (Figure 3.6b) The nanowire is then positioned onto another metal mesh TEM grid (of much larger grid dimensions) which has been cut to expose individual posts. (Figure 3.6c) The FIB is then used to make another, much stronger, Pt weld from the wire to the post and the weak attachment to the manipulator is broken by pulling the manipulator away. (Figure 3.6d) Once attachment to the grid is made, the sample was then loaded into a FEI Tecnai G2 F20 S-Twin 200 keV TEM for imaging. The post numbers with adequate wire samples were then noted and the sample was loaded into the Imago Scientific LEAP 3000X HR (Madison, WI) for analysis. Samples were evaporated using the pulsed laser mode with 532 nm green laser, 200 kHz pulse rate and 0.5 nJ laser power.

3.2.2 LEAP data analysis

Since the reconstruction of the LEAP data is an extremely complex process, it will not be discussed in detail here. Training on data reconstruction by a trained LEAP technician is a necessity (and suggested by Imago Scientific). Only after sufficient training should one attempt reconstruction and data analysis. For reconstruction purposes, it is sufficient to say that TEM images of the nanowire prior to the LEAP run are compared to the final reconstructed image and modification to the shank angle, detector efficiency and compression ratio are made to match the image as closely as possible. The TOFMS was typically calibrated against the B signal prior to quantitative and qualitative elemental analysis of the nanowires.

3.3 Results

Figure 3.7 presents a TEM image prior to LEAP analysis of a LaB₆ nanowire and corresponding 3D reconstruction. Figure 3.7a depicts a thick amorphous coating on the nanowire, not typically seen in the previous nanowire results presented in chapter 2. The origin of the amorphous layer is from the welding process used to attach the nanowire to the post which utilizes a metal-organic Pt precursor. Upon further investigation, it was determined that once the nanowire is exposed to a small electric field and ultrahigh vacuum conditions, the amorphous layer desorbs leaving the pristine nanowire. The LEAP reconstruction was conducted according the measurement obtained in the TEM imaging. The dots represent individual atoms and the dot color represents the chemical identity as determined by the TOFMS.

The LEAP reconstruction also indicates the absence of any detectable Pd atoms in the bulk of the wire. (Figure 3.8) This suggests that the Pd, unlike Au, does not diffuse into the nanowire during the growth process. Furthermore, the RE:B ratio of the nanowire falls within the stoichiometric region defined by the binary phase diagram. These results validate the TEM findings that the materials are of high quality, and also provide some of the first direct measurements of B quantity in REB₆ materials. The lateral dimensions of the nanowires measured by the TEM were used to optimize the reconstruction parameters. Table 3.1 shows the composition results of the TOFMS versus the EDX analysis. The EDX analysis shows that the RE:B ratio is about 9:1 while the TOFMS estimates it to be very close to the 6:1 ratio as expected from the HRTEM analysis and XRD. ZAF corrected EDS, which accounts for matrix effects such as atomic number, re-absorption of emitted x-rays and fluorescence, traditionally provides the most accurate elemental analysis but greatly underestimated the boron content of all REB₆ samples.

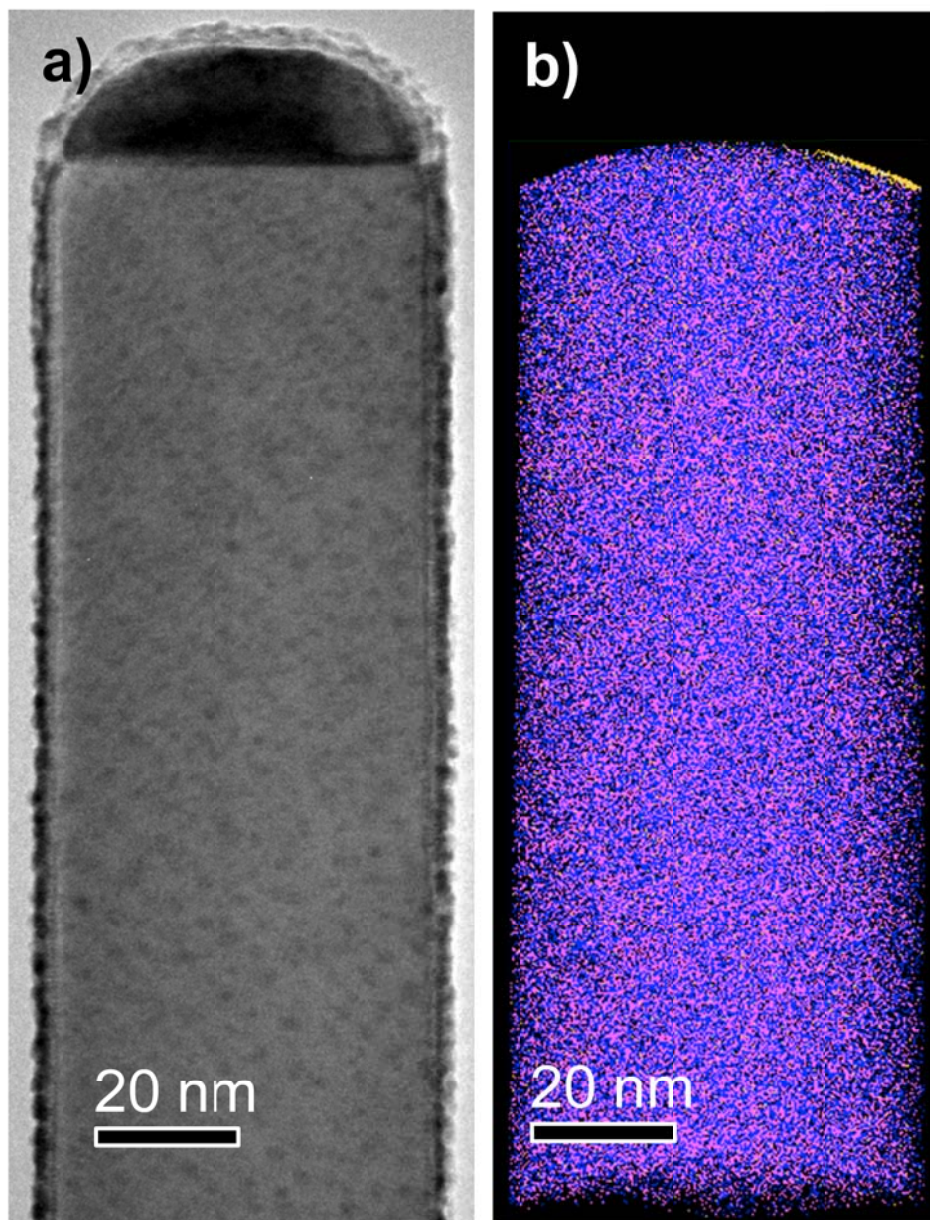


Figure 3.7 TEM image (a) and LEAP reconstruction (b) of a LaB_6 nanowire: La (purple), B (blue), and Pd (yellow).

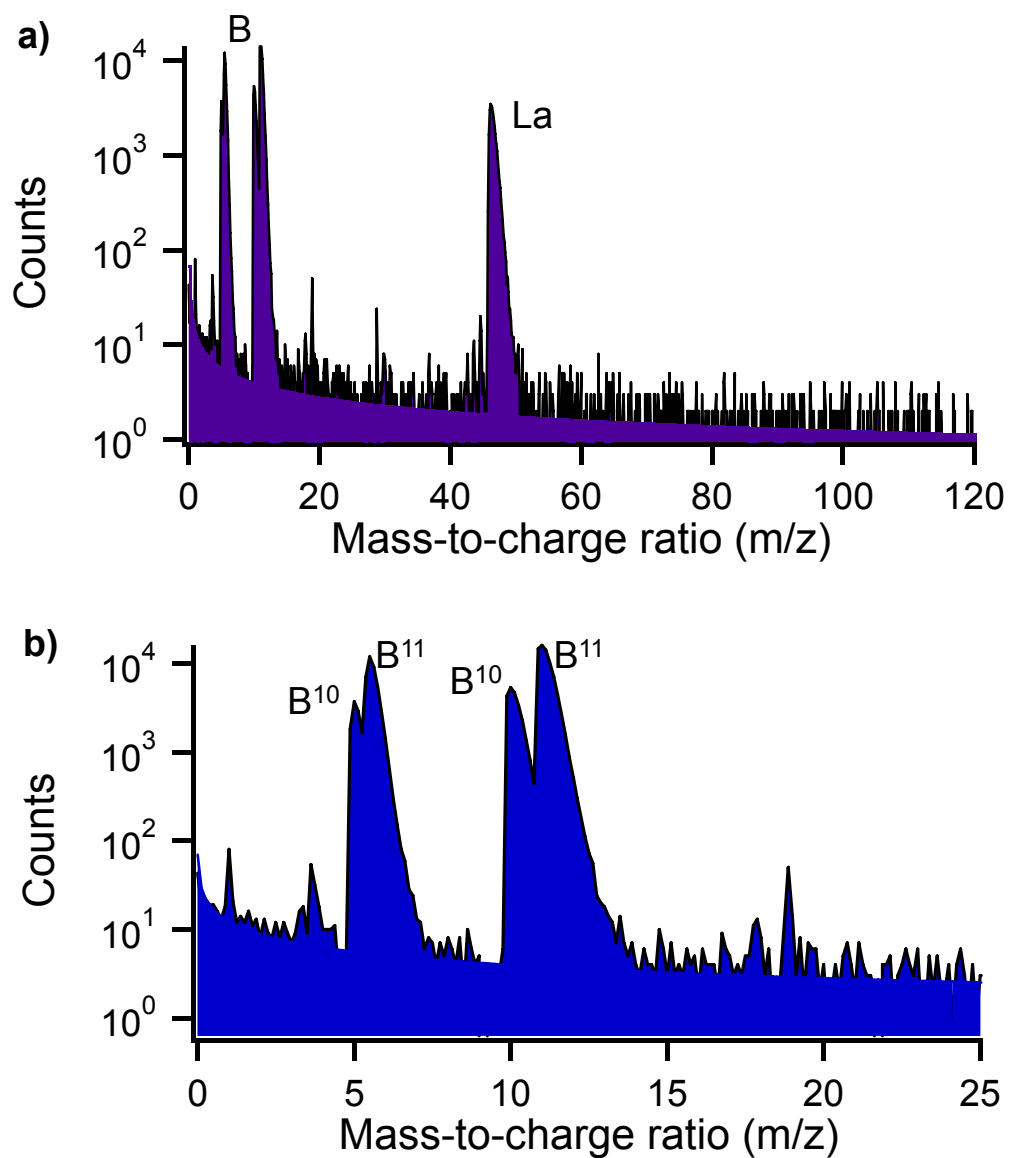


Figure 3.8 Mass spectra of a reconstructed LaB_6 nanowire. (a) Complete TOFMS indicating the presence of only La and B. (b) Enlarged section of the low mass-to-charge ratio region of the graph showing the separation of the naturally occurring B isotopes.

Table 3.1 Boron composition analysis of the REB₆ nanowires

REB ₆	LEAP (atomic %)	EDS (atomic %)	
		Uncorrected	ZAF corrected
YB ₆	84.92	98.691	8.843
LaB ₆	86.18	98.782	44.102
SmB ₆	79.70	97.978	4.670
HoB ₆	84.60	97.353	1.166

Though the LEAP technique proved quite useful for the compositional analysis of the nanowires, several complications arose: 1) The expected crystal plane by crystal plane evaporation of the materials was not noticed and 2) none of the materials analyzed showed the Pd particle composition, even though the TEM analysis indicated it was there. Of the first complication, it is likely that the octahedral B clusters don't evaporate only when the peak intensity of the pulse interacts with the REB₆ nanowire (as would theoretically be expected). It was noticed that small evaporation events continue to occur after the maximum intensity of the pulse has interacted with the nanowire. The continued evaporation process is identified in the large tails seen on the B TOFMS peaks and also in monitoring the evaporation process as the LEAP is running. (Figure 3.8b) This suggests that the B clusters are in pseudo-excited state and likely have several unsaturated bonds; allowing them to continue evaporating after the peak intensity portion of the pulse has interacted with the nanowire. With respect to the Pd particle, upon application of the pulse, most nanowires exhibited a "major evaporation event". This type of event occurs when a rapid evaporation of materials occurs and there are many simultaneous events occurring on the detector at one time. These simultaneous events cannot be separated from each other and information regarding chemical identity and position are lost. This is likely to occur in the LEAP analysis of these materials for one reason: the work function the REB₆ is much lower than that of the Pd:B:RE alloy at the tip. Basic electron transport in materials states that electrons flow in the direction of lower potential energy (i.e. flow in the direction of lower work function to higher work function). When flow is opposite of that direction, a potential energy barrier called a Schottky barrier is formed and charge accumulation occurs at the interface. The electrons can flow past this barrier but this

usually leads to considerable resistive heating at the interface (thermal energy used to increase the potential energy of the electrons). This resistive heating leads to a larger “effective” heating of the tip and a much larger evaporation event than expected for the laser energy.

To minimize the possibility of a major evaporation event, either the nanowire can be coated with another material which better matches the work function of the particle or a much larger diameter nanowire can be used which will be able to dissipate the resistive heat better than the smaller diameter nanowire tips. To minimize the complexity of the reconstructed nanowire, the larger diameter nanowires were attempted first. Figure 3.9 depicts the LEAP reconstruction of a large diameter tip nanowire. The top down image of the reconstruction further confirms the accuracy of the reconstruction as the square cross-section seen in the SEM images is reproduced. (Figure 3.9e) The TOFMS results confirm that VLS growth mechanisms as both La and B atoms were found to be dissolved inside the nanoparticle. Si was also found dissolved in the Pd particle to a very large extent. This is not all that surprising given that palladium silicides are formed at fairly low temperatures.¹³ (Figure 3.10) Si and Pd diffusion appear to occur only within a few nm of the particle wire interface, with no detectable Si or Pd in the bulk of the nanowire. (Figure 3.11 and 3.6) LEAP analysis was not able to be continued to a significant degree past the particle:wire interface as the nanowire would fracture once the interface was reached on every occasion. This is likely due to the previously mentioned Schottky barrier and a decreased particle:wire interface leading to a large resistive heating event or large simultaneous charge flow through the wire. Figure 3.12 are before and after TEM images of a nanowire used in LEAP analysis. Figure 3.12c shows what appears to be a solidified

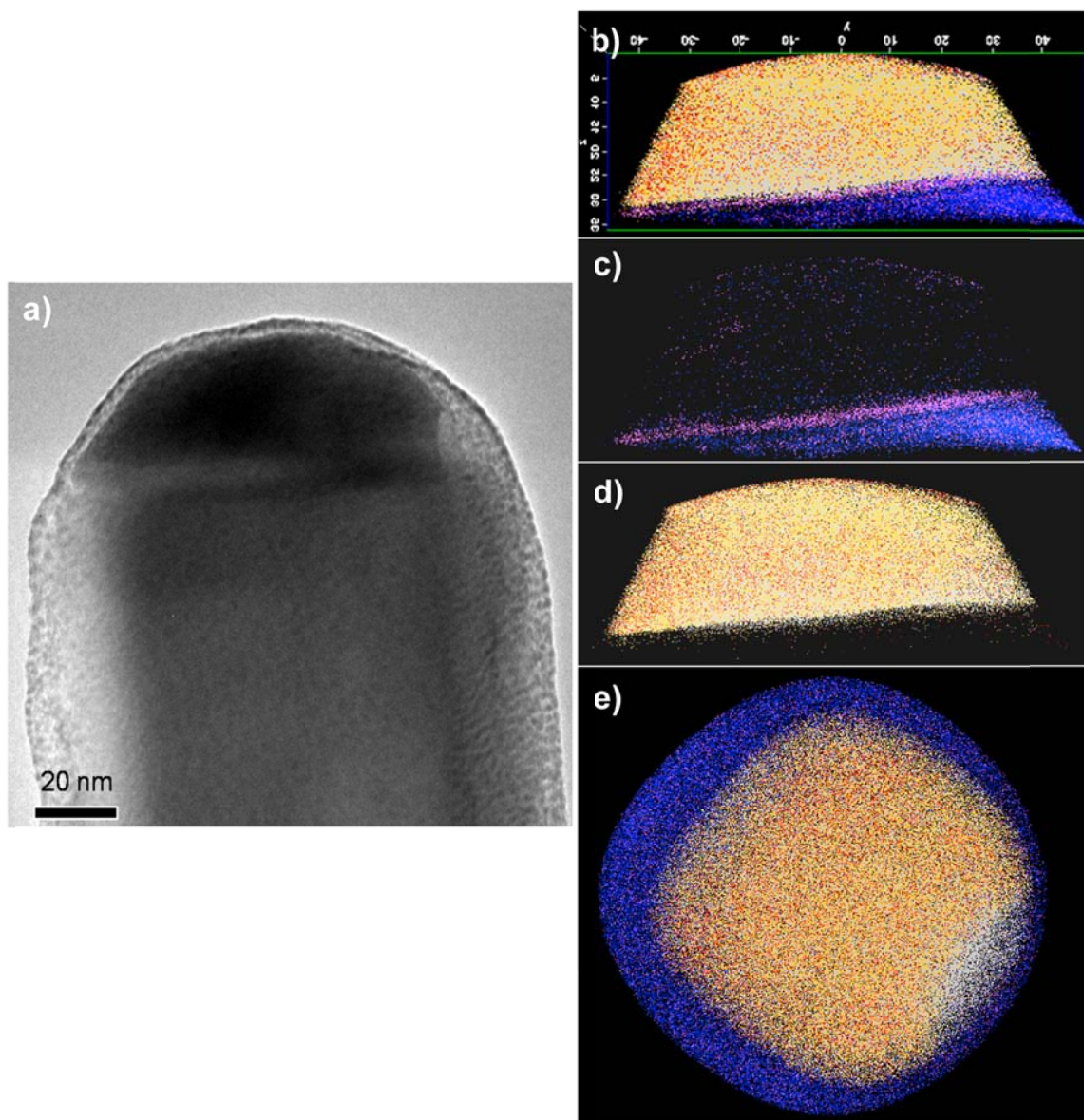


Figure 3.9 LEAP reconstruction of a LaB₆ nanowire catalyst particle. (a) TEM image of the nanowire before LEAP tomography. Reconstructions showing all the atoms (b), only La (pink) and B (blue) (c), and only Pd (yellow), Si (grey) and O (red) (d). (e) A top view of the tip showing rectangular cross-section of the wire.

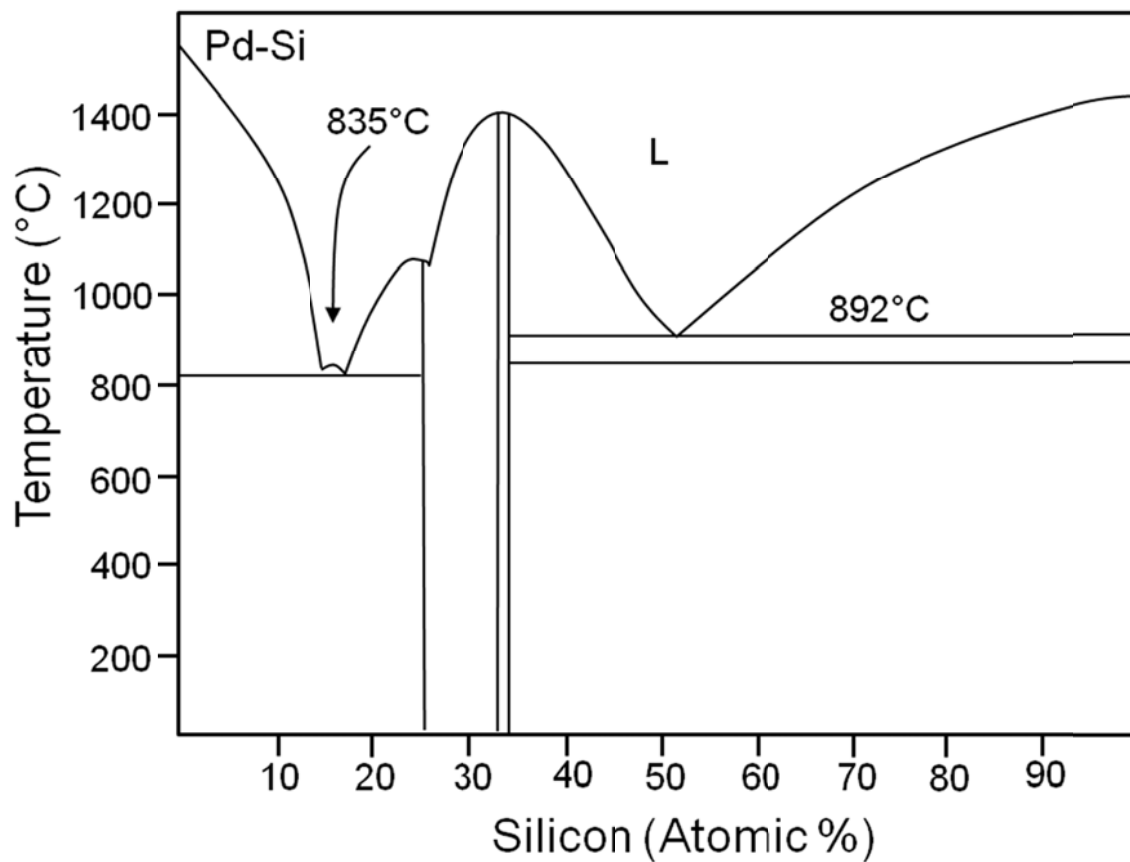


Figure 3.10 Pd-Si binary phase diagram.¹³

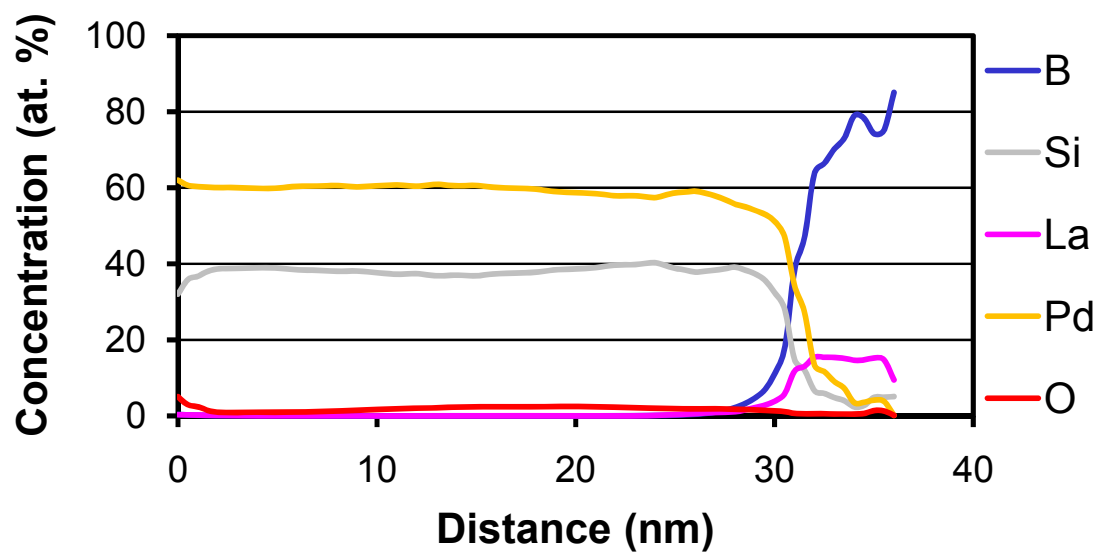


Figure 3.11 Z-direction concentration profile for the LEAP reconstructed LaB₆ catalyst particle.

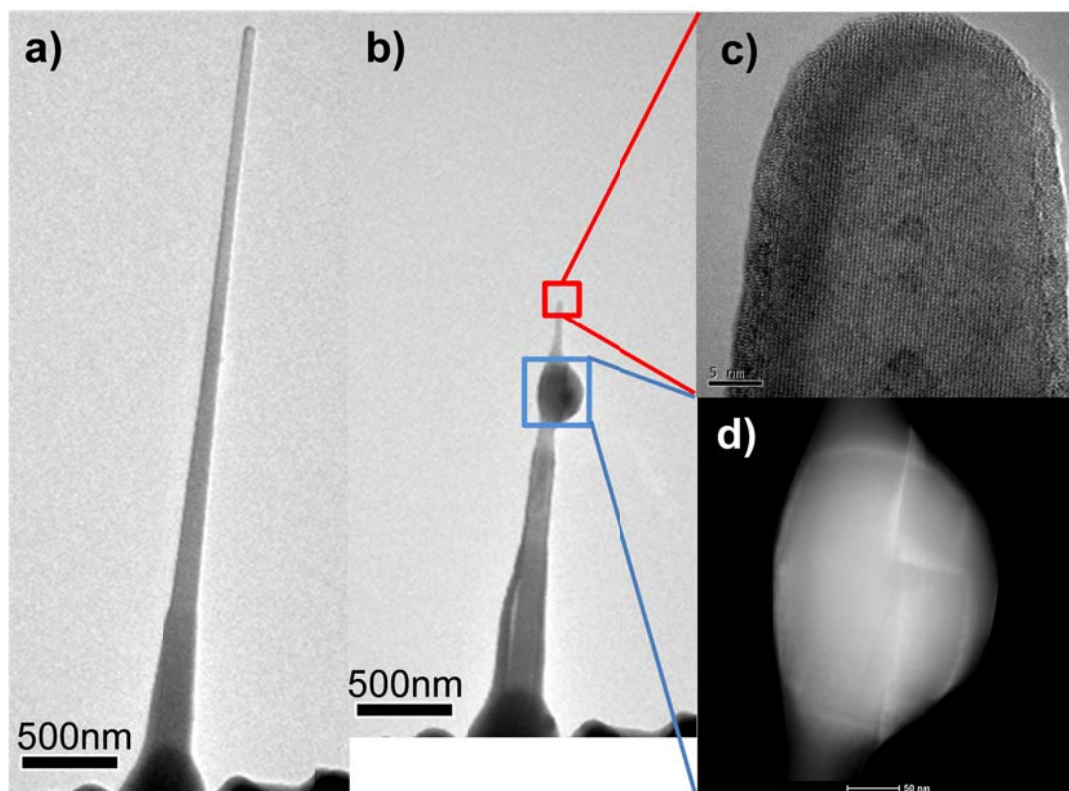


Figure 3.12 TEM images of a LaB₆ nanowire (a) before and (b) after the LEAP analysis. (c) HRTEM image of the tip (red square, top) showing its single crystal nature and cubic lattice structure. (d) High angle dark field image of the solidified melt (blue square, bottom) showing possible grain boundaries.

melt, likely caused by the local heating of the nanowire from the pulsed laser evaporation.

3.4 Y doped NdB_6

As mentioned in the introduction of chapter 2, REB_6 materials are nearly perfectly latticed matched across the entire RE group, making them extremely difficult to distinguish from one another crystallographically. (Table 2.1) Furthermore, dopant level addition of other RE species would not be detectable by EDX as several atomic percent is needed for accurate quantification. LEAP could be an extremely powerful analytical tool when analyzing doped nanowire species of the REB_6 nanowires due to its low detection levels (<100 ppm sensitivity), excellent mass/charge ratio separation abilities and its subnanometer 3D location resolution.

Yttrium doped NdB_6 nanowires were grown utilizing the previously mentioned CVD method outlined in chapter 2. In a typical experiment, .025 g YCl_3 was thoroughly mixed with 0.275 g NdCl_3 by mortar and pestle and loaded onto a quartz boat. The Si substrates were drop coated with Pd nanoparticles and placed down-stream from the salt. The furnace was ramped to 1000C and decaborane and argon were introduced at 0.75scm and 10 scm respectively. Figure 3.13 is atypical SEM image of the as synthesized $\text{Nd}_x\text{Y}_{1-x}\text{B}_6$ nanowires. Figure 3.14 are TEM images of (a) the small diameter doped nanowire and (b) large diameter doped nanowire. The dark particle at the tip of the nanowires indicates the materials are capped by a nanoparticle and most appear to be single crystalline. Small diameter nanowires exhibited the expected (100) growth direction while the large diameters nanowires appear to have a crystal plane in the center

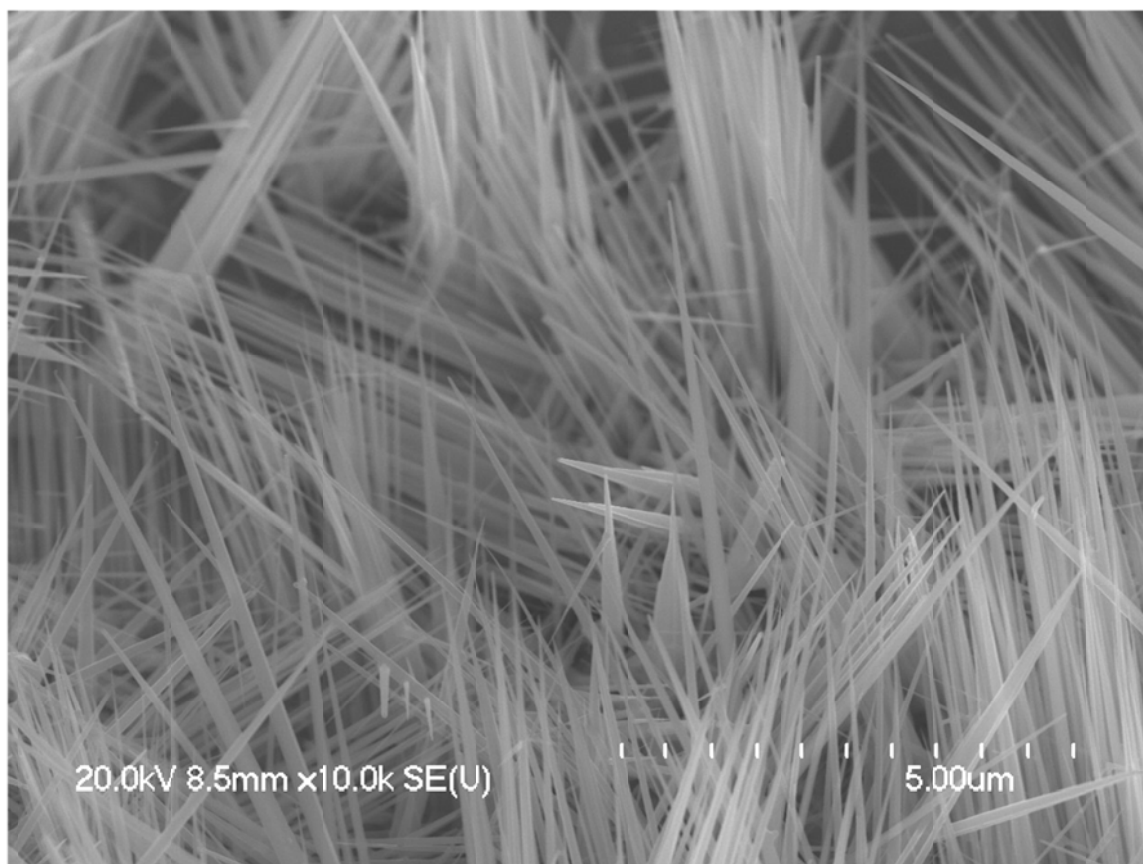


Figure 3.13 Typical SEM image of Y doped NdB₆ nanowires.

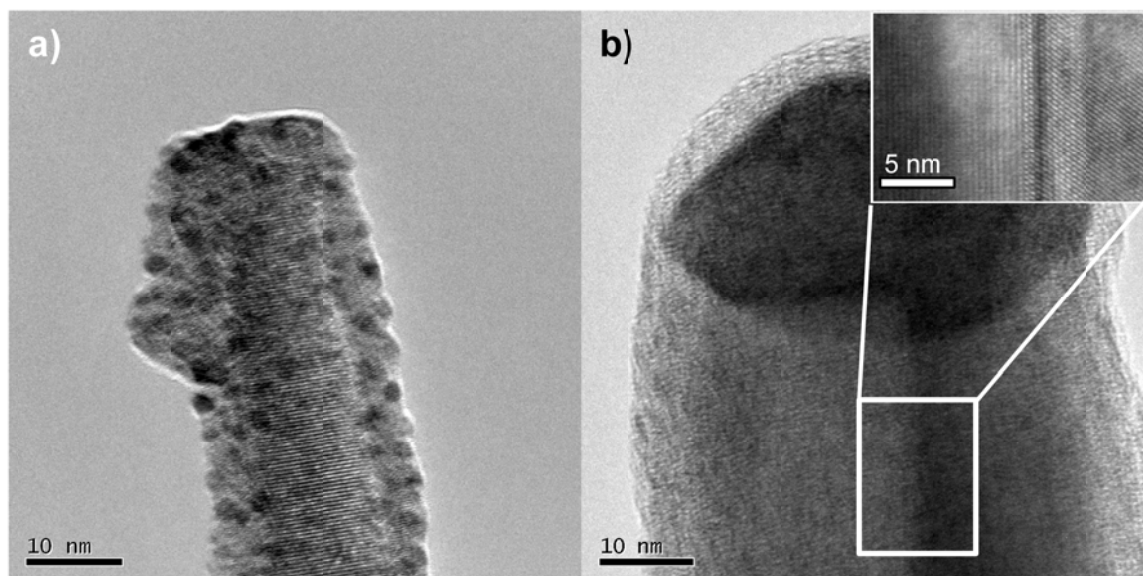


Figure 3.14 Typical TEM images of (a) small diameter and (b) large diameter Y doped NdB_6 nanowires. Inset in (b) is the post LEAP analysis of the dark line showing crystal plane and two different growth directions. Note that the black particles in (a) are likely to be Pt or PtC particles deposited from the FIB welding process.

of the nanowire. EDX analysis was unable to confirm the presence of Y in the nanowires, suggesting that either Y did not incorporate or it was present only to a very small extent. The latter was assumed as this crystal plane phenomenon was never seen in any of the undoped nanowire growth trials.

Figure 3.15 shows the LEAP analysis of the small diameter and large diameter doped nanowires. It can be seen that Y does indeed exist in the as synthesized nanowire, and the distribution is uniform along the length of the nanowire. However, there also appears to be a lateral concentration gradient in both the small diameter nanowire and large diameter nanowire (a and c). Figure 3.15c shows an isosurface which clearly show a lateral concentration gradient. A top down view (inset c) shows that the concentration is highest at an apex. Analysis of several nanowire systems shows that the highest concentration regions occur on both the nanowire face and apex. Figure 3.16 is possible graphical explanation of the observed results on a nanowire with high apex dopant concentration. Since the concentration of Y in both wires is very similar, it may be inferred that the large diameter nanowire with the crystal plane was formed by the intergrowth to two separate nanowires early on in the growth process. (Figure 3.12a) The lateral distribution of the Y can be explained by the VS solid deposition that occurs when the wires are grown in specific regions of the furnace. Since the substrates are placed horizontally in the furnace instead of vertically, the nanowires themselves can cause a shadowing effect on the VS growth on one of the sides of the nanowire.

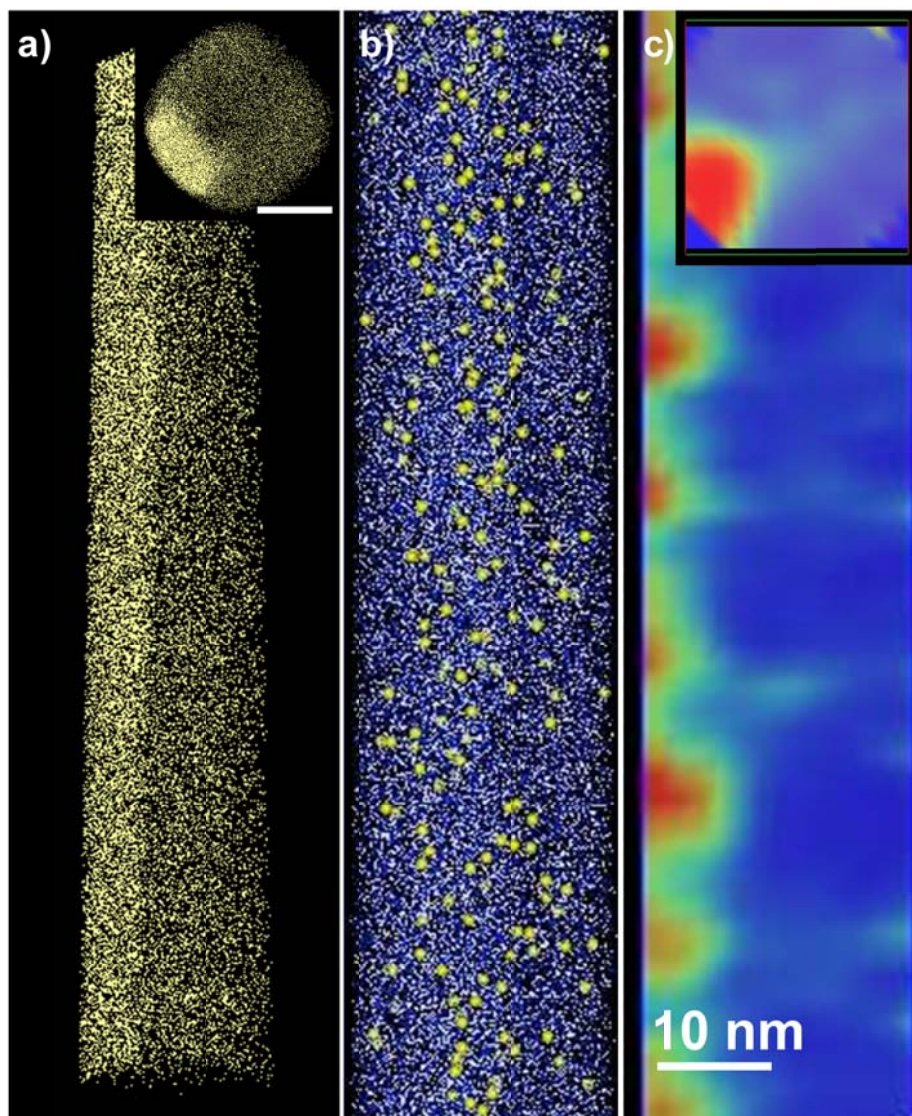


Figure 3.15 LEAP reconstruction of Y doped NdB_6 nanowires. (a) Y only reconstruction showing the lateral concentration gradient of small diameter nanowire. Inset is top-down view showing high face concentration (scale bar 10 nm). (b) and (c) Large diameter Y doped NdB_6 showing the vertical uniformity of the Y incorporation and isosurface showing lateral gradient. Inset in (c) is the top down view showing the high apex concentration of Y.

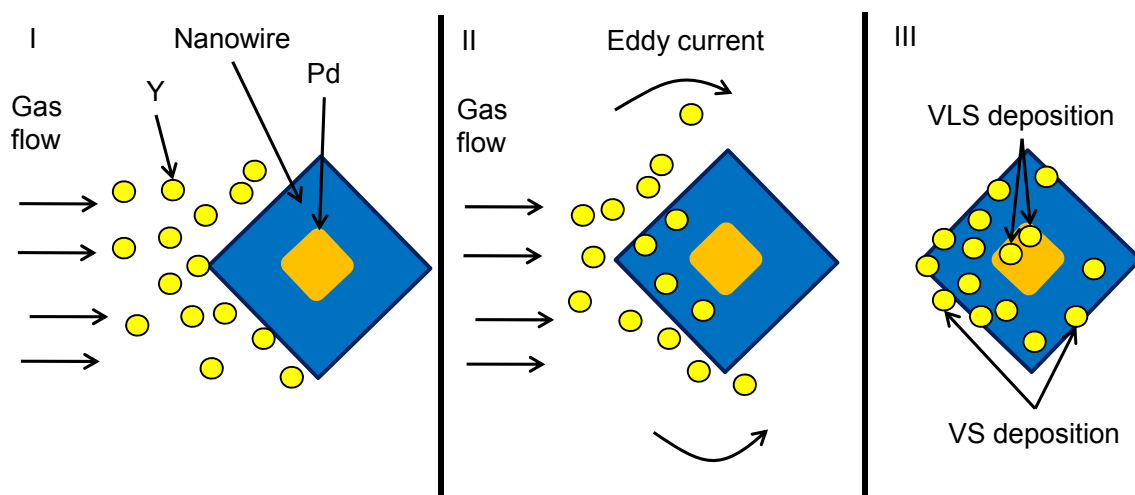


Figure 3.16 Top view schematic of a possible mechanism for dopant incorporation into the hexaboride nanowires. (I) Y atoms approaching the nanostructure, (II) the Y atoms begin depositing on the surface of the structure with eddy currents helping to deposit a small amount of material at the backside of the structure and (III) Y is also incorporated into the nanostructure by VLS.

3.5 Conclusions

LEAP tomography was successfully used to identify the chemical composition of the as-synthesized REB_6 nanowires. The developed TEM enhanced LEAP technique proved an effective method for analyzing nanomaterials which could not be easily grown well separated or oriented for the substrate surface. Furthermore, the TEM enhanced technique provided ideal structural images and z-contrast that greatly improved the accuracy of the reconstruction process. By combining the TEM and LEAP technique, the crystallographic properties were accurately deduced and matched with the compositional data from the LEAP analysis. Further improvements in the materials preparation are still needed, however, to fully understand the interfacial chemistry of the nanowires and the catalyst particle.

3.6 References

1. Kelly, T.F., Camus, P.P., Larson, D.J., Holzman, L.M. & Bajikar, S.S. On the many advantages of local-electrode atom probes. *Ultramicroscopy* **62**, 29-42 (1996).
2. Kelly, T.F. & Larson, D.J. Local electrode atom probes. *Mater. Charact.* **44**, 59-85.
3. Kelly, T.F., Larson, D.J., Thompson, K., Alvis, R.L., Bunton, J.H., Olson, J.D. & Gorman, B.P. Atom probe tomography of electronic materials. *Annu. Rev. Mater. Res.* **37**, 681-727 (2007).
4. Kelly, T.F. & Miller, M.K. Invited Review Article: Atom probe tomography. *Rev. Sci. Instrum.* **78**, 031101-20 (2007).
5. Miller, M.K. & Forbes, R.G. Atom probe tomography. *Mater. Charact.* **60**, 461-469 (2009).
6. Seidman, D.N. & Stiller, K. An atom-probe tomography primer. *MRS Bull.* **34**, 717-724 (2009).
7. Thompson, K., Booske, J.H., Larson, D.J. & Kelly, T.F. Three-dimensional atom mapping of dopants in Si nanostructures. *Appl. Phys. Lett.* **87**, 052108-3 (2005).
8. Seidman, D.N. Three-dimensional atom-probe tomography: Advances and applications. *Annu. Rev. Mater. Res.* **37**, 127-158 (2007).
9. Perea, D.E., Allen, J.E., May, S.J., Wessels, B.W., Seidman, D.N. & Lauhon, L.J. Three-dimensional nanoscale composition mapping of semiconductor nanowires. *Nano Lett.* **6**, 181-185 (2005).

10. Allen, J.E., Hemesath, E.R., Perea, D.E., Lensch-Falk, J.L., LiZ.Y, Yin, F., Gass, M.H., Wang, P., Bleloch, A.L., Palmer, R.E. & Lauhon, L.J. High-resolution detection of Au catalyst atoms in Si nanowires. *Nat. Nanotechnol.* **3**, 168-173 (2008).
11. Perea, D.E., Lensch, J.L., May, S.J., Wessels, B.W. & Lauhon, L.J. Composition analysis of single semiconductor nanowires using pulsed-laser atom probe tomography. *Appl. Phys. A-Mater.* **85**, 271-275 (2006).
12. Perea, D.E., Hemesath, E.R., Schwalbach, E.J., Lensch-Falk, J.L., Voorhees, P.W. & Lauhon, L.J. Direct measurement of dopant distribution in an individual vapour-liquid-solid nanowire. *Nat. Nanotechnol.* **4**, 315-319 (2009).
13. Massalski, T.B. & International, A.S.M. Binary alloy phase diagrams (ASM International, Materials Park, Ohio, 1990).

Chapter 4

Applications of REB₆ nanostructures: Electron emitters and electrode nanoprobes

4.1 REB₆ nanostructures as electron emitters

4.1.1 Introduction

The major applications in the past 50 to 60 years have been in vacuum microelectronics as electron emitting materials due to 1) their low work-function, 2) their extremely high melting points (>2000 °C), 3) their low vapor pressures at elevated temperatures, 4) their resistant to oxidation in air up to 400°C and 5) their metallic conductivity.^{1, 2} CeB₆ and LaB₆ had wide spread use as cathodes for CRT televisions, traveling wave tubes, and electron sources in electron microscopes for several decades.³ However, as device designs began to shrink and a need for decreased power consumption became a major concern, REB₆ materials synthesis was not able to maintain pace with the dimension reduction. Only until nanomaterials were being implemented in new vacuum electronic applications was the synthesis of REB₆ materials revisited. The resurgence in interest was fueled by the pursuit of a better understanding of both thermionic emission and field emission processes at the nanoscale.

Thermionic emission is in general, considered a classical phenomenon in which an electron in the Fermi level is provided enough thermal energy to overcome the work function of the material and ejected into a vacuum. (Figure 4.1) This mechanism was described by Richardson and Dushman mathematically by:

$$J(T) = A_R T^2 e^{-\phi/k_b T} \quad (4.1)$$

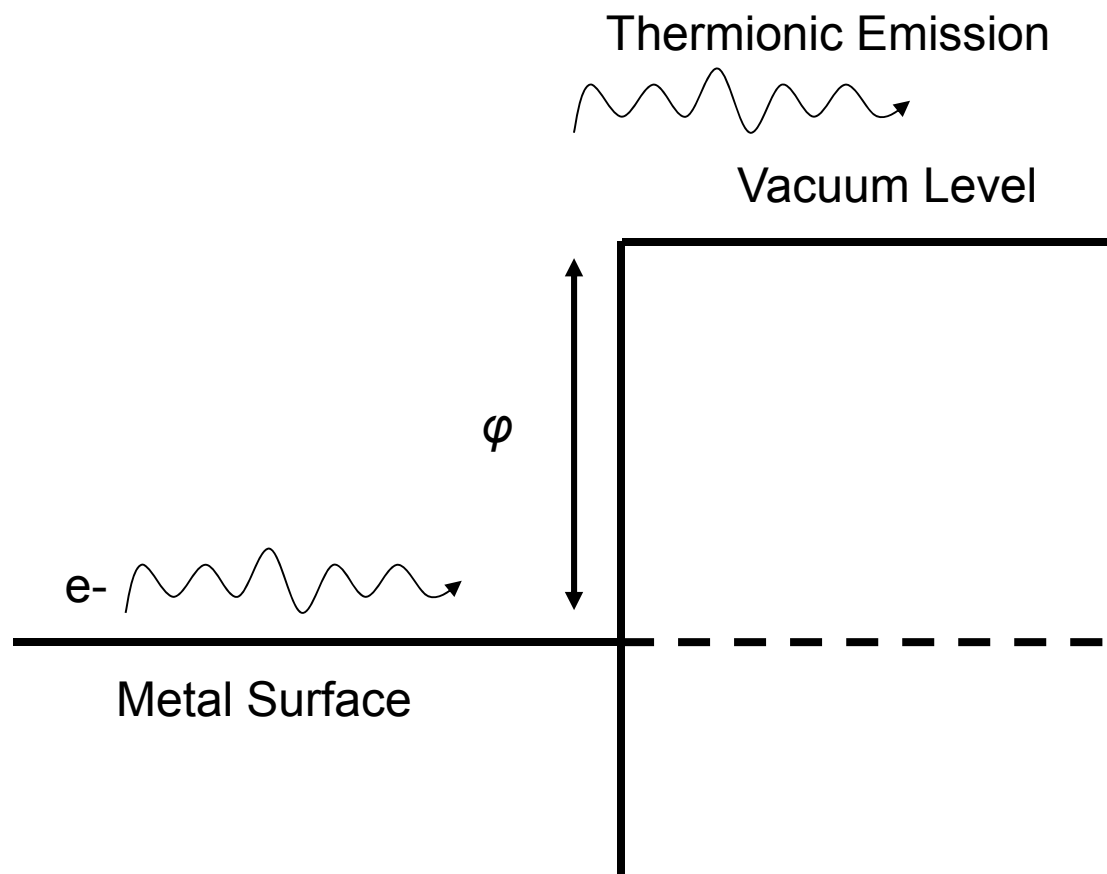


Figure 4.1 Schematic illustrating the principle of thermionic emission. An electron traveling normal to the metal's surface must be supplied enough energy, in the form of thermal heating, to overcome the work function, ϕ , and escape into the vacuum.

where T is the emitter temperature, A_R is the Richardson constant and k_B is the Boltzmann constant.⁴⁻⁷ The major problems associated with this type of electron emission are that it typically requires very high temperatures (>1000 °C) and ultra-high vacuum conditions, $\sim 1 \times 10^{-9}$ Torr or lower.

To circumvent the need for extremely high temperatures, scientists apply external electric fields to increase the electron emission by several orders of magnitude without the need for heating. This phenomenon was termed “field emission”. Field emission is a quantum mechanical phenomenon analogous to quantum tunneling. Under the influence of an external electric field, the potential energy barrier is distorted in such a manner that the Fermi level electrons of the emitting material can tunnel through the potential energy barrier (a classically forbidden region) and be ejected into the vacuum. (Figure 4.2) This emission process was proposed by Fowler and Nordheim in 1927 and was described by the equation:

$$I = 6.2 \times 10^{-6} \frac{\mu^{1/2}}{(\chi + \mu)\chi^{1/2}} \times (F)^2 \times \exp\left(\frac{-2.1 \times 10^8 \times \chi^{3/2}}{F}\right) \quad (4.2)$$

where I is the current density of the emitter in amperes per square centimeter, μ is the electron distribution in the Fermi-Dirac statistics which is equivalent to the thermodynamic partial potential of an electron (given in volts), χ is the thermionic work function in volts, and F is the applied electric field and is given in volts per centimeter.⁸⁻¹³

Due to the enormous body of work available on field emission, the complete derivation of the above equation will not be discussed.^{5, 7-13} There are, however, numerous modifications to the equation, but it is sufficiently important to mention that, with respect to nanomaterials, F is typically given by $\beta = (V/d)$. In this case, β is known as the electric field enhancement factor associated with the height and tip diameter of the

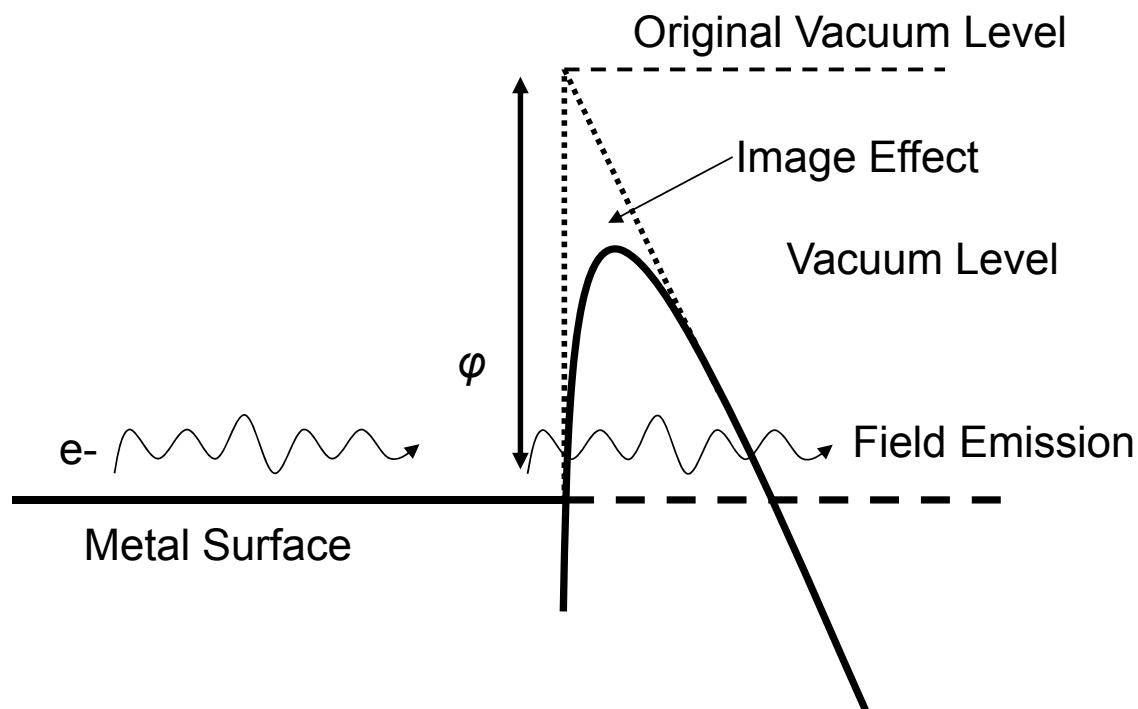


Figure 4.2 Schematic illustrating the field emission phenomenon. An applied external electric field leads to the folding down of the potential energy barrier. The image effect leads to a further decrease in the potential energy barrier by rounding off the top of the potential energy. The folding of the potential energy barrier allows for an electron traveling normal to a metal's surface to tunnel through a classically forbidden region and into the vacuum level.

nanostructure (aspect ratio), V is the applied voltage and d is the anode cathode separation distance. More generally, the current density, I , from an emitting surface is governed by several simple, and in theory, easily measurable quantities; shape and size of the emitting surface (β), the work function of the emitter (ϕ), the applied voltage (V) and the anode-cathode separation distance (d).

Based on the findings of the Fowler-Nordheim equation, there exist two sets of adjustable parameters: 1) d and V , which are device design dependent parameters and 2) ϕ and β , which are material-dependent parameters. The method of increasing the efficiency of an emitter that provides the most scientific merit is to optimize β and ϕ for a given material. Optimal values for β and ϕ are dependent on the specific application of the device; 1) large current densities, 2) small energy spread of the emitted electrons or 3) both. In general, materials should have a large β while simultaneously maintaining a small ϕ , with the former being more crucial than the latter.

Provided a large enough enhancement factor, a material can experience a phenomenon known as field penetration.⁶ Field penetration occurs when the work function of an emitting material is lowered due to a slight increase in the folding of the potential energy barrier. (Figure 4.2 and 4.3) This folding leads to a much larger change in the image effect. This leads to an increase in the thermionic emission component and a larger spread in the energy of the emitted electrons. For applications that purely rely on the number of electrons, such as cathode ray tubes or traveling wave tubes, the increase in energy spread is inconsequential. In applications such as electron beam in electron microscopy, the increase in energy spread of the electron beam can be detrimental because it leads to decreased resolution.

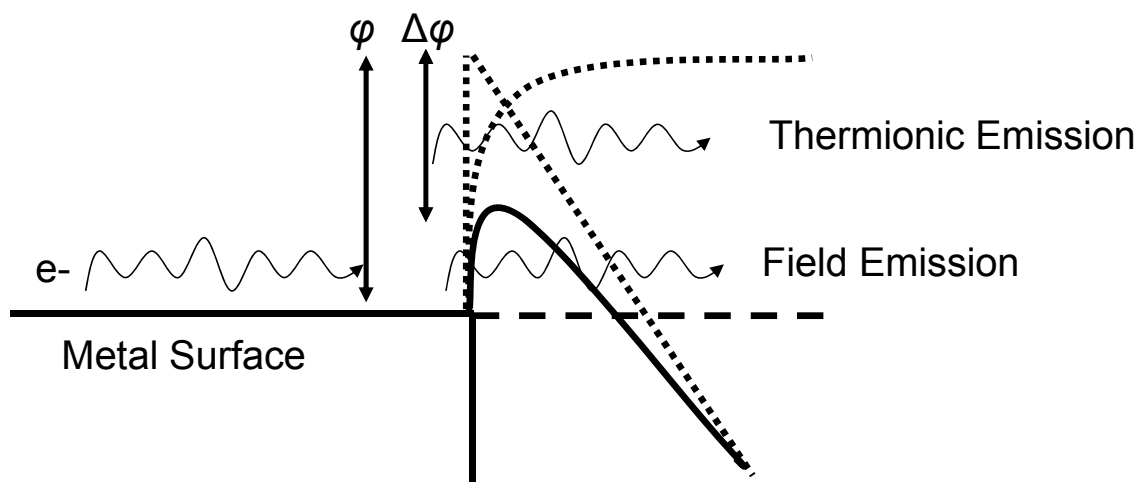


Figure 4.3 Schematic illustrating the lowering of the work function due to an increasing applied field. Because of field penetration into the material's surface and an increase in the image effect, electrons traveling normal to a materials surface now have enough energy to emit by tunneling through the potential energy barrier (field emission) or they can pass over the top of the potential energy barrier (thermionic emission).

Currently there are two bodies of research being conducted: 1) field emission of individual single crystalline nanowires grown by VLS and 2) emission from arrays synthesized by the self-catalyzed method.¹⁴⁻¹⁸ Though both have shown their respective materials are efficient field emitters; neither has studied the emission process with respect to optimization of the anode-cathode separation distance or substrate choice. Further information in these areas could be used to further improve the mathematical model of nanoscale electron emission.

4.1.2 Experimental methods

As-synthesized materials produced from the synthetic strategies developed in Chapter 2 were used in device fabrication. Figure 4.4 is a schematic of the “sandwich” design employed for emission properties testing. In general, the device is comprised of an anode (stainless steel), a cathode (REB₆ materials grown on a conductive substrate) and spacers (Teflon). A Keithley 2410 source meter was used apply the voltage to the anode and measure the current flowing from the cathode after the vacuum reached $\sim 10^{-7}$ Torr.

Several studies were conducted to optimize the emission process: 1) The relationship between the anode-cathode separation distance and turn-on voltage was investigated by varying the spacer height from 75 μm to 125 μm and 2) (100) Si and IBAD-deposited ZrN were compared to determine the relationship between emission efficiency and substrate used for growth of the LaB₆ nanowire arrays.

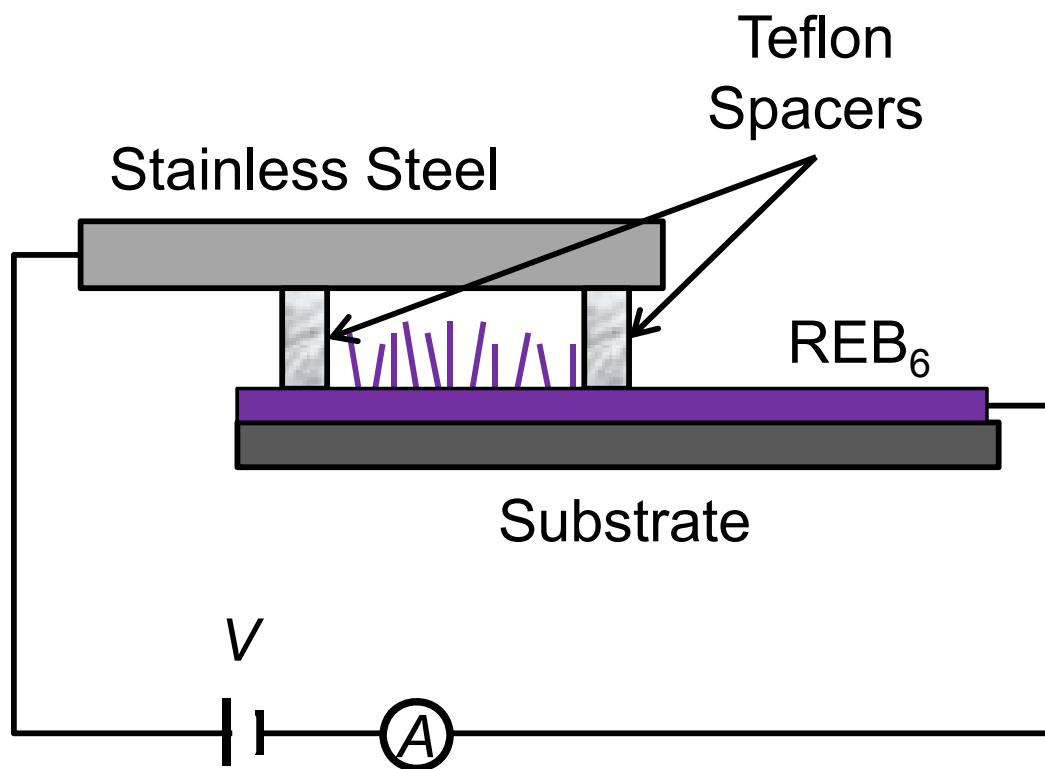


Figure 4.4 Schematic of REB₆ sample sandwich for field emission testing.

4.1.3 Results

Figure 4.5 is the typical emission data of LaB₆ nanowires grown on n-type (100) Si substrate (black) and IBAD-deposited ZrN substrate (red) at a working distance of 75 μm. The samples were normalized with respect to emission area and are plotted as current density versus the applied voltage. The LaB₆ materials synthesized on ZrN substrates produced more current per unit area than the LaB₆ materials synthesized on Si substrates. Several reasons could be contributing to this phenomenon: 1) as determined by XRD and SEM, the materials synthesized on ZrN have better alignment than materials synthesized on Si and 2) the density of the nanomaterials on the ZrN is more optimal than it is on the Si, producing less screening and therefore better field emission. SEM imaging determined the densities of the nanowires on both substrates appear to be very similar, implying that the likely cause of the improved emission is due to the improved orientation of the LaB₆ nanowires.

The data was input into a Fowler-Nordheim (F-N) plot to determine the enhancement factor of the materials and validate the orientation hypothesis. (Figure 4.6) The F-N plot was constructed from the SI unit based Fowler-Nordheim equation,

$$\frac{I}{A} = \frac{1.5 \times 10^{-6}}{\phi} \times \left(\frac{V}{d}\right)^2 \times \beta^2 \times \text{EXP}\left(\frac{10.4}{\phi} - \frac{6.44 \times 10^9 \times \phi^{1.5} \times d}{\beta \times V}\right) \quad (4.3)$$

where (I/A) is equal to the current density, J . When the field emission data is plotted as (J/V^2) versus $(1/V)$, the slope, k , of the F-N plot is given by:

$$k = \frac{-6.44 \times 10^9 \times \phi^{1.5} \times d}{\beta} \quad (4.4)$$

By substituting in the anode-cathode separation distance, d , the work function of the emitter, ϕ , and the slope, the enhancement factor can be determined.

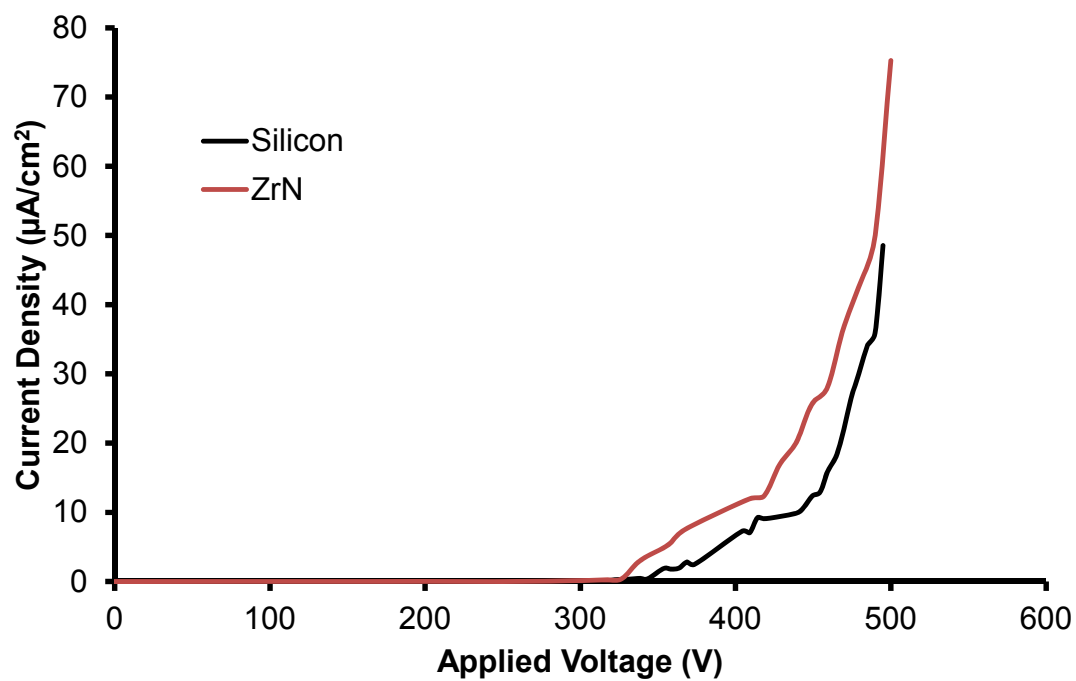


Figure 4.5 Field emission curves normalized to emission area for LaB₆ nanowire arrays grown on (100) Si (black) and IBAD-deposited ZrN (red) substrates at a 75- μm separation distance.

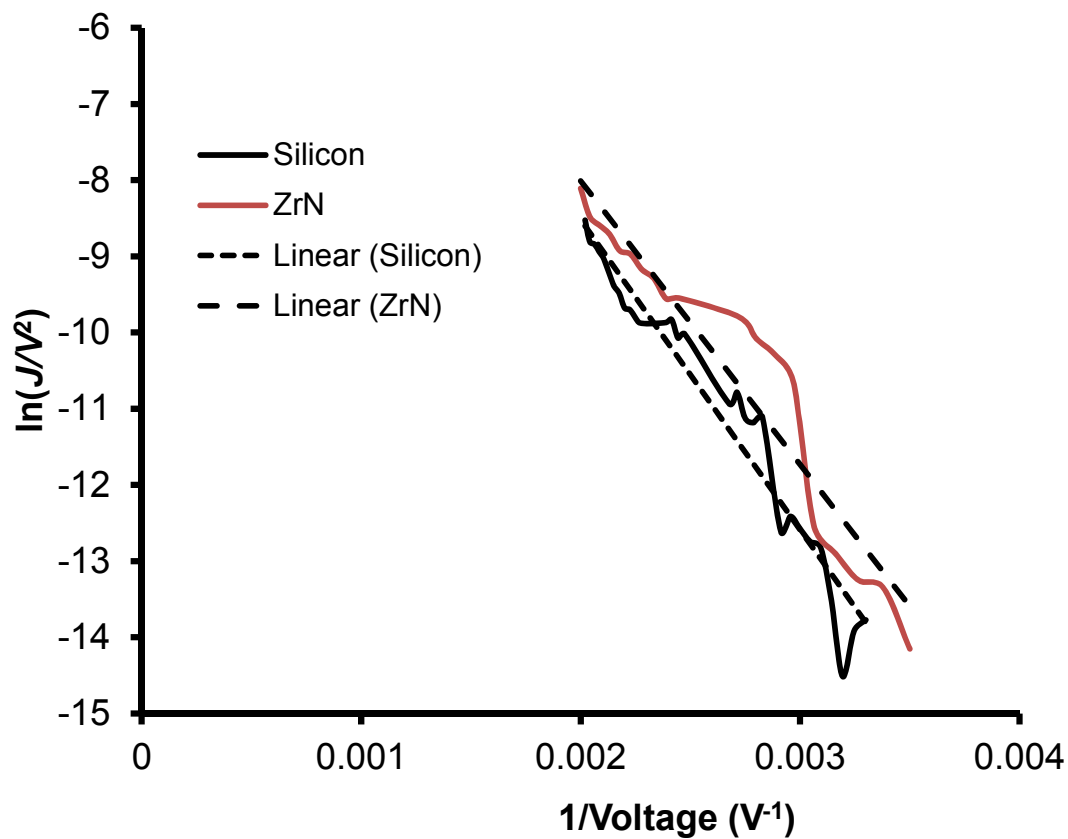


Figure 4.6 F-N plot normalized to emission area for LaB_6 nanowire arrays grown on (100) Si (black) and IBAD-deposited ZrN (red) substrates at a 75- μm separation distance.

Deviation from linearity was identified in the center of both of the F-N plots. This deviation is likely due to nanowire failure events occurring during the emission process, most probably caused by arcing due to the small working distance. The enhancement factors calculated from the F-N plots confirms that the LaB₆ grown on ZrN has a much larger enhancement factor, roughly 3 times, than the LaB₆ grown on Si: $\beta_{\text{ZrN}} = 1254$ while $\beta_{\text{Si}} = 515$. The increased orientation of the LaB₆ grown on ZrN likely leads to increased field penetration of the nanowire array and more efficient charge collection as the emitter is directed toward the anode.

The results of the varied anode cathode spacing are presented in Figure 4.7 and 4.8. Si substrates were used instead of the ZrN substrates for this study as there were difficulties in obtaining field emission from the LaB₆ grown on ZrN at the larger working distances. Figure 4.7 depicts the results of the field emission process normalized to the emission area only. As expected, the materials at the shorter working distance produce much more current at lower voltages than the materials at the larger working distance. However, when normalized for the working distance also and plotted as current density versus electric field, the emission at the larger working distance appears to be much more efficient. Furthermore, the maximum current density of the material also greatly increased with an increase in the working distance. At the 75- μm working distance, the sample would begin arcing considerably after about 500 V, thereby limiting the testing range of the sample.

The F-N plot of the samples is presented in Figure 4.9. The slope of the 125- μm is considerably shallower than that of the 75- μm sample. This indicates right away that there is an increase in the enhancement factor. From calculations, it was determined that

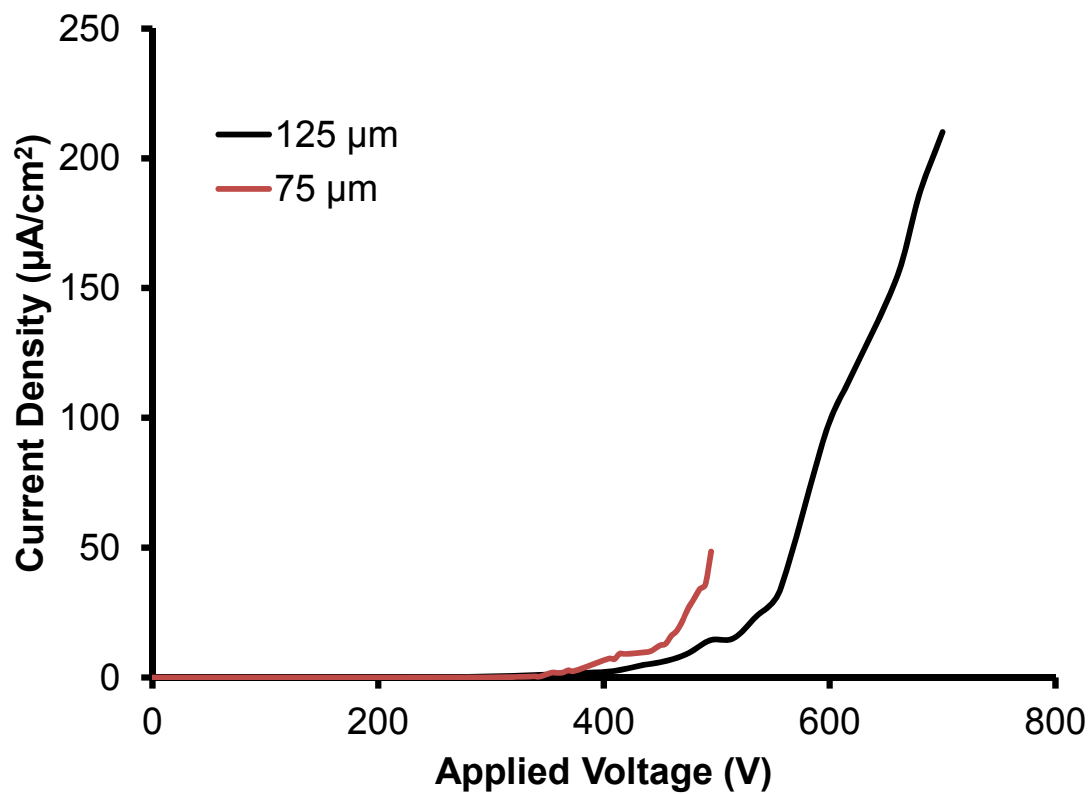


Figure 4.7 Field emission curves normalized to emission area for LaB₆ nanowire arrays grown on (100) Si substrates at 125 μm (black) and 75 μm (red).

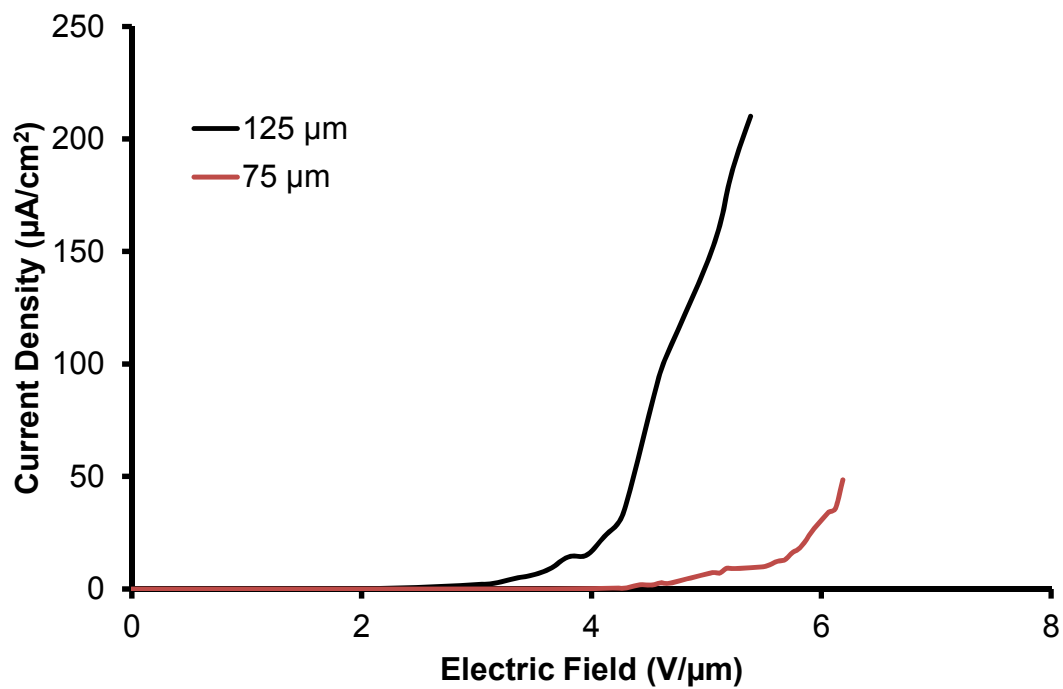


Figure 4.8 Field emission curves normalized to emission area and separation distance for LaB_6 nanowire arrays grown on (100) Si substrates at 125 μm (black) and 75 μm (red).

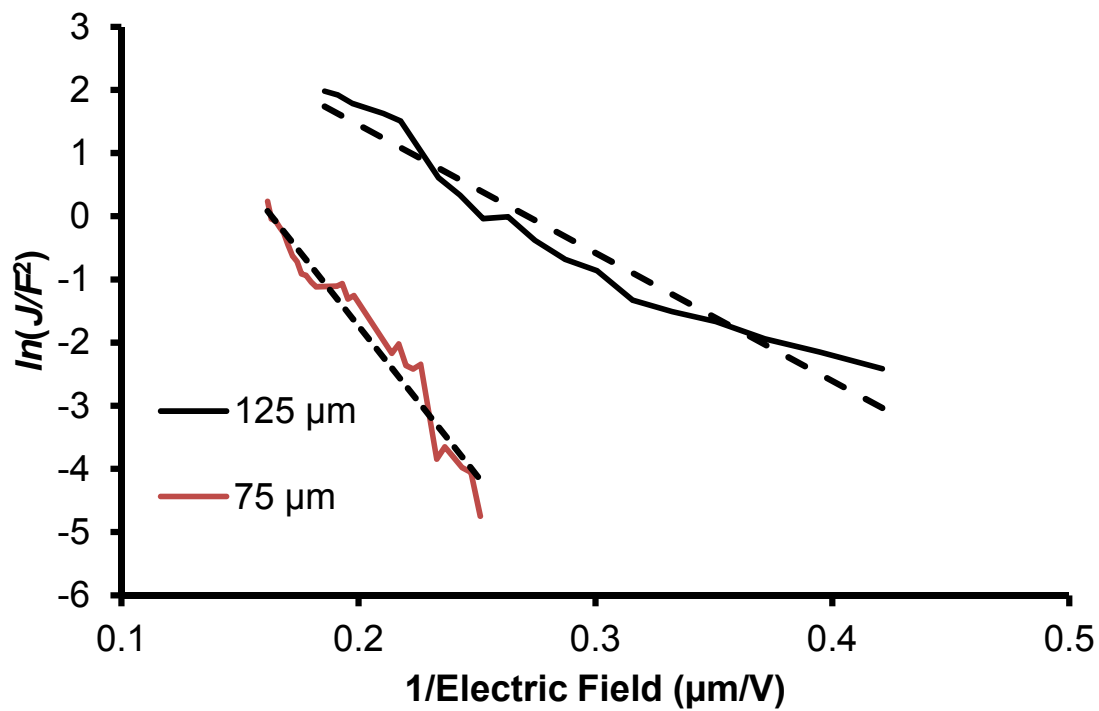


Figure 4.9 F-N plot normalized to emission area and separation distance for LaB_6 nanowire arrays grown on (100) Si substrates. 125 μm (black) and 75 μm (red) separation distances.

there was an increase of 3 times: $\beta_{125\mu\text{m}} = 1394$ and $\beta_{75\mu\text{m}} = 515$. This increase is probably due to an improvement in both electric field penetration and an increase in charge collection efficiency.

4.1.4 Conclusions

Field emission studies were conducted to optimize the anode-cathode separation distance and substrate choice for improving the electron emission properties of REB_6 nanowire arrays. By adjusting the separation distance, it was determined that though the field emission followed Folwer-Nordheim type behavior, it was much less efficient at smaller working distances. Furthermore, arcing is problematic at anode-cathode working distances less than $125\ \mu\text{m}$, which leads to increased emitter failure and large fluctuations in the emission current over time. Further decreasing the pressure in the system is the most likely solution to this issue, though with the currently available equipment it is not feasible and not overly practical for device applications. In varying the substrate used for growing the LaB_6 , it was found that the ZrN substrates allowed for more efficient electron emission at similar working distances than materials synthesized using Si substrates. It is most probable that the enhanced orientation of the LaB_6 , as discussed in Chapter 2, on the ZrN lead to much improved field penetration into the emitter array and the enhanced orientation also likely lead to improved charge collection.

4.2 REB_6 nanoobelisks as nanomanipulator probes

4.2.1 Introduction

Advanced development of high aspect ratio and small electrode probes is of significant importance in the electrical characterization of nanostructures and failure analysis of integrated circuits (IC) with shrinking device cells. The semiconductor

industry has passed another critical milestone along Moore's Law, the 32-nm node configuration. According to the International Technology Roadmap for Semiconductors (ITRS), the half distance between adjacent lines of DRAM memory cells is scheduled to shrink from 52 nm in 2009 to 22.5 nm in 2016.¹⁹ Such IC failure analysis is currently performed by physical contact at the electrodes of single and multiple cell or devices and probing their current conductance behavior using electrode nanoprobe equipped in a nanomanipulator under a scanning electron microscope.

The two major challenges in probing the nanoscale are 1) probing small contacts and 2) probing small geometries or simultaneously probing several adjacent nanoscale contacts within short distance from each other. There are major differences between microprobing to various forms of nanoprobe. At the 90-nm node, optical micro-probing fails in its capability to find non-visual failures. At 32-nm node configuration and below, the electrical contact pads made of either tungsten or copper become soft. This leads to shorting due to smearing by the probes. Moreover, the new geometric arrangement of contact pads requires the majority of the available tungsten probes to be sharper or thinner. The distance between neighboring contacts are so short that exceptionally precise control is absolutely required to maintain probe separations and their stability. To overcome these challenges and to accommodate the shrinking IC feature size by 2016, these nanoprobe have to be mechanically robust, highly conductive, but yet with diameters in the sub-40-nm diameter range or less and with high aspect ratio.

Currently, commercial sharp electrode nanoprobe are made of tungsten because it is a relatively inexpensive refractory metal. These probes generally have average diameters of 80 nanometers. While procedures to fabricate tungsten tips of diameters down to 40

nanometers are reported in the literature, sharp tungsten tips are prone to oxidation and formation of thick oxide layers at the tips if left under ambient conditions and not used right away. Low temperature oxidation of metals is commonly believed to be caused by the tunneling of electrons from the metal to the growing oxide layer to occupy the acceptor levels of oxygen molecules or atoms on the oxide surface.²⁰ This generates an electric field to promote the migration of metal cations or oxygen anions into or through the oxide to further the oxide growth. For a flat metal surface, the growth of oxide typically stops at thickness of a few nanometers at which the tunneling current diminishes rapidly. However, the oxide layers at sharp metal tips of high aspect ratio are typically much thicker than those of flat surfaces because of the enhanced electric field at the tips due to their high curvature.²¹ Hence, such sharp oxide coated probe tips would require an oxide etch step and an *in situ* resistive heating inside the vacuum chamber of a scanning electron microscope to remove all oxide before precise electrical measurements. These procedures are not only tedious but they also often lead to tips diameters above 50 nanometers which are undesirable for probing device cells down the ITRS road map. (Private communication with Mr. Taylor Cavanah, business manager at the probe manufacturer, Zyvex Instruments Division of DCG Systems (formerly Zyvex Instruments, LLC)) Platinum or platinum-iridium tips, while can be made with small tip diameters by electrochemical techniques, are generally too expensive and soft for the nanoprobng measurements with nanomanipulators.

Robust, high aspect ratio nanostructures with high electrical conductivity, high chemical stability, and well-defined sub-40 nm diameters are potential materials to create the next revolutionary nanoscale electrode probes. However, nanowire or nanotube

structures such as silicon carbide nanowires and carbon nanotubes are in general too flexible for robust physical contact probing when the geometry of these materials reaches smaller than 50 nm diameters and aspect ratios of 10 or more. Also, many semiconductor materials have considerable resistance at the nanoscale due to their high resistivities; further hindering their application toward this technology. The REB₆ nanostructures, such as nanoobelisks, presented previously are desirable probe materials because they are less prone to oxidation, the obelisk structure is not prone to flexing and the resistivity is generally on the order of $\mu\Omega\text{-cm}$ to tens of $\mu\Omega\text{-cm}$.

4.2.2 Experimental methods

4.2.2.1 Tungsten probe preparation

Tungsten probes were prepared by dc etching in a NaOH solution.^{22, 23} Typically, the W wire (99.99% from McMasterCarr, Robbinsville, NJ) was lowered in the solution and centered in a stainless steel counter electrode. (Figure 4.10) Applied voltage, NaOH concentration and etch time were varied from 3.5V to 8V and 2M to 3.5M and 5 min to 45 minutes, respectively, to optimize the tip diameter of the W tip to between 200-500 nm. After etching, W probes were then sonicated in 2M KOH solution for 1 minute and then etched by a 5% (by volume) HF solution prior to Pd deposition. Pd was electrochemically deposited by linear sweep voltametry using 0.5 M H₂SO₄ and 10mM PBS solutions, both of which were 1mM in K₂PdCl₄, and by direct deposition of Pd nanoparticles from solution (Pd particle from Chapter 2 were used). (Figure 4.11) The scan rate for the linear sweep voltametry was varied between 50mV/s to 1V/s to control the amount of Pd deposited on the W tips.

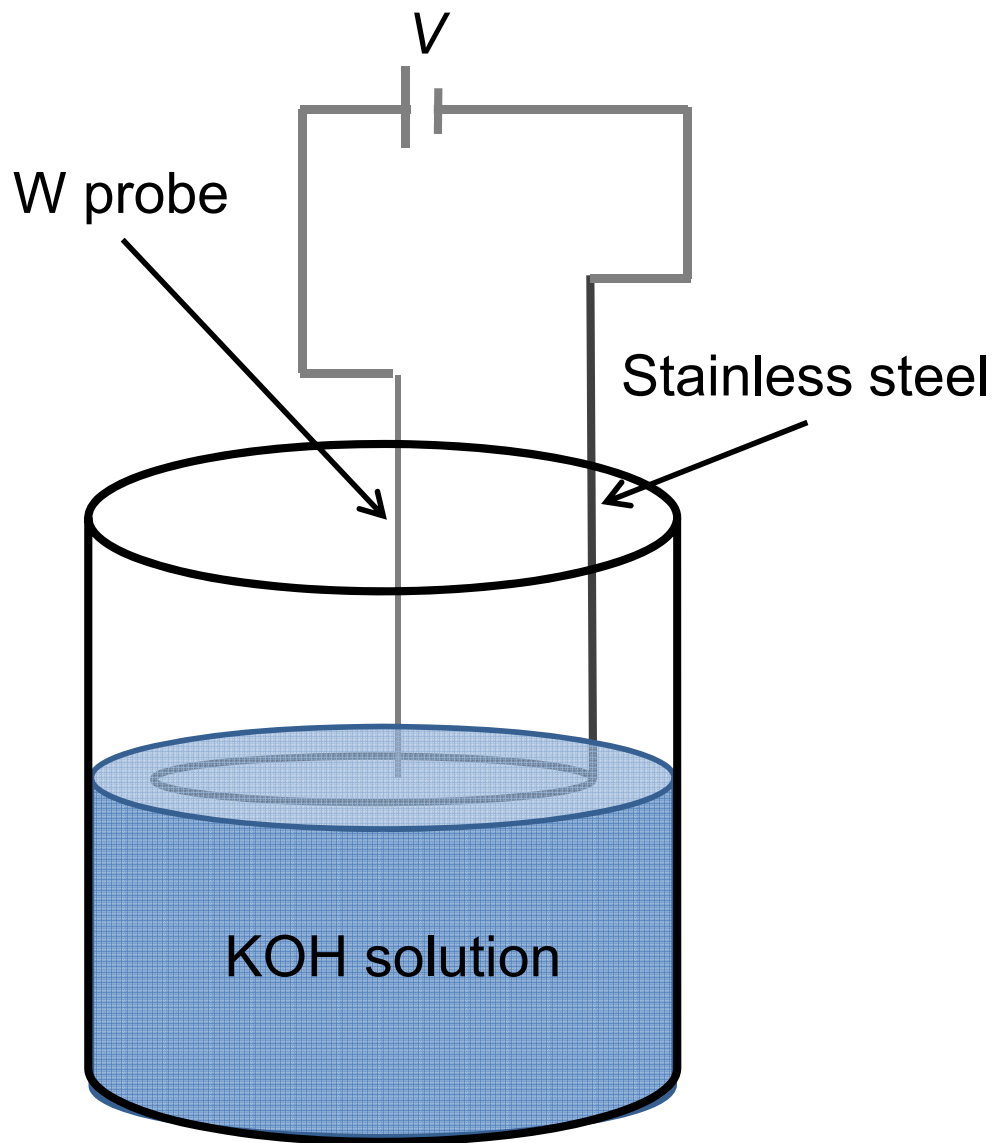


Figure 4.10 Schematic of the tungsten wire etching station. The tungsten probe is lowered into the center of the immersed stainless steel ring. Then a voltage is applied until the end of the tungsten wire falls off.

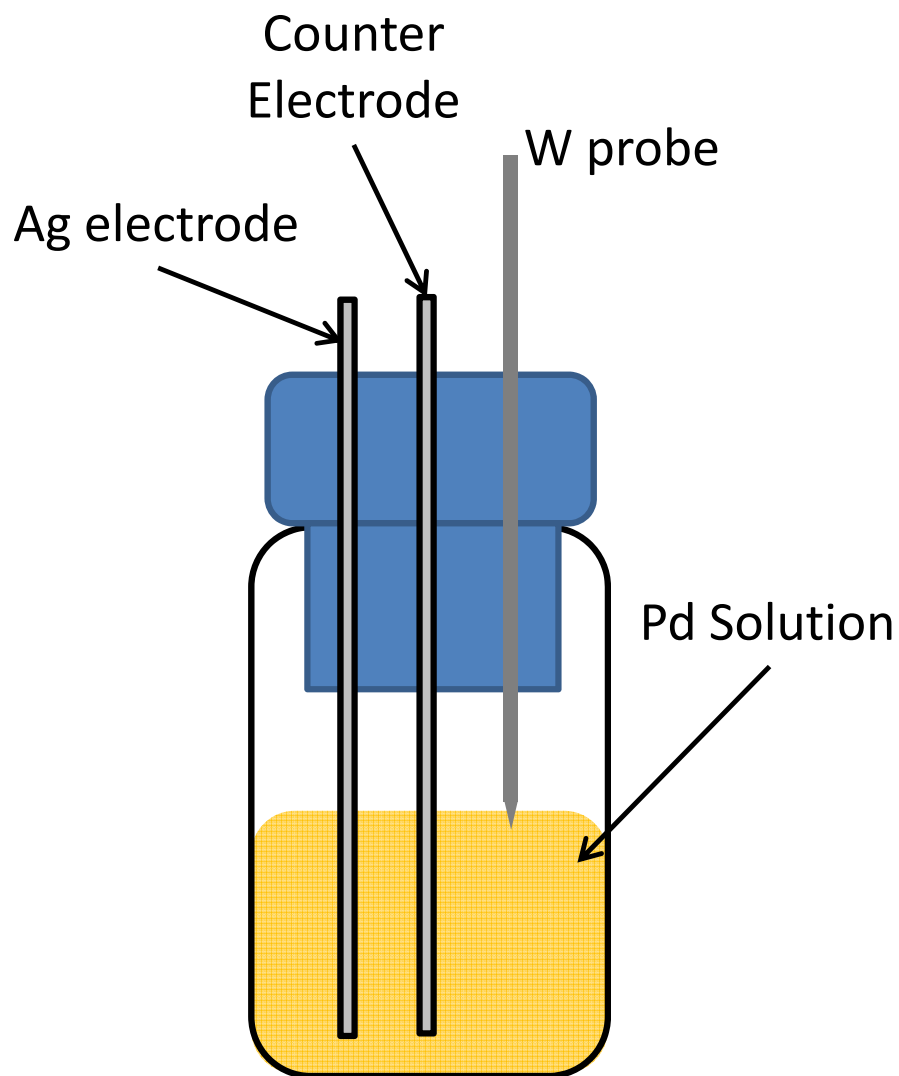


Figure 4.11 Schematic of the electrochemical used for the linear sweep voltammetry deposition of Pd.

4.2.2.2 REB₆ nanoobelisk growth

Synthetic conditions utilized in the growth of LaB₆ on the tips of the W probes are outlined in Chapter 2.^{24, 25} Since wire lengths necessary for use in the nanomanipulator are too long to fit vertically inside of the 1” tube furnace, a graphite rod was modified to mount the wires horizontally. (Figure 4.12)

4.2.3 Results

Tungsten probes were imaged in the SEM prior to Pd deposition. Figure 4.13 are some representative SEM images of the various probe shapes and dimensions achieved during the etching process. It was found that by applying a lower potential and using a 3M NaOH solution that the optimal diameter of about 200-500 nm can be routinely achieved. (Figure 4.13b) The linear sweep voltametry deposited Pd results are presented in Figure 4.14. Figure 4.14a is the deposition results using a large scan range and a 50mV/s scan rate. These conditions lead to a uniform coating of Pd over the entire immersed probe surface. Figure 4.14b are the results from a small scan range and a 1V/s scan rate showing the formation of isolated Pd clusters. Though the degree of coverage can be varied by adjusting the scan conditions, there appears to be no control over where the material is being deposited. This suggests that the deposition is not being effected by the enhanced electric field at the tip of the probe as was hoped.

Figure 4.15 are SEM images of the as-deposited probe tips. Figure 4.15a and c are zoom-out SEM image from the 50 mV/s scan rate and nanoparticle deposited Pd respectively. As expected, nanowire formation the W probe was non-specific to the tip and generally was located where Pd deposition has occurred. In Figure 4.15 a and b, though the Pd did not deposit locally at the tip, a single nanowire protruding from

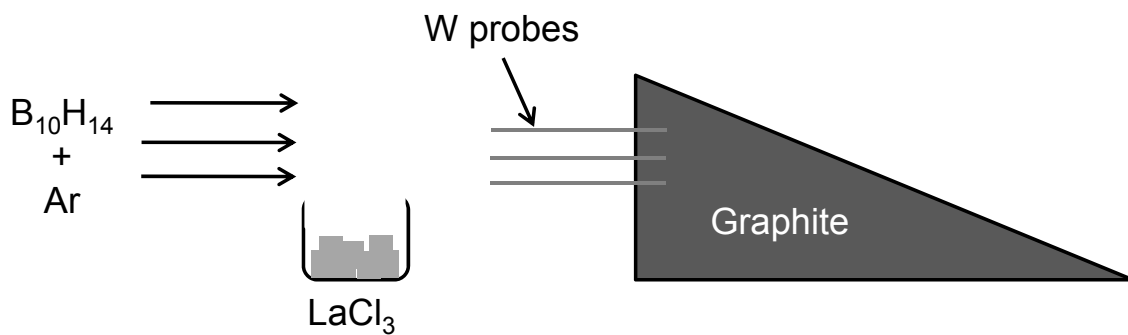


Figure 4.12 Schematic of the deposition modification used for probe deposition. Grey triangle is the graphite holder used to mount the probes horizontally.

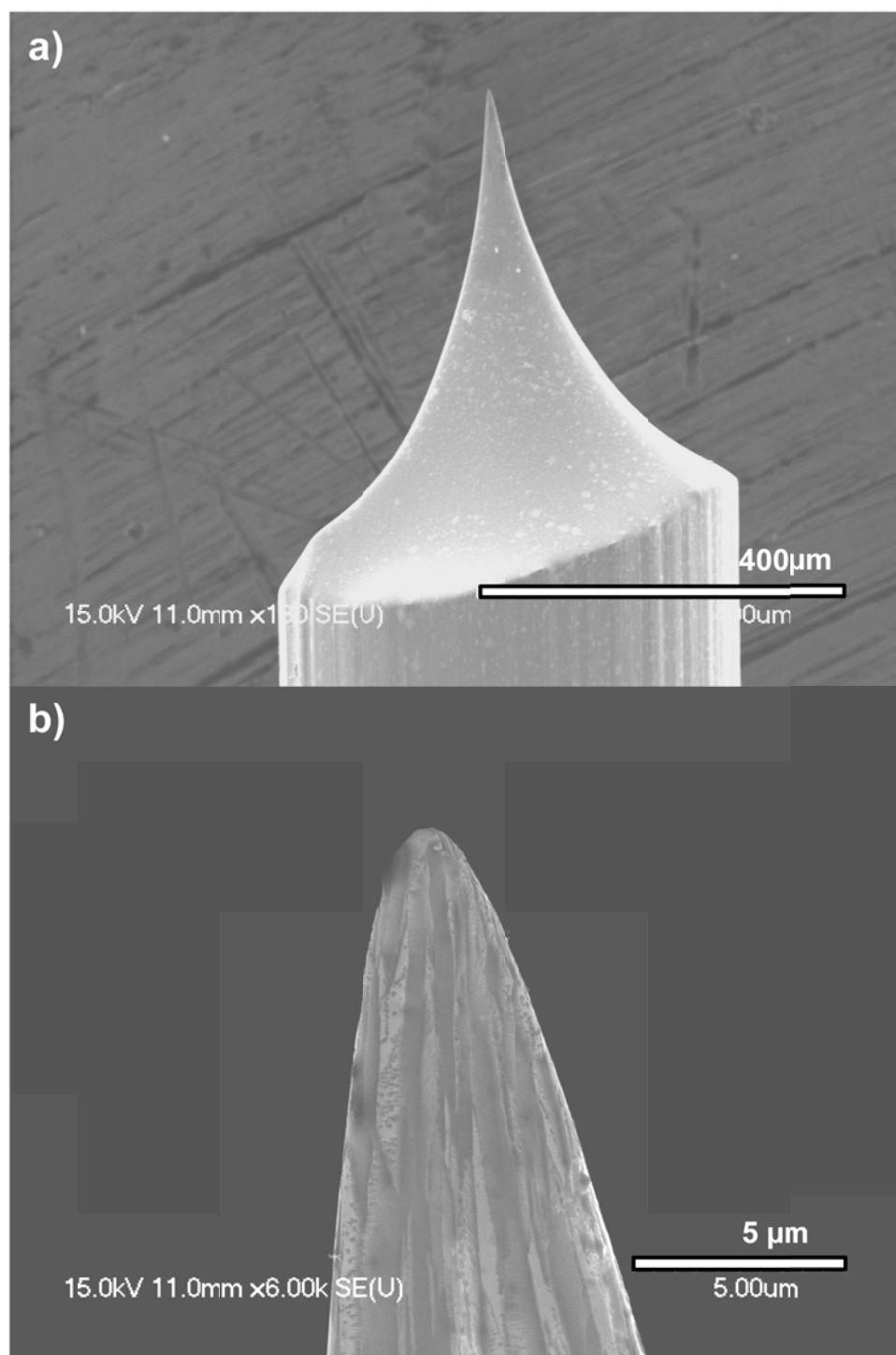


Figure 4.13 SEM images of NaOH etched W wires. a) zoom-out image of an etched probe and b) zoom-in image of the W probe tip.

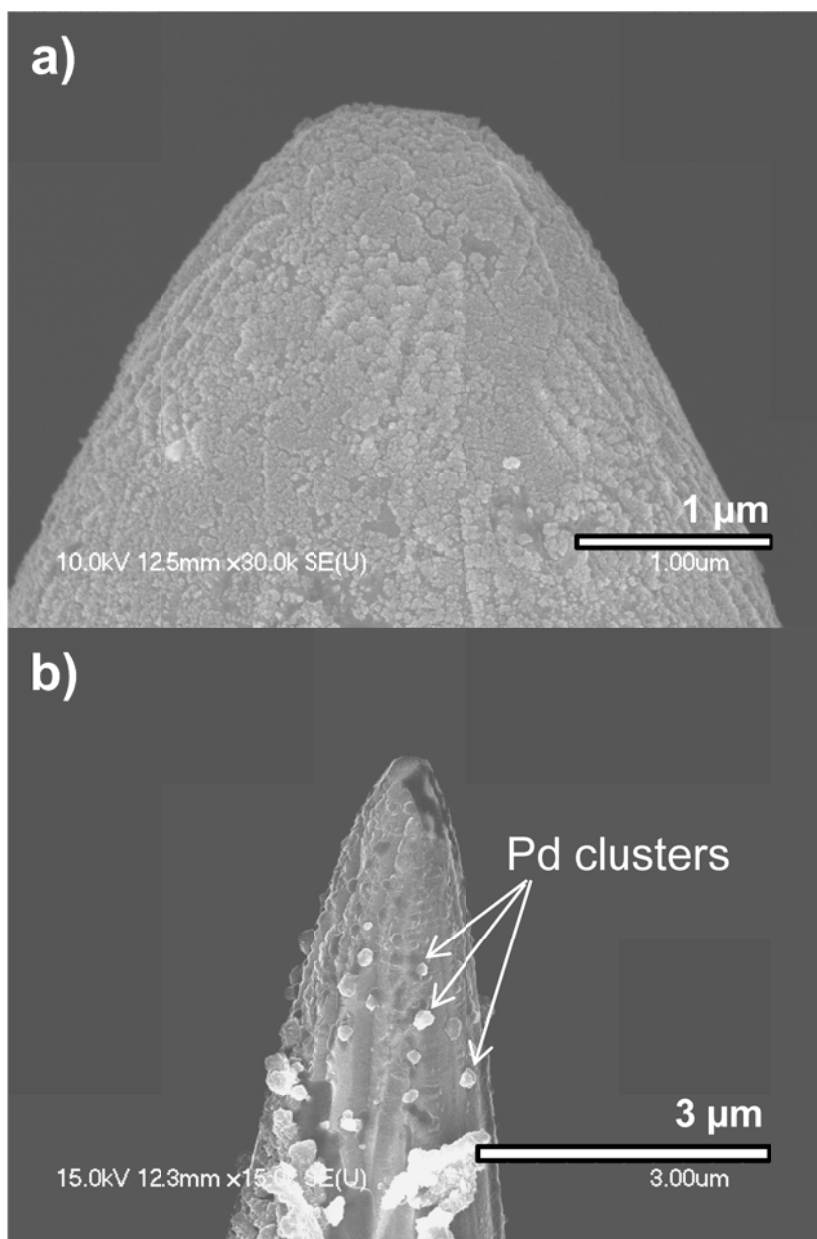


Figure 4.14 SEM images of linear sweep voltametry deposited Pd (H_2SO_4 solution) on W probes. a) 50 mV/s scan rate and b) 1V/s scan rate (indicated by white arrows).

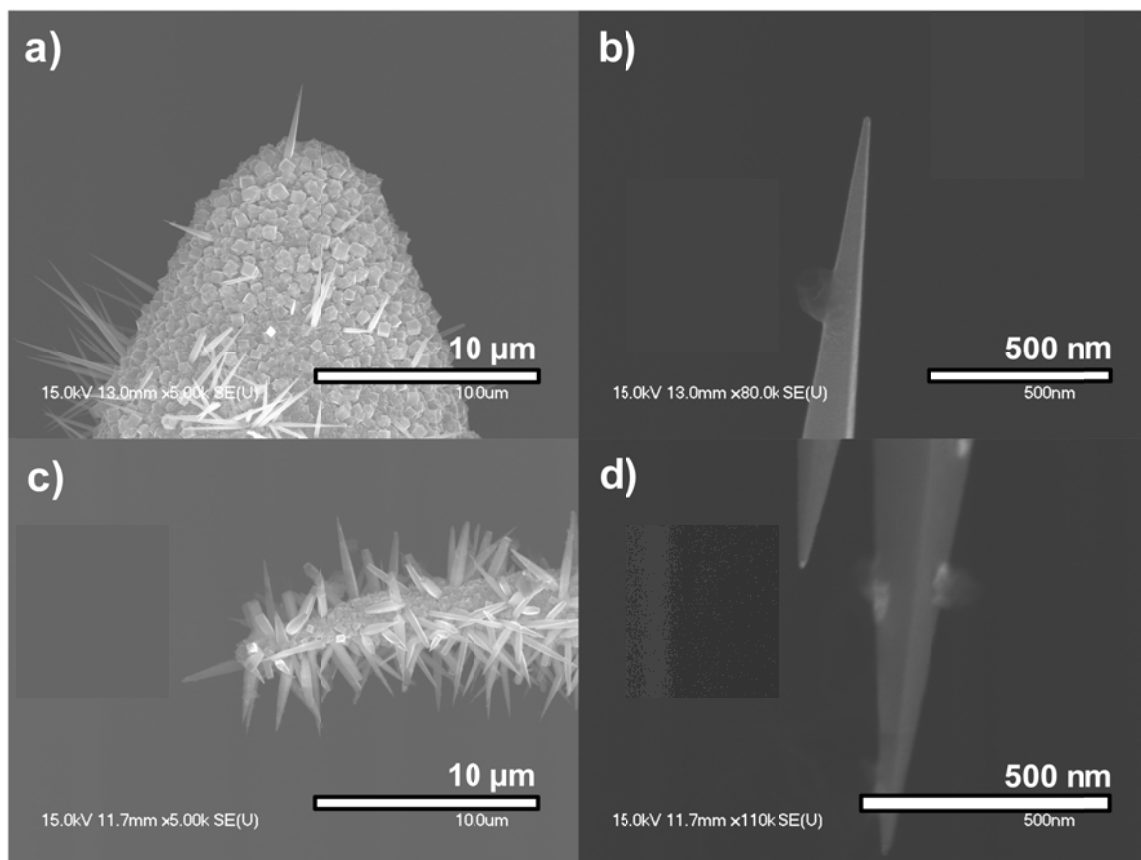


Figure 4.15 SEM images of as-synthesized LaB₆ nanoobelisks on W probes. a) and c) are zoom-out images of linear sweep voltametry and nanoparticle deposited Pd probes, respectively. b) and d) are zoom-in images of a) and c).

the tip of the W probe can be readily identified. 4.15b and d) are zoom-in SEM images of the nanowire tips grown from the W probes in 4.15a and c respectively. The diameters appear to be very similar between the electrodeposited and the nanoparticle deposited Pd.

4.2.4 Conclusions

Robust oxidation resistant conductive nanoprobes were synthesized using the previously developed chemical vapor deposition method. Tungsten probes were reproducibly etched to diameters between 200-500 nm using DC etching in 3M NaOH solution. Linear sweep voltametry was used to deposit both clusters and continuous films of Pd onto the etched W probe tips prior to loading into the horizontal tube furnace. The combination of scanning voltametry in H₂SO₄ solution and CVD process was able to produce occurrences of nanowires directionally grown from the tip and generally had diameters of less than 25 nm.

References

1. Matkovich, V.I. Boron and refractory borides (Springer-Verlag, Berlin; New York, 1977).
2. Samsonov, G.V. High-temperature compounds of rare earth metals with nonmetals (Consultants Bureau, New York, 1965).
3. Warner, D.J., Branam, R.D. & Hargus, W.A. Ignition and plume characteristics of low-current cerium and lanthanum hexaboride hollow cathodes. *J. Propul. Power* **26**, 130-134 (2010).
4. Herring, C. & Nichols, M.H. Thermionic emission. *Rev. Mod. Phys.* **21**, 185 (1949).
5. Jensen, K.L., O'Shea, P.G. & Feldman, D.W. Generalized electron emission model for field, thermal, and photoemission. *Appl. Phys. Lett.* **81**, 3867-3869 (2002).
6. Koeck, F.A.M. & Nemanich, R.J. Field penetration and its contribution to field enhanced thermionic electron emission from nanocrystalline diamond films. *Diam. Relat. Mater.* **15**, 2006-2009.
7. Murphy, E.L. & Good, R.H. Thermionic emission, field emission, and the transition region. *Phys. Rev.* **102**, 1464 (1956).
8. Esaki, L. Long journey into tunneling. *Science* **183**, 1149-1155 (1974).
9. Forbes, R.G. & Deane, J.H.B. Reformulation of the standard theory of Fowler-Nordheim tunnelling and cold field electron emission. *P. Roy. Soc. A-Math Phy.* **463**, 2907-2927 (2007).

10. Fowler, R.H. & Nordheim, L. Electron emission in intense electric fields. *P. Roy. Soc. A* **119**, 173-181 (1928).
11. Maheshwari, V. & Saraf, R.F. High-resolution thin-film device to sense texture by touch. *Science* **312**, 1501-1504 (2006).
12. Maksymovych, P., Jesse, S., Yu, P., Ramesh, R., Baddorf, A.P. & Kalinin, S.V. Polarization control of electron tunneling into ferroelectric surfaces. *Science* **324**, 1421-1425 (2009).
13. Zhu, W., Kochanski, G.P. & Jin, S. Low-field electron emission from undoped nanostructured diamond. *Science* **282**, 1471-1473 (1998).
14. Xu, J.Q., Chen, X.L., Zhao, Y.M., Zou, C.Y. & Ding, Q.W. Single-crystalline PrB6 nanowires and their field-emission properties. *Nanotechnology* **18**, 5 (2007).
15. Xu, J.Q., Zhao, Y.M., Ji, X.H., Zhang, Q. & Lau, S.P. Growth of single-crystalline SmB6 nanowires and their temperature-dependent electron field emission. *J. Phys. D-Appl. Phys.* **42**, 6 (2009).
16. Xu, J.Q., Zhao, Y.M. & Zhang, Q.Y. Enhanced electron field emission from single-crystalline LaB6 nanowires with ambient temperature. *J. Appl. Phys.* **104**, 4 (2008).
17. Zhang, H., Tang, J., Zhang, Q., Zhao, G.P., Yang, G., Zhang, J., Zhou, O. & Qin, L.C. Field emission of electrons from single LaB6 nanowires. *Adv. Mater.* **18**, 87-91 (2006).
18. Zhang, H., Zhang, Q., Zhao, G.P., Tang, J., Zhou, O. & Qin, L.C. Single-crystal line GdB6 nanowire field emitters. *J. Am. Chem. Soc.* **127**, 13120-13121 (2005).

19. International Roadmap Committee. NA (International Technology Roadmap for Semiconductors, 2009).
20. Cabrera, N. & Mott, N.F. Theory of the oxidation of metals. *Rep. Progr. Phys.* **12**, 163 (1949).
21. Nowak, C., Kirchheim, R. & Schmitz, G. Electric-field-induced low temperature oxidation of tungsten nanowires. *Appl. Phys. Lett.* **89**, 143104-3 (2006).
22. Bastiman, F., Cullis, A.G., Hopkinson, M. & Briston, K.J. Two step optimized process for scanning tunneling microscopy tip fabrication. *J. Vac. Sci. Technol. B* **28**, 371-375.
23. Hong, P.N., Cuong, V.V., Thang, B.H., Khoi, P.H. & Minh, P.N. Fabrication of carbon nanotubes on tungsten tips. *J. Korean Phys. Soc.* **52**, 1386-1389 (2008).
24. Brewer, J.R., Deo, N., Wang, Y.M. & Cheung, C.L. Lanthanum hexaboride nanoobelisks. *Chem. Mat.* **19**, 6379-6381 (2007).
25. Wang, G., Brewer, J.R., Chan, J.Y., Diercks, D.R. & Cheung, C.L. Morphological evolution of neodymium boride nanostructure growth by chemical vapor deposition. *J. Phys. Chem. C* **113**, 10446-10451 (2009).

Chapter 5

Growth of gadolinium nitride thin films by chemical vapor deposition

5.1 Introduction

The synthesis of materials combining both ferromagnetic and semiconductor properties has been an elusive but persistent goal of spintronics researchers.¹ The advantages of ferromagnetic semiconductors are their potential as spin-polarized carrier sources which can be easily integrated into semiconductor devices.¹⁻⁴ Towards these goals, the unusual magnetic and electronic properties of rock salt structured gadolinium nitride (GdN) have attracted an increasing research interest. (Figure 5.1) Although the magnetic properties of GdN were once widely debated, most researchers now accept that GdN is ferromagnetic in nature.⁵⁻¹¹ However, there is still a large amount of disagreement over the classification and verification of other properties of GdN. For an example, one study suggests that GdN is an insulator, but its results do not rule out the possible existence of a semi metallic state.¹² However, another study suggests that GdN is a semiconductor⁷ instead because the resistivity of GdN was found to decrease with increasing temperature. If the postulated half-metallic nature of GdN is confirmed, GdN would have great potential applications to produce spin-filtering devices.^{9, 13, 14} Hence, further research is needed to elucidate the controversial findings and physical property predictions of GdN.

The lack of sufficient experimental data to verify the electronic structures and electrical properties of GdN is partially due to the difficulties associated with the synthesis of high quality GdN crystals and thus their availability. The high melting point

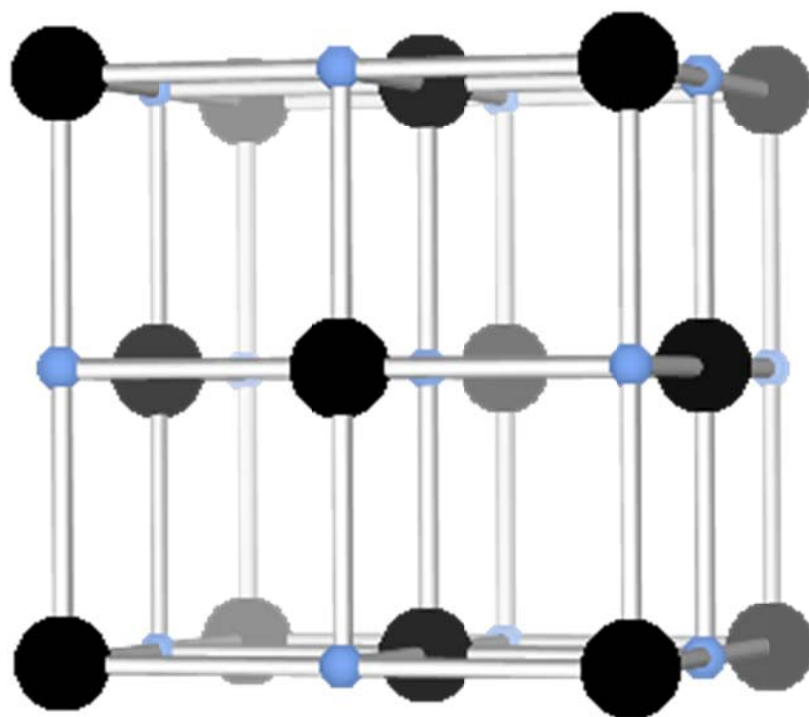


Figure 5.2 Unit cell of gadolinium nitride. Gd (black) and N (blue).

of GdN makes it extremely difficult to directly grow GdN single crystals with consistent and well defined properties.^{9, 15, 16}

Several crystal growth methods such as reactive ion sputtering, hot isostatic pressure synthesis and mechanical milling lead to disordered crystal structure which hampers ordered flow of electrons through the material and can even alter the electrical and magnetic properties.^{9, 15} First-principle calculations confirm these findings, suggesting that even small variations in lattice spacing can alter the electronic properties from half-metallic to semi-metal and ultimately to semiconducting.⁷ This lends the possibility of tuning the properties of the materials for specific applications by dopant incorporation. High quality GdN materials are necessary to determine the material's fundamental properties and allow the study of the effect of dopants and defects on the electronic structure. Previous studies have shown the possibility to synthesize high quality GaN-capped GdN thin films by epitaxial growth on (100) magnesium oxide (MgO) surfaces using a low-energy ion-beam-assisted molecular beam epitaxy technique (MBE).⁵ Nonetheless, this method is costly, time consuming and not easily scalable. Moreover, GdN films produced by MBE so far are reported to have lattice spacing smaller than expected. Therefore, there is still a critical need to develop other methodologies to fabricate highly oriented GdN crystals and films in a low cost, high throughput and reproducible manner for further materials examination.

5.2 Experimental Method

GdN thin films were produced by a chemical vapor deposition scheme with gadolinium (III) chloride hexahydrate and ammonia as the chemical precursors. The reaction was carried out in a 1-foot long horizontal 1"-diameter quartz tube furnace at

925 °C and at a pressure of 100 mTorr for 5-20 min. (Figure 5.2). The overall empirical reaction is:



In a typical experiment, gadolinium (III) chloride hexahydrate (0.3 g $\text{GdCl}_3 \cdot 6\text{H}_2\text{O}$, 99%, Aldrich-Sigma, Milwaukee, WI) was placed on a quartz boat in the upstream end of in a 1" quartz tube furnace at 8 cm from the furnace center. A single-side epi-polished lanthanum aluminum oxide (LaAlO_3) square crystal with [100] orientation with $\pm 0.5^\circ$ miscut (0.5 cm x 0.5 cm x 0.05 cm, $< 5 \text{ \AA}$ surface roughness, MTI cooperation, Richmond, CA) was placed on the quartz boat at a position 6 cm downstream from the $\text{GdCl}_3 \cdot 6\text{H}_2\text{O}$ source material. (Figure 5) Nitrogen gas was introduced to the system at a flow rate of 50 standard cubic centimeters per minute (sccm). The furnace was first heated to a temperature of 400 °C for 10 min. to remove the water content from the $\text{GdCl}_3 \cdot 6\text{H}_2\text{O}$. The furnace was then heated to 925 °C. The nitrogen flow was stopped and anhydrous ammonia was introduced to the system at 5 sccm. The localized temperature at the position of the $\text{GdCl}_3 \cdot 6\text{H}_2\text{O}$ was 762 °C whereas that at the LaAlO_3 substrate position was 966 °C. After a 5-20-min. long reaction, the ammonia flow was stopped and nitrogen added to the reactor at 150 sccm. The furnace was allowed to cool to room temperature. The samples were stored under vacuum before any characterization.

The as-deposited samples were characterized by x-ray diffractometry (XRD) using a Bruker-AXS D8 Discover equipped with a parallel beam point detector (Bruker AXS Inc. Madison, WI). The weighted average wavelength of the $\text{Cu K}\alpha$ x-ray is 1.544 Å. This weighted value was used to calculate the lattice parameters of the GdN films. Rocking

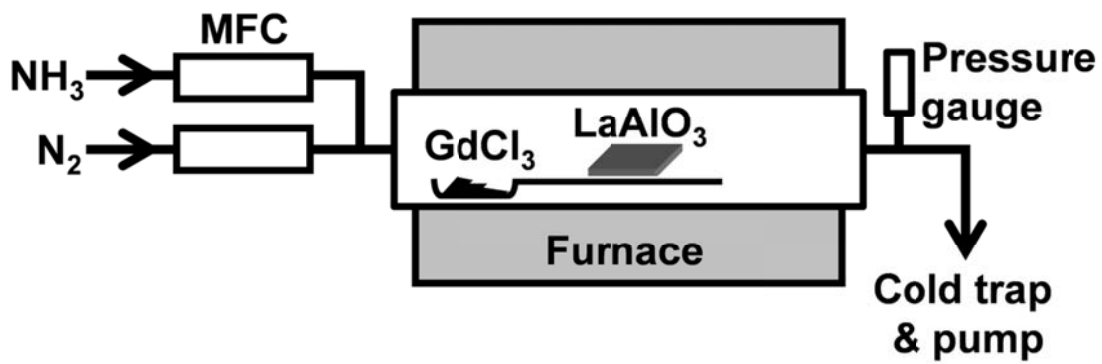


Figure 5.2 Schematic of the chemical vapor deposition set up.

curves of the samples were obtained around 35.9° . The crystal orientation of the GdN thin films was determined by comparing the measured diffraction spectra with the standard ICDD record of GdN crystals. The topography of the as-deposited films were measured using an atomic force microscope (Multi-mode atomic force microscope with a Nanoscope IIIa controller, Veeco Metrology, Inc., Santa Barbara, CA) in tapping mode with silicon probes (Force modulation etched silicon probe, Nanosensor, Gmb, Germany). The thicknesses of the as-deposited films were determined by cross-sectional analysis with a field emission scanning electron microscope (FESEM) operated at 10 kV (Hitachi S4700 field-emission SEM, Hitachi High Technologies America, Pleasanton, CA).

5.3 Sample Characterization

5.3.1 X-ray diffraction

The structural identity of the as-synthesized films was confirmed by matching their XRD pattern with the standard GdN cubic phase pattern (ICDD card # 15-0888) from the ICDD database. Figure 5.3 shows a log-scale 2θ XRD pattern of a 1- μm thick thin film grown at 1000°C for 10 min. The XRD pattern shows a very strong (200) GdN reflection at 35.9° with intensity of about $50\text{-}100 \times 10^3$ counts per each 30-min. scan. Very weak (111) and (220) GdN peaks, which have about three to four orders of magnitude lower intensity than that of the (200) peak, can sometimes be detected. This peak is probably due to the growth of GdN at the terrace crystal steps of slightly miscut and/or twinning commonly found in LaAlO_3 substrates.¹⁷ Peaks located at 26.7° , 31.7° and 40.9° with even smaller intensity of about 50-100 counts suggests the presence of Gd_2O_3 . The

presence of such weak oxide peaks is expected because the non-passivated GdN film samples oxidize in air.

The reported value for an ideal, relaxed GdN lattice parameter a is 4.999 \AA .⁵ The average lattice parameter a calculated from the (200) GdN reflection from our samples is $4.99 \pm 0.01 \text{ \AA}$, which is in very good agreement with the literature values. GdN films made by previously reported molecular beam epitaxy methods were found to completely oxidized in tens of seconds. The fact that our films survived a 30-min.-long *ex situ* XRD measurement in air suggests that our micron thick films did not oxidize as rapidly as previously reported. Furthermore, the rocking curves at the (200) peak position of the textured GdN films on LaAlO_3 had full widths at half maximum (FWHM) of 1.2° . This provides further indication of the improved and high quality of the GdN films than the one previously reported in the literature (FWHM of (200) peak = 1.4°)⁵ (Figure 5.3 inset).

5.3.2 Growth Rate

The growth rate of the GdN films under the described condition was determined by measurements of the film thickness versus reaction time. Reactions were run for 5, 10, 15 and 20 min. The resulting samples were cleaved in half for the SEM cross-sectional analysis. Figure 5.4 is an SEM cross-section image of a sample deposited for 20 min. The film thickness of this sample was measured to be *ca.* 2.02 \mu m . The textured film growth can be inferred from the column-like structures indicated by the arrows. A plot of the film thickness of 5-, 10-, 15- and 20-min samples versus time yields an average film growth rate of approximately $102 \pm 5 \text{ nm/min}$. under the described growth condition. Even though the samples were packed under vacuum during the transport to the SEM facility,

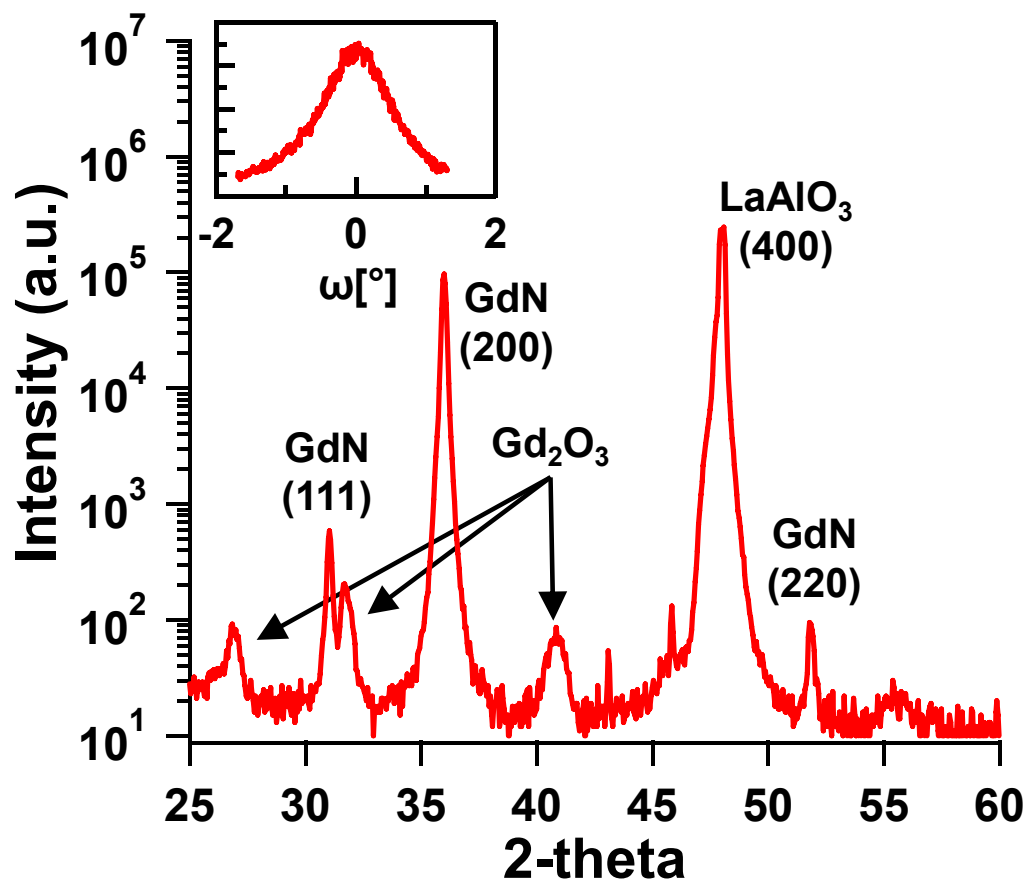


Figure 5.3 X-ray diffraction pattern of a GdN film grown on (100) LaAlO₃ by CVD. The intensity of the (200) GdN diffraction peak is about 3 orders of magnitude higher than those of Gd₂O₃ and other GdN diffraction peaks of other orientations. (Inset) Rocking curve of the same sample at 35.9°.

the samples had to be removed and cleaved under ambient conditions for the microscopy. Thus, it was inevitable to expose the samples to air which led to surface oxidation and eventual delamination of these GdN films. Since the growth substrate LaAlO_3 is an insulator, this sometimes leads to the charging of the samples observed during the electron microscopy sessions.

5.3.3 Surface Structure

The surface morphology of the CVD GdN films was studied using atomic force microscopy (AFM). Figure 5.5 depicts an AFM height image of a 1- μm thick CVD GdN film. The average “grain” (particle) size of this film is 209 ± 26 nm. The root-mean-square roughness value (R_{ms}) for this film of 61 ± 3 nm. By the end of the 1-hour long AFM microscopy session, the color of the sample was observed to change from the metallic golden color to clear and colorless, which indicates the transformation of the material to its oxide form. The large R_{ms} value could possibly be attributed to several factors such as rapid growth rate and large film thickness, both of which could lead to the nucleation of large grains and therefore increased surface roughness.¹⁸

5.3.4 Growth Model

Using the present XRD data and the crystal structures of both the films and the substrates, we postulated that our results could be attributed to a close cube-on-cube lattice matching relationship between GdN and LaAlO_3 as $[100]_{\text{GdN}} \parallel [100]_{\text{LaAlO}_3}$.⁵ The crystal structures shown in Figure 5.6 represents a $[100]$ GdN thin film on the top of a (100) LaAlO_3 surface. If the lattice alignment is viewed over several cells, for example, $3 \times [100]_{\text{GdN}}$ ($3 \times 4.999 \text{ \AA} = 14.997 \text{ \AA}$) and $4 \times [100]_{\text{LaAlO}_3}$ ($4 \times 3.79 \text{ \AA} = 15.16 \text{ \AA}$), a lattice mismatch

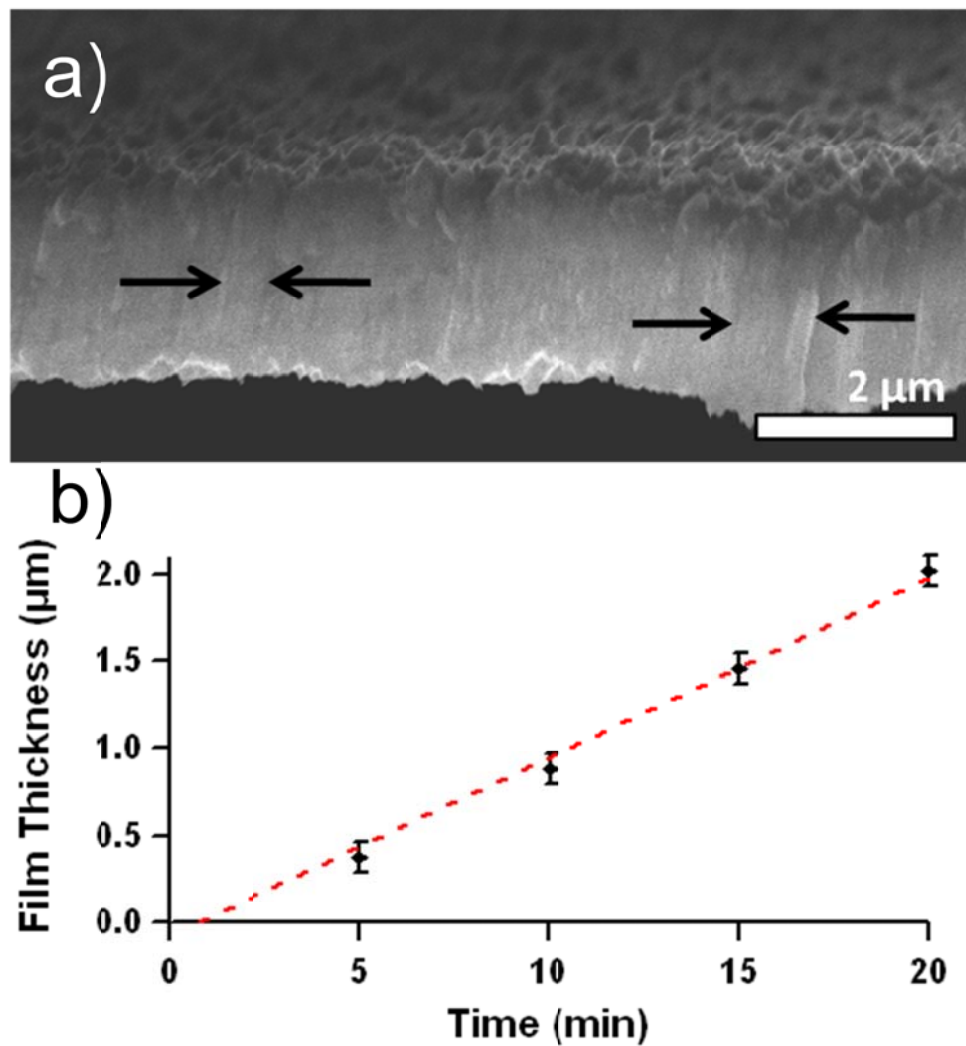


Figure 5.4 (a) Tilted SEM cross sectional image of a delaminated GdN film grown on a (100) LaAlO₃ crystal surface. (Arrows) Thin film columnar structures indicating textured growth. (b) Plot of film thickness as a function of deposition time.

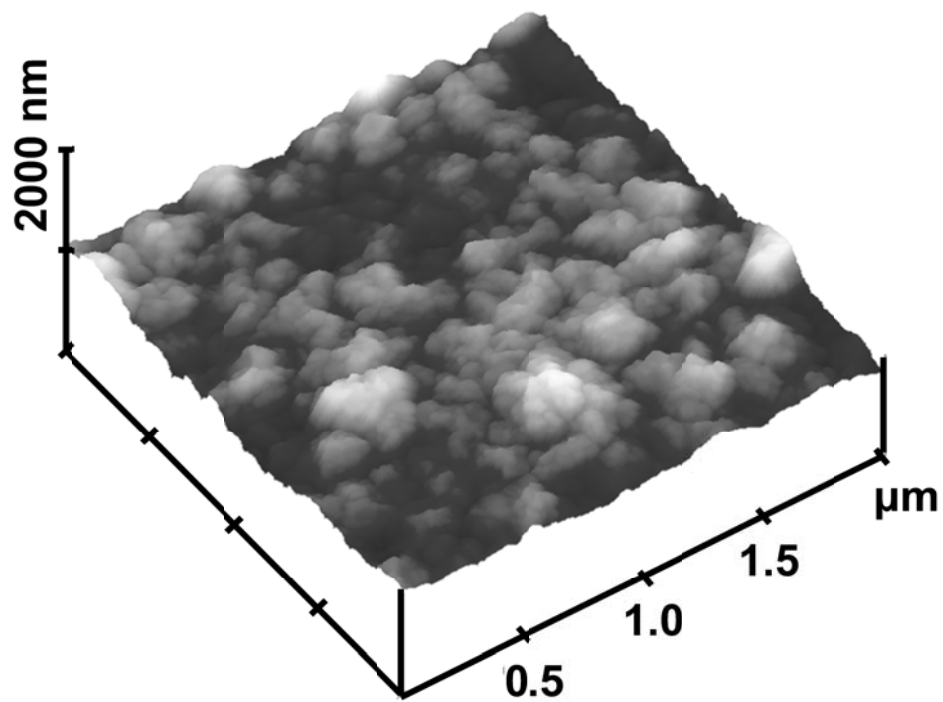


Figure 5.5 Atomic force microscopy height image of an as-deposited 1- μm thick GdN film.

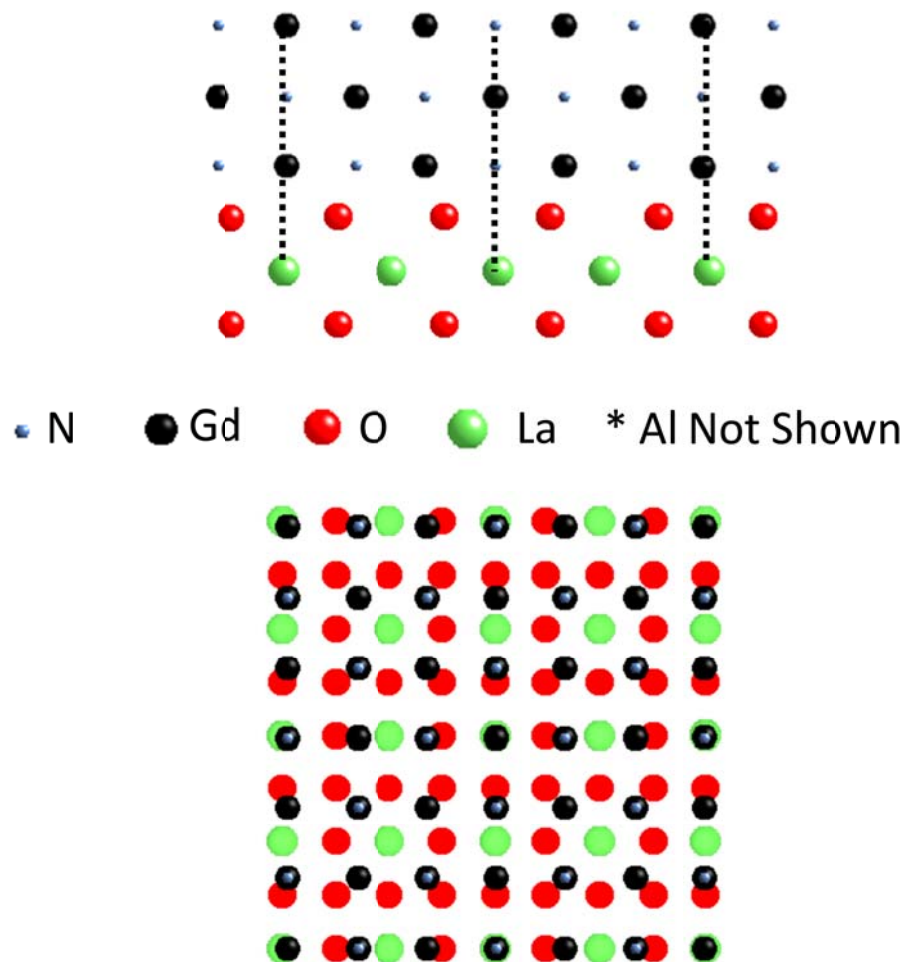


Figure 5.6 Schematic showing the lattice matching of (001) GdN film growth on a (100) LaAlO₃ crystal surface.

of only 1.1% is observed which is on the order of other high quality epitaxial film growth relationships. In this postulated model, every 4th Gd atom aligns closely to the face-center holes of the oxygen octahedral. Short range lattice matching and identical plane epitaxy have previously been used to explain different systems of oriented film growth film on superlattice-site-matched substrates such as MgO on GaAs.¹⁹ In this latter case, the in-plane relationship between the cubic MgO and zinc-blend GaAs follows $[110]_{\text{MgO}} \parallel [100]_{\text{GaAs}}$ with a 4:3 rectangular coincident site lattice.

5.4 Conclusion

I have reported the substrate directed growth of [100] textured gadolinium nitride thin films on (100) lanthanum aluminum oxide (LaAlO₃) single crystal substrates via chemical vapor deposition (CVD). GdN adopts a NaCl rock salt structure whereas LaAlO₃ has a pseudo cubic perovskite structure.²⁰ We applied (100) oriented LaAlO₃ single crystals as the growth substrates due to the lattice matching between the (100) planes of GdN and LaAlO₃. The as-grown dark golden films were typically of about 0.5-1.5 micrometers thick. Their crystallinity was determined by x-ray diffraction (XRD) using the rocking-curve and 2-theta configurations. The morphology of the film was characterized by scanning electron microscopy (SEM) and atomic force microscopy (AFM).

The GdN thin-films synthesized by the presented CVD technique have both methodological and qualitative advantages over films synthesized using other reported techniques. CVD offers a rapid film growth rate of high-quality GdN films with thickness of 1.5 μm in 15 min. This drastically contrasts the slow growth rates reported using other techniques. Previous attempts to synthesize high-quality textured GdN thin films resulted

in a film thickness of only 17 nm in 15 min.⁵ The rocking curve from the CVD GdN thin films had full widths at half maximum (FWHM) of 1.2° , which is comparable to the FWHM of the rocking curve (1.4°) obtained from films grown on a (100) MgO surface by molecular beam epitaxy.⁵

5.5 References

1. Wolf, S.A., Awschalom, D.D., Buhrman, R.A., Daughton, J.M., von Molnar, S., Roukes, M.L., Chtchelkanova, A.Y. & Treger, D.M. Spintronics: A spin-based electronics vision for the future. *Science* 294, 1488-1495 (2001).
2. Zutic, I., Fabian, J. & Das Sarma, S. Spintronics: Fundamentals and applications. *Rev. Mod. Phys.* 76, 323 (2004).
3. Jiang, X., Wang, R., van Dijken, S., Shelby, R., Macfarlane, R., Solomon, G.S., Harris, J. & Parkin, S.S.P. Optical detection of hot-electron spin injection into GaAs from a magnetic tunnel transistor Source. *Phys. Rev. Lett.* 90, 256603 (2003).
4. Wang, D., Park, S., Lee, Y., Eom, T., Lee, S., Lee, Y., Choi, C., Li, J. & Liu, C. Epitaxial ZnMnO/ZnO coaxial nanocable. *Cryst. Growth Des.* 9, 2124-2127 (2009).
5. Gerlach, J.W., Mennig, J. & Rauschenbach, B. Epitaxial gadolinium nitride thin films. *Appl. Phys. Lett.* 90, 3 (2007).
6. Lambrecht, W.R.L. Electronic structure and optical spectra of the semimetal ScAs and of the indirect-band-gap semiconductors ScN and GdN. *Phys. Rev. B* 62, 13538-13545 (2000).
7. Duan, C.G., Sabiryanov, R.F., Liu, J.J., Mei, W.N., Dowben, P.A. & Hardy, J.R. Strain induced half-metal to semiconductor transition in GdN (vol 94, pg 237201, 2005). *Phys. Rev. Lett.* 96, 1 (2006).

8. Larson, P. & Lambrecht, W.R.L. Electronic structure of Gd pnictides calculated within the LSDA+U approach. *Phys. Rev. B* 74, 9 (2006).
9. Leuenberger, F., Parge, A., Felsch, W., Fauth, K. & Hessler, M. GdN thin films: Bulk and local electronic and magnetic properties. *Phys. Rev. B* 72, 8 (2005).
10. Duan, C.G., Sabirianov, R.F., Mei, W.N., Dowben, P.A., Jaswal, S.S. & Tsymbal, E.Y. Magnetic ordering in Gd monopnictides: Indirect exchange versus superexchange interaction. *Appl. Phys. Lett.* 88, 3 (2006).
11. Granville, S., Ruck, B.J., Budde, F., Koo, A., Pringle, D.J., Kuchler, F., Preston, A.R.H., Housden, D.H., Lund, N., Bittar, A., Williams, G.V.M. & Trodahl, H.J. Semiconducting ground state of GdN thin films. *Phys. Rev. B* 73, 5 (2006).
12. Xiao, J.Q. & Chien, C.L. Proximity effects in superconductor/insulating-ferromagnet NbN/GdN multilayers. *Phys. Rev. Lett.* 76, 1727 (1996).
13. Duan, C.G., Sabirianov, R.F., Mei, W.N., Dowben, P.A., Jaswal, S.S. & Tsymbal, E.Y. Electronic, magnetic and transport properties of rare-earth monopnictides. *J. Phys.-Condes. Matter* 19, 32 (2007).
14. Aerts, C.M., Strange, P., Horne, M., Temmerman, W.M., Szotek, Z. & Svane, A. Half-metallic to insulating behavior of rare-earth nitrides. *Phys. Rev. B* 69, 045115 (2004).
15. Li, D.X., Sumiyama, K., Suzuki, K. & Suzuki, T. Spin-glass behavior in mechanically milled crystalline GdN. *Phys. Rev. B* 55, 6467-6472 (1997).
16. Leuenberger, F., Parge, A., Felsch, W., Baudelet, F., Giorgetti, C., Dartyge, E. & Wilhelm, F. X-ray magnetic circular dichroism at the Gd L-2,L-3 absorption

- edges in GdN layers: The influence of lattice expansion. *Phys. Rev. B* 73, 7 (2006).
17. Koren, G. & Polturak, E. Is LaAlO_3 a viable substrate for the deposition of high quality thin films of $\text{YBa}_2\text{Cu}_3\text{O}_{7-\delta}$? *Semicond. Sci. Tech.* 15, 1335 (2002).
 18. Sakama, H., Osada, G., Tsukamoto, M., Tanokura, A. & Ichikawa, N. Epitaxial growth of anatase TiO_2 thin films on $\text{LaAlO}_3(100)$ prepared using pulsed laser deposition. *Thin Solid Films* 515, 535-539 (2006).
 19. Hung, L.S., Zheng, L.R. & Blanton, T.N. Epitaxial-growth of MgO on (100) GaAs using ultrahigh-vacuum electron-beam evaporation. *Appl. Phys. Lett.* 60, 3129-3131 (1992).
 20. Yang, C.Y., Huang, Z.R., Yang, W.H., Zhou, Y.Q. & Fung, K.K. Crystallographic study of lanthanum aluminate by convergent-beam electron diffraction. *Acta Crystallogr. Sec. A* 47, 703-706 (1991).

Chapter 6

Conclusions

6.1 Summary and future directions

The work presented in this dissertation described in detail the synthesis, characterization and device application of REB₆ nanomaterials and GdN thin films. Materials were prepared by the gas phase reaction of rare earth chlorides with decaborane and ammonia, respectively, and were characterized by a range of techniques including SEM, TEM, XRD, LEAP, Van der Pauw measurements and Hall effect measurements.

Chapter 1 introduced rare earth metals and rare earth compounds and discussed the origins of their similar chemical and physical properties. Chapter 1 also discussed the importance of characterizing materials electronically and structurewise. This chapter examined, in detail, the Van der Pauw and Hall effect measurement techniques for determining electronic properties of crystalline materials and the use of x-ray diffraction for characterizing their crystalline quality.

Chapter 2 introduces REB₆ materials, their properties and compares the past and present synthesis methods. The development of a chemical vapor deposition method for the general synthesis of REB₆ nanostructures was examined in detail by varying the growth temperatures and locations of the silicon substrate. The REB₆ nanomaterials were characterized by SEM, TEM and XRD and were found to be single crystalline and had (100) growth directions. The Van der Pauw and Hall effect measurements conducted on CVD grown thin films determined that the materials had similar electronic properties as compared to results published in literature.

Continued research on the templated growth of REB_6 nanostructures is necessary for the optimization of the materials toward current nanoscale device applications. This includes further improving the deposition process and improving the crystalline quality of the IBAD-deposited ZrN thin films. Also, measurement of the electronic properties of the individual REB_6 nanostructures still needs to be conducted to determine the quality of the nanowires and their nanoscale charge transport properties.

Chapter 3 introduces local electrode atom probe tomography (LEAP) and discusses its advantages over traditional materials characterization techniques such as TEM, EDS and XPS. The chapter also describes the development of a TEM based LEAP which allows for the crystallographic and compositional analysis of individual nanowires without substrate templating. The LEAP results provided the first ever 3-D atomic level composition maps of rare earth hexaboride materials and determined that the nanowire were stoichiometric REB_6 . The LEAP also determined that the nanowires had no Pd diffused into the bulk from the catalyst particle. The first-ever RE-doped REB_6 nanowires were also synthesized and analyzed. LEAP analysis determined that the doped nanowire had a lateral dopant concentration profile and a model for dopant incorporation into the nanowires was developed.

Chapter 4 discusses the historical application of REB_6 single crystals and thin films and introduces the theory of electron emission. The field emission properties of REB_6 nanowires arrays were tested by adjusting the varying the growth substrate and the anode-cathode separation distance. The emission studies indicated the IBAD-deposited ZrN substrates improved the emission properties of the REB_6 arrays while increasing the separation distance made the emission process more efficient. Next, the application of

REB₆ nanoobelisks as nanoscale electronic probes was discussed. A tungsten etching process was developed to generate tungsten wires with 200-500 nm tip diameters. Pd particles were deposited on the tips by linear sweep voltametry and the nanoobelisks were synthesized using chemical vapor deposition. Single LaB₆ nanoobelisks were grown from several of the tungsten probes and had tip diameters of < 25 nm.

Further improvements in the deposition of the Pd and the REB₆ nanowires still need to be address. The deposition of the Pd is possibly the most important step in the process of the making single nanowire manipulator probes. If the deposition can be controlled and localized at the tip, it is reasonable to believe that on axis growth of the REB₆ nanowires could be achieved through the use of electric field enhanced CVD.

Chapter 5 examines the application of the hydride vapor phase based CVD synthesis of REB₆ materials toward the synthesis of other RE compounds. The synthesis of gadolinium nitride thin films was examined by varying the precursor flux, growth time and substrate. The growth rate of the CVD synthesized GdN was much faster than that of previously reported results and the LaAlO₃ substrate provided an excellent template for orientation of the (100) crystallographic plane. Device application for GdN thin films is limited due to its rapid oxidation in air. Depositing thin film capping layers of GaN could be a possible route to limit the oxidation of the thin films without significantly altering its electronic properties.